



UNITED NATIONS
UNIVERSITY

UNU-GTP

 **ORKUSTOFNUN**



Sulphur deposits in Leirhnjúkur, Krafla area, NE-Iceland

Maureen Nechesa Ambunya

**PROCESSING AND INVERTING RESISTIVITY SOUNDINGS FROM
MT. LONGONOT FIELD, KENYA. AN INTERPRETATION OF THE
SUBSURFACE RESISTIVITY STRUCTURE IN THE CONTEXT
OF THE GEOTHERMAL FIELD**

Report 4
December 2017



UNITED NATIONS
UNIVERSITY

UNU-GTP

Geothermal Training Programme

Orkustofnun, Grensasvegur 9,
IS-108 Reykjavik, Iceland

Reports 2017
Number 4

**PROCESSING AND INVERTING RESISTIVITY SOUNDINGS FROM
MT. LONGONOT FIELD, KENYA. AN INTERPRETATION OF THE
SUBSURFACE RESISTIVITY STRUCTURE IN THE CONTEXT OF
THE GEOTHERMAL FIELD**

MSc thesis

School of Engineering and Natural Sciences
Faculty of Earth Sciences
University of Iceland

by

Maureen Nechesa Ambunya
Kenya Electricity Generating Company
Reservoir Engineering department
P.O. Box 785, Naivasha
KENYA
mambunya@kengen.co.ke

United Nations University
Geothermal Training Programme
Reykjavík, Iceland
Published in December 2017

ISBN 978-9979-68-463-3 (PRINT)
ISBN 978-9979-68-464-0 (PDF)
ISSN 1670-7427

This MSc thesis has also been published in August 2017 by the
School of Engineering and Natural Sciences, Faculty of Earth Sciences
University of Iceland

INTRODUCTION

The Geothermal Training Programme of the United Nations University (UNU) has operated in Iceland since 1979 with six-month annual courses for professionals from developing countries. The aim is to assist developing countries with significant geothermal potential to build up groups of specialists that cover most aspects of geothermal exploration and development. During 1979-2017, 670 scientists and engineers from 60 developing countries have completed the six month courses, or similar. They have come from Africa (39%), Asia (35%), Latin America (14%), Europe (11%), and Oceania (1%). There is a steady flow of requests from all over the world for the six-month training and we can only meet a portion of the requests. Most of the trainees are awarded UNU Fellowships financed by the Government of Iceland.

Candidates for the six-month specialized training must have at least a BSc degree and a minimum of one-year practical experience in geothermal work in their home countries prior to the training. Many of our trainees have already completed their MSc or PhD degrees when they come to Iceland, but many excellent students with only BSc degrees have made requests to come again to Iceland for a higher academic degree. From 1999 UNU Fellows have also been given the chance to continue their studies and study for MSc degrees in geothermal science or engineering in cooperation with the University of Iceland. An agreement to this effect was signed with the University of Iceland. A similar agreement was also signed with Reykjavik University in 2013. The six-month studies at the UNU Geothermal Training Programme form a part of the graduate programme.

It is a pleasure to introduce the 55th UNU Fellow to complete the MSc studies under a UNU-GTP Fellowship. Maureen Nechesa Abunya, BSc in Physics from Kenya Electricity Generating Company – KenGen, completed the six-month specialized training in Reservoir Engineering at UNU Geothermal Training Programme in October 2014. Her research report was entitled: *Natural-state model update of Olkaria Domes geothermal field*. After one and a half year of geothermal energy work in Kenya, she came back to Iceland for MSc studies in Geophysical Exploration at the School of Engineering and Natural Sciences, Faculty of Earth Sciences, University of Iceland in January 2016. In August 2017, she defended her MSc thesis presented here, entitled: *Processing and inverting resistivity soundings from Mt. Longonot field, Kenya. An interpretation of the subsurface resistivity structure in the context of the geothermal field*. Her studies in Iceland were financed by the Government of Iceland through a UNU-GTP Fellowship from the UNU Geothermal Training Programme. We congratulate Maureen on the achievements and wish her all the best for the future. We thank the School of Engineering and Natural Sciences, Faculty of Earth Sciences, University of Iceland for the cooperation, and her supervisors for the dedication.

Finally, I would like to mention that Maureen's MSc thesis with the figures in colour is available for downloading on our website www.unugtp.is, under publications.

With warmest greetings from Iceland,

Lúdvík S. Georgsson, Director
United Nations University
Geothermal Training Programme

ACKNOWLEDGEMENTS

My sincere gratitude goes to United Nations University Geothermal Training Programme (UNU-GTP) for awarding the scholarship for this study. To Mr. Lúdvík S. Georgsson, the Director of the UNU Geothermal Training Programme for the opportunity to take part in the studies, the Deputy Director, Mr. Ingimar Gudni Haraldsson, for his help and support, Ms. Thórhildur Ísberg, Mr. Markús A. G. Wilde and Ms. Málfríður Ómarsdóttir for their great support during my study and stay in Iceland. To my advisors, Gylfi Páll Hersir and Ásdís Benediktsdóttir, geophysicists at Iceland GeoSurvey (ÍSOR) and Professor Magnús Tumi Gudmundsson at the University of Iceland for their diligent assistance and constructive feedback and knowledge during my research project.

To my employer, the Kenya Electricity Generating Company Ltd. for the study leave. To Reykjavik energy for making data available while practicing processing of MT data. My sincere thanks to Charles Muturia Lichoro for his great assistance with the data modelling and for being there whenever I needed his help. To Ammon Omiti who made the data available. To UNU MSc and PhD students, thank you for the magnificent time and discussions we shared.

Thanks to my wonderful mother for her love and encouragement, and my sister Phanice for the great support. To my lovely husband Justice for his continuous support and encouragement. Finally, I thank God for His sufficient grace that made the programme possible.

DEDICATION

I dedicate this work to my son Prince Avidan who arrived to the world majestically during my research and to my daughter Michelle Nelima for her patience with me as I pursue my studies.

ABSTRACT

Exploration of geothermal resources has become an important practice in volcanic regions. Geophysical methods play a major role in surface exploration studies of geothermal resources. Among the geophysical methods used in exploration are resistivity methods as well as seismic, gravity and magnetic methods. Electrical resistivity methods, Magnetotellurics (MT) and Transient Electromagnetics (TEM), which are commonly used in mapping the subsurface resistivity variations, are described in this work.

The MT and TEM data, which are used in this study were collected in the Mt. Longonot high temperature geothermal field in Kenya, located within the Great East African Rift System. As a part of this project the data were processed and 1-D inverted, and the results presented as resistivity cross sections and depth slices.

Strong geothermal manifestations and recent eruptions are indicative of a heat source under the caldera, which could be at a shallow depth beneath the summit crater.

From the results found using 1-D modelling of the MT/TEM data, the resistivity structure of Mt. Longonot field has mainly four resistivity sections. A high resistivity zone of unaltered formations close to the surface, a low-resistivity anomaly observed at shallow depth, a high resistivity zone associated with the change in alteration minerals from low to high temperature mineralogy, and a conductive zone that dominates to the southeast of the study area and just below the summit crater. It could be associated with a heat source.

It can be inferred from the study that Mt. Longonot is a fracture controlled geothermal system. This is because the conductive layer is aligned along the eruption centers that are in line with the Tectono Volcanic Axis structure and the numerous volcanic centers to the southeast of the field.

TABLE OF CONTENTS

	Page
1. INTRODUCTION.....	1
2. MT. LONGONOT AND THE EAST AFRICAN RIFT SYSTEM	3
2.1 Tectonic features	3
2.2 Geographical setting of the study area	4
2.3 Geology of Mt. Longonot geothermal area	5
2.4 Geothermal manifestations and structures in Mt. Longonot area.....	10
2.5 Hydrology of Mt. Longonot	10
2.6 Previous geoscientific studies and outcomes.....	11
2.6.1 Thermal survey.....	11
2.6.2 Gravity survey.....	12
2.6.3 Geochemical studies.....	12
3. APPLYING RESISTIVITY IN GEOTHERMAL AREAS	15
3.1 Resistivity methods	15
3.2 Resistivity of water bearing rocks	15
3.3 Specific resistivity	15
3.4 Conduction mechanism in geothermal systems.....	16
3.5 Factors affecting resistivity	17
3.5.1 Water rock interaction.....	17
3.5.2 Porosity	18
3.5.3 Temperature	19
3.5.4 Salinity of the pore fluid.....	19
3.6 Resistivity structure of geothermal systems	20
4. MAGNETOTELLURIC (MT) METHOD.....	21
4.1 MT theory.....	21
4.2 Source field of MT signals	21
4.3 MT Principles	22
4.3.1 Assumptions used in MT.....	22
4.3.2 Maxwell's equations	22
4.3.3 Uniform half space.....	26
4.3.4 Layered earth.....	27
4.3.5 Skin depth.....	29
4.4 MT transfer functions	29
4.4.1 Geomagnetic transfer functions	29
4.4.2 Impedance tensor	30
4.4.3 Mathematical rotation of impedance tensor	33
4.4.4 Geoelectrical strike analysis.....	34
4.4.5 Dimensionality measures	35
4.5 Problems in MT measurements	37
4.5.1 MT static shift problem.....	37
4.5.2 Dead band problem	38
5. TEM SURVEY	40
5.1 Theory	40
6. ACQUISITION AND PROCESSING OF EM DATA FROM MT. LONGONOT GEOTHERMAL AREA.....	43
6.1 TEM data processing.....	43
6.2 MT data processing	45
6.2.1 MT field setup and data collection.....	45
6.2.2 The MT data processing technique	46

	Page
6.2.3 Data review and editing.....	46
6.2.4 Estimation of transfer functions	47
6.2.5 Remote reference and MT impedance estimation	48
7. MODELING AND INTERPRETATION OF EM FROM MT. LONGONOT FIELD	51
7.1 Overview	51
7.2 1-D inversion program	51
7.3 1-D joint inversion of TEM and MT soundings.....	53
7.4 Static shifts correction of MT in Mt Longonot	53
8. 1-D JOINT INVERSION RESULTS.....	56
8.1 1-D Cross-sections.....	56
8.2 1-D resistivity depth slices	62
8.3 Discussion of 1-D inversion results.....	65
8.4 Geo-electric strike analysis of MT data.....	65
8.4.1 Zstrike	65
8.4.2 Tipper and induction arrow	65
8.5 Geologic and geothermal interpretation	68
9. CONCLUSIONS AND RECOMMENDATIONS.....	69
REFERENCES.....	70
APPENDIX A: Location and elevation of TEM and MT soundings	77
APPENDIX B: Processed MT data.....	80
APPENDIX C: 1-D joint inversion of TEM and MT data.....	98
APPENDIX D: 1-D inversion of MT data using geospatial static shift distribution.....	104
APPENDIX E: Resistivity depth slice	111

LIST OF FIGURES

1. Geothermal areas within the Kenyan Rift, Africa.....	2
2. The East African Rift System.	3
3. Location of Mt. Longonot geothermal field within Kenyan rift	4
4. Map in UTM coordinates showing Olkaria ring structure and both the outer and inner Mt. Longonot caldera.....	5
5. DEM of the Kenyan Rift System with the black lines showing the general orientation of the rift.	6
6. Central Kenyan Rift System.	7
7. Mt. Longonot geological sequence	8
8. InSAR data from Mt. Longonot show vertical movement of up to 9 cm.....	9
9. Mt. Longonot features.....	9
10. A piezometric map of Southern Kenya Rift showing the flow of water.....	10
11. Surface geothermal features verified by SKM during the 2010 fieldwork.	11
12. Gravity anomaly map and W-E profile through Mt. Longonot Crater	12
13. Map in UTM coordinates showing the extent of a buried caldera	13
14. CO ₂ concentration in the vicinity of Mt. Longonot	13

15.	Mapview figures showing temperature based on H ₂ S geothermometer and H ₂ S concentration..	14
16.	Typical ranges of electrical resistivity (Ωm) and conductivity (Sm^{-1}).....	16
17.	Resistivity definition layout	16
18.	Conduction mechanisms in a pore	16
19.	Profile from well KJ-18 in Krafla, NE-Iceland showing CEC	18
20.	Example of pores spaces	18
21.	Electrical resistivity of a NaCl solution as a function of temperature.....	19
22.	Typical resistivity structure of a high temperature geothermal field where the host rocks are volcanic.....	20
23.	A summary of the general resistivity structure of a high temperature field.....	20
24.	The setup of an MT sounding	21
25.	Variations of the magnetosphere due to interaction with the solar wind	21
26.	Energy refraction at the boundary between two media of refractive indices.....	22
27.	Electric and magnetic field response for a homogeneous half-space.....	27
28.	An N-layered earth.....	27
29.	Two-layered earth	27
30.	Homogenous conducting half space with sinusoidal wave	29
31.	N-layered earth model with σ varying in z-direction.....	31
32.	Geometry of electromagnetic field components over a 2-D Earth.....	31
33.	A 3-D earth model.....	32
34.	The rotation of axes clockwise by angle θ' ($^\circ$), from OX and OY (north and east) to OX' and OY'.....	33
35.	Polar diagrams of the impedance tensor	36
36.	Current channelling due to an inhomogeneous conductivity	38
37.	Total current distribution and secondary electric field due to topography and correction for the topographical effect.....	38
38.	Electric field distortion.....	38
39.	The mean natural magnetic field amplitude spectrum in gamma ($\gamma=nT$)	39
40.	The central loop TEM configuration	40
41.	Late time apparent resistivity for a homogeneous half space	42
42.	Voltage response for homogeneous half space	42
43.	Display from TemxZ program.	43
44.	Flow diagram showing inversion algorithm improvement of the model based on misfit.....	44
45.	Two examples of an inversion done by the TEMTD program.	44
46.	MT layout.....	45
47.	The processing steps used.....	46
48.	Time series data acquired by a 5-channel MT data acquisition system.....	47
49.	EDI output showing apparent resistivity and phase curves.....	50
50.	TEM location map of the Mt. Longonot field and MT location map of the same area	52
51.	Sample MT and TEM data plot after 5 iteration in the Occam's inversion.	53
52.	Examples of the results of joint 1-D inversion of TEM and MT data	54
53.	Histogram and spatial distribution of static shift parameters.....	54
54.	A typical example of joint 1-D inversion of TEM and MT data.....	55
55.	Location of the cross-sections.....	56
56.	Resistivity cross-section obtained from 1-D joint inversion of TEM and MT data.....	57
57.	Resistivity cross-section obtained from 1-D joint inversion of TEM and MT data.....	58
58.	Resistivity cross-section obtained from 1-D joint inversion of TEM and MT data	58
59.	Resistivity cross-section obtained from 1-D joint inversion of TEM and MT data.....	59
60.	Resistivity cross-section obtained from 1-D joint inversion of TEM and MT data.....	60
61.	Resistivity cross-section obtained from 1-D joint inversion of TEM and MT data.....	60
62.	Resistivity cross-section obtained from 1-D joint inversion of TEM and MT data.....	61
63.	Resistivity cross-section obtained from 1-D joint inversion of TEM and MT data.....	61
64.	Resistivity cross-section obtained from 1-D joint inversion of TEM and MT data.....	62

	Page
65. Resistivity at 1500 m a.sl. from 1-D inversion of TEM and MT data	63
66. Resistivity at 1000 m b.sl. from 1-D inversion of TEM and MT data	64
67. Resistivity at 4000 m b.sl. from 1-D inversion of TEM and MT data	64
68: Rose diagram of the Zstrike for the period interval, 0.01-10 s.	66
69: Rose diagram of the Zstrike for the period interval, 10-1000 s.	66
70. Rose diagram of the Tipper strike for the period interval, 0.01-10 s.	67
71. Rose diagram of the Tipper strike for the period interval, 10-1000 s.	67
72. Induction arrows for the period 100 s.	68

LIST OF TABLES

1. Mt. Longonot geological history	10
2. Classification of several electrical methods and their depth of penetration.....	15
3. Location and elevation of TEM and MT soundings.	84

NOMENCLATURE AND ABBREVIATIONS

1-D	One dimensional
2-D	Two dimensional
3-D	Three dimensional
ρ (Ωm)	Bulk (measured) resistivity
ρ_w (Ωm)	Resistivity of the pore fluid
Φ_t	Fractional porosity
\mathbf{E} (Vm^{-1})	Electrical field
\mathbf{J} (Am^{-2})	Electric current density
σ (Sm^{-1})	Electric conductivity
I (A)	Electric current
CEC (meqg^{-1})	Cation-exchange capacity
AC/ DC	Alternating current/ Direct current
η (Cm^{-3})	Electric charge density of free charges
\mathbf{B} (T)	Magnetic induction
ϵ (F/m)	Electric permittivity
\mathbf{D} (Cm^{-2})	Electric displacement
μ (H/m)	Magnetic permeability
\mathbf{H} (Am^{-1})	Magnetic intensity
Ka	Thousand years
Bp	Before present
DEM	Digital elevation models
InSAR	Interferometric synthetic aperture radar (InSAR)
EM	Electromagnetic
EARS	East African Rift System
EDI	Electrical Data Interchange files
MT	Magnetotelluric
AMT	Audio magnetotelluric
m a.sl	Metres above sea level
m b.sl	Metres below sea level
TEM	Transient Electromagnetic
TE	Transverse Electric
TM	Transverse Magnetic

TemxZ	Program for processing Zonge TEM data
TEMTD	1-D MT/TEM inversion program
ÍSOR	Iceland GeoSurvey
KenGen	Kenya Electricity Generating Company
GOGA	Great Olkaria geothermal area
Aus	Additional units

1. INTRODUCTION

One of the geophysical methods used in geothermal exploration is resistivity measurements. Resistivity of rocks is sensitive to temperature and geothermal mineral alteration. The two factors are directly related to parameters characterizing geothermal reservoir (Flóvenz et al., 2012). For this reason, electrical resistivity methods such as Magnetotellurics (MT) and Transient Electromagnetics (TEM) are the most powerful geophysical tools used in geothermal exploration for decades to check the geothermal properties of geothermal systems prior to drilling. With these methods, the physical properties of the Earth's crust are examined (Eysteinnsson et al., 1994). As a result, geophysical exploration methods play a major role in demarcating geothermal resources. These methods in combination with other exploration methods such as geology and geochemistry are used to site wells that are then drilled to extract the hot fluids required for geothermal utilization.

Currently the most utilized geophysical methods in geothermal exploration are electrical resistivity methods, Magnetotellurics (MT) and Transient Electromagnetics (TEM). Properties influencing the electrical resistivity of rocks are fluid content, porosity, degree of fracturing, temperature, and mineral content (Keller, 1989). In the presence of conductive clay minerals such as smectite and metallic mineralization, resistivity is reduced. In volcanic rocks, there are authigenic minerals that are ten times more conductive than the surrounding rocks. As long as these altered minerals are connected, they will decrease the resistivity of rock matrices significantly (Nelson and Anderson, 1992). Increase in temperature reduces resistivity of rocks. This is due to higher ionic kinematics. However, in geothermal areas, this scenario can be reversed whereby an increase in temperature causes high temperature minerals like epidote to increase the rock resistivity (Árnason and Flóvenz, 1995). In the case of unaltered rocks formation, moderate to high resistivity units are usually recorded (hundreds to thousands of Ωm), but fault zones will show lower resistivity when they contain fluid (Eberhart-Phillips et al., 1995). Saline fluids within pore spaces and fracture openings can reduce the resistivity of a rock matrix considerably (Eysteinnsson et al., 1994).

Geothermal potential is rampant in many African countries that are located within the East African Rift System (EARS). Within the EARS, volcanic eruptions take place in various locations resulting in heat energy being transferred to the surface in form of earthquakes, hot springs and vapour radiations. Some of the countries within EARS with geothermal potential are Eritrea, Djibouti, Ethiopia, Kenya, Tanzania, Uganda, Rwanda, the Democratic Republic of Congo (DRC), Zambia, Malawi, Mozambique and Madagascar. Kenya and Ethiopia are the only countries exploiting geothermal energy (Teklemariam, 2013). Kenya has an installed capacity of 636 MWe and Ethiopia has installed capacity of about 7 MWe. Geothermal energy resource potential within the EARS is estimated to be more than 15,000 MWe (Teklemariam, 2013).

In the Kenyan rift, which is a segment of the East African Rift System, numerous geothermal activities are found. There are about fourteen high temperature geothermal prospect areas (Figure 1) that are linked with Quaternary volcanic centers arising in the axial region of the Kenyan rift (Omenda, 1998). The process of rifting and events of geothermal activities is primarily due to shallow magma chambers or intrusives below the young volcanoes within the rift axis. Currently, there are two geothermal fields under exploitation for electricity production: the GOGA (Great Olkaria geothermal area) area and the Eburru geothermal field (Figure 1).

The GOGA field is inside a major volcanic complex cut by N-S trending normal rifting faults and defined by several volcanic rhyolitic domes. Exploration of the GOGA commenced in 1956 and thereafter deep drilling began in 1973. Currently, there are five power plants installed and producing electricity in GOGA; Olkaria I with 45 MWe capacity, Olkaria II with 105 MWe capacity, Olkaria III operated by OrPower4 Inc. with 140 MWe capacity, Olkaria IV with 150 MWe capacity and Olkaria I AUs (Additional Units) with 150 MWe capacity. Surrounding GOGA geothermal prospects, are Suswa to the south, Mt. Longonot to the east and Eburru to the north east (Figure 1). Eburru is currently producing 2.5 MWe from one of the six exploratory wells.

This study is based on EM resistivity survey of Mt. Longonot geothermal prospect area. The TEM data from the field have been processed and inverted for while EDI files from KenGen are used to study and interpret the subsurface resistivity structure of the Mt. Longonot prospect field in the context of the geothermal field. Data from Reykjavik Energy was used for practicing the processing technique of MT through SSMT2000 and MTEditor programs.

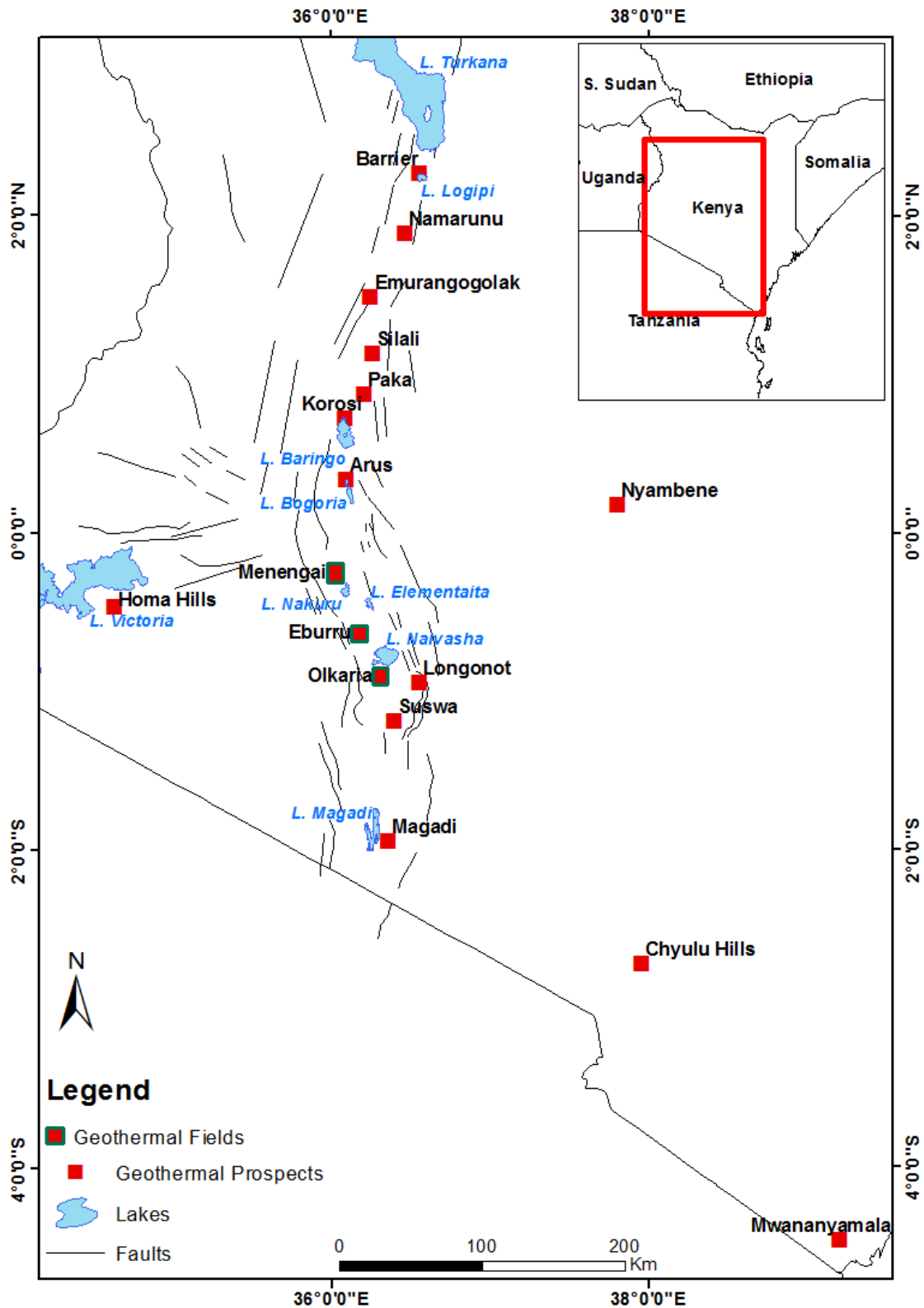


FIGURE 1: Geothermal areas within the Kenyan Rift, Africa (modified from Clarke et al., 1990; and Simiyu, 2010)

2. MT. LONGONOT AND THE EAST AFRICAN RIFT SYSTEM

2.1 Tectonic features

The East African Rift System (EARS) is located within the Eastern horn of Africa and extends southwards (Figure 2). A rift can be defined as a fracture on the Earth's surface that expands over time. The EARS is a part of a continental divergent zone where spreading results in the thinning of the crust and the eruption of lava and associated volcanic activities (Lagat, 2004). Active seismicity, volcanic activity and heat flux characterize the rift system.

In the case of EARS, the Earth's tectonic forces are creating a new tectonic plate by splitting apart an older one (African plate). The process displayed in the EARS has inspired geologists to name the new plates the Nubian Plate that makes up most of Africa and the Somalian plate which is the smaller one (Figure 2). These two plates are moving away from each other and away from the Arabian Plate to the north. The triple junction of the Nubian, Somalian and Arabian Plates is in the Afar region of Ethiopia (Chorowicz, 2005).

Figure 2 shows the main branches of EARS. The **Eastern rift** that consists of the Afar region, Ethiopian rift, Omo-Turkana lowlands, Kenya (Gregory) rift and the North Tanzanian divergence. The **Western rift** that consists of the great rift lakes including Lake Tanganyika, Lake Rukwa and Southern segment consisting of Malawi rift and finally the **Southeastern rift** (Chorowicz, 2005; Saemundsson, 2010).

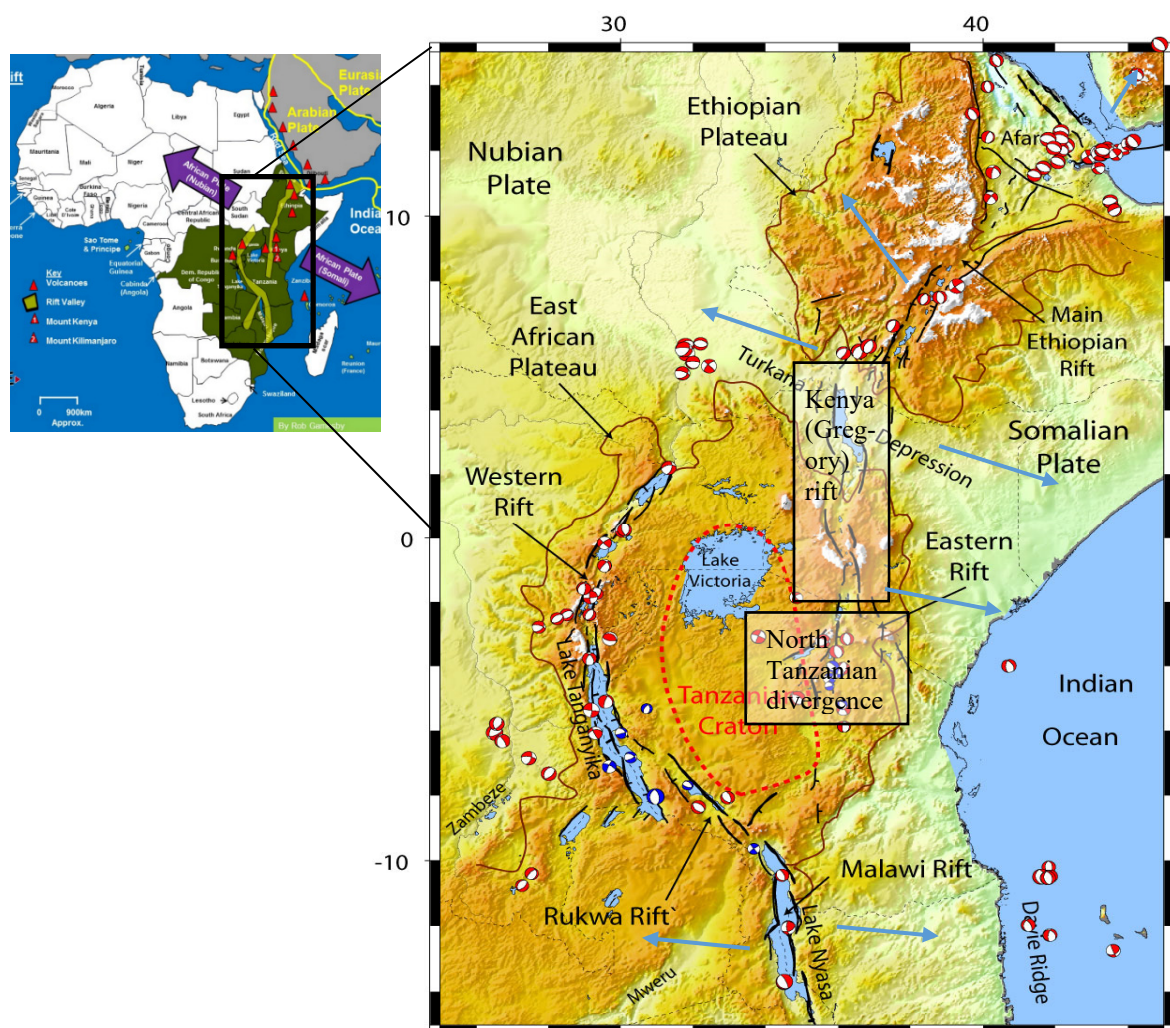


FIGURE 2: The East African Rift System: the red and white filled circles indicate the focal mechanisms for earthquakes in the area and blue arrows are the spreading directions (modified from web.ics.purdue.edu/~ecalais/projects/ear/tectonics.jpg)

The EARS formation is through a domal uplift and spreading. These processes in turn cause the brittle crust to fracture into a series of normal faults giving the classic horst and graben structure of rift valleys (MacGregor, 2015). An assumption for EARS from one of the popular models is that an elevated heat flow from the mantle is triggering thermal bulges in central Kenya and the Afar region of north-central Ethiopia. Most current geological thinking holds that mantle plumes beneath the continent heats the overlying crust causing it to expand and fracture initiating bulges (Wood and Guth, 2013). A triple junction is created from the three dominant fractures radiating from a point with an angular separation of 120°. The stretching process associated with rift formation is often preceded by huge volcanic eruptions, with lava flow over large areas and are usually restricted on the flanks of the rift (MacGregor, 2015). The lava erupted along fissures (rather than at individual volcanoes). The oldest and well defined rift is situated in the Afar region of Ethiopia and is usually referred to as the Ethiopian Rift.

2.2 Geographical setting of the study area

Mt. Longonot is a stratovolcano located to the southeast of Lake Naivasha within the Kenyan Rift, Africa. It is approximately 100 km northwest of Nairobi at the southern end of the Kenyan rift bounded by faulted Mau Escarpment to the west (Figure 3). The Mountain is among the fourteen geothermal fields within the Great Rift Valley of Kenya. It is between the rhyolite dome field of Olkaria, which is 10 km to the west and the phonolite-dominated Suswa located about 30 km to the south (Figure 3). Its crater floor measures about 3.2 km from east to west. The crater rim on the northern part of the mountain reaches an elevation of 2886 m. Deep ridges on the entire perimeter of the crater mainly characterize it.

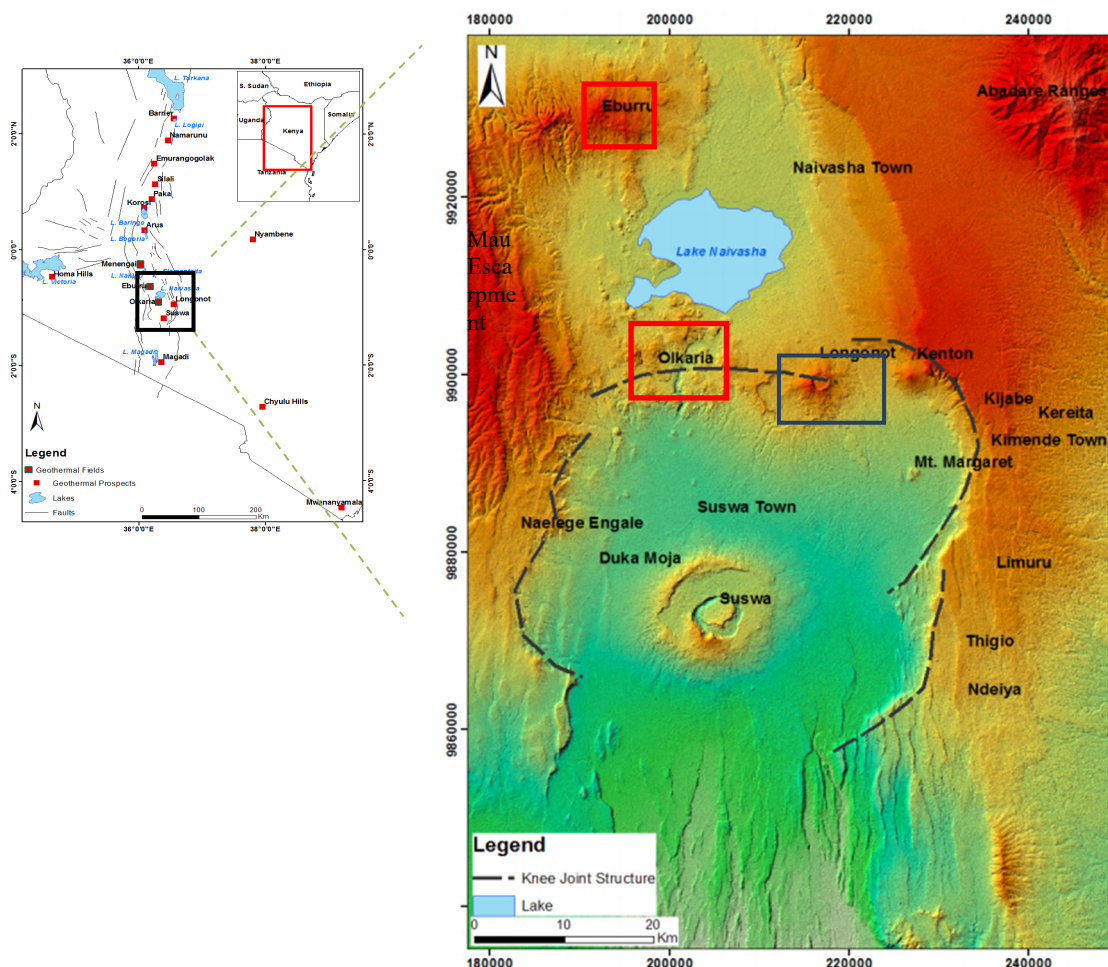


FIGURE 3: Location of Mt. Longonot geothermal field within Kenyan rift: Red boxes are fields under utilization Olkaria and Eburru. Blue box is the study area, the dashed lines outline the Knee joint structure (modified from Munyiri, 2016)

The Mountain has furrows with enormous fissures and lava canyons and it is expected that the most recent eruption at Longonot happened about 200 years ago inside the summit crater along a north-northwest trending volcano-tectonic axis (JICA and WestJEC, 2010). As it is one of the geothermal areas located in the Kenyan rift system (Figure 3), several studies have been conducted to assess its geothermal resource potential (Alexander and Ussher, 2011; Ármannsson, 1987; KenGen, 1998b). Mt. Longonot volcano is located along the periphery of a circular structure known as the Knee joint structure that measures approximately 50 km by 30 km in diameter. The bounding fault scarps are up to 800 m high, implying a down faulting of similar magnitude. The floor of the circular structure is relatively flat due to infill of lacustrine sediments formed by catastrophic floods from Lake Naivasha, which occurred at about 10-30 Ka BP (Munyiri, 2016).

2.3 Geology of Mt. Longonot geothermal area

Several geological studies have been conducted on the Kenyan rift (Thompson and Dodson (1963); Allen et al. (1989); Clarke et al. (1990); Lagat (2003)). In Mt. Longonot area, geological activity is documented to have started around 400,000 years BP (Lagat, 2003). Major pyroclastic eruptions happened from about 21,000 to 6,000 years ago. The former produced the outer caldera structure now visible on the western flanks of Mt. Longonot. The outer caldera of Mt. Longonot is structurally well noticeable and the western most part of the outer caldera lies in the Olkaria geothermal area (Figure 4). The Northeastern part of the caldera is poorly exposed probably covered by younger trachytic lava flows. The Mt. Longonot inner caldera is conspicuous in satellite images and shows a central vent system which is symmetrical and shows a circular central vent system of about 2 km in diameter (Munyiri, 2016).

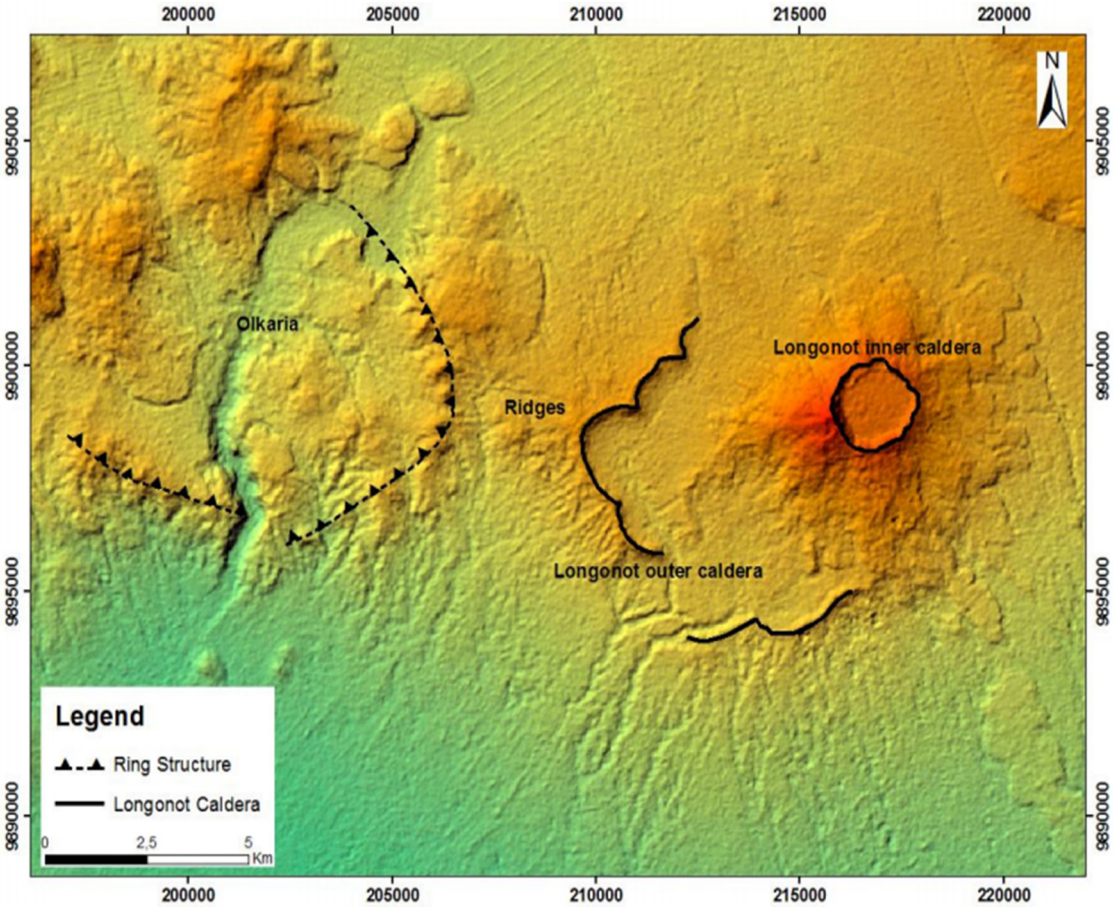


FIGURE 4: Map in UTM coordinates showing Olkaria ring structure and both the outer and inner Mt. Longonot caldera (Munyiri, 2016)

Study of Digital Elevation models (DEMs) shows the existence of a lateral shift of faults along the Kenyan rift slopes (Munyiri, 2016). There is significant lateral shift resulting in the formation of E-W fault zones and successive displacement of the N-S regional rifting (Figure 5).

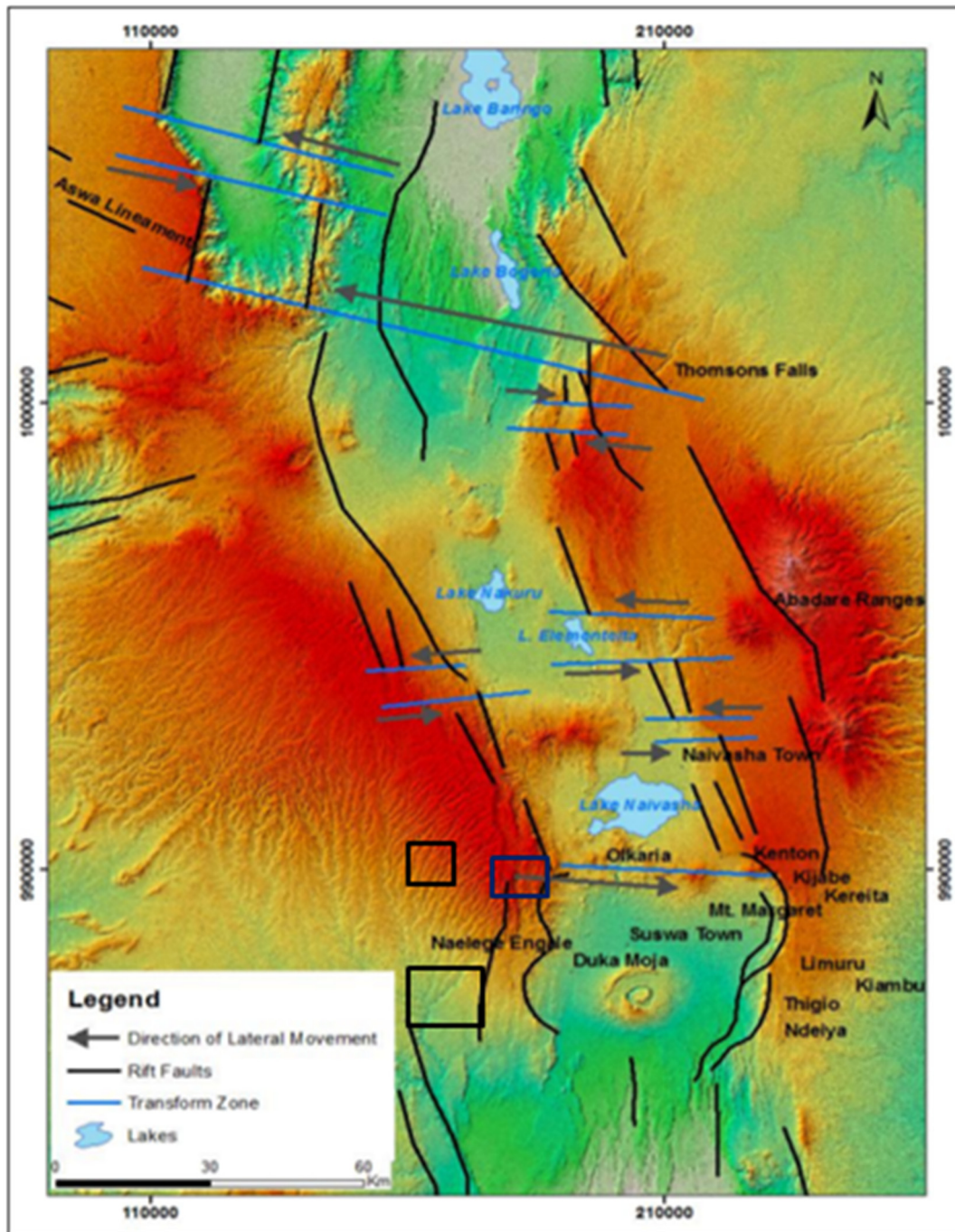


FIGURE 5: DEM of the Kenyan Rift System with the black lines showing the general orientation of the rift. The blue solid lines are showing areas affected by transform faulting whereas the black arrows indicate the trend of lateral movements (modified from Munyiri, 2016)

Local transform faulting is reported to be present in the area between the Domes field and the outer caldera rim of Mt. Longonot where similar E-W fault trends are perceived. The zone has characteristic ridges aligned in an E-W direction. The ridges show recent tectonic movements reproduced by folding and normal faulting on younger pyroclastics. Changes in fault orientation (N-S strike to E-W trend) as seen in the structural map (Figure 6) support the theory of transform faulting that may be connected to the Aswa lineament (transform zone) (Munyiri, 2016).

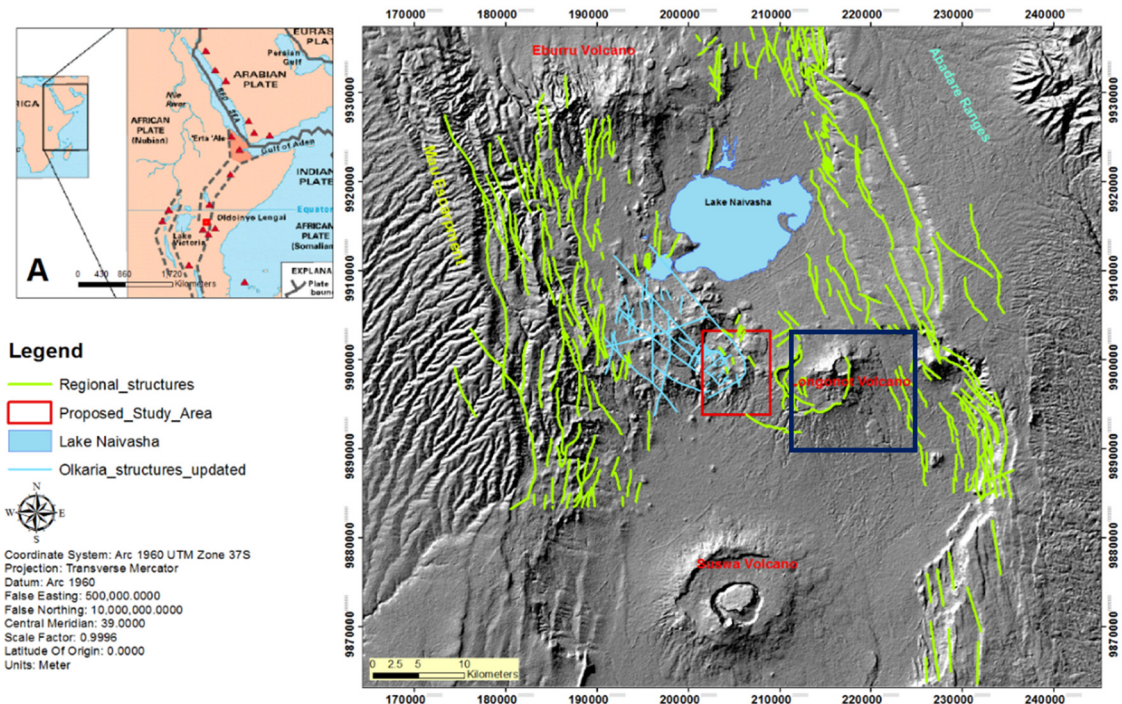


FIGURE 6: Central Kenyan Rift System showing the general orientation of the regional structures. Note the orientation of structures going from N-S north of Mt. Longonot to E-W just west of and around Mt. Longonot. The dark blue inset is the study area (modified from Munyiri, 2016)

Figure 7 shows a geological map of the region. There are mainly three periods of occurrence, pre-caldera, syn-caldera and post-caldera (Lagat, 2003). Caldera collapse was succeeded by incident of central volcano with crater on the caldera floor and a major NW-SE tectono-volcanic axis (Figure 9).

Evidence of activity during the pre- and syn- caldera epochs in the region is limited. This may be due to widespread post-caldera pyroclastics in the region. Syn-caldera formation activity comprises deposits of ignimbrite and pumice lapilli and ash deposits. Lower and upper mixed basalt/trachyte lavas (Clarke et al., 1990) and trachyte lavas were also erupted during this period (Figure 7). The most recent activity is emission of trachyte lava on the north and the southwest flanks of the cone and mixed basalt/trachyte lava on the crater floor, which are assessed to be about 200 yrs BP (Clarke et al., 1990).

The existence of a caldera is evident by a sequence of arcuate ridges (Figure 7) on the northern, western and the southern parts of the summit crater (Lagat, 2003). The major NNW-SSE orientation structure (TVA-the Tectono-Volcanic Axis) of flank eruption centers and fissures on Mt. Longonot Volcano (Figure 9) passes through the summit crater and may be the surface manifestation of the ongoing regional tectonics (Lagat, 2003). Parallelism of major volcano alignments and regional faults at Mt. Longonot suggests that regional tension fractures that traverse the shallow magma chambers are used as conduits for transporting magma from the magma chambers. Table 1 shows the history and nature of the volcanism that is consistent with the development and continued presence of a large magma chamber at relatively shallow depths (Lagat, 2003).

The magma chamber is believed still to be molten to some extent as demonstrated by the recent volcanic activity at Mt. Longonot (Alexander and Ussher, 2011). This is assumed to be the driving heat source of the geothermal system. There are no faults visible on the surface of Mt. Longonot due to hindrance by dense deposits of pyroclastics and lava flows (Lagat, 2003). The rift valley in the locality of Mt. Longonot is measured to be spreading at 3.2 mm/year toward the east and southeast (Stamps et al., 2008) of the region. Periodic geodetic activity was recorded at Mt. Longonot in 2004–2006. It revealed the presence of active magmatic systems beneath Mt. Longonot volcano (Biggs et al., 2009). Its uplift was recorded 9 cm between 2004 and 2006 (ESA, 2010) (Figure 8). The uplift is likely associated with a flow through a complex plumbing system. The periodic nature of the activity is consistent to activity of the volatile-rich cap to a crystal rich magma chamber beneath the volcano.

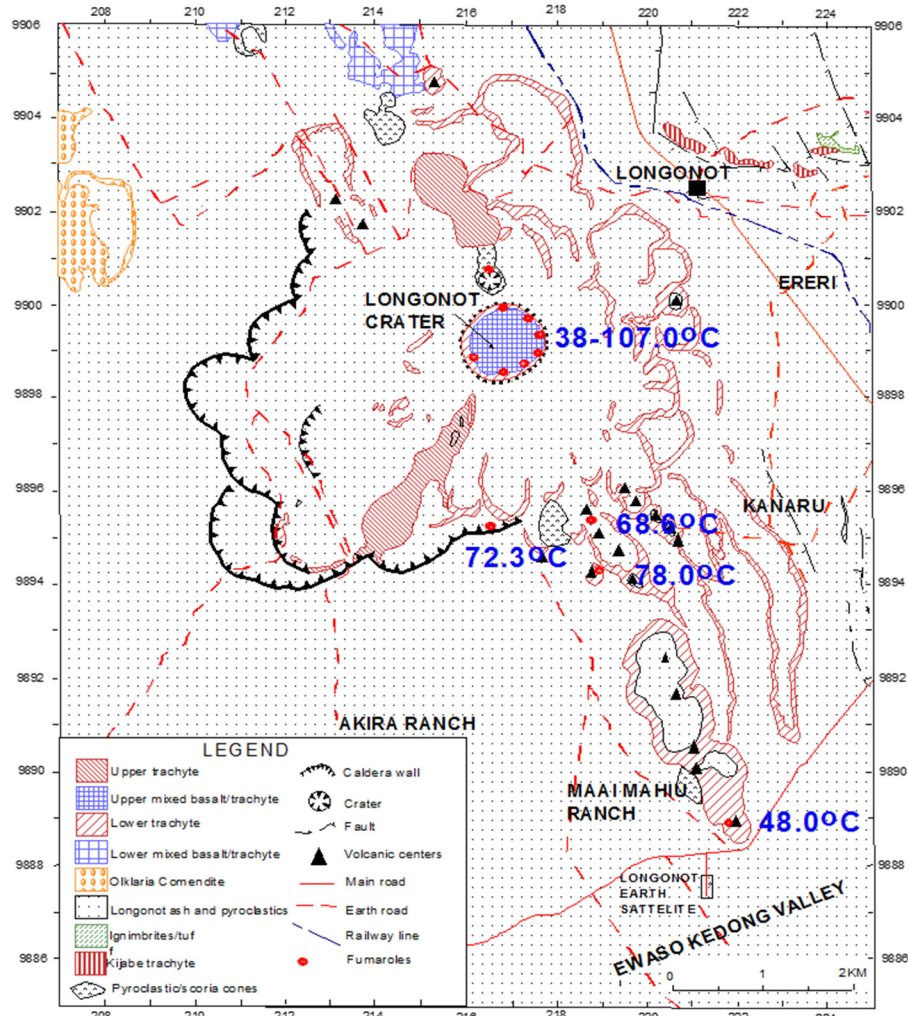


FIGURE 7: Mt. Longonot geological sequence (upper figure: modified from Munyiri, 2016) and the arcuate ridges (lower figure: KWS, 2017)

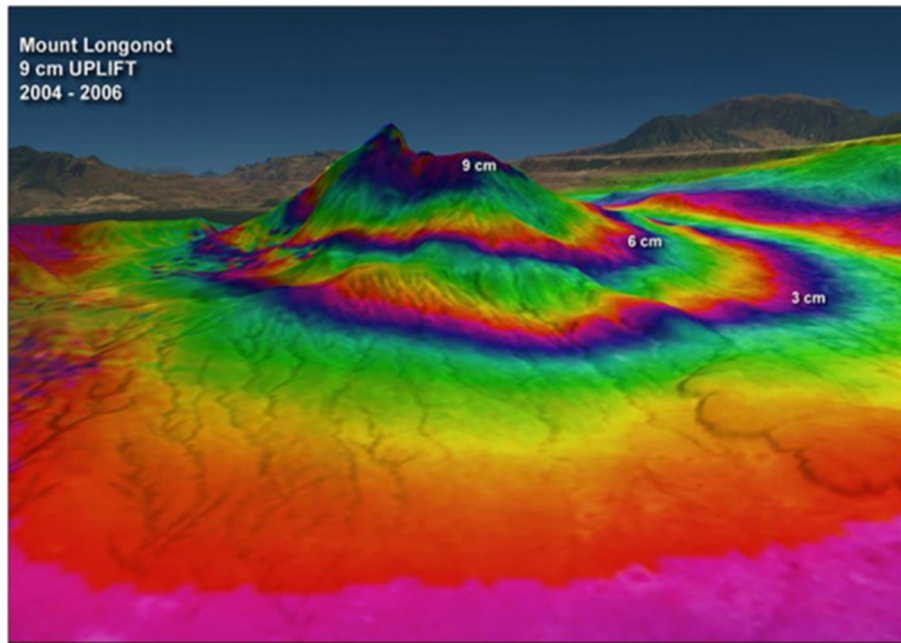


FIGURE 8: InSAR data from Mt. Longonot show vertical movement of up to 9 cm between 2004 and 2006 (ESA, 2010; Munyiri, 2016)

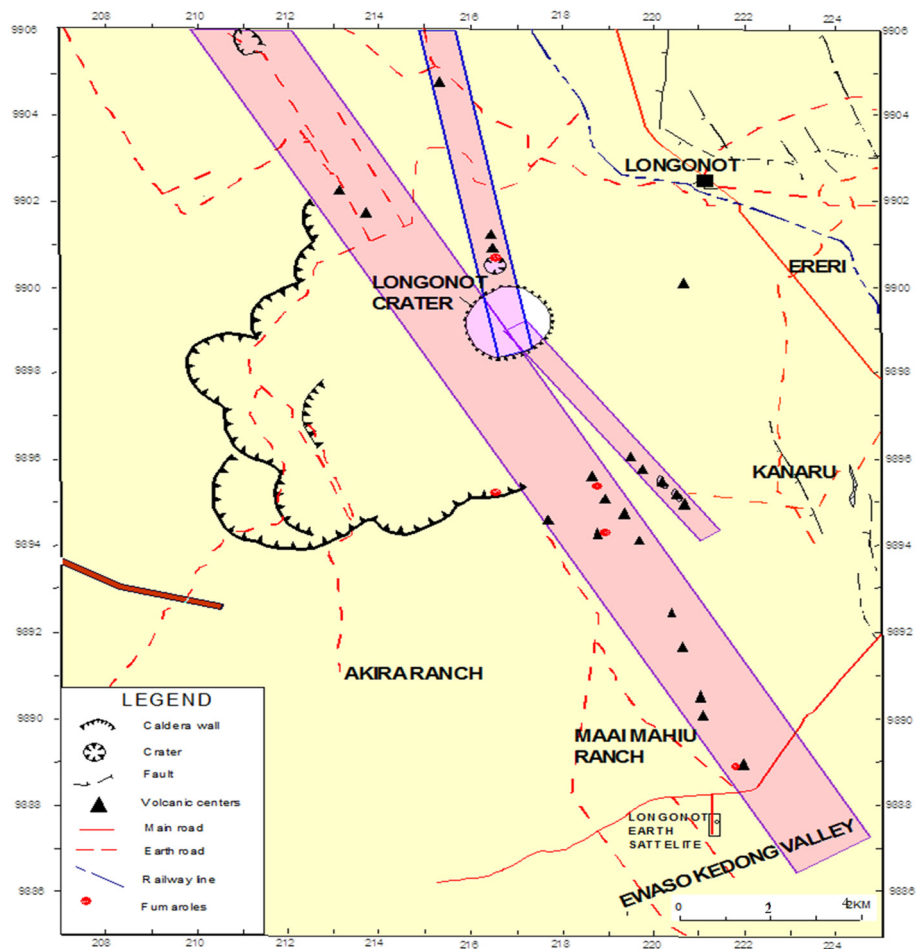


FIGURE 9: Mt. Longonot features: purple solid blocks - TVA, black triangle - volcanic centers, red dots - fumaroles, black dots - hot grounds (modified from Munyiri, 2016)

TABLE 1: Mt. Longonot geological history

Mt. Longonot products	Age (yrs BP)	Event
“Shield” volcanics	>0.4 m	Pre-caldera
Lower trachyte ignimbrite Trachyte pumice lapilli and ash Upper trachyte ignimbrite	9150±110	Syn-caldera
Base surge trachyte pumice and ash Trachyte pumice Trachyte ash Mixed basalt/trachyte lava Trachyte lava and interflow pumice Trachyte ash and pumice Mixed basalt trachyte lava Trachyte lava	----- ----- 3280 ±120 180 ±50	Post-caldera

2.4 Geothermal manifestations and structures in Mt. Longonot area

There are several structures evident in the vicinity of Mt. Longonot field. These include Tectono-Volcanic Alignments (TVA’s) trending NNW-SSE and NW-SE, a caldera wall and faults among others (Figure 9). The area is also marked with active and extinct geothermal manifestations that occur as fumaroles, altered ground and sulphur deposits. Trace element studies carried out in Mt. Longonot volcano show that it is comagmatic. This indicates the existence of a large, highly progressed and long lived magmatic system under the caldera (Clarke et al., 1990). Existence of hydrothermally changed lithics indicates that the geothermal system under the volcano has attained temperatures greater than 250°C (Geotermica Italiana, 1989). These manifestations are structurally controlled, occurring along faults and fractures (Figure 9).

2.5 Hydrology of Mt. Longonot

The hydrogeology of Mt. Longonot is mainly controlled by Eastern rift flank faults, fractures, rift floor faults, rock types and tectono volcanic axes along the rift floor. From the piezometric map shown in Figure 10, it can be inferred that the recharge of fluid is in lateral direction from the wings of the rift as well as alongside the rift floor heading southwards (Clarke et al., 1990). Isotope studies by Ármannsson (1987) showed that Mt. Longonot reservoir is perhaps recharged from rainfall on the eastern side of the Rift Valley. The numerous faults within the escarpment and on the floor of the rift causes the ground water to flow from the escarpments to the centre (Pastor, 2001). The flow then follows longer flow paths reaching

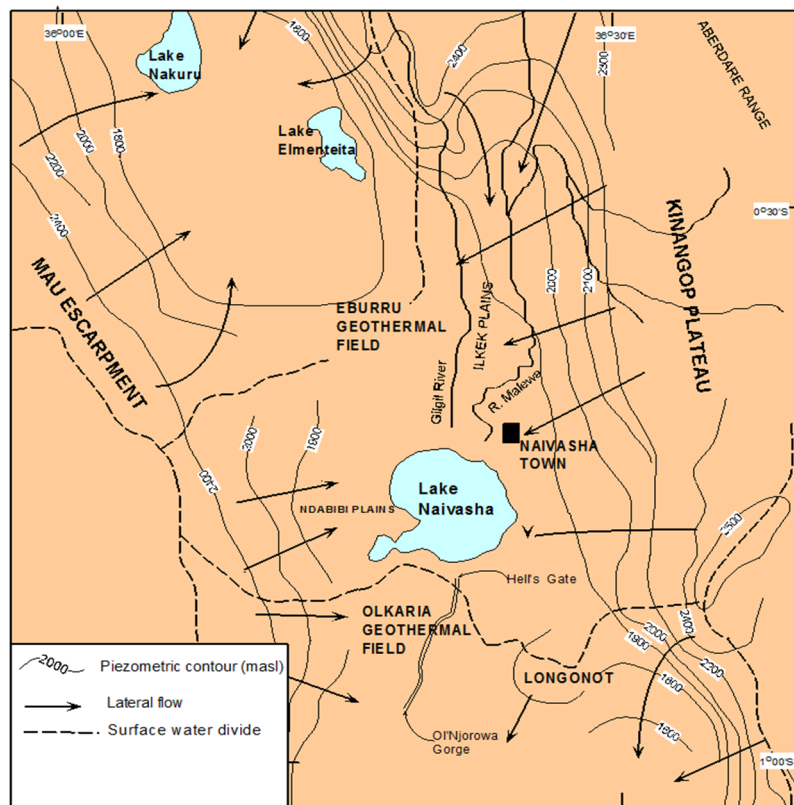


FIGURE 10: A piezometric map of Southern Kenya Rift showing the flow of water (Clarke et al., 1990)

greater depths. Recharge to Mt. Longonot could also be from Lake Naivasha due to southward sloping of the rift floor causing the axial flow. The axial groundwater flow through the geothermal system is controlled by the N-S trending faults and fractures. However, the recharge could be shallow. For a deep recharge into the system, the major rift forming faults control the flow and recharge.

2.6 Previous geoscientific studies and outcomes

Several studies have been done in the Kenyan rift by various authors for a better understanding of the geothermal potential of the rift. Although Mt. Longonot volcanic complex was mentioned in previous studies done by Gregory (1920), Scott (1980) conducted the first comprehensive revision. The study was mainly concentrated on volcanic history of Mt. Longonot creating the chronology and original measurements of its volcanic products. Later on in 1985 to 1987, British Geological Survey sent a team of geologist to conduct a thorough survey work at Mt. Longonot and the surrounding prospects (Alexander and Ussher, 2011). The study provided a better understanding of Mt. Longonot geothermal system (Clarke et al., 1990); Kenya Electricity Generating Company (KenGen) conducted a comprehensive geoscientific study at Mt. Longonot. The Geothermal resource region was estimated to be 10 km² and with a projected power output of 128 MWe (KenGen, 1998a). In 2010, Sinclair Knight Merz (SKM), Auckland, New Zealand carried out fieldwork in Mt. Longonot and came up with many findings, which also coincided with previous studies. Some of the outcomes of the study are conversed below.

2.6.1 Thermal survey

The 2010 study conducted by SKM, revealed the locations of geothermal manifestations in Mt. Longonot field. The study shows that the manifestations lie either inside the crater or on the main alignment of flank eruption centers and fissures (the TVA) or alongside the edge of the caldera (Figure 11). The manifestations along the caldera wall occur to the south. This region is where pre-caldera rocks are exposed beneath a somewhat thinner pyroclastic cover. It is believed that the topographic caldera rim lies very close to the ring fracture (Clarke et al., 1990; Alexander and Ussher, 2011).

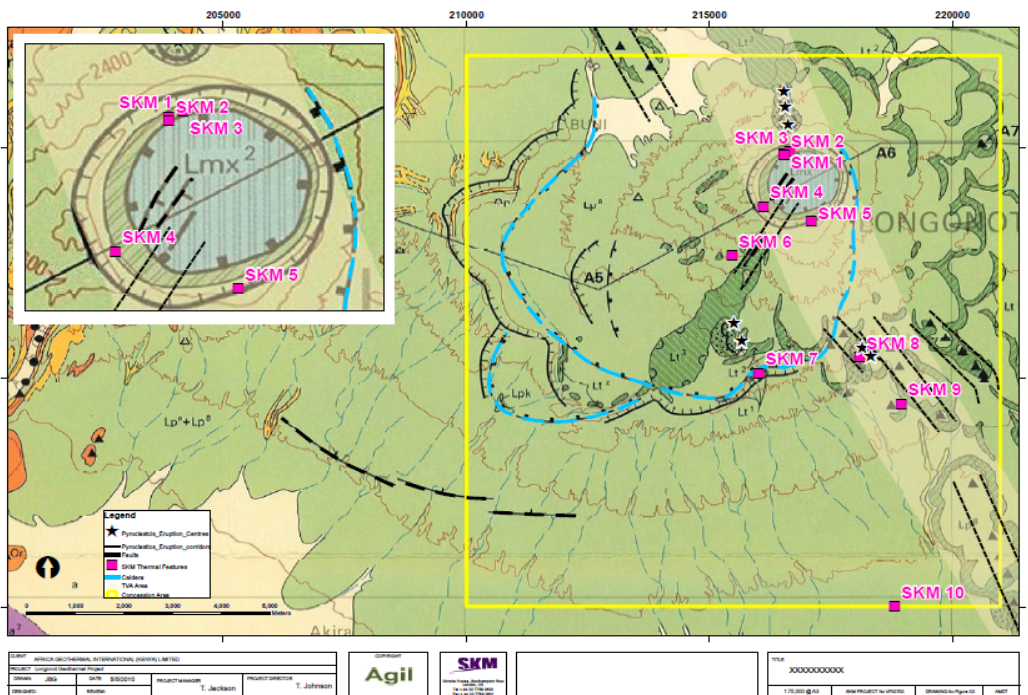


FIGURE 11: Surface geothermal features verified by SKM during the 2010 fieldwork. Uncertain structural margin of Mt. Longonot caldera is in blue. Geologic base map from Clarke et al., 1990 (Alexander and Ussher, 2011)

2.6.2 Gravity survey

In the previous study carried by Geotermica Italiana (1989), it was suggested that Mt. Longonot crater collapsed corresponding to a gravimetric low due to the possible joint outcome of the light pyroclastic filling of the caldera and of the low-density trachytic magma chambers (Figure 12). The study carried out by SKM in 2010 showed that the old Mt. Longonot caldera borderline (Figure 13) might lie beyond the previously specified caldera rim (Alexander and Ussher, 2011). This is an indication of multiple caldera eruptions that took place. In the studies of SKM, a density value of $2.1 \times 10^{-3} \text{ kgm}^{-3}$ was used in the calculation of terrain and Bouguer anomalies. The value represents the average density of the survey area.

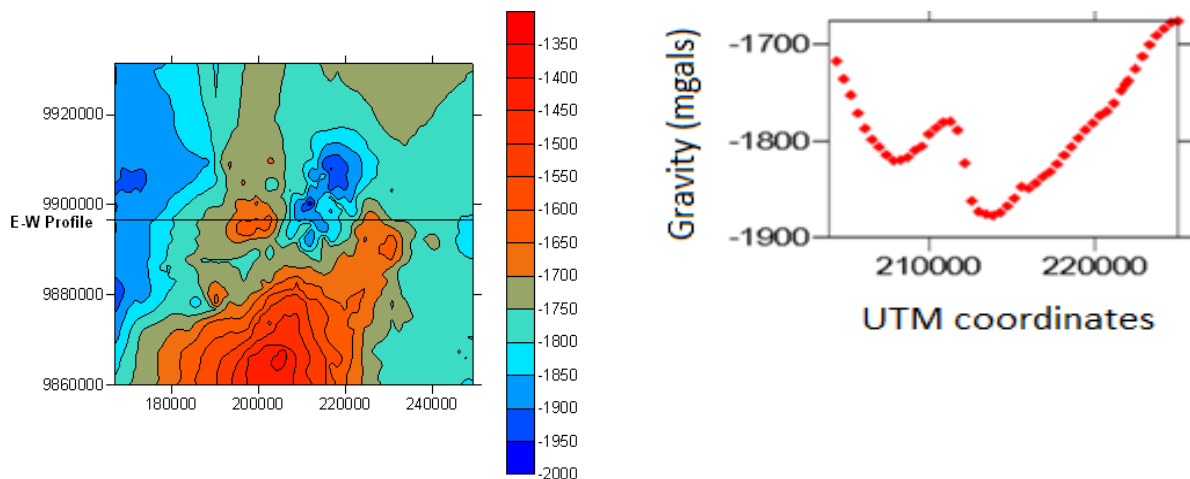


FIGURE 12: Gravity anomaly map (left) and W-E profile through Mt. Longonot Crater (right). On the figure to the left: Red circle is the crater and the black line shows the location of the profile on the figure to the right (modified from Alexander and Ussher, 2011)

Figure 13 shows a map of the gravity anomaly revealing the extent of low gravity of a buried caldera (dashed line) as inferred from the Bouguer anomaly. The map was created from the data collected by SKM and regional gravity data from the Kenya gravity catalog (Swain and Khan, 1977). The currently mapped caldera structure (solid black line) and the Mt. Longonot Crater are nested within this inferred caldera structure border line (Alexander and Ussher, 2011). The low gravity anomaly within the caldera is possibly the pyroclastic cover and a low-density magma chambers. The steep gravity gradients in the east and northeast part of survey area could be an indication of structural controls in the area.

2.6.3 Geochemical studies

Study by Ármannsson (1987) showed that steam in Mt. Longonot indicates signs of mixing and condensation. This is also seen in the fumaroles located south of Mt. Longonot volcano. Within the Longonot Mountain, there are indications of high carbon dioxide concentration (Figure 14). Mineral buffers in geothermal fluids define the tendency of the gases to expand or escape at depth thus completely affecting carbon dioxide distribution (Ármannsson, 1987). According to discussions from Arnórsson and Gunnlaugsson (1985), geothermal waters close to calcite together with quartz, epidote and prehnite are considered to guide carbon dioxide concentrations at temperatures of 230°C and above but zeolites at lower temperatures.

Results from the studies carried out by KenGen (1998a), showed that a high reservoir temperature, greater than 250°C is seen to the south of the crater as inferred from the analysis of H_2S geothermometers indicating a high temperature geothermal system (Figure 15). From the H_2S geothermometers, a high concentration of H_2S is seen at LF9 (fumarole sample station) implying a hot magmatic body (Figure 15) (KenGen, 1998a).

Trace element studies indicate that Mt. Longonot volcanics are comagmatic, hence signifying the existence of a large, highly progressed and long lived magmatic system under the caldera (Clarke et al., 1990). Presence of hydrothermally transformed rocks indicates that the geothermal system under the volcano has attained 250°C (Geotermica Italiana, 1989).

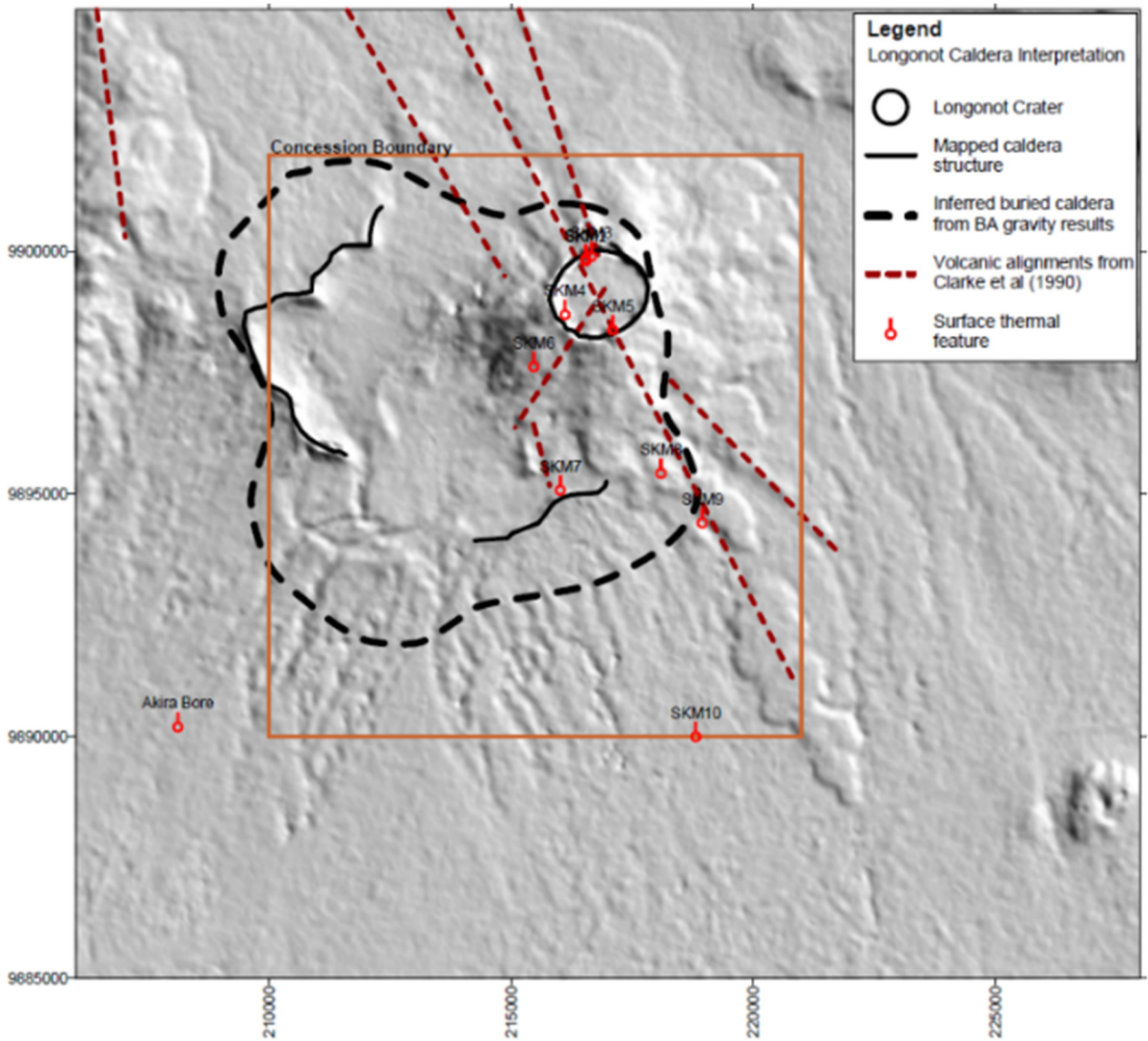


FIGURE 13: Map in UTM coordinates showing the extent of a buried caldera (dashed line) as inferred from the Bouguer gravity anomaly (Alexander and Ussher, 2011)

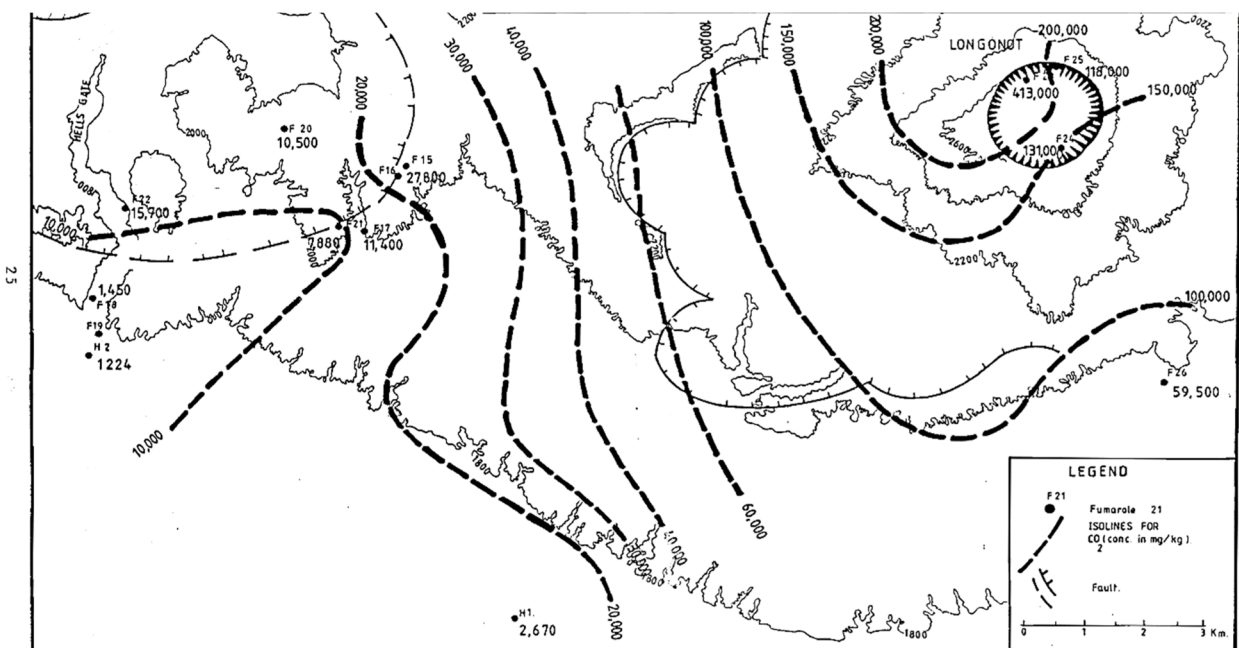


FIGURE 14: CO₂ concentration in the vicinity of Mt. Longonot (Ármansson, 1987)

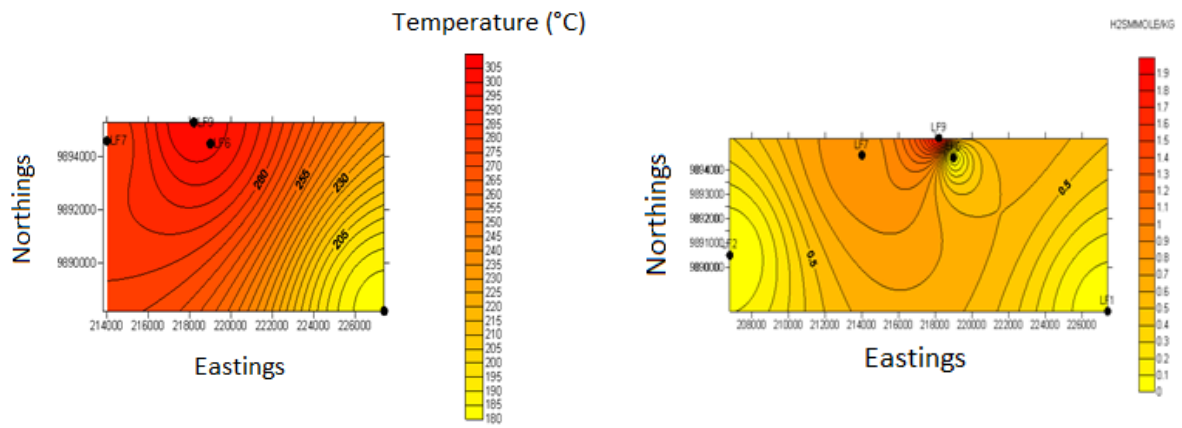


FIGURE 15: Mapview figures showing temperature based on H₂S geothermometer (left) and H₂S concentration (right) in the south east of Mt. Longonot area (KenGen, 1998a)

3. APPLYING RESISTIVITY IN GEOTHERMAL AREAS

3.1 Resistivity methods

There are two categories of resistivity sounding methods applied in geothermal exploration; Direct Current (DC) methods and Alternating Current (AC) methods. In both categories, electrical current is injected or induced within the Earth and the resulting signal monitored at the surface. DC methods are split into different kinds, mostly subject to the setup array. These include Schlumberger, Wenner and dipole-dipole arrays. In these methods, current is normally injected into the ground by a set of electrodes on the surface and the signal produced is the electrical field that is measured as the potential difference over a definite distance (Mariita, 1986).

AC methods, also referred to as electromagnetic methods are when an external magnetic field is used to induce currents in the earth. There are mainly two types of AC methods, which are used in geothermal exploration, Magnetotelluric (MT) and transient electromagnetic (TEM) methods. In the MT method, natural variations in the earth's electromagnetic field are used to induce an alternating current in the ground. The parameters measured on the surface are the magnetic field and the generated electric field (Vozoff, 1991). In the TEM method, current is injected into a loop on the surface, which generates a magnetic field. The current is then turned off and a secondary magnetic field is created that will in turn induce currents in the ground (Árnason, and Flóvenz, 1995). The observed signal is the decaying magnetic field triggered by the induced currents.

Subject to the source of the current, the resistivity methods can be clustered further into passive or active method as shown in Table 2.

TABLE 2: Classification of several electrical methods and their depth of penetration

Method	Direct current	Alternating current
Passive		MT (several km)
Active	Schlumberger (1000 m) Wenner (1000 m) Dipole-dipole (a few km)	TEM (1000 m)

3.2 Resistivity of water bearing rocks

From the definition of resistivity as a bulk property of a material relating how well a material allows electric currents to flow through, it is controlled directly by the properties of concern, such as temperature, porosity, salinity and alteration (Hersir and Árnason, 2010). These parameters characterize the reservoir of a geothermal system and resistivity has a direct relation to them. Electrical resistivity measurements are therefore, usually carried out in geothermal areas, as it is one of the most powerful geophysical prospecting method in geothermal exploration. In any geophysical measurement, there is often a trade-off between parameters, which is a very common problem. An example in resistivity data is the trade-off between resistivity value and thickness of a layer in the Earth. To solve such ambiguities, some constrictions are forced on the parameters from other studies. Palacky (1987) was able to categorize different rock types according to their conductivity (resistivity) (Figure 16).

3.3 Specific resistivity

The specific resistivity, ρ , is defined through Ohm's law, where the electric field, E [V/m] at a point in a material is proportional to the current density, J [A/m²] (Hersir and Árnason, 2010):

$$E = \rho J \quad 3-1$$

The constant, ρ known as the specific resistivity, varies from one material to another. It is measured in Ωm . The reciprocal of resistivity is conductivity ($1/\rho=\sigma$) (Hersir and Árnason, 2010). It is also defined

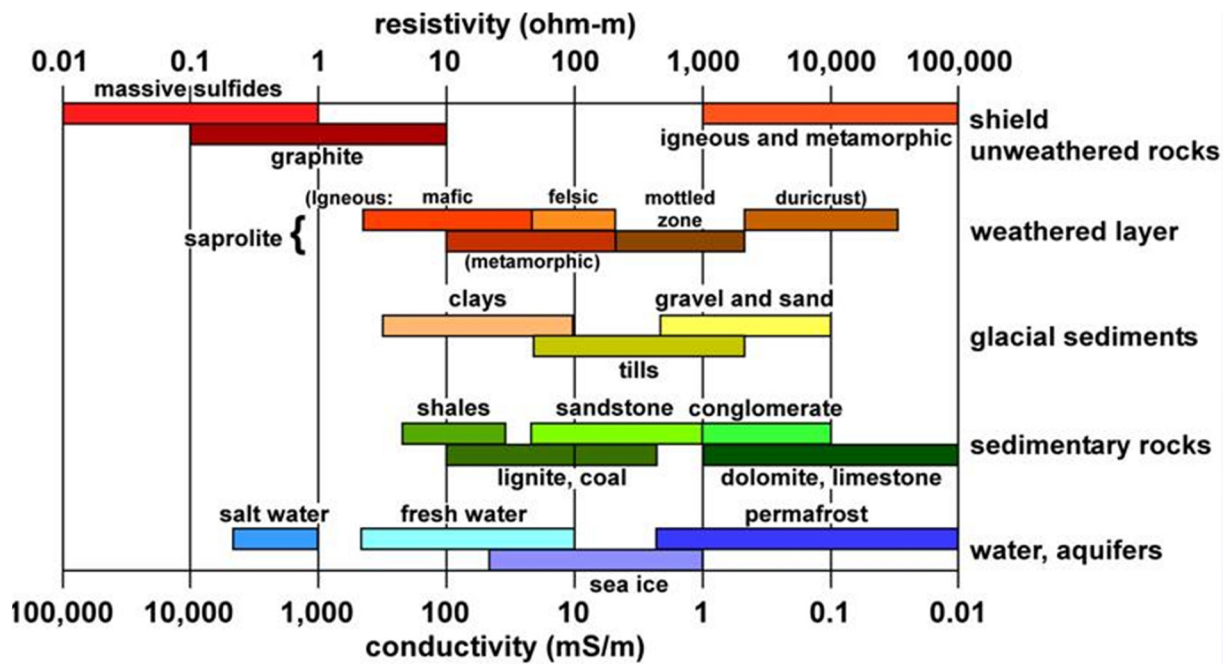


FIGURE 16: Typical ranges of electrical resistivity (Ωm) and conductivity (Sm^{-1}) for selected rocks (Palacky, 1987)

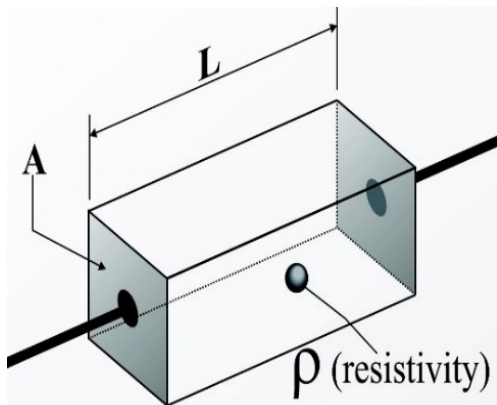


FIGURE 17: Resistivity definition layout (http://www.duncaninstr.com/FIG_1.jpg)

as the fraction of the potential difference, ΔV [V/m], to the current, I [A], across a material that has a cross-sectional area of 1 m^2 and is 1 m long (Figure 17) (Hersir and Árnason, 2010):

$$\rho = \frac{\Delta V}{I} \quad 3-2$$

3.4 Conduction mechanism in geothermal systems

There are mainly three types of electrical conduction mechanism of which two are illustrated in Figure 18. Mineral conduction is in most cases negligible as the rock matrix acts as an insulator. Due to the existence of conductive minerals like sulphides in some geothermal rocks conduction happens by the movement of electrons in the body of mineral grains. At high temperatures, the conductivity of the rock medium becomes significant. The matrix conductivity follows Arrhenius formula (Lasaga, 1984):

$$\sigma_m(T) = \sigma_0 e^{-E/kT} \quad 3-3$$

where σ_m is the matrix conductivity, σ_0 is the conductivity at infinite temperature, E is the activation energy (eV), k is the Boltzmann constant (eV/°K) and T is the temperature in °K.

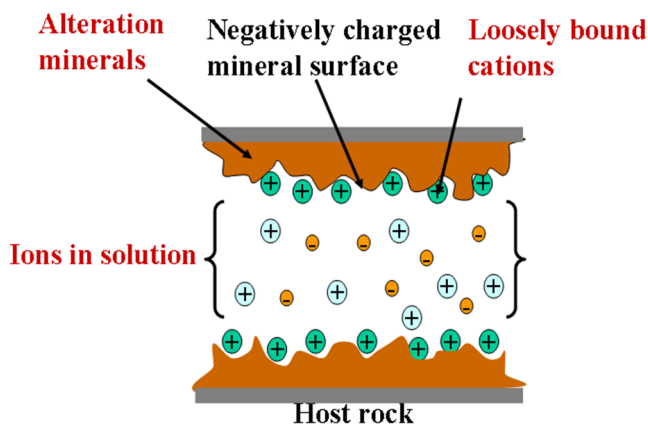


FIGURE 18: Conduction mechanisms in a pore (Hersir and Árnason, 2010).

At high temperatures, partial melt will increase the conductivity. For temperatures

above 400°C, it can be expected that at the core of the geothermal system, the matrix conductivity will have an increasing impact on the overall conductivity.

Pore fluid conduction is when conduction is by ions dissolved in the fluid (Figure 18). Pure water has a high resistivity ($10^6 \Omega\text{m}$), but if the water contains dissolved ions the resistivity decreases dramatically to $0.01 \Omega\text{m}$ or less. As a result, conduction through the liquid phase tends to dominate the conductivity in unaltered rocks. Most of the common components of rocks are extremely resistive, while some components such as sulphides are relatively conductive. Consequently, conduction over the liquid phase tends to provide most of the conduction in fresh and unaltered rock sample, though the liquid phase makes up a small part of the total volume.

Surface conduction is where conduction is by absorbed ions bound on the pore surface (Figure 18). Surface conduction happens because interchangeable ions are near grain boundaries. Since these ions are quite loosely bound, they can contribute to the conductivity of the rock in a manner similar to ionic conductivity in pore water. The number of interchangeable ions differs depending on the existing minerals, being paramount in clays (particularly smectites and zeolites), and almost insignificant in most silicates. Surface conduction can make an important contribution to the conductivity of hydrothermally altered rocks especially in clays that are common in geothermal systems.

3.5 Factors affecting resistivity

3.5.1 Water rock interaction

Interaction between rocks and hot fluids in geothermal areas leads to alteration processes forming secondary minerals. The type of alteration that takes place is normally determined by fluid composition, temperature and permeability (Henley and Ellis, 1983). At medium to low temperatures in basalts, clays, zeolites oxides and hydroxides (Omiti, 2013; Mehegan et al., 1982) usually dominate the secondary minerals. Temperatures of 220-300°C create a region of mixed clays. As temperatures increase to between 230 and 300°C, another region of epidote and chlorite is formed. At temperatures greater than 300°C, epidote and actinolite become dominant (Omiti, 2013). Chlorite and epidote minerals have low mobility of ions bound in crystal lattice making the resistivity in such zones to be quite high. Hence, the resistivity of the reservoir rock is highly dependent on the minerals present not necessarily on temperature.

The concept of CEC (Cation-Exchange-Capacity)

Different alteration processes give rise to zones of different CEC values. The resistivity of the cap layer decreases with temperature until a high resistive core is reached (Flóvenz et al., 2012). Generally, minerals will adsorb or desorb cations along the pore surface when they are in contact with water. The conduction of electrical current in the rock is through pore fluid and pore walls. When the alternating minerals have a high CEC value, conduction of the rock will be higher. The mobile ions forming a conductive layer on the surface of the pore walls will cause a surface conduction. The higher the CEC of the clay mineral the higher is the surface conduction and the ions mobility is correlated to CEC of the mineral phase (Weisenberger et al., 2016).

For smectite, the CEC values are in the range of 0.8–1.5 meqg⁻¹ (Ellis, 1987). Chlorite has CEC of some 0.01 meqg⁻¹ (Thomas, 1976). Because of this big dissimilarity between the CEC values of smectite and chlorite, it clarifies the difference in conductivity between the smectite-zeolite and the chlorite-epidote alteration zones (Flóvenz et al., 2012).

Research done by Weisenberger et al. (2016), in well KJ-18 in Krafla, NE Iceland shows that CEC values decrease with increasing depth (Figure 19). From Figure 19 the CEC values are in good agreement with the alteration zones described by clay mineral alteration (Figure 19). The trend of the measured CEC values is comparative to the trend of the resistivity logs of a high temperature geothermal system. At shallow depths where the resistivity is high, CEC values are low and at low resistivity the CEC values are high (maximum, above 40 meq/100 g). Thereafter, the CEC values start to decline

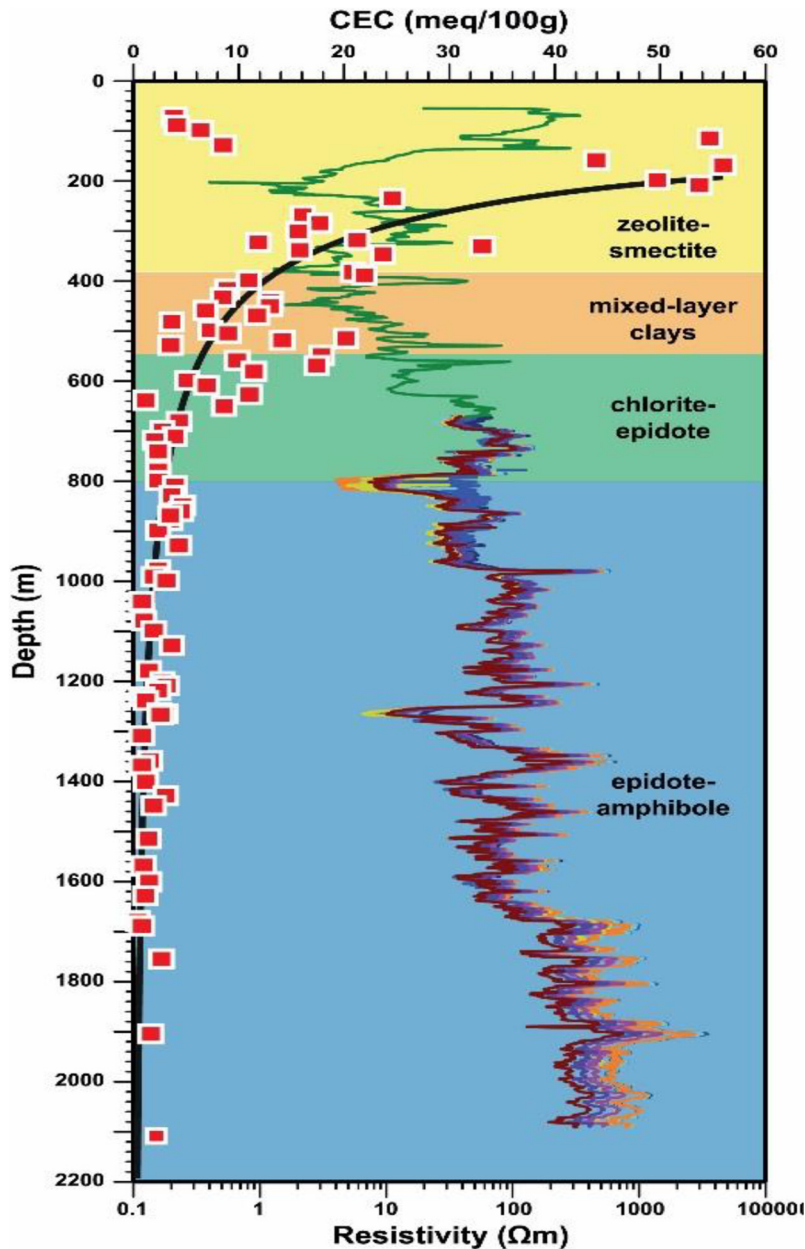


FIGURE 19: Profile from well KJ-18 in Krafla, NE-Iceland showing CEC (red squares and trend-line), alteration zones and electrical resistivity logs (Weisenberger et al., 2016). Resistivity log series were carried out during heating-up of the well (Vilhjálmsón et al., 2016)

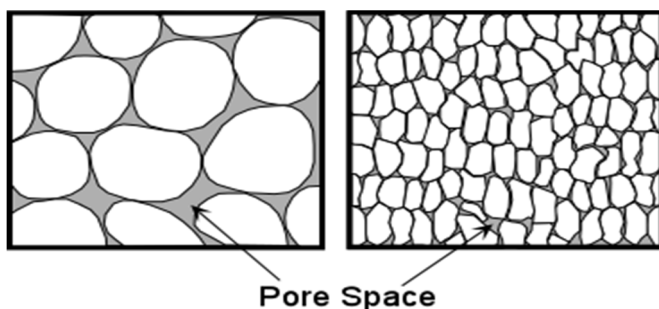


FIGURE 20: Example of pores spaces (<http://www.tulane.edu/~sanelson/images/pores.gif>)

exponentially below about 210 m depth before attaining a stable state level at about 1000 m depth (Weisenberger et al., 2016).

3.5.2 Porosity

Porosity is defined as the fraction between the pore volume and total volume of a rock matrix (Figure 20). These pore spaces must be interlocked to enable fluid to move and hence influencing the resistivity (Flóvenz et al., 2012). There are mainly three forms of porosity that control fluid conduction in a rock matrix (Hersir and Björnsson, 1991);

Intergranular porosity where the pores are made as spaces between elements in a dense material, e.g. in sediments and volcanic ash.

Joints-fissures porosity where fine fractures produced by tension and cooling of the rock, e.g. in igneous rocks and lava. There are also isolated saturated spherical pores that are created from gas bubbles originally locked in the cooling magma. In this type of porosity, the isolated pores are insignificant to the overall conductivity of the rock matrix.

Vugular porosity formed through gas formation. The pores are big and uneven due to the melting and washing away of the material (Flóvenz et al., 2012). In all categories of porosity, there are

generally some separated voids known as storage pores and finer joining pores termed fracture pores. Electric transmission in water-saturated porous rocks takes place essentially through these joined pores. From many investigations, it has been confirmed that, in various cases resistivity of water-bearing rocks vary roughly as the inverse square of the porosity. This empirical law (Equation 3-4) is known as Archie's law (Archie, 1942). It clarifies how resistivity depends

on porosity if other conduction mechanism in the rocks is controlled by ionic conduction in the pore fluid:

$$\rho = \rho_w a \Phi_t^{-n} \quad 3-4$$

where ρ is bulk (measured) resistivity; ρ_w is resistivity of the pore fluid; Φ_t is fracture porosity as a proportion of the total volume; a is an empirical parameter, which varies from < 1 for intergranular porosity to > 1 for joint porosity, usually around 1; and n is cementing factor, an empirical parameter, usually 1-2 (Flóvenz et al., 2012).

3.5.3 Temperature

For typical geothermal reservoir temperatures, the conduction in the rock matrix is normally negligible. In geothermal reservoirs, the main electrical conduction mechanisms are conduction by pore-fluid and surface conduction. Both of these conduction mechanisms depend on temperature particularly the surface conduction. From Figure 21, it is seen that at temperatures above 300°C dielectric permittivity of water is reduced causing a decrease in the number of dissociated ions in the solution thus increasing resistivity in the fluid. Dakhnov (1962) described the relationship between temperature and resistivity using the formula:

$$\rho = \frac{\rho_{w0}}{1 + \varphi (T - T_0)} \quad 3-5$$

where ρ is resistivity (Ωm) of the fluid at temperature T ; ρ_{w0} is resistivity (Ωm) of the fluid at reference temperature T_0 ; φ is temperature coefficient of the resistivity and is approximately $0.023^\circ C^{-1}$ for $T_0 = 25^\circ C$ (Flóvenz et al., 2012).

The importance of temperature variations of electrolytes on the resistivity of rocks is greatest at temperatures below 150°C but decreases with an increase in temperatures due to mineral alteration (Omiti, 2013). This is because different minerals form at different temperatures. These minerals have different CEC values at the same time. Example, epidote forms at high temperatures but has low CEC values compared to smectites that form at lower temperatures but have high CEC values.

3.5.4 Salinity of the pore fluid

Salinity is a measure of the amount of dissolved salts in water. Zhdanov and Keller (1994) described the relationship between conductivity and salinity using the formula:

$$\sigma = \frac{1}{\rho} = F \cdot (c_1 q_1 m_1 + c_2 q_2 m_2 + \dots) \quad 3-6$$

where σ is conductivity (S/m), F is Faraday's number ($9.65 \cdot 10^4$ C/mole), c_i is concentration of ions, q_i is valence of ions, m_i is mobility of ions.

From the equation, it is established that, conductivity of the rock increases with increased salinity of the pore fluid.

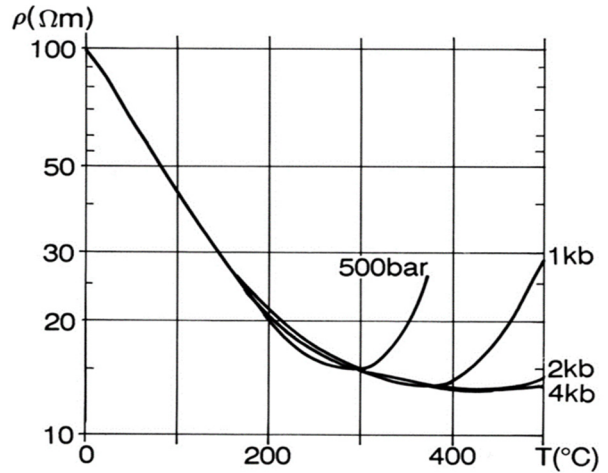


FIGURE 21: Electrical resistivity of a NaCl solution as a function of temperature at different pressures (Hersir and Björnsson, 1991; modified from Quist and Marshall, 1968)

3.6 Resistivity structure of geothermal systems

Interpretation of resistivity over the past couple of decades has proven to be generally the same in all high temperature geothermal fields in volcanic environments. The resistivity structure is usually characterized by a curving structure with a conductive (low resistivity) cap underlain by a resistive core (high resistivity) (Figure 22). Theoretically, resistivity decreases with increase in temperature and depth. However, it is not the case in volcanic areas. The conductive cap comprises of rocks with considerable amount of conductive alteration minerals (smectite) that have a high CEC (Weisenberger et al., 2016).

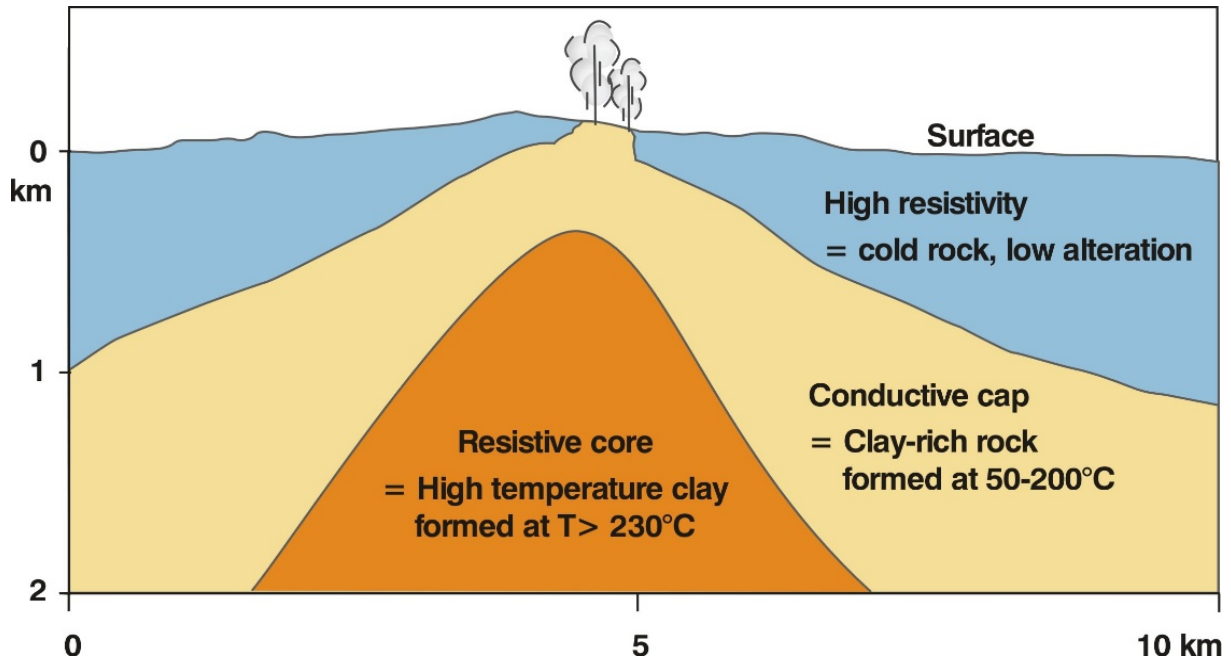


FIGURE 22: Typical resistivity structure of a high temperature geothermal field where the host rocks are volcanic (Hersir, 2016)

Figure 23 summarizes the relationship between subsurface resistivity, hydrothermal alteration, temperature, and conduction mechanism. From the figure, being able to discover the estimated 220-240°C anomalies with resistivity measurements would help immensely in the search for reservoirs appropriate for power generation. Mostly the apparent resistivity change seems to be fixed by the type of clay mineral alteration (Flóvenz et al., 2005). In summary, the subsurface resistivity structure in high temperature geothermal fields reproduces the hydrothermal alteration. Due to water-rock interaction and chemical conveyance by geothermal fluid, the primary minerals in the host rock matrix are altered into different minerals (Flóvenz et al., 2012). Porosity and permeability control the extend of alteration. If the temperature that yields the alteration mineralogy prevails, then the resistivity structure can be used to envisage temperature. Nevertheless, if cooling occurs, the alteration remains and so does the resistivity structure (Flóvenz et al., 2012).

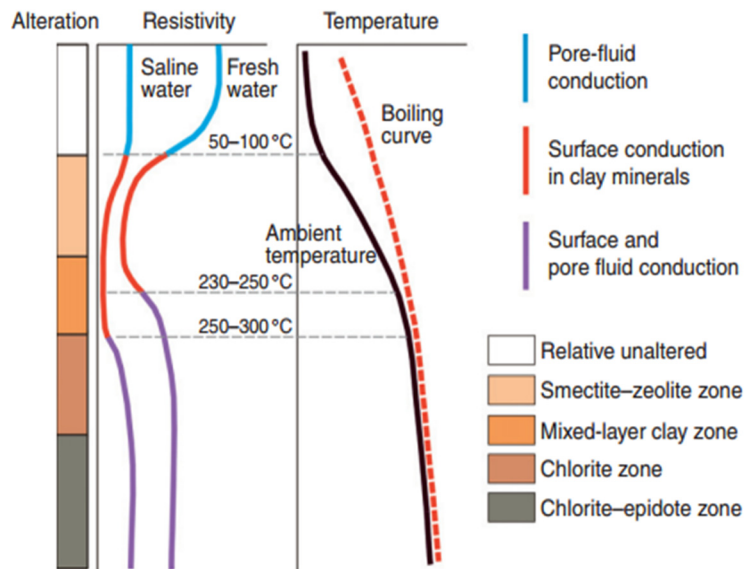


FIGURE 23: A summary of the general resistivity structure of a high temperature field in the basaltic crust in Iceland (Flóvenz et al., 2012; based on Flóvenz et al., 2005)

4. MAGNETOTELLURIC (MT) METHOD

4.1 MT Theory

The magnetotelluric (MT) method is a passive electromagnetic technique used in geophysical exploration that records time variations of Earth's natural electromagnetic field over a wide frequency range. It was first advocated and established by Tikhonov (1950) and Cagniard (1953). The source of energy for magnetotellurics is a natural resource of energy of an external origin. The external energy reaches the Earth as a primary energy. The Earth acts like a good conductor; hence, the primary energy penetrates into the Earth. Current will then be induced to produce a secondary magnetic field. The current induced is known as the telluric current. The sole purpose of MT survey is imaging of electrical properties of the earth (Vozoff, 1991). The natural electromagnetic waves penetrate vertically into the earth due to the huge difference in resistivity between the air and the earth and hence producing a vertical refraction of the electromagnetic wave conveyed into the earth (Vozoff, 1972). Data acquisition for an MT station is through measuring two horizontal magnetic components H_x and H_y and the resulting two horizontal electrical field components, E_x and E_y and the vertical magnetic field, H_z (Figure 24). The resulting time-series data are recorded and Fourier transformed to the frequency domain for further processing resulting in the impedance tensors describing apparent resistivity and phase values.

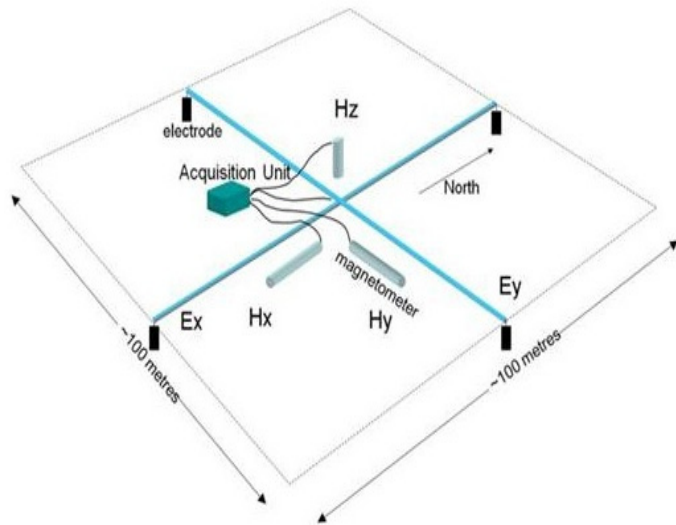


FIGURE 24: The setup of an MT sounding (<http://en.openei.org/wiki/Magnetotellurics>)

4.2 Source field of MT signals

The natural source signals used in MT surveys are generated in the atmosphere and magnetosphere. MT signals with frequency less than 1 Hz, are created through the interaction between the magnetosphere and the solar wind. As the solar wind radiates streams of protons, they move into the space intersecting with the Earth's ambient magnetic field and produce a low frequency electromagnetic energy that penetrates into the Earth (Figure 25). The penetration of the electromagnetic waves obeys Snell's law of refraction. An illustration of this is found in Figure 26 where energy travelling from the space medium with index of refraction n_1 and incident at an angle θ_1 is refracted on the surface of the earth medium with index of refraction n_2 and an angle θ_2 according to Snell's Law (Wolf, 2004).

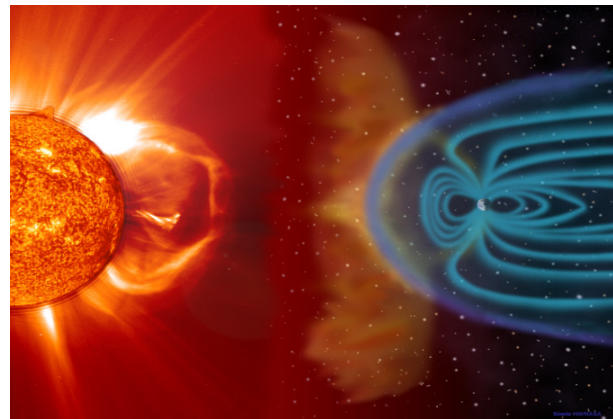


FIGURE 25: Variations of the magnetosphere due to interaction with the solar wind (SOHO, 2010)

From Figure 26 and using Snell's law:

$$\frac{\sin\theta_1}{\sin\theta_2} = \frac{\lambda_1}{\lambda_2} = \frac{n_2}{n_1} = \frac{v_1}{v_2}$$

v (m/s) is velocity in the respective medium, λ is wavelength in the respective medium and n is the refractive index of the respective medium.

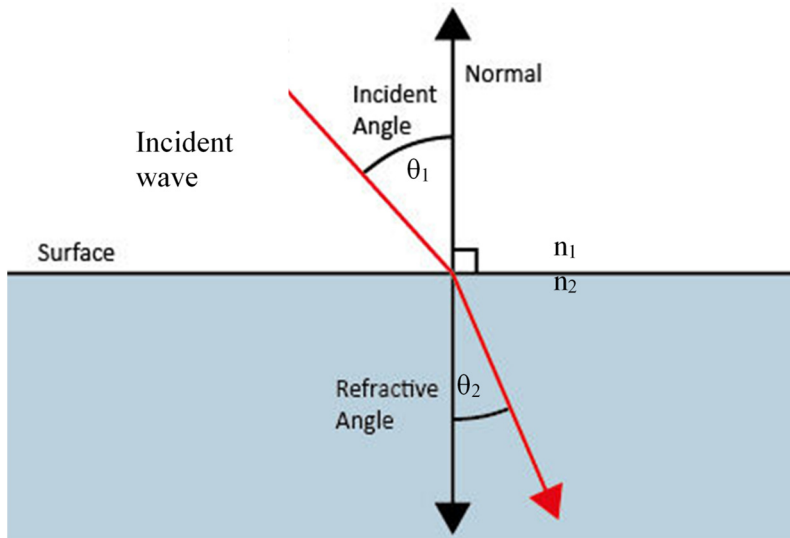


FIGURE 26: Energy refraction at the boundary between two media of different refractive indices with $n_2 > n_1$. Since the velocity is lower in the second medium ($v_2 < v_1$), the angle of refraction θ_2 is less than the angle of incidence θ_1

It can be inferred that $\frac{\sin\theta_1}{\sin\theta_2} = \frac{\text{Im}(k_2)}{k_1}$ where k_1 in free space is $\omega c = \omega\sqrt{(\mu_0\epsilon_0)}$ and $\text{Im}(k_2) = \sqrt{(\omega\mu_0\sigma/2)}$. Hence, the ratio of sines is $\sqrt{(\sigma/2\omega\epsilon)}$ which is $\gg 1$ in MT conditions. Note that $\delta = 1/\text{Re}(k_2) = 1/\text{Im}(k_2)$. Examples of natural signals are sunspot activity and auroras. For MT signal with frequency greater than 1 Hz are generated by worldwide thunderstorms and lightning activities. The energy created travels as a wave-guide between the Earth's surface and ionosphere as part of the energy enters into the Earth. Time varying electromagnetic waves are hence created. EM waves are small in strength and have to be

measured at least for 24 hours at each station to acquire high quality MT data.

4.3 MT principles

4.3.1 Assumptions used in MT

There are several assumptions considered and applied in electromagnetic induction in the Earth (Telford et al., 1990). Since the MT technique depends on the penetration of the EM energy into the Earth, there are essentially two assumptions under which MT method operates: First, a quasi-static approximation is assumed by neglecting shift currents. Mathematically, the wave equation of EM transmission becomes the diffusion equation. Secondly, we assume a plane wave source. When the wave approaches the Earth, the natural EM fields spread vertically into the Earth because of the large resistivity contrast at the air-Earth interface (Figure 27). This in turn causes a vertical refraction of EM fields transferred into the Earth (Vozoff, 1972). The varying horizontal magnetic field induces a varying horizontal electric field perpendicularly through Faraday's law. Hence, the electric field in the conducting Earth creates the telluric currents (Vozoff, 1991).

4.3.2 Maxwell's equations

Maxwell's equations represent one of the best-designed and a brief way to state the basics of electricity and magnetism. Working relationships in the field can be established from them. They are in differential form as follows.

i. Gauss's law for electricity

$$\nabla \cdot \mathbf{D} = \eta \quad 4-1$$

$\mathbf{D} = \epsilon\mathbf{E}$ for isotropic and linear medium

ii. Gauss's law for magnetism

$$\nabla \cdot \mathbf{B} = 0 \quad 4-2$$

iii. *Faraday's law of induction*

$$\nabla \times \mathbf{E} = -\frac{\partial \mathbf{B}}{\partial t} \quad 4-3$$

iv. *Ampère's law*

$$\nabla \times \mathbf{H} = \mathbf{J} + \frac{\partial \mathbf{D}}{\partial t} \quad 4-4$$

$\mathbf{B} = \mu \mathbf{H}$ for isotropic and linear magnetic medium; and $\mathbf{J} = \sigma \mathbf{E}$

$\nabla \cdot \mathbf{E}$ and $\nabla \times \mathbf{E}$ denote the vector operations divergence and curl, respectively. Symbols used; η is electric charge density of the free charges, \mathbf{B} is magnetic induction, ϵ is electric permittivity, \mathbf{J} is current density, \mathbf{D} is electric displacement, μ is magnetic permeability, \mathbf{H} is magnetic intensity.

Within the Earth, the dielectric permittivity values range from $8.85 \cdot 10^{-12}$ F/m in vacuum and air (ϵ_0) to about $80 \cdot \epsilon_0$ F/m in water. It can also vary subject to the frequency of the electromagnetic fields (Christopherson, 1998). For most of the Earth materials and for air, the absolute magnetic permeability μ given by $\mu = \mu_r \mu_0$ can be approximated to its value in vacuum, $\mu_0 = 4\pi \cdot 10^{-7}$ H/m, μ_r is the relative permeability. However, in highly magnetized media this value can be greater due to an increase in the magnetic susceptibility below the Curie point temperature known as Hopkinson effect (Radhakrishnamurthy and Likhite, 1970). In this study Hopkins effect is irrelevant. The relative permeability is almost equal to 1. And hence $\mu \sim \mu_0$.

Gauss's law for electricity states, "The overall electric flux over any closed surface equals the net charge inside that surface divided by ϵ_0 . The connection between electric field and charge distribution allows the electric field lines to start from positive charges and terminate on negative charges". Gauss's law on magnetism, states, "The net magnetic flux through a closed surface equals zero. The number of magnetic field lines that enter a closed volume must equal the number of magnetic field lines that leave that volume. Magnetic field lines cannot begin or end at any point. If they did, isolated magnetic monopoles would exist at those points" (McNeil, 2004). Magnetic monopoles have never been perceived, thus confirming this theory.

Faraday's law of induction states, "The line integral of the electric field around any closed path (which equals the EMF) equals the rate of change of magnetic flux through any surface area bounded by that path" (McNeil, 2004). It defines the connection between an electric field and a varying magnetic flux. Ampère-Maxwell's equation states, "The line integral of the magnetic field around any closed path is determined by the sum of the net conduction current through that path and the rate of change of electric flux through any surface bounded by that path" (McNeil, 2004). It defines the connection between magnetic and electric fields and electric currents.

According to Faraday's law the time variations in the magnetic field induce corresponding oscillations in the electric field flowing in a closed loop with its axis oriented in the direction of the inducing field. This electric field then induces a secondary, internal magnetic field proportional to the total current flow in accordance with Ampère's law. Ampère's law represents two kinds of current flow, one (\mathbf{J}) in which charge carriers flow through a medium without hindrance which is usually called Ohmic, and another, $\frac{\partial \mathbf{D}}{\partial t}$ in which charge separation, and hence an opposing electric field, arises also known as displacement current.

In MT work, assumptions are applied when processing data from Maxwell's equation;

- That sinusoidal time variations are generally chosen
- Propagation of energy from a faraway source is a vertical incident plane wave (Telford et al., 1990).

$$\mathbf{E}(t) = \mathbf{E}_0 e^{i\omega t} \quad 4-5$$

$$\mathbf{H}(t) = \mathbf{H}_0 e^{i\omega t}$$

where ω (Hz) is the angular frequency of the electromagnetic oscillations.

The derivatives of \mathbf{E} and \mathbf{H} with respect to time are, therefore, given by;

$$\frac{\partial \mathbf{E}}{\partial t} = i\omega \mathbf{E}_0 e^{i\omega t}, \quad \frac{\partial \mathbf{H}}{\partial t} = i\omega \mathbf{H}_0 e^{i\omega t} \quad 4-6$$

The above assumptions are applied to Equations 4-3 and 4-4 in coordinate space as discussed below.

Faraday's law of induction using $\mathbf{B} = \mu\mathbf{H}$, simplifying the equation:

$$\nabla \times \mathbf{E} = -\mu \frac{\partial \mathbf{H}}{\partial t}$$

$$\text{a.} \quad \frac{\partial E_z}{\partial y} - \frac{\partial E_y}{\partial z} = -\mu \frac{\partial H_x}{\partial t} \quad 4-7$$

hence,

$$-\frac{\partial E_y}{\partial z} = -\mu \frac{\partial H_x}{\partial t} = -i\omega\mu H_x$$

$$\text{b.} \quad \frac{\partial E_x}{\partial z} - \frac{\partial E_z}{\partial x} = -\mu \frac{\partial H_y}{\partial t} \quad 4-8$$

hence,

$$\frac{\partial E_x}{\partial z} = -\mu \frac{\partial H_y}{\partial t} = -i\omega\mu H_y$$

Note: $\frac{\partial E_z}{\partial y} = 0$ and $\frac{\partial E_z}{\partial x} = 0$ as the waves are vertically incident plane waves and $\frac{\partial E_y}{\partial x} - \frac{\partial E_x}{\partial y} = -\mu \frac{\partial H_z}{\partial t} = 0$ because there is no a vertical component.

Ampère's law using $\mathbf{J} = \sigma\mathbf{E}$ and $\mathbf{D} = \epsilon\mathbf{E}$, simplifying the equation:

$$\nabla \times \mathbf{H} = \sigma\mathbf{E} + \epsilon \frac{\partial \mathbf{E}}{\partial t}$$

$$\text{a.} \quad \frac{\partial H_z}{\partial y} - \frac{\partial H_y}{\partial z} = \sigma E_x + \epsilon \frac{\partial E_x}{\partial t} \quad 4-9$$

hence,

$$-\frac{\partial H_y}{\partial z} = \sigma E_x + \epsilon \frac{\partial E_x}{\partial t} = (\sigma + i\omega\epsilon)E_x$$

$$\text{b.} \quad \frac{\partial H_x}{\partial z} - \frac{\partial H_z}{\partial x} = \sigma E_y + \epsilon \frac{\partial E_y}{\partial t} \quad 4-10$$

hence,

$$\frac{\partial H_x}{\partial z} = \sigma E_y + \epsilon \frac{\partial E_y}{\partial t} = (\sigma + i\omega\epsilon)E_y$$

By differentiating Equation 4-7 with respect to z and using Equation 4-10:

$$\frac{\partial^2 E_y}{\partial z^2} = i\omega\mu \frac{\partial H_x}{\partial z} = i\omega\mu(\sigma + i\omega\varepsilon)E_y \quad 4-11$$

By differentiating Equation 4-8 with respect to z and using Equation 4-9:

$$\frac{\partial^2 E_x}{\partial z^2} = -i\omega\mu \frac{\partial H_y}{\partial z} = i\omega\mu(\sigma + i\omega\varepsilon)E_x \quad 4-12$$

$\frac{\partial H_z}{\partial y} = 0$ and $\frac{\partial H_z}{\partial x} = 0$ as the waves are vertically incident plane waves, and $\frac{\partial H_y}{\partial x} - \frac{\partial H_x}{\partial y} = \sigma E_z + \varepsilon \frac{\partial E_z}{\partial t} = 0$, because there is no a vertical component.

Equations 4-11 and 4-12 define the behaviour of the electromagnetic field transmission in a homogeneous media. In a non-conductive medium $\sigma = \text{zero}$, the equations become wave equations. The factor $i\omega\mu(\sigma + i\omega\varepsilon)$ can be denoted as k^2 , where k is defined as the wave number:

$$k^2 = i\omega\mu(\sigma + i\omega\varepsilon) \quad 4-13$$

Equations 4-11 and 4-12 can be simplified to Helmholtz equations, using Equation 4.13, as:

$$\frac{\partial^2 E_y}{\partial z^2} = k^2 E_y, \quad \frac{\partial^2 E_x}{\partial z^2} = k^2 E_x \quad 4-14$$

$$\frac{\partial^2 H_x}{\partial z^2} = k^2 H_x, \quad \frac{\partial^2 H_y}{\partial z^2} = k^2 H_y \quad 4-15$$

The resistivity of subsurface rocks is usually in the range of $\rho \approx 1-10^4 \Omega\text{m}$ (or $\sigma \approx 1-10^{-4}$). In MT measurements, the frequency is normally in the range of $10^{-4}-10^4$ Hz. Taking the permittivity of free-space, $\varepsilon_0 = 8.85 \cdot 10^{-12}$ F/m and the relative dielectric permittivity in the range 1-100, the maximum value of the product ω and ε in Equation 4-13 is:

$$(\omega\varepsilon)_{\max} = 2\pi f \varepsilon_0 \varepsilon_r = 2\pi \cdot 10^4 \cdot 8.85 \cdot 10^{-12} \times 100 \approx 5 \cdot 10^{-5}$$

Thus for $\sigma > 10^{-4}$, $\sigma \gg \omega\varepsilon$; the propagation constant k reduces to:

$$k^2 \approx i\omega\mu\sigma \quad 4-16$$

The general solutions to Equations 4-14 and 4-15 are ordinary differential equations given by,

$$E_y = (A_y e^{kz} + B_y e^{-kz}) e^{i\omega t} \quad 4-17$$

$$E_x = (A_x e^{kz} + B_x e^{-kz}) e^{i\omega t} \quad 4-18$$

$$H_y = \frac{-k}{i\omega\mu} (A_x e^{kz} - B_x e^{-kz}) e^{i\omega t} \quad 4-19$$

$$H_x = \frac{k}{i\omega\mu} (A_y e^{kz} - B_y e^{-kz}) e^{i\omega t} \quad 4-20$$

where A and B are constants, which are assessed by applying boundary conditions.

For a homogeneous earth, E_x , E_y , H_x and H_y vanish as z approaches ∞ . This situation leads us to the following: as $z \rightarrow \infty$, $\mathbf{H} \rightarrow 0$ and $\mathbf{E} \rightarrow 0 \Rightarrow A_x = 0$ and $A_y = 0$, and we get:

$$E_y = B_y e^{-kz} e^{i\omega t} \quad 4-21$$

$$E_x = B_x e^{-kz} e^{i\omega t} \quad 4-22$$

$$H_y = \frac{k}{i\omega\mu} B_x e^{-kz} e^{i\omega t} = \frac{k}{i\omega\mu} E_x \quad 4-23$$

$$H_x = \frac{-k}{i\omega\mu} B_y e^{-kz} e^{i\omega t} = -\frac{k}{i\omega\mu} E_y \quad 4-24$$

4.3.3 Uniform half space

For a homogeneous half-space, with conductivity σ and a normally incident plane wave (linear, homogeneous and isotropic), the orthogonal \mathbf{E} and \mathbf{H} fields are constant in direction and magnitude over planes perpendicular to the vertically, downward $+z$, direction of propagation. The ratio of the electric field to magnetic field intensity ($\frac{E_x}{H_y}$) gives an impedance term Z which is the characteristic measure of EM properties of the sub surface medium. It constitutes the basic MT response function. For a plane wave we have:

$$Z_{xy} = \frac{E_x}{H_y} = \frac{i\omega\mu}{k} \quad 4-25$$

The phase angle by which it lags is $\frac{\pi}{4}$ (Figure 27).

The true resistivity of the half space is given by:

$$\rho = \frac{1}{\sigma} \quad 4-26$$

By substituting Equation 4-16 into equation 4-26, and using the definition in Equation 4-25 we obtain:

$$\rho = \frac{1}{\sigma} = \frac{|Z|^2}{\mu\omega} \quad 4-27$$

ω the angular velocity is equal to $2\pi f$ and $T = 1/f$ which is the period in s:

$$\rho = \frac{T}{2\pi\mu} |Z|^2 \quad 4-28$$

From the above equation, it implies that for a homogenous and isotropic earth, the resistivity of the earth is related to the characteristic impedance through the relation (Cagniard, 1953):

$$\rho = \frac{T}{2\pi\mu} |Z|^2 = \frac{T}{2\pi\mu} \frac{|E|^2}{|H|^2} \quad 4-29$$

$$k = \sqrt{i\omega\mu\sigma} \quad 4-30$$

From \sqrt{i} which can be written as $(1+i)/\sqrt{2}$, the value of k can be written as:

$$k = (1+i) \sqrt{\frac{\omega\mu\sigma}{2}} \quad 4-31$$

Thus, k has a real and imaginary part. The real part is linked to the attenuation and the imaginary part is linked to the phase. The exponential of \mathbf{E} and \mathbf{H} can be written as:

$$e^{-kz} e^{i\omega t} = e^{\left(-\sqrt{\frac{\omega\mu\sigma}{2}} - i\sqrt{\frac{\omega\mu\sigma}{2}}\right)z} e^{i\omega t} \quad 4-32$$

The amplitude part is, $e^{-\sqrt{\frac{\omega\mu\sigma}{2}}z}$ and the phase part is, $e^{-i\sqrt{\frac{\omega\mu\sigma}{2}}z}$

The field attenuates exponentially and is delayed linearly in phase with increasing z . Thus, the phase of Z_{xy} can be written as:

$$\varphi = \tan^{-1} \left\{ \frac{\text{Imaginary } \frac{|E_x|}{|H_y|}}{\text{Real } \frac{|E_x|}{|H_y|}} \right\} \quad 4-33$$

Note that, $Z_{xy} = \frac{E_x}{H_y}$, $Z_{yx} = \frac{E_y}{H_x}$

For a non-uniform Earth the resistivity in Equation 4-29 is the apparent resistivity ρ_a , which is frequency dependent. This is seen in the case of the 1-D, 2-D and 3-D situations. In these cases, the phase angle is not equal to $\frac{\pi}{4}$ (Figure 27).

4.3.4 Layered earth

Assuming the earth is flat consisting of N layers and for each layer there is a uniform conductivity, permeability and permittivity. The electromagnetic field probing in the earth is a downward-travelling plane electromagnetic wave (Figure 28). The plane wave impedance is given by the formula (Ward and Wannamaker, 1983):

$$\hat{Z}_N = Z_N$$

where $Z_i = \frac{i\omega\mu}{k_i}$ is the intrinsic impedance of the i^{th} layer, d_i is the thickness of i^{th} layer, $k_i = \sqrt{i\omega\mu\sigma_i}$, \hat{Z}_i is impedance at the top of the i^{th} layer and $\hat{Z}_1 = Z_0$ is the impedance at the surface:

$$\hat{Z}_i = Z_i \frac{\hat{Z}_{i+1} + Z_i \tanh(ik_i d_i)}{Z_i + \hat{Z}_{i+1} \tanh(ik_i d_i)} \quad 4-34$$

If we consider an Earth model with two layers of resistivity ρ_1 and ρ_2 (Figure 29), Equation 4-34 will be of the form:

$$\hat{Z}_1 = Z_1 \frac{\hat{Z}_2 + Z_1 \tanh(ik_1 d_1)}{Z_1 + \hat{Z}_2 \tanh(ik_1 d_1)} \quad 4-35$$

$$k_1 = \sqrt{i\omega\mu\sigma_1} = \sqrt{\frac{i2\pi\mu}{\rho_1 T}} \quad 4-36$$

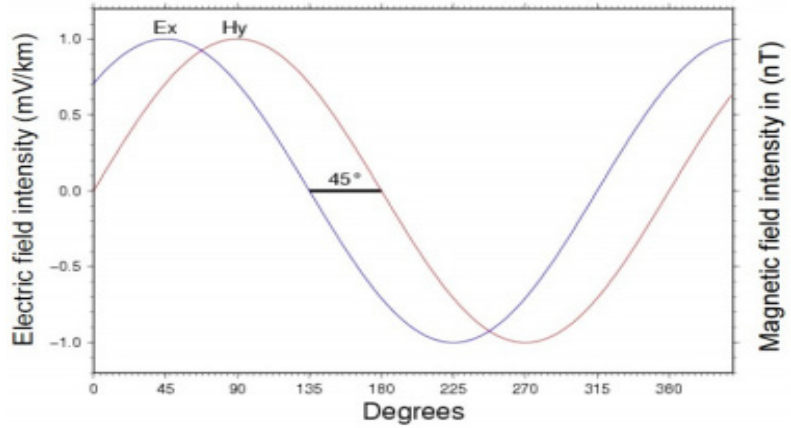


FIGURE 27: Electric and magnetic field response for a homogeneous half-space (Hersir, 2016)

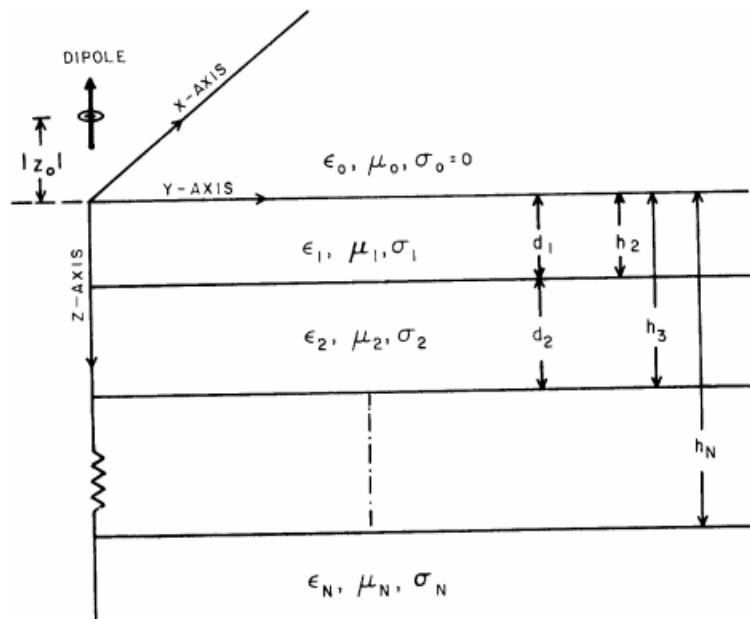


FIGURE 28: An N-layered earth

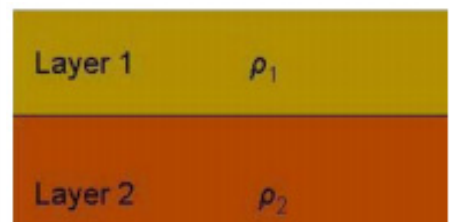


FIGURE 29: Two-layered earth

For large periods (T), $\tanh(ik_1d_1)$ is approximately ik_1d_1 and $\hat{Z}_2 = Z_2$. Hence, Equation 4-35 can be rewritten as:

$$Z_0 = \hat{Z}_1 = Z_1 \left[\frac{Z_2 + iZ_1k_1d_1}{Z_1 + iZ_2k_1d_1} \right] \quad 4-37$$

For $\rho_1 \gg \rho_2$, it means we have a conductor at depth d_1 and $Z_1 \gg Z_2$ Equation 4-37 becomes:

$$Z_0 \approx iZ_1k_1d_1 = \frac{i\omega\mu}{k_1} k_1d_1 = -\omega\mu d_1 \quad 4-38$$

Apparent resistivity is then given by:

$$\begin{aligned} \rho_a &= \frac{1}{\omega\mu} |Z_0|^2 \\ &= \frac{1}{\omega\mu} (\omega\mu d_1)^2 \\ &= \omega\mu d_1^2 \\ &= \frac{2\pi\mu d_1^2}{T} \end{aligned} \quad 4-39$$

The depth to the good conductor, d_1 , can be calculated from Equation 39 at long periods, T, as:

$$d_1 = \sqrt{\frac{\rho_a T}{2\pi\mu}} \quad 4-40$$

On $\log_{10} \rho_a$ vs. $\log_{10} T$ plots, Equation 4-40 is a straight line with slope of -45° .

$$\log_{10} \rho_a = \log_{10} 2\pi\mu d_1^2 - \log_{10} T.$$

These asymptotic descending lines are called “d lines” (Berdichevsky and Dmitriev, 1976).

For $\rho_1 \ll \rho_2$, it means we have a conductor at depth d_1 and $Z_1 \ll Z_2$. Equation 4-37 becomes:

$$Z_0 \approx \frac{Z_1}{ik_1d_1} = \frac{\omega\mu}{k_1^2 d_1} = \frac{1}{\sigma_1 d_1} = \frac{1}{S} \quad 4-41$$

S is the conductance of layer 1.

Using the apparent resistivity equation given by:

$$\begin{aligned} \rho_a &= \frac{1}{\omega\mu} |Z_0|^2 \\ &= \frac{1}{\omega\mu} \frac{1}{S^2} \\ &= \frac{T}{2\pi\mu} \frac{1}{S^2} \end{aligned} \quad 4-42$$

The conductance of the uppermost layer can be calculated from apparent resistivity for long periods as:

$$S = \sqrt{\frac{T}{2\pi\mu\rho_a}} \quad 4-43$$

On $\log_{10} \rho_a$ vs. $\log_{10} T$ plots, Equation 4-43 is a straight line with slope of $+45^\circ$.

$$\log_{10} \rho_a = \log_{10} T - \log_{10}(2\pi\mu S^2).$$

These asymptotic ascending lines are called “S lines” (Berdichevsky and Dmitriev, 1976) and the slope of the ρ_a curve is always between -1 and 1 (between -45° and 45°). Another scenario is physically impossible. In this study the case for a two layered Earth is not considered.

4.3.5 Skin depth

In a homogenous medium, the dispersion element defines the penetration depth of the fields known as the skin depth (δ). The skin depth is defined as the depth at which the amplitude of the wave is reduced to $\frac{1}{e}$ (about 37%) of its original value at the surface. The penetration depends on time of the oscillating electromagnetic fields, i.e. $H, E \sim e^{i\omega t}$. It is a vertical incident plane wave. For this reason, the skin depth is used as a scale length for the time-varying field, or an approximation of how deep such a wave penetrates into the earth (Figure 30). It is given by the following estimated relationship:

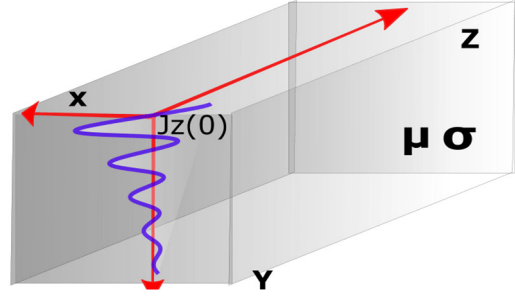


FIGURE 30: Homogenous conducting half space with sinusoidal wave (<http://www.debipattnaik.com/tag/skin-depth/>)

$$\delta = \frac{1}{\text{Real}(k)} = \frac{\sqrt{2}}{\sqrt{\omega\mu\sigma}} = \sqrt{\frac{2T\rho}{2\pi\mu}} \quad 4-44$$

ω is the angular frequency of the sinusoidal wave, σ is the conductivity, μ is the permeability; and δ is the skin depth of the material.

For $\mu = 4\pi \cdot 10^{-7}$:

$$\delta = \frac{1}{\text{Real}(k)} = \sqrt{\frac{2T\rho}{2\pi\mu}} = \sqrt{\frac{2T\rho}{2\pi \cdot 4\pi \cdot 10^{-7}}} = \sqrt{\frac{10^7}{4\pi^2}} \cdot \sqrt{T\rho} \quad 4-45$$

$$\delta \approx 500\sqrt{T\rho}$$

where, δ = Skin depth (m); T = Period (s); and ρ = Resistivity (Ωm).

Equation 4-45 represents the exponential decay of the amplitude with depth in a simplified form (Spies, 1989; Simpson and Bahr, 2005). It is proportional to the square root of the period T , meaning that the skin depth increases with the increasing period T . In order to reach greater depth of penetration, data need to be acquired at sufficiently long periods (low frequencies penetrate deeper than high frequencies). While the high frequencies will only image near surface structures. Signals penetrate deeper in resistive material. The skin depth explains the limitations of the EM technique, particularly the decreasing resolution with increasing depth of penetration.

4.4 MT transfer functions

4.4.1 Geomagnetic transfer functions

A relationship between the horizontal and vertical magnetic fields can be formulated as:

$$H_z = \mathbf{T} \cdot \mathbf{H}$$

$$H_z = T_{zx}H_x + T_{zy}H_y$$

$[H_z]$ is the vertical magnetic field and $[\mathbf{T}]$ is the vertical geomagnetic transfer function referred to as Tipper which is dimensionless.

A composite vector reveals the relationship between the horizontal and vertical components of the magnetic field. The vertical component is produced by horizontal conductivity gradients in the earth. For 1-D or a homogeneous Earth, the Tipper is zero ($T_{zx} = T_{zy} = 0$) due the absence of an induced vertical magnetic field. The postulation is that the occurrence of electromagnetic fields is perpendicular to the Earth's surface. In 1-D models, the electromagnetic fields do not change direction with depth. For 2-D Earth, the coordinate system can be rotated so that the x-axis is in the strike direction which is called T-strike, $T_{zx} = 0$ but $T_{zy} \neq 0$. This is done by minimizing $|T_{zx}|$.

4.4.2 Impedance tensor

Many researchers have studied the concept of the estimation of impedance tensor element. The investigators include Neves (1957), Cantwell (1960), Bostick and Smith (1962), Swift (1967), and Reddy and Rankin (1975). Their methods use power spectral density approximations of orthogonal \mathbf{E} and \mathbf{H} field data. The recorded electric and magnetic field components E_x , E_y , H_x , H_y and H_z may be viewed as a superposition of the presumably plane-wave (TE-mode) source field and the reproduced field at the surface of an inhomogeneous earth. Processing of the data lies in spectral analysis of temporal variations and determination of local transfer functions connecting the field components to each other.

The theory of transfer functions in electromagnetics has been implemented from linear system theory. The conduction activity in the Earth works as an invariant linear system, and the field components are input and output functions. The transfer functions derived are invariant under field and reflect only the electrical properties of the earth (Berdichevsky and Zhdanov, 1984).

Assuming a time-varying quasi-uniform horizontal magnetic field above the surface of the Earth, which induces an electric field within the Earth, the relation between the electric and magnetic fields at the surface of the Earth can be defined by the magnetotelluric transfer function $[\mathbf{Z}]$, the impedance tensor. It is estimated from the measured horizontal electric and magnetic fields and is the crucial objective in a magnetotelluric surveying.

$$[\mathbf{E}] = [\mathbf{Z}][\mathbf{H}] \quad 4-46$$

where \mathbf{E} and \mathbf{H} are the horizontal electric and magnetic fields in the spectral domain.

The relationship between the horizontal electromagnetic field components leading to magnetotelluric transfer function, is represented by the following matrix equation;

$$\begin{bmatrix} E_x \\ E_y \end{bmatrix} = \begin{bmatrix} Z_{xx} & Z_{xy} \\ Z_{yx} & Z_{yy} \end{bmatrix} \begin{bmatrix} H_x \\ H_y \end{bmatrix} \quad 4-47$$

or

$$\begin{cases} E_x = Z_{xx} H_x + Z_{xy} H_y \\ E_y = Z_{yx} H_x + Z_{yy} H_y \end{cases}$$

where $[\mathbf{Z}]$ is the impedance tensor represented as, $\begin{bmatrix} Z_{xx} & Z_{xy} \\ Z_{yx} & Z_{yy} \end{bmatrix}$.

Z_{xy} and Z_{yx} are known as the primary impedances (the off diagonal elements) while Z_{xx} and Z_{yy} the supplementary ones (the diagonal elements). They are contributions from parallel components of the electric and magnetic field.

1-D impedance tensor

The conductivity σ changes only with depth in 1-D layered earth (Figure 31). In this case, the impedance tensor is written as;

$$Z_{1D} = \begin{bmatrix} 0 & Z_{xy} \\ -Z_{xy} & 0 \end{bmatrix} \quad 4-48$$

The apparent resistivity ρ_a and the phase of Z (φ) for layered earth are given by;

$$\rho_a = \frac{1}{\omega\mu} |Z|^2 \quad 4-49$$

$$\varphi = \tan^{-1} \left\{ \frac{\text{Imaginary } Z}{\text{Real } Z} \right\} \quad 4-50$$

Note that, $Z_{xy} = \frac{E_x}{H_y}$, $Z_{yx} = \frac{E_y}{H_x} = -Z_{xy}$

Both the apparent resistivity ρ_a and the phase φ are frequency dependent, $\omega = 2\pi f$.

2-D impedance tensor

In 2-D earth, the conductivity σ fluctuates with depth and in one horizontal direction. The resistivity is constant in the other horizontal direction normally known as the electromagnetic strike or geo-electrical strike direction. The diagonal elements of the impedance tensor Z_{xx} and Z_{yy} are equal in magnitude but opposite in sign, on the other hand the off-diagonal elements Z_{xy} and Z_{yx} are not the same. A 2-D impedance tensor can be written as,

$$Z_{2D} = \begin{bmatrix} Z_{xx} & Z_{xy} \\ Z_{yx} & Z_{yy} \end{bmatrix}$$

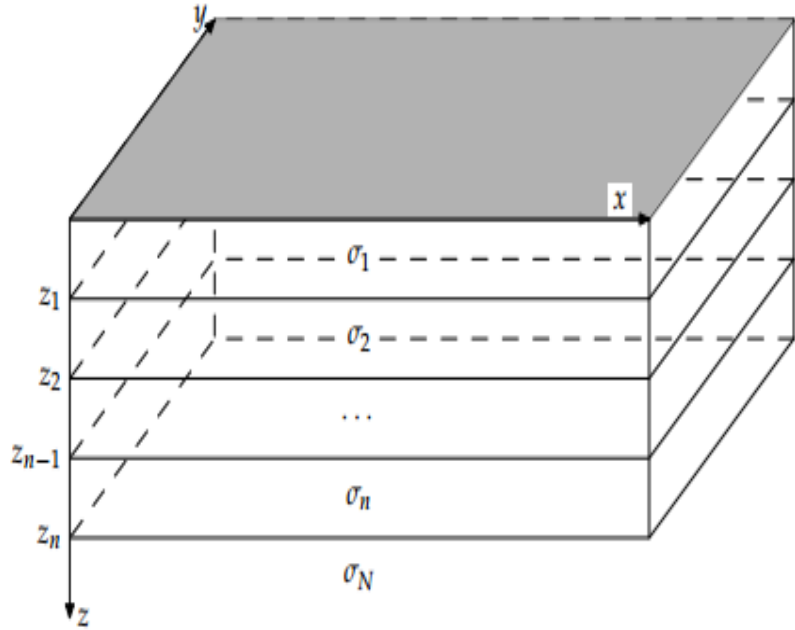


FIGURE 31: N-layered earth model with σ varying in z-direction

When the electric field is parallel to the electromagnetic strike, it is referred to as Transverse Electric (TE) mode or E-polarization, whereas Transverse Magnetic (TM) mode or B-polarization is when the magnetic field is parallel to the electromagnetic strike. Since the current should be conserved across a discontinuity, the incident electric field E_x should also be discontinuous. All other fields are continuous. Since there are no along-strike variations in the conductivity, the TM mode and TE-mode can be given as:

$$\left. \begin{aligned} \frac{\partial E_x}{\partial y} &= \frac{\partial B_z}{\partial t} = i\omega B_z \\ \frac{\partial E_x}{\partial z} &= \frac{\partial B_y}{\partial t} = -i\omega B_y \\ \frac{\partial B_z}{\partial y} - \frac{\partial B_y}{\partial z} &= \sigma\mu E_x \end{aligned} \right\} \text{TE mode} \tag{4-51}$$

$$\left. \begin{aligned} \frac{\partial B_x}{\partial y} &= \sigma\mu E_z \\ \frac{\partial B_x}{\partial z} &= -\sigma\mu E_y \\ \frac{\partial E_z}{\partial y} - \frac{\partial E_y}{\partial z} &= i\omega B_x \end{aligned} \right\} \text{TM mode}$$

For a 2-D Earth, (Figure 32) E_x is dependent only on H_y and H_z . The three field components in Figure 32 contain the transverse electric (TE) mode with the impedance (Z_{xy}) calculated from E_x , H_z and H_y . The transverse magnetic (TM) mode comprises the H_x , E_y , and E_z field components, with the impedance (Z_{yx}) calculated from E_y and H_x (Reynolds, 2011). The TE mode is most sensitive to a long strike conductor. In the TM mode, the electric current flows through the borders between sections of different resistivities, which causes electric charges to build up on interfaces. Thus, the TM mode is more effective than the TE mode at locating boundaries between regions of differing

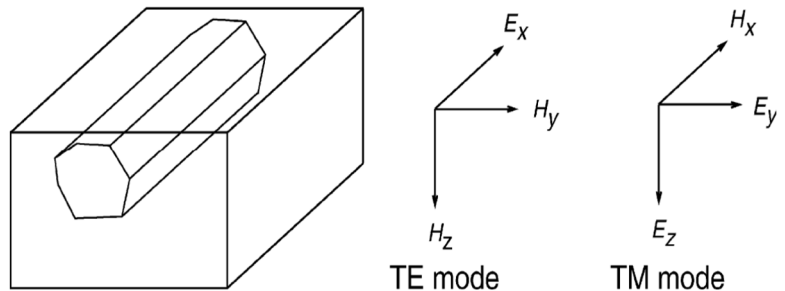


FIGURE 32: Geometry of electromagnetic field components over a 2-D Earth (Unsworth, 2007)

resistivity. For a 2-D Earth with the x-axis parallel to the geoelectric strike direction, the impedance tensor can be written as:

$$Z_{2D} = \begin{bmatrix} 0 & Z_{xy} \\ Z_{yx} & 0 \end{bmatrix} = \begin{bmatrix} 0 & Z_{TE} \\ Z_{TM} & 0 \end{bmatrix}$$

The above equation yields the following two sets of apparent resistivities and impedance phases:

TE mode

$$\begin{aligned} \rho_{xy} &= \frac{1}{\omega\mu} |Z_{xy}|^2 \\ \phi_{xy} &= \tan^{-1} \left\{ \frac{\text{Imaginary } Z_{xy}}{\text{Real } Z_{xy}} \right\} \end{aligned} \quad 4-52$$

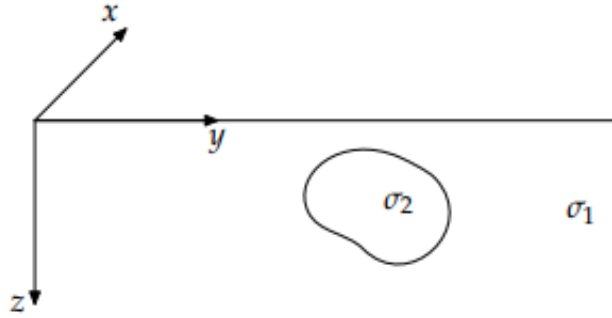
TM mode

$$\begin{aligned} \rho_{yx} &= \frac{1}{\omega\mu} |Z_{yx}|^2 \\ \phi_{yx} &= \tan^{-1} \left\{ \frac{\text{Imaginary } Z_{yx}}{\text{Real } Z_{yx}} \right\} \end{aligned} \quad 4-53$$

Note that, $Z_{xy} = \frac{E_x}{H_y}$, $Z_{yx} = \frac{E_y}{H_x}$

3-D impedance tensor

For a subsurface structure that is 3-dimensional (Figure 33), all the four elements of the impedance tensor are non-zero.



$$Z_{3D} = \begin{bmatrix} Z_{xx} & Z_{xy} \\ Z_{yx} & Z_{yy} \end{bmatrix}$$

The conductivity σ changes in all directions and hence, Maxwell's equations cannot be divided into two modes. There is lack of rotational direction through which the diagonal elements of the impedance tensor can vanish or any other component of the Tipper vector. Consequently, all the tensor elements are considered in the interpretation.

FIGURE 33: A 3-D earth model

The apparent resistivity can be derived from the full impedance tensor. The rotational dependent apparent resistivities for Z_{xy} and Z_{yx} and the phase ϕ

$$\begin{aligned} \rho_{xy} &= \frac{1}{\omega\mu} |Z_{xy}|^2 \\ \phi_{xy} &= \tan^{-1} \left\{ \frac{\text{Imaginary } Z_{xy}}{\text{Real } Z_{xy}} \right\} \\ \rho_{yx} &= \frac{1}{\omega\mu} |Z_{yx}|^2 \\ \phi_{yx} &= \tan^{-1} \left\{ \frac{\text{Imaginary } Z_{yx}}{\text{Real } Z_{yx}} \right\} \end{aligned} \quad 4-54$$

Furthermore, the rotational independent apparent resistivity and phase based on Z_{det} and Z_{ave} are defined as:

$$\begin{aligned} Z_{det} &= \sqrt{Z_{xx}Z_{yy} - Z_{xy}Z_{yx}} \\ \rho_{det} &= \frac{1}{\omega\mu} |Z_{det}|^2 \end{aligned} \quad 4-55$$

$$\varphi_{\det} = \arg(Z_{\det})$$

$$Z_{\text{ave}} = \frac{Z_{xy} - Z_{yx}}{2}$$

$$\rho_{\text{ave}} = \frac{1}{\omega\mu} |Z_{\text{ave}}|^2$$

$$\varphi_{\text{ave}} = \arg(Z_{\text{ave}})$$

4-56

Z_{\det} and Z_{ave} are invariant under rotation.

4.4.3 Mathematical rotation of impedance tensor

MT measurements are generally not performed in the strike direction. This is because the geoelectrical structure might not be known. Subsequently, the measuring axes generally don't match with the axes parallel and perpendicular to geoelectrical strike. Nonetheless, for a 2-D case, it is possible to rotate the measuring axes mathematically by an angle θ in the horizontal plane, so the diagonal components of the impedance tensor become zero and the new X' axis is parallel to the geoelectrical strike (Figure 34). The tensor \mathbf{Z} can be rotated to any other coordinate system by an angle θ with the rotation matrix, $\mathbf{R}(\theta)$ while $\mathbf{R}^T(\theta)$ is the transpose of $\mathbf{R}(\theta)$,

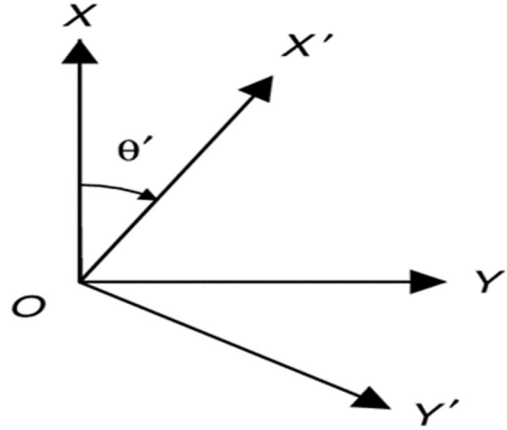


FIGURE 34: The rotation of axes clockwise by angle θ' (θ), from OX and OY (north and east) to OX' and OY'

$$\bar{\mathbf{Z}}(\theta) = \mathbf{R}(\theta)\mathbf{Z}(\omega)\mathbf{R}^T(\theta)$$

4-57

$$\mathbf{R}(\theta) = \begin{bmatrix} \cos\theta & \sin\theta \\ -\sin\theta & \cos\theta \end{bmatrix}, \mathbf{R}^T(\theta) = \begin{bmatrix} \cos\theta & -\sin\theta \\ \sin\theta & \cos\theta \end{bmatrix}$$

Explicit components of the MT transfer function (rotated impedances) of the above equation can thus be written as;

$$\left. \begin{aligned} \bar{Z}_{xy}(\theta) &= Z_{xy} \cos^2(\theta) + (Z_{xx} + Z_{yy})\sin\theta\cos\theta - Z_{yx} \sin^2(\theta) \\ \bar{Z}_{yx}(\theta) &= Z_{yx} \cos^2(\theta) + (Z_{yy} - Z_{xx})\sin\theta\cos\theta - Z_{xy} \sin^2(\theta) \\ \bar{Z}_{xx}(\theta) &= Z_{xx} \cos^2(\theta) + (Z_{xy} + Z_{yx})\sin\theta\cos\theta + Z_{yy} \sin^2(\theta) \\ \bar{Z}_{yy}(\theta) &= Z_{yy} \cos^2(\theta) + (Z_{yx} - Z_{xy})\sin\theta\cos\theta - Z_{xx} \sin^2(\theta) \end{aligned} \right\} \quad 4-58$$

These equations can further be simplified as below:

$$\left. \begin{aligned} \bar{Z}_{xy}(\theta) &= D_2 + S_1 \sin\theta\cos\theta \\ \bar{Z}_{yx}(\theta) &= D_2 - D_1 \sin\theta\cos\theta \\ \bar{Z}_{xx}(\theta) &= S_1 + S_2 \sin\theta\cos\theta \\ \bar{Z}_{yy}(\theta) &= -D_1 - D_2 \sin\theta\cos\theta \end{aligned} \right\} \quad 4-59$$

where S_1, S_2, D_1 and D_2 are the modified impedances (Vozoff, 1972):

$$\left. \begin{aligned} S_1 &= Z_{xx} + Z_{yy}, & S_2 &= Z_{xy} + Z_{yx} \\ D_1 &= Z_{xx} - Z_{yy}, & D_2 &= Z_{xy} - Z_{yx} \end{aligned} \right\} \quad 4-60$$

The rotated modified impedances are then written as (Vozoff, 1991):

$$\left. \begin{aligned} \bar{S}_1 &= \bar{Z}_{xx} + \bar{Z}_{yy} = S_1 \\ \bar{S}_2 &= \bar{Z}_{xy} + \bar{Z}_{yx} = \cos^2\theta S_2 - \sin^2\theta D_1 \\ \bar{D}_1 &= Z_{xx} - Z_{yy} = \cos^2\theta D_1 - \sin^2\theta S_2 \\ \bar{D}_2 &= \bar{Z}_{xy} - \bar{Z}_{yx} = D_2 \end{aligned} \right\} \quad 4-61$$

Hence, S_1 and D_2 are rotationally invariant (Simpson and Bahr, 2005). These independent rotational invariants originated in three complex magnitude conventionally used in MT were conveyed by Szarka and Menvielle (1997).

- The trace $S_1 = Z_{xx} + Z_{yy}$
- The off diagonals difference elements $\bar{D}_2 = \bar{Z}_{xy} - \bar{Z}_{yx}$
- The determinant $Z_{det} = Z_{xx}Z_{yy} + Z_{xy}Z_{yx}$

The diagonal elements $Z_{xx} = Z_{yy} = 0$ and the off diagonal elements, $Z_{xy} = -Z_{yx}$ in a 1-D isotropic medium (Cagniard, 1953). Therefore, Equation 4-58 for a 1-D earth is reduced to:

$$\left. \begin{aligned} \bar{Z}_{xy}(\theta) &= Z_{xy} \\ \bar{Z}_{yx}(\theta) &= Z_{yx} \\ \bar{Z}_{xx}(\theta) &= 0 \\ \bar{Z}_{yy}(\theta) &= 0 \end{aligned} \right\} \quad 4-62$$

From Equation 4-62, we can see that for 1-D isotropic medium the impedance tensor is independent of the measuring axis. The apparent resistivity and phase relationship with rotated impedances are conveyed as:

$$\left. \begin{aligned} \bar{\rho}_{xy} &= \frac{1}{\omega\mu} |Z_{xy}|^2, & \bar{\varphi}_{xy} &= \arg(\bar{Z}_{xy}) \\ \bar{\rho}_{yx} &= \frac{1}{\omega\mu} |Z_{yx}|^2, & \bar{\varphi}_{yx} &= \arg(\bar{Z}_{yx}) \end{aligned} \right\} \quad 4-63$$

4.4.4 Geoelectrical strike analysis

The geoelectrical strike analysis of MT data helps in determining the strike of the dominant 2-D geoelectrical structure although the noise and local distortion may be challenging. The direction in which the conductivity of a 2-D structure does not vary is termed as the strike direction (standard conductivity axis). The angle between the principle conductivity axis and the x-axis is called the strike angle θ_0 – sometimes called Zstrike or Swift angle. Generally, the strike angle is the least steady parameter, which can be calculated from MT data (Jones and Groom, 1993).

For a 2-D model, the impedance tensor is given by:

$$Z_{2D} = \begin{bmatrix} 0 & Z_{xy} \\ Z_{yx} & 0 \end{bmatrix} = \begin{bmatrix} 0 & Z_{TE} \\ Z_{TM} & 0 \end{bmatrix}$$

where Z_{TE} and Z_{TM} relate the fields parallel and perpendicular to the strike direction, respectively.

The angle of strike θ_0 is obtained from the measured impedances by maximizing suitable function of the off diagonal impedance elements under rotation of the axis. For a 2-D model, the most common estimation is based on the maximization of the off diagonal components of the MT tensor or minimization of the diagonal ones. The sum of the squared modules of these components are used (Vozoff, 1972):

$$\begin{aligned} |\bar{Z}_{xx}|^2 + |\bar{Z}_{yy}|^2 &= \text{minimum} \\ |\bar{Z}_{xy}|^2 + |\bar{Z}_{yx}|^2 &= \text{maximum} \end{aligned}$$

Hence, the resultant strike angle is known as Swift angle (Swift, 1967) presented as:

$$\theta_0 = \frac{1}{4} \tan^{-1} \frac{(Z_{xx} - Z_{yy})(Z_{xy} + Z_{yx})^* + (Z_{xx} + Z_{yy})^*(Z_{xy} - Z_{yx})}{|Z_{xx} - Z_{yy}|^2 - |Z_{xy} + Z_{yx}|^2} \quad 4-64$$

where * symbolizes the complex conjugate.

It should be noted here that the equation involves a 90° ambiguity, which can only be resolved through the use of the Tipper as pointed out below. The angle for 1-D and 2-D structures, \bar{Z}_{xx} and \bar{Z}_{yy} are usually zero. However, because of the noise in the measured data Z_{xx} and Z_{yy} are never zero even after rotation. They only become smaller. In a 3-D structure, Z_{xx} and Z_{yy} may still be significant after rotation.

4.4.5 Dimensionality measures

The structure of the earth has dimensionality that can be investigated from MT data with the help of parameters such as skew, Tipper, ellipticity and polar diagrams. The technique provides a useful information before performing 2-D and 3-D inversion.

Skew

Using equation 4-63b, the 3-dimensionality of the impedance is often described by the skew, which is calculated by the following equation (Patra and Mallick, 1980). S_1 and D_2 (equation 4-63b) are invariant under rotation, hence their ratio as well. The magnitude of the ratio describes the skew (Swift, 1967) given by:

$$S = \frac{|Z_{xx} + Z_{yy}|}{|Z_{xy} - Z_{yx}|} = \frac{|S_1|}{|D_2|} \quad 4-65$$

If the MT data are noiseless, the skew for 1-D and 2-D structures will be zero. Skew values above 0.2 are an indication of 3-D structure and/or high level of noise.

Tipper

Tipper is a parameter often used for directional analysis and relates the vertical component of the magnetic field to its horizontal components:

$$H_z = T_x H_x + T_y H_y$$

where T_x and T_y are the x and y components of the Tipper, respectively.

For 1-D Earth, the Tipper value is 0, that is, $T_x = T_y = 0$. The Tipper helps to resolve uncertainty in strike and in particular the 90° ambiguity of the strike as based on the impedances only and discussed above. The modulus of the Tipper is rarely as great than 1, with 0.1 to 0.5 being the most common range. Since the vertical component of the magnetic field is weak, the lower part of the range is often noisy. Tipper can display which side of a contact is more conductive. This is because for a near conductor-resistor boundary, the near surface current density parallel to strike is larger on the conductive side (Vozoff, 1991).

Induction arrows

The Tipper vector can be decomposed into two vectors in the horizontal xy plane. The vectors are commonly called induction arrows. They have the role of deducing the presence of lateral conductivity variations. Two convention illustrations of the real induction arrows exist: the reversed (Parkinson convention, Parkinson, 1959) and the non-reversed (Schmucker or Wiese convention). In the non-reversed convection, the vectors point away from lateral increase in electrical conductivity (Wiese, 1962). The arrows have a real and imaginary part:

$$\begin{aligned}\vec{T}_{re} &= (\text{Re}(T_{zx}), \text{Re}(T_{zy})) - \text{in phase} \\ \vec{T}_{im} &= (\text{Im}(T_{zx}), \text{Im}(T_{zy})) - \text{out of phase}\end{aligned}\quad 4-66$$

The magnitude of the arrows can be written as:

$$\begin{aligned}T_{re} &= (\text{Re } T_{zx}^2 + \text{Re } T_{zy}^2)^{\frac{1}{2}} \\ T_{im} &= (\text{Im } T_{zx}^2 + \text{Im } T_{zy}^2)^{\frac{1}{2}}\end{aligned}\quad 4-67$$

The magnitude of the induction arrows depends on both how close the sounding is to the conductor and the conductivity contrast. The bigger the contrast and closer the conductor, the longer are the arrows. The directions of the arrows are defined by:

$$\begin{aligned}\phi_{re} &= \tan^{-1} \frac{\text{Re}T_{zy}}{\text{Re}T_{zx}} \\ \phi_{im} &= \tan^{-1} \frac{\text{Im}T_{zy}}{\text{Im}T_{zx}}\end{aligned}\quad 4-68$$

ϕ_{re} and ϕ_{im} are clockwise positive from the x-axis (usually geomagnetic North) along which the coherency between vertical and the horizontal magnetic field is at its maximum. For a 2-D Earth, the direction of the induction arrow is perpendicular to the true orientation of the regional strike. For a 3-D Earth, the direction diverges and points away from the conductive body.

Impedance polar diagrams

The connection between the components of magnetotelluric and induction matrices and coordinates of the x and y axes are best described through polar diagrams. A polar diagram is a trace of the tip of a vector as the direction of that vector moves through 360°. Polar diagrams show the modulus of a component of the impedance tensor as a function of the rotation angle θ ($0 < \theta < 2\pi$) at different frequencies:

$$\begin{aligned}Z_{xy}(\theta) &= Z_{xy} \cos^2 \theta + (Z_{yy} + Z_{xx})\sin\theta\cos\theta - Z_{yx} \sin^2 \theta \\ Z_{xx}(\theta) &= Z_{xx} \cos^2 \theta + (Z_{xy} + Z_{yx})\sin\theta\cos\theta - Z_{yy} \sin^2 \theta.\end{aligned}$$

Principal impedances are Z_{xy} and Z_{yx} , and diagonal impedances are Z_{xx} and Z_{yy} (Reddy et al., 1977). Polarization diagrams can be used quantitatively to make decisions about the geometry of an inhomogeneity and provide information about the MT data dimensionality. For example in a 1-D

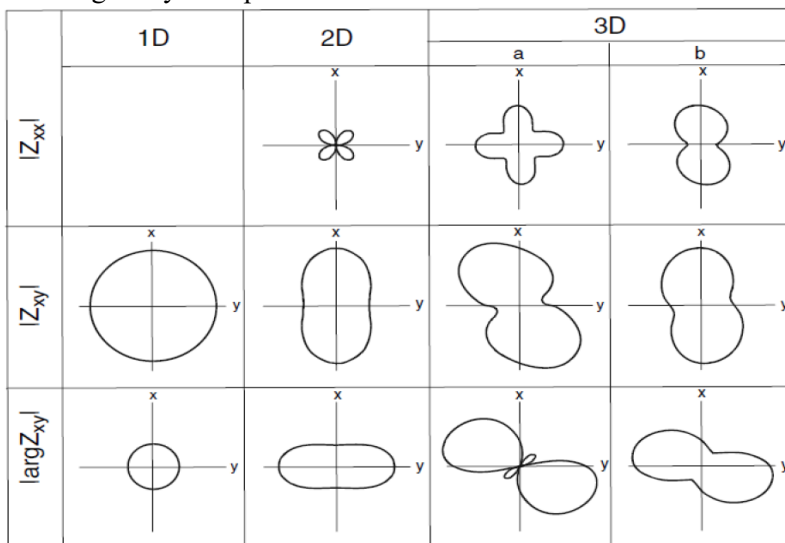


FIGURE 35: Polar diagrams of the impedance tensor (Berdichevsky and Dmitriev, 2002)

resistivity structure, the off diagonal impedance polar diagrams are circular, while the polar diagrams for the diagonal impedances reduce to a point (Figure 35). For 2-D or 3-D resistivity structures, the major impedances extend in a direction either parallel or perpendicular to the strike (Reddy et al., 1977). The 2-D polar diagrams are elliptical, and stretch along the symmetry lines. The polar diagrams attain the shape of a cloverleaf. In 3-D, polar diagrams start to change away from symmetry lines and their sizes become greater, mostly at the lower frequency.

4.5 Problems in MT measurements

4.5.1 MT static shift problem

The MT method suffers a problem known as the static shift. This integral uncertainty in the MT data is mainly formed by local near-surface resistivity irregularities close to the sounding site (Sternberg et al., 1988; Árnason, 2008; Árnason et al., 2010). It is conveyed by scaling the apparent resistivity by an unknown factor (shift on log scale). This shift is independent of frequency (Jones and Groom, 1993) and does not affect the phase curve. The static shift factor S , cannot be determined directly from MT data recorded at a single site. A parallel shift between two polarizations of the apparent resistivity curves is a clear indicator that static shift is present in the data. The correct level of the apparent resistivity curves may lie above, below or between the measured responses. The shifts in apparent resistivity curve can lead to large errors in inverted data. A good example is if there is a shift downwards by $S = 0.1$ there will be ten times too low resistivity values when interpreting and about three times too little depth to resistivity boundaries (Árnason, 2008).

In volcanic environments, 2-D and 3-D models may contain irrelevant structure if static shifts are not rectified. This is because near surface resistivity variations are often extreme. A static shift multiplier below one results in too low resistivity, and decreased depth to boundaries, whereas a multiplier above one results in too high resistivity, and increased depth to boundaries. Therefore, MT curves are shifted upwards when measuring directly over surficial resistive bodies and shifts downwards when measuring over conductive bodies. This ambiguity cannot be resolved using MT data alone (Hersir et al., 2013). Electromagnetic methods, such as TEM, that measure magnetic fields only do not have static shift problems (Simpson and Bahr, 2005). Therefore, TEM data can be used in conjunction with MT data from the same site in order to correct the static shift. The processes that cause static shift in MT measurements as proposed by Jiracek (1990) are:

Current distortion

In MT survey, both electric and magnetic components are measured. The electric current flowing in the Earth encounters a conductivity anomaly which affects its flow path. The type of anomalous conductivity controls how current is channelled. Currents are directed into a higher conductivity anomaly but are swerved from a lower conductivity anomaly. Current distortion is caused by charge distributions accumulated on the surface of shallow bodies. Due to the principal electric field, charges build up on the margins of conductivity anomalies are subject to the conductivity of the anomalous region compared to its surroundings. In a resistive region, the positive charges accumulate on the side facing the primary electric field, inducing a secondary electric field in and around the conductivity anomaly leading to lateral flow-around effect. Within the resistive body, the secondary field is in the direction of the primary field (Figure 36). In a conductive anomaly, a negative charge build-up occurs on the side facing the primary electric field, inducing a secondary electric field that opposes the primary field due to lateral current gathering effect (Figure 36). The distribution of secondary fields outside the anomalous body depends on the geometry of the primary fields.

Topographic effects

Since in volcanic environment, topography is usually not smooth but rough, static distortion can be produced where currents concentrate beneath depressions and disperse under peaks (Figure 37). Due to galvanic effects, the electric field increases in valleys and decrease on hills. Consequently, MT fields and current concentrations are higher in a valley and lower on a hill. This results in the upward or downward shift for the apparent resistivity curve known as static shift. Shift correction by TEM can significantly account for the topographical effects. Resistivity at the valley, ρ_v is larger than resistivity at the top of the hill ρ_h .

In the central-loop TEM method, the measured signal is the decay rate of the magnetic field from the current distribution induced by the current turn-off in the source loop. At early times, surface resistivity structure influences the dispersion of current down into the Earth with time. At late times, conductivity structure at depth influence the apparent resistivity. Therefore, central loop TEM soundings can be used to correct for static shifts in MT soundings (Pellerin and Hohmann, 1990).

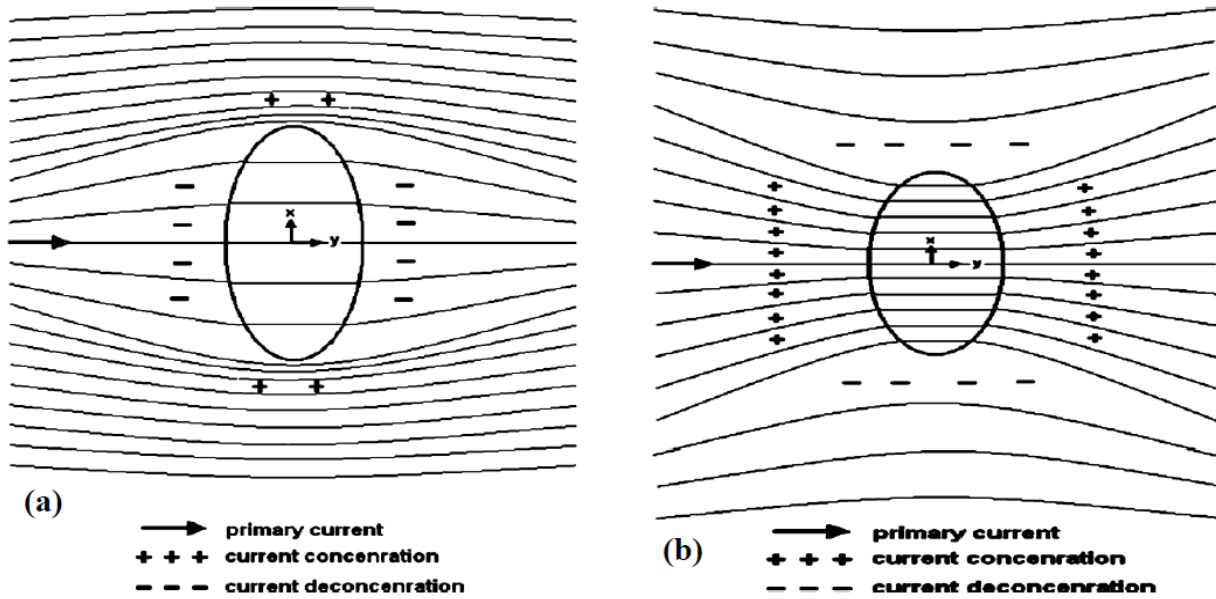


FIGURE 36: Current channelling due to an inhomogeneous conductivity showing; a) Flow-around effect in the vicinity of a resistive and b) Current-gathering effect in a conductive inclusion (Jones, 1983)

Electric field or voltage distortion

Figure 38 shows the electric field distortion as a result of the vertical resistivity inhomogeneity. The electric field is higher in the resistive layer. This is because of the slow flow of current that causes an increase of the voltage to occur within the same layer. When reaching geological rock matrix with high conductivity (low resistive layer), all layers below will be affected and move upward. In different situation, the layers move downwards due to the appearance of low conductivity layer (high resistive layer) in place. Example, if $\rho_1 > \rho_2$ the electric field and the apparent resistivity would be higher in the central domain than outside.

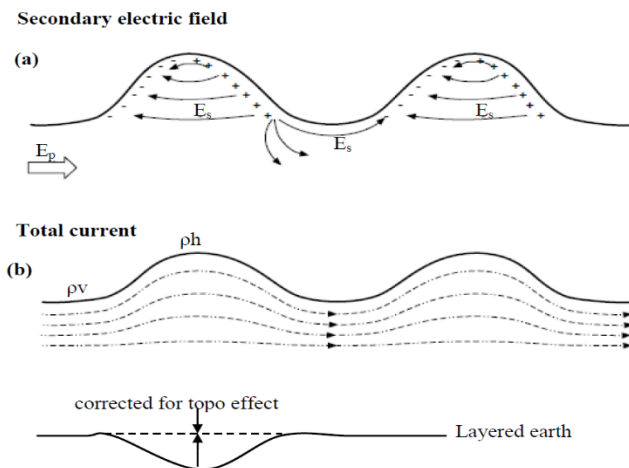


FIGURE 37: Total current distribution and secondary electric field due to topography and correction for the topographical effect (Jones, 1983)

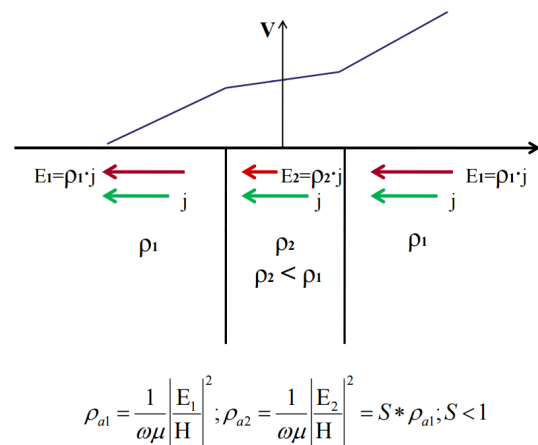


FIGURE 38: Electric field distortion (Árnason, 2008)

4.5.2 Dead band problem

MT data acquisition is also prone to the dead band problem. It occurs in the frequency band ranging between 0.5 and 5 Hz (0.2 to 2 s) for low frequencies and for AMT (Audio-frequency Magnetotellurics: a high-frequency sources in the audio range of > 1 Hz generated by thunderstorms worldwide), the dead

band is encountered in range of 1-5 kHz (Figure 39). Noise due to wind is highest in both mentioned frequency ranges, hence creating a weak signal to noise ratio. From the EM principle; higher frequencies, greater than 1 Hz (short periods) are produced from thunderstorm activity near the Equator and distributed as waves called Spherics between the ionosphere and the Earth (Flóvenz et al., 2012). It is ascribed to inductive source mechanisms, one below 1 Hz and the other above 1 Hz hence causing a reduction in MT data quality.

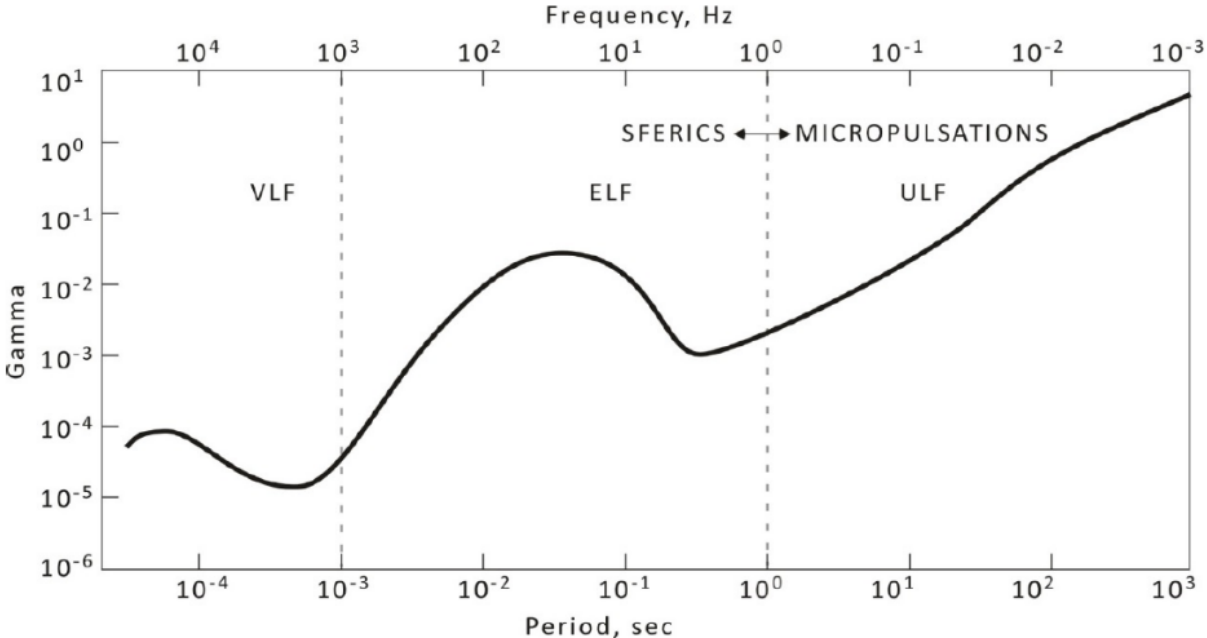


FIGURE 39: The mean natural magnetic field amplitude spectrum in gamma ($\gamma=nT$) as a function of the period (Flóvenz et al., 2012)

5. TEM SURVEY

5.1 Theory

The TEM method uses a controlled and time-varying created magnetic field to induce currents within the Earth. A primary magnetic field is generated by an artificial current source. The induced subsurface currents will in turn generate a secondary magnetic field that is measured as voltage in a receiver loop. In the field setup, a loop of wire is placed on the ground (Figure 40) and a constant current is transmitted in the transmitter loop. A constant magnetic field of known strength is then built up. The current is normally turned on and off at preset times leaving the magnetic field without its source which responds by inducing an image of the source loop. The current and the magnetic field decay with time and induce electrical currents at greater depths in the ground. The decay rate of the magnetic field is observed by measuring the voltage induced in a receiver coil as a function of time. This is normally done at prefixed time gates equally spaced on a log scale (Figure 40). The decay rate of the magnetic field is dependent on the current spreading, which in turn depends on the resistivity structure of the Earth. The induced voltage in the receiver loop can be deduced in terms of the subsurface resistivity structure. The induced voltage is a function of time after the current in the transmitter loop is turned off. The transmitter and receiver are synchronized either by connecting them through a reference cable or by high-precision crystal clocks. This is to enable the receiver to get to know when the transmitter turns off the current.

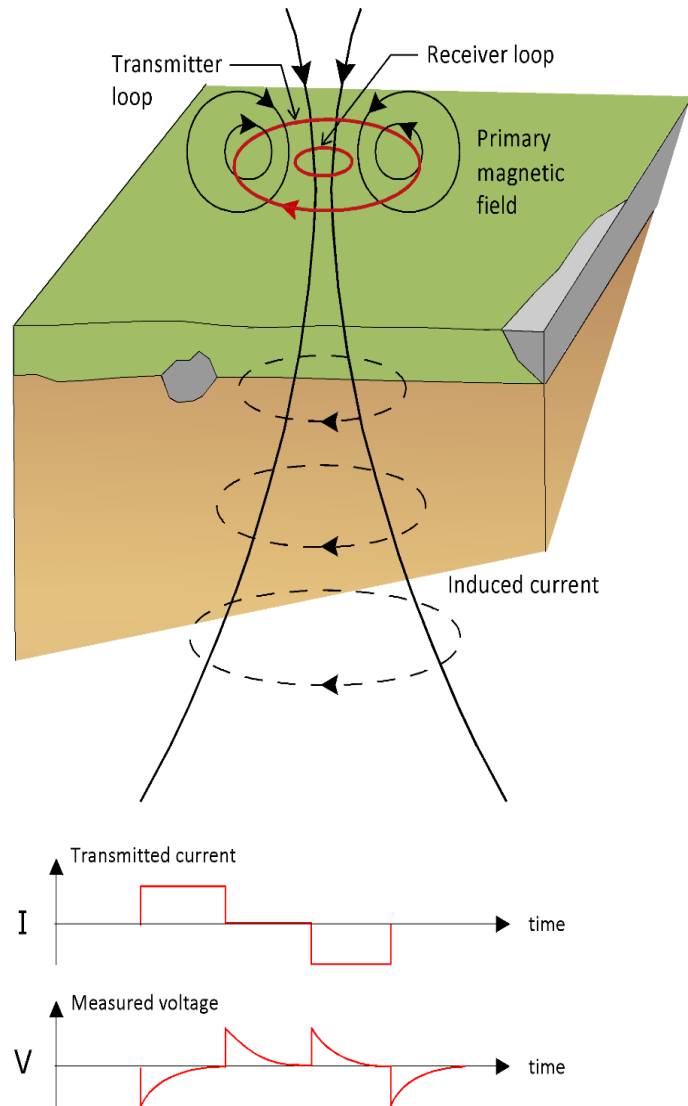


FIGURE 40: The central loop TEM configuration showing the current in the transmitter loop and the voltage in the receiver loop, both as a function of time (Flóvenz et al., 2012)

Turning off the current immediately induces infinite voltages in the source loop. Consequently, the transmitters are intended to turn off the current linearly from maximum to zero in a short but finite time called turn-off time. The zero time of the transients is the time when the current has become zero and the time gates are located relative to this (Palacky, 1987). This entails that the receiver has to recognize the turn-off time. To ease the effect of EM noise, a number of sets of the recorded transients are stacked before they are stored in the receiver memory.

The depth of penetration of the TEM method depends on the resistivity underneath the sounding site as well the equipment setup geometry, the produced current, and its frequency (Árnason, 1989). The depth of penetration increases with time after the current turn-off. Different frequencies of the current signal are then used. High frequencies penetrate to shallow depths and low frequencies are used for deep probing. According to Nabighian and Macnae (1991), the depth to which eddy currents can reach in the Earth depends on the time from the current turn off and the conductivity of the Earth. Sternberg et al.

(1988) demonstrated that the dispersion depth (time domain equivalent of skin depth) of the central loop TEM method is given as:

$$\delta_{\text{TEM}} \approx 1.28 \sqrt{\frac{t}{\sigma\mu}} \quad 5-1$$

where δ_{TEM} (m) is the skin depth, t (s) is time, σ is the conductivity, μ is the magnetic permeability [H/m].

Calculation of the voltage in central loop TEM

At late times, the induced voltage in the receiving coil on a homogeneous half-space of conductivity, σ is given by (Arnason, 1989):

$$V(t, r) \approx I_0 \frac{C(\mu\sigma r^2)^{\frac{3}{2}}}{10 \pi^{\frac{1}{2}} t^{\frac{5}{2}}} \quad 5-2$$

$$C = A_r n_r A_s n_s \frac{\mu}{2\pi r^3}$$

where n_r = Number of turns on the receiver coil
 A_r = Area of the receiver coil [m²]
 A_s = Area of the transmitter loop [m²]
 n_s = Number of turns in transmitter loop
 t = Time elapsed after the current in the transmitter is turned off [s]
 μ = Magnetic permeability [H/m]
 $V(t, r)$ = Transient voltage [V]
 r = Radius of the transmitter loop [m]
 I_0 = Current in the transmitter loop [A].

By solving Equation 5-2 for the resistivity, one obtains definition of the late time apparent resistivity as a function of various variables:

$$\rho_a(t, r) = \frac{\mu}{4\pi} \left[\frac{2I_0 \mu A_r n_r A_s n_s}{5t^{\frac{5}{2}} V(t, r)} \right]^{\frac{2}{3}} \quad 5-3$$

where the induced voltage (V) is measured at the time t elapsed, after the current in the transmitter loop has been turned off. r represents the radius of the transmitter loop, the effective area (cross-sectional area times the number of windings) of the transmitter loop ($A_s n_s$), and the receiver coil ($A_r n_r$); and the current strength (I_0) and magnetic permeability in vacuum (μ_0).

The induced voltage is a function of time elapsed after the current has been turned off. The distributed current is dispersed into three phases with respect to time. In the first phase, the induced voltage is constant in time followed by the second phase where the voltage starts to decline with time and increasing negative slope on a log-log scale.

In the third phase, the voltage response declines with time. The slope of the response curve in this phase is -5/2 (Figure 42). The switch from early to late times is shifted to earlier times as the resistivity of half space increases (Figure 41). The apparent resistivity at early times increases with decreasing resistivity of the half space (Figure 41). When the apparent resistivity for a homogenous half-space is plotted as a function of time, it approaches asymptotically the true resistivity of the half space for late times (Figure 41). The response curve has a similar form for the different half-space resistivities.

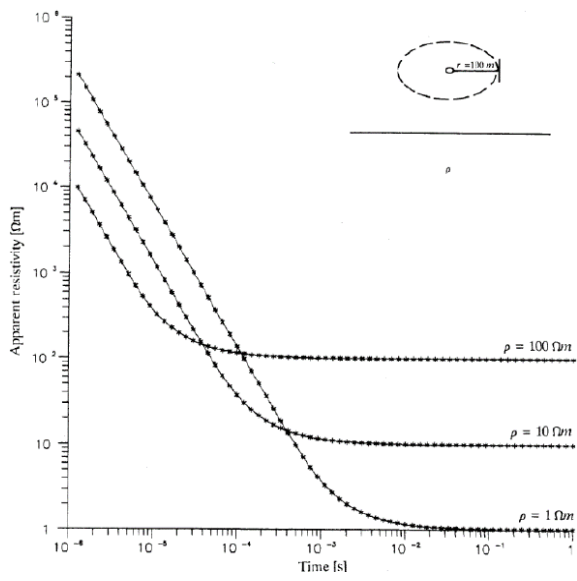


FIGURE 41: Late time apparent resistivity for a homogeneous half space (from Árnason, 1989)

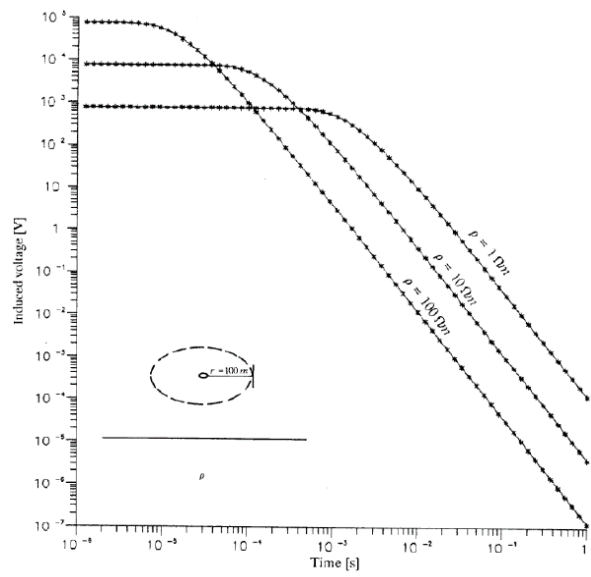


FIGURE 42: Voltage response for homogeneous half space (from Árnason, 1989)

6. ACQUISITION AND PROCESSING OF EM DATA FROM MT. LONGONOT GEOTHERMAL AREA

6.1 TEM data processing

The soundings used in this study were carried out using Zonge TEM equipment and a central loop configuration. Half duty square wave current was transmitted into a source loop (square) at 16 Hz, 4 Hz and 2 Hz. The Zonge TEM system is comprised of a transmitter, 24-bit multifunction receiver, voltage regulator, 1.0 mm² transmitter cable and a receiver coil with a dipole moment of about 10,000 Am².

In Mt. Longonot field, a setup of 300 m x 300 m transmitter loop was used for the current wave transmission. The transmitter high precision controller crystals are warmed up for some time and then synchronized with the receiver. This is to ensure that the induced voltage in the receiver coil at the center of the loop is measured at the right time after the current is turned off (Palacky, 1987). The transmitters are designed to turn off the current linearly from maximum to zero in a short but finite time called turn-off time (TOFF). This implies that the receiver has to know the TOFF. The TOFF is measured by the transmitter and fed by the operator into the receiver. The depth of penetration of the sounding increases with time after the current is turned off. Different frequencies of the current signal are therefore used, high frequencies for shallow depths and low frequencies for deep probing (the time gates are normally scale with the period T).

The receiver memory stores data that comprises voltages at the time gates for the selected frequency, selected gain and effective area of the antenna. The source loop size and the value of the transmitted current is normally the same during the measurement, but to reduce influence of noise on the data, several datasets are recorded, processed and stacked. The program TemxZ was used to process the raw TEM data from the Zonge GDP-32 receivers (Árnason, 2006a). The purpose of the TemxZ software is to analyze the datasets, omit outliers, perform stacking and calculate late time apparent resistivity. The program calculates averages and standard deviations of the data acquired at same frequency and then computes late time apparent resistivity as a function of time after turn-off. Unreliable data points (noisy readings) are also removed before the data can be used for interpretation. Figure 43 is an example of the data collected by using Zonge GDP-32 receiver coil at a high frequency (16 Hz, red data points) and a low frequency (2 Hz, yellow data points). The inversion process uses the output *.inv files from the TemxZ program.

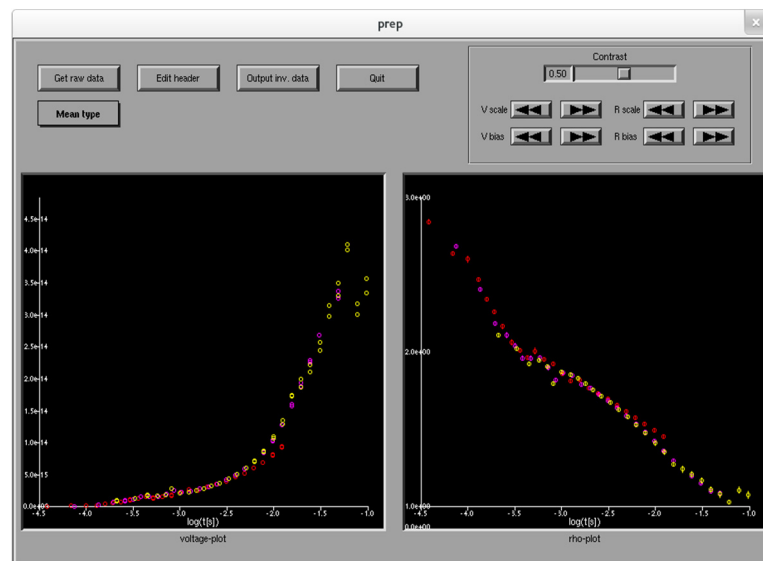


FIGURE 43: Display from TemxZ program. On the left side is the stabilized voltages against log-time for all data sets while the right side displays apparent resistivity against log time calculated from mean values for each segment

In this work, the modelling of TEM resistivity soundings was performed by using forward modelling and thereafter an inversion process (Figure 44). An algorithm is used in forward modeling to compute the apparent resistivity curve that is then compared with the measured data. The forward algorithm computes the induced transient voltages in the receiver as the summation of the responses from sequential current turn-on and turn-off times. The transient responses are computed as induced voltages and late time apparent resistivity as a function of time. The apparent resistivity curve is inverted using TEMTD software, an inversion algorithm that creates a 1-D isotropic horizontally layered Earth model

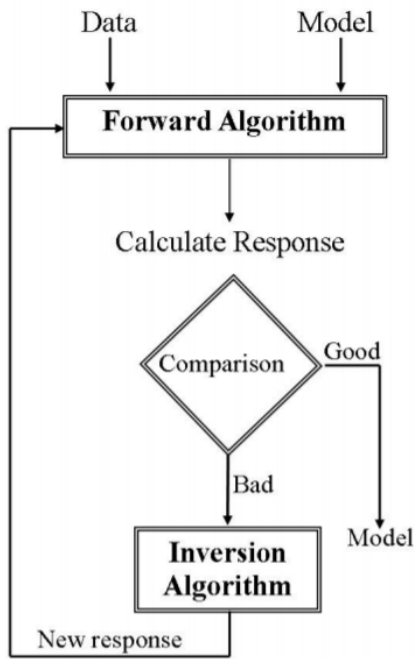


FIGURE 44: Flow diagram showing inversion algorithm improvement of the model based on misfit

that best fits the data (Árnason, 2006b). For all the layers in the inversion, both the resistivity and layers' thicknesses can vary (Figure 45). Inversion (Occam inversion) starts with data and an educated guess of an initial model. The inversion algorithm improves the model in an iterative process by calculating modifications to the model from the differences between the measured data and the response of the model until a satisfactory agreement has been reached. It is based on the hypothesis that resistivity fluctuates smoothly with depth rather than in distinct layers.

In the Occam inversion, numerous thin layers of fixed thicknesses approximate the smooth variations and only the resistivity value is inverted for (Figure 45). The best fit is attained when the misfit function χ^2 (chi²), which is the mean-square variance between measured and calculated values, is lowest. The damping is achieved by utilizing both first derivatives and second derivatives, to obtain smooth models. The actual function that is minimized is the potential (P) instead of the weighted mean-square misfit, χ^2 (chi²).

$$P = \chi^2 + \alpha D_{S1} + \beta D_{S2} + \gamma D_{D1} + \delta D_{D2}$$

where D_{S1} and D_{S2} are the first and second order derivatives of log-conductivities in the layered model. D_{D1} and D_{D2} are the first and second order derivatives of the logarithms of the ratios of layer depths. The coefficients α , β , γ and δ are the comparative contributions of the varied damping terms. The method of Occam inversion for this case was chosen, as it was the most consistent through a variety of inversion attempts. The TEMTD program employs the nonlinear least-squares inversion of

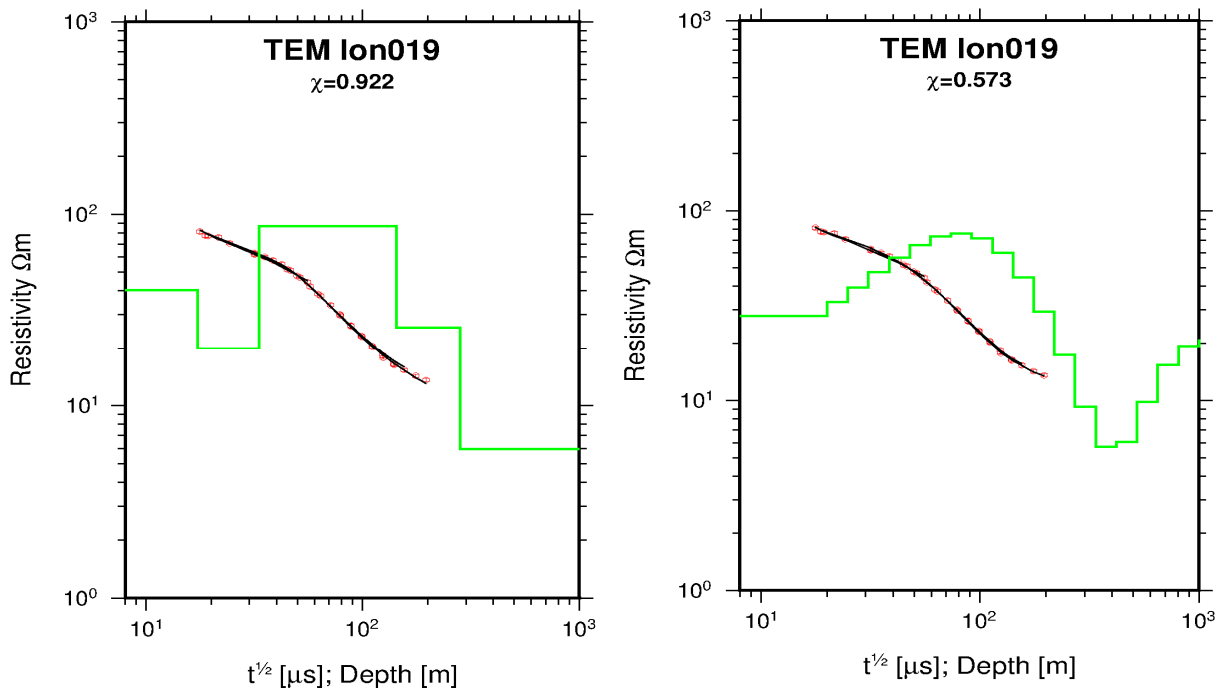


FIGURE 45: Two examples of an inversion done by the TEMTD program. Left panel: Layered model of TEM sounding lon019 where both the layer thickness and resistivity values are inverted for and no limitation is on the resistivity differences between layers. Right panel: Occam model of TEM sounding lon019 where the thicknesses are small and fixed and the resistivity value in the layers is inverted for. The red dots are measured late-time apparent resistivities, the green line is the model and the black solid line is the apparent resistivity. calculated from the model

the Levenberg-Marquardt type as described by Árnason (1989) where the misfit function is the mean-square variance between measured and calculated values, χ^2 (chi²), weighted by the standard deviation of the measured values.

Figure 45 below illustrates the two TEM apparent resistivity inversions. In 1-D inversion, it is assumed that the Earth consists of horizontal layers with different resistivity values and thicknesses. In layered-model inversion, resistivity values and layer thicknesses are inverted for while in Occam inversion, only resistivity values are inverted for as the layer thicknesses increase exponentially with depth. In the layered model, there is no restriction on the resistivity changes between layers (Figure 45), left part). In the Occam inversion, the thicknesses are fixed while the resistivity of the layers is changed (Figure 45, right part). It is important to keep in mind that the depth of exploration of the TEM soundings is much greater in a resistive Earth than in conductive environments. This is because the fields decay faster in conductive materials than in resistive

6.2 MT data processing

6.2.1 MT field setup and data collection

A 5-channel MT data acquisition equipment from Phoenix Ltd. (MTU-5A) was used for data collection in Mt. Longonot field. It has the capacity of measuring the MT signals in the frequency range of $1.3 \cdot 10^{-5}$ Hz to 400 Hz (Phoenix Geophysics, 2009). The instrument consist of a data logger (MTU), three magnetic induction coils connected by a particular induction coil cables for measuring the magnetic fields and two pairs of electric dipoles coupled by shielded cables for measuring the electric fields. The MTU screens the acquisition procedure by filtering, amplifying and converting data into digital format to enable the storage into memory card. The electrodes forming a dipole and induction coils are usually buried in the ground to moderate temperature discrepancies.

For a common practice, one electric dipole is oriented in the magnetic north-south direction and other one in east-west position. Though this is not restricted, it can as well be placed in true north direction but when the magnetic north is used, the magnetic declination angle has to be known. The electrodes are non-polarizable made by a plastic pot with a porous bottom filled with a lead chloride solution. The bottom of each electrode is soiled with bentonite to prevent the electrolyte from drying up and salty water is poured in each hole before the electrode is placed in it. This is to enhance good ground contact and electrical conductivity. In cases where long period MT data are to be collected, the use of bentonite clay is not desirable. This is because it dries out over recording time duration and thereafter causes the potential difference to drift (Simpson and Bahr, 2005). All the electric dipoles are put in place; the magnetic coils are placed orthogonally to the electrodes (Figure 46), one in x-direction, one in y-direction and the third one at the centre of the equipment setup in the z-direction. A remote reference station is placed away from any form of cultural noise. It is set to record continuously during the survey. The data obtained from this station are used during data processing to obtain a better quality data with high signal to noise ratio (Gamble et al., 1979). The real time GPS (Global Positioning System) for time series synchronization with satellites is connected to the MTU-5A acquisition unit.

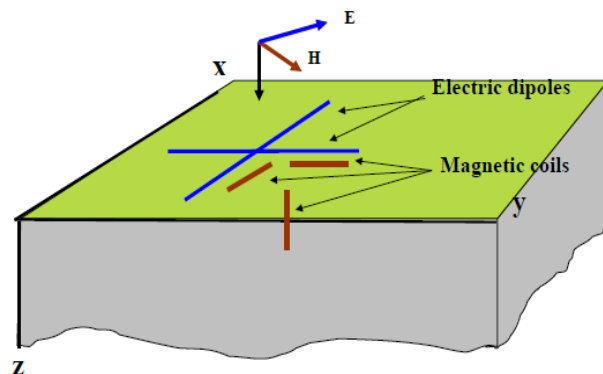


FIGURE 46: MT layout

6.2.2 The MT data processing technique

The main objective of data processing is to pick sets of smooth, recurring Earth response functions from time series signals. During the survey, the time series data is recorded and stored in a memory card by the MT data logger. The time series data are electric and magnetic field time-variations of the MT data measured as a function of time. The time series comprise harmonic components of varied frequencies. It is observed that waves with high frequencies are attenuated at shallow depth and they are not able to penetrate deep. However, the waves with low frequencies have the capability of probing deeper into the Earth.

Time series Data

↓
Fourier Transform

Frequency Domain

↓
Robust

Resistivity / Frequency

The time series are then downloaded from the MTU units of each station. Then the data are scrutinized for quality using a program called the Synchro-Time Series Viewer (Phoenix Geophysics, 2005). The program is capable of viewing and printing the graphical illustrations of the raw time series data, power spectra that are resulting from the time series data and coherence amid pairs of orthogonal electric and magnetic elements.

The processing of MT data converts the time varying geo electric field components into earth response functions that comprise information regarding the dispersion of the conductivity structure. Due to the noise contained in the measured data, data processing in geophysics deals with reducing the noise from the measured data and increasing the signal-to-noise ratio. It includes the processing or reduction of the collected bulk data to a new data set that is ready for numerical modelling. A systematic data processing is listed as shown in Figure 47.

FIGURE 47: The processing steps used

6.2.3 Data review and editing

The time series (example Figure 48) for each station are divided into M segments containing N data points per segment. The N value is chosen based on the recorded time window such that each segment contains periods equally spaced on logarithmic scale. Furthermore, each time window must be divided into a sufficient number of segments for further statistical estimation of the transfer functions. Each segments scrutinized for the purpose of identifying and removing trends and noise effects. The action is performed automatically or manually by using MTEditor program (Phoenix Geophysics, 2005).

A computer program SSMT2000 from Phoenix Geophysics (2005) is used to perform time series processing by using a robust processing technique and editing the results (Egbert and Booker, 1986). Fast Fourier Transforms (FFT) are normally used to transform the measured time series to the frequency domain (Vozoff, 1991). A raw spectrum with a number of data points divided into N/2 frequencies is obtained. These frequencies are equally distributed on a log scale, ideally 6-10 period per decade. The final spectra are smoothed by averaging over neighboring frequencies using a window function (Parzen-Window Density Estimation). The auto and cross spectra segments which are products of the field components and their complex conjugates, are calculated from segments of the original time series for each frequency. The auto-spectra density, in the frequency band f_{j-m} to f_{j+m} around the central frequency, f_j is calculated by:

$$\langle A(f_j) \rangle = \sqrt{\frac{1}{2m+1} \sum_{k=j-m}^{j+m} A_k A_k^*} = \langle A_j A_j^* \rangle^{\frac{1}{2}} \quad 6-1$$

* means complex conjugate, where A represents **E** or **H**. Its square is the auto power spectral density at f_j .

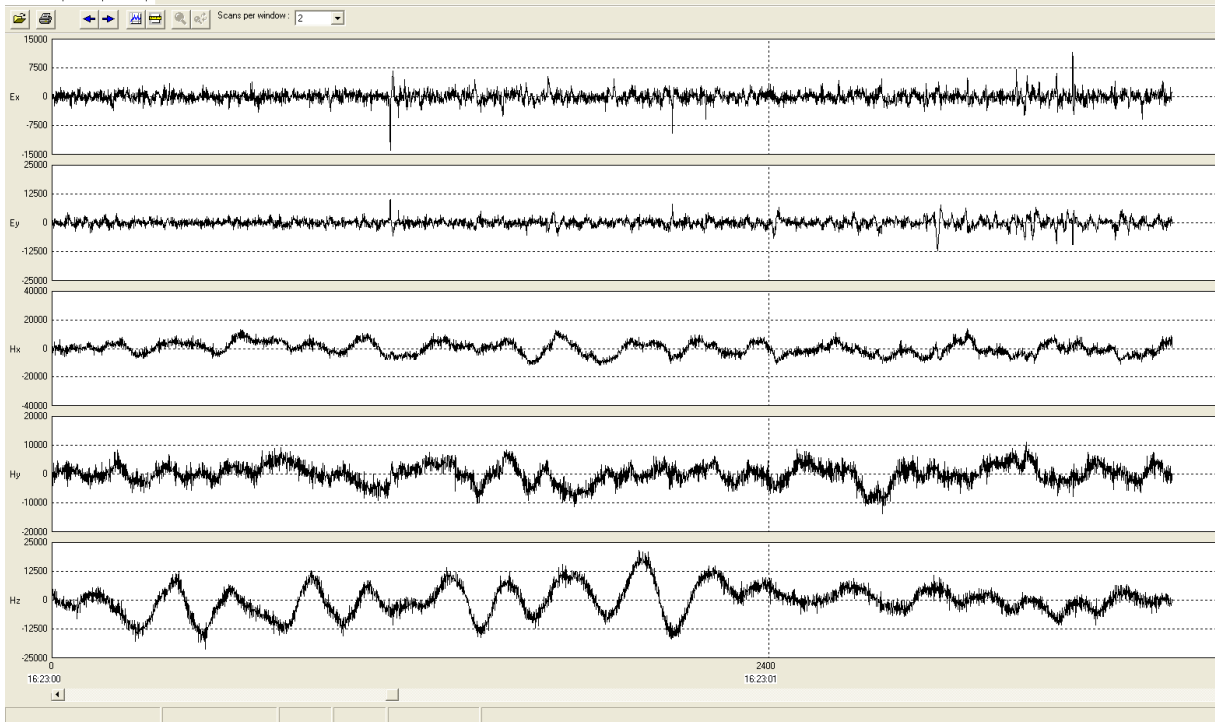


FIGURE 48: Time series data acquired by a 5-channel MT data acquisition system at Mt. Longonot Geothermal area. The first two series are the electric components in x and y direction, respectively. The magnetic components are the three subsequent series in x, y and z direction, respectively

In addition, the cross power density at f_j of two channels A and B:

$$\langle A(f_j), B(f_j) \rangle = \sqrt{\frac{1}{2m+1} \sum_{k=j-m}^{j+m} A_k B_k^*} = \langle A_j B_j^* \rangle^{\frac{1}{2}} \quad 6-2$$

To determine the tensor elements time series are Fourier transformed by:

$$\begin{aligned} E_x(t) &\rightarrow E_x(\omega) & H_x(t) &\rightarrow H_x(\omega) \\ E_y(t) &\rightarrow E_y(\omega) & H_y(t) &\rightarrow H_y(\omega) \end{aligned}$$

The coherency (which is between 0 and 1) of the two channels can be defined as:

$$\text{coh}(A_j B_j) = \frac{1}{2m+1} \sum_{k=j-m}^{j+m} \frac{| \langle A_k B_k^* \rangle |}{\sqrt{\langle A_k A_k^* \rangle \langle B_k B_k^* \rangle}} = \text{coh}(A, B)_j \quad 6-3$$

6.2.4 Estimation of transfer functions

MT transfer function relates the measured magnetic and electric fields at a given frequency. It depends the electrical properties of a material over which the EM waves are propagating. However, it does not depend on the source of EM wave. The calculation of MT transfer functions essentially averages the spectra over a number of closely spaced frequencies of the equivalent field components in the frequency domain. This can be obtained from the electric and magnetic field spectra segments as well as Tipper (geomagnetic transfer functions):

$$\begin{aligned} E_x(\omega) &= Z_{xx} H_x(\omega) + Z_{xy} H_y(\omega) \\ E_y(\omega) &= Z_{yx} H_x(\omega) + Z_{yy} H_y(\omega) \\ H_z(\omega) &= J_{zx} H_x(\omega) + J_{zy} H_y(\omega) \end{aligned}$$

The measured electromagnetic fields contain noise and uncertainties in the impedance tensor due to estimation of plane wave field. Hence, many record sets are considered that will allow averaging to decrease the noise. The impedance equations are solved assuming Z_{ij} to be constant over an averaging frequency band that has to be narrow enough. In each frequency band, each equation has cross power produced in the frequency domain by multiplying the impedances by the complex conjugates of the magnetic spectra, H_x^* and H_y^* hence, giving independent equations as follows:

$$\begin{aligned}
\langle E_x H_x^* \rangle &= Z_{xx} \langle H_x H_x^* \rangle + Z_{xy} \langle H_y H_x^* \rangle \\
\langle E_y H_x^* \rangle &= Z_{yx} \langle H_x H_x^* \rangle + Z_{yy} \langle H_y H_x^* \rangle \\
\langle E_x H_y^* \rangle &= Z_{xx} \langle H_x H_y^* \rangle + Z_{xy} \langle H_y H_y^* \rangle \\
\langle E_y H_y^* \rangle &= Z_{yx} \langle H_x H_y^* \rangle + Z_{yy} \langle H_y H_y^* \rangle \\
\langle H_z H_x^* \rangle &= J_{zx} \langle H_x H_x^* \rangle + J_{zy} \langle H_y H_x^* \rangle \\
\langle H_z H_y^* \rangle &= J_{zx} \langle H_x H_y^* \rangle + J_{zy} \langle H_y H_y^* \rangle
\end{aligned} \tag{6-4}$$

The above equations can be solved for Z_{ij} as:

$$\begin{aligned}
Z_{xx} &= \frac{\langle E_x H_x^* \rangle \langle H_y H_y^* \rangle - \langle E_x H_y^* \rangle \langle H_y H_x^* \rangle}{\langle H_x H_x^* \rangle \langle H_y H_y^* \rangle - \langle H_x H_y^* \rangle \langle H_y H_x^* \rangle} \\
Z_{xy} &= \frac{\langle E_x H_x^* \rangle \langle H_x H_y^* \rangle - \langle E_x H_y^* \rangle \langle H_x H_x^* \rangle}{\langle H_y H_x^* \rangle \langle H_x H_y^* \rangle - \langle H_y H_y^* \rangle \langle H_x H_x^* \rangle} \\
Z_{yx} &= \frac{\langle E_y H_x^* \rangle \langle H_y H_y^* \rangle - \langle E_y H_y^* \rangle \langle H_y H_x^* \rangle}{\langle H_x H_x^* \rangle \langle H_y H_y^* \rangle - \langle H_x H_y^* \rangle \langle H_y H_x^* \rangle} \\
Z_{yy} &= \frac{\langle E_y H_x^* \rangle \langle H_x H_y^* \rangle - \langle E_y H_y^* \rangle \langle H_x H_x^* \rangle}{\langle H_y H_x^* \rangle \langle H_x H_y^* \rangle - \langle H_y H_y^* \rangle \langle H_x H_x^* \rangle} \\
J_{zx} &= \frac{\langle H_z H_x^* \rangle \langle H_y H_y^* \rangle - \langle H_y H_x^* \rangle \langle H_z H_y^* \rangle}{\langle H_x H_x^* \rangle \langle H_y H_y^* \rangle - \langle H_y H_x^* \rangle \langle H_x H_y^* \rangle} \\
J_{zy} &= \frac{\langle H_z H_y^* \rangle \langle H_x H_x^* \rangle - \langle H_z H_x^* \rangle \langle H_x H_y^* \rangle}{\langle H_x H_x^* \rangle \langle H_y H_y^* \rangle - \langle H_y H_x^* \rangle \langle H_x H_y^* \rangle}
\end{aligned} \tag{6-5}$$

6.2.5 Remote reference and MT impedance estimation

The remote reference technique is commonly applied in MT data acquisition and it involves an additional MTU (usually magnetic) located at an electronically quiet site away from cultural noise (Goubau et al., 1979; Clarke et al., 1983). The natural part of the induced field can be anticipated to be coherent over longer distances, whereas noise is normally random and incoherent. The problem faced in auto-powers of the magnetic field is the biasing effect of noise. The coherent noise present in the data at a single site will cause the impedance estimate, Z_{ij} , to be biased. In order to avoid the effect of noise, the remote site should be far from the local site (at least 20 km) so that the sources of noise are not correlated. By multiplying the linear correlation of electric and magnetic field spectra of the impedance tensor in Equation 6-5 with the remote site components, R_x^* and R_y^* and averaging over a number of determinations, the pairs of concurrent equations for impedance can be solved to get the following remote reference estimates of the impedance tensor elements Z_{ij} as follows:

$$\begin{aligned}
Z_{xx} &= \frac{\langle E_x R_x^* \rangle \langle H_y R_y^* \rangle - \langle E_x R_y^* \rangle \langle H_y R_x^* \rangle}{\langle H_x R_x^* \rangle \langle H_y R_y^* \rangle - \langle H_x R_y^* \rangle \langle H_y R_x^* \rangle} \\
Z_{xy} &= \frac{\langle E_x R_x^* \rangle \langle H_x R_y^* \rangle - \langle E_x R_y^* \rangle \langle H_x R_x^* \rangle}{\langle H_y R_x^* \rangle \langle H_x R_y^* \rangle - \langle H_y R_y^* \rangle \langle H_x R_x^* \rangle} \\
Z_{yx} &= \frac{\langle E_y R_x^* \rangle \langle H_y R_y^* \rangle - \langle E_y R_y^* \rangle \langle H_y R_x^* \rangle}{\langle H_x R_x^* \rangle \langle H_y R_y^* \rangle - \langle H_x R_y^* \rangle \langle H_y R_x^* \rangle} \\
Z_{yy} &= \frac{\langle E_y R_x^* \rangle \langle H_x R_y^* \rangle - \langle E_y R_y^* \rangle \langle H_x R_x^* \rangle}{\langle H_y R_x^* \rangle \langle H_x R_y^* \rangle - \langle H_y R_y^* \rangle \langle H_x R_x^* \rangle}
\end{aligned} \tag{6-6}$$

R_x and R_y signify the magnetic components, H_x and H_y of the remote reference station, respectively.

Though one can use the E_x and E_y components of the remote reference station, it is more common to use the magnetic field since the horizontal magnetic field is known to be less liable to polarization, and is less contaminated by noise than the electric field. Remote reference technique also provides estimations of noise in each of the channel (Gamble et al., 1979). It makes it possible to approximate the noise in each of the impedance elements at each frequency. Nevertheless, in many situations with high noise effects, the resulting cross-powers may not be as smooth as desired. Consequently, physical editing in the MTEditor programme of the weighted apparent resistivity values for each frequency will help produce sensible results and smoother curves. The cross-power files created by SSMT2000 are used as input files in MTEditor, which is a windows based programme. Graphical presentation are displayed after merging the cross-powers. This permits the viewing of the different features of the soundings, such as apparent resistivity, phase, impedance, strike direction, coherence and many others across the full frequency range that was acquired. The programme also permits the removal of individual cross-powers from the calculations. The edits are made by changing a mask and not by deleting the data (Phoenix Geophysics, 2005). This enables easy restoration of individual cross-powers or return to the initial view whenever it is needed. The programme has an auto-edit ability that rapidly masks cross-powers that lie too far from the mean. This often saves substantial time in the editing process. The output of MT-Editor (edi file) is ran through spec2edi Linux based program developed at ISOR which computes several MT parameters (some are not implemented in MTEditor) and produces the results in Electrical Data Interchange (EDI) standard format (Figure 49). The file is then ready for plotting and exporting to the interpretation software for multidimensional inversion.

Figure 49 shows examples of apparent resistivity and phase angle from Mt. Longonot. It can be deduced that at periods below 1 s they display 1-D response with decreasing apparent resistivity values and decreasing phase with increasing period. For periods above 10 s, curves start to split apart for station lmt01a and for lmt02 and lmt108, the splitting starts from about 1 s. This is an indication of a non-one-dimensionality. High phase values ($> 45^\circ$) at short periods indicate a conductor at shallow depth.

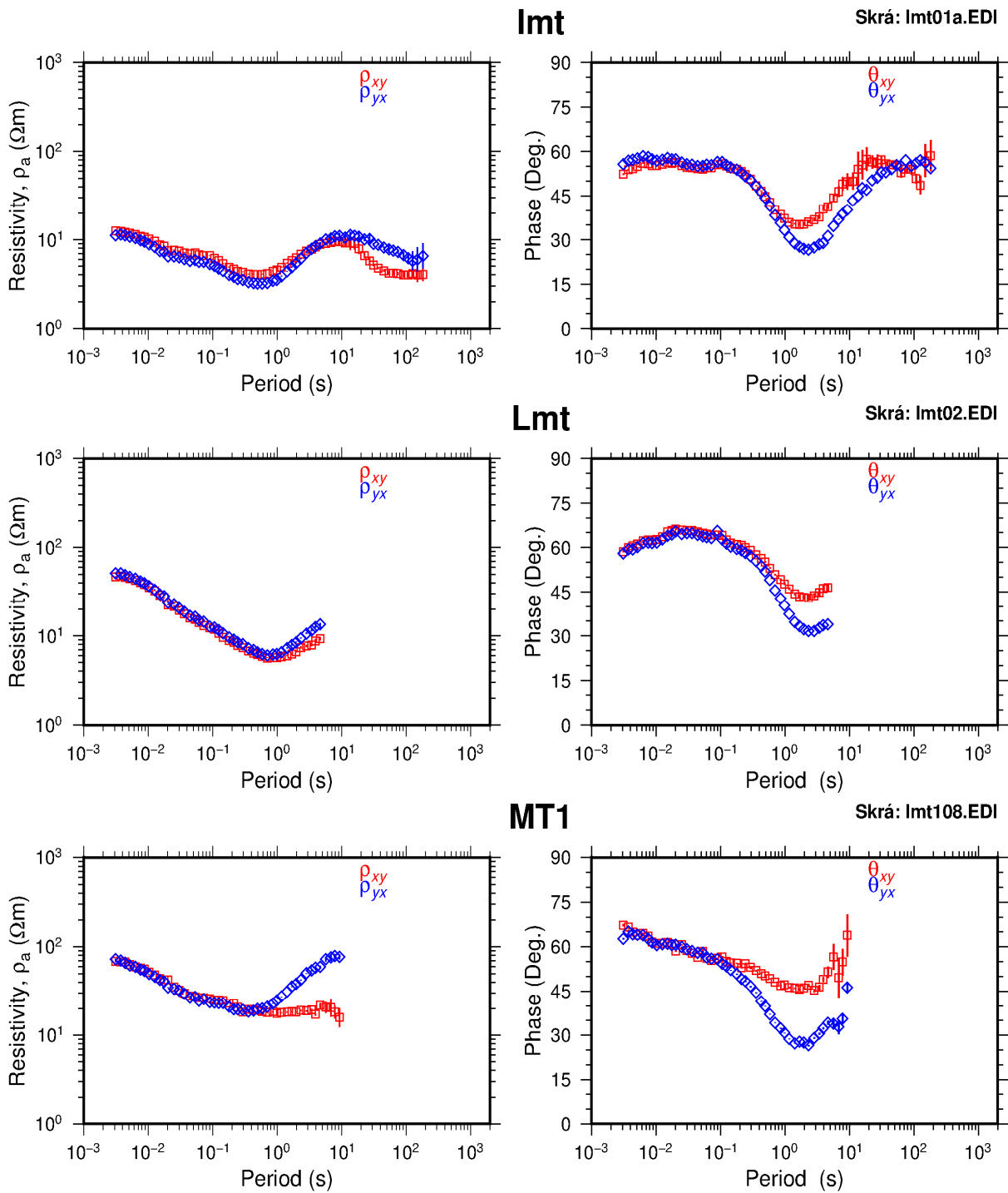


FIGURE 49: EDI output showing apparent resistivity and phase curves. Typical examples of apparent resistivity and phase curves of MT soundings in the Mt. Longonot area (red and blue symbols are xy and yx data, respectively)

7. MODELING AND INTERPRETATION OF EM FROM MT. LONGONOT FIELD

7.1 Overview

Some 84 TEM and 85 MT soundings collected in and around the Mt. Longonot geothermal area are used in this study for interpretation of the subsurface resistivity structure in line with the geothermal field (Figure 50). After processing MT and TEM data the next step is modelling and interpretation of the processed data. The basic reasons for interpretation are:

- Gain a better understanding of the high-temperature geothermal system;
- To eliminate the effects initiated by local near-surface resistivity inhomogeneities;
- To define the suitable strike direction for interpretation;
- To comprehend the essential dimensionality of the data.

Modelling of the data attains the delineation of geophysical exploration target under research. The use of the EM method was originally based on 1-D interpretation and different developers have contributed to the inversion codes which are being used today (Constable et al., 1987; Smith and Booker, 1991). Information regarding resistivity distribution below the area of interest is achieved through inversion processes. The algorithm of inversion is often referred to as Occam's inversion since it looks for the simplest model that explains the data. Inversion processes steered to the development of TEMTD program for 1-D inversion (Árnason, 2006b), REBOCC program (Reduced Basis Occam) for 2-D inversion (Siripunvaraporn and Egbert, 2000) and WSINV3DMT program for 3-D inversion (Siripunvaraporn et al., 2005) were established. In this study project, a broad-spectrum overview of 1-D EM inversion schemes have been performed to understand the subsurface resistivity structure in the context of the geothermal energy of Mt. Longonot field.

7.2 1-D inversion program

In this study, the TEMTD program is used to 1-D invert MT apparent resistivity and phase jointly with TEM data. The MT parameters are derived from the rotationally invariant determinant of the tensor elements. Knútur Árnason at ÍSOR (Árnason, 2006b) developed the TEMTD program. The 1-D inversion of TEM and MT data can be done separately or jointly. The program inverts MT apparent resistivity and phase resulting from either of the off-diagonal elements of the MT tensor (xy and yx modes), the rotationally invariant determinant or the average of the off-diagonal elements. For a 1-D inversion, the program does both standard layered inversion (inverting resistivity values and layer thicknesses) and Occam's inversion with exponentially increasing fixed layer thicknesses with depth. In the joint inversion process (Figure 51); a static shift multiplier is to fit both the TEM and MT data with the response of the same model and is also inverted for. The program assumes a square source loop and the receiver coil to be at the centre of the source loop. The current waveform is presumed to be half-duty bipolar semi-square wave (equal current-on and current-off segments). It is with exponential current turn-on and linear current turn-off. For MT data, the program assumes standard EDI format for of impedance and apparent resistivity and phase data (Árnason, 2006b).

The program comprises a user stated damping of first (sharp steps) and second order derivatives (oscillations) of logarithm of resistivity and layer thicknesses (model parameters) (Árnason, 2006b). The programme solves both forward and inverse problems. The inversion problem is to define those model parameters, which give the model response closest to the measured response. The forward problem estimates the response from a given model. Árnason (1989) describes the inversion algorithm used in the program as the Levenberg-Marquardt non-linear least square inversion. The root-mean-square variance between measured and calculated values, χ^2 , is the misfit function weighted by the standard deviation of the measured values. It is desirable to have a small χ^2 , indicating that the model explains the data well. One can decide in case of the TEM data whether the program fits the measured voltage values or the late time apparent resistivity values. It is usually appropriate to sacrifice fit of a dataset in favour of smooth resistivity variation when fitting electromagnetic data for a rough model (Constable et al., 1987). Under-parameterization of the inverse problem tends to suppress structure that could be significant, whereas over-parameterization leads to structure that is redundant, and not truly resolvable by the available data (Constable et al., 1987).

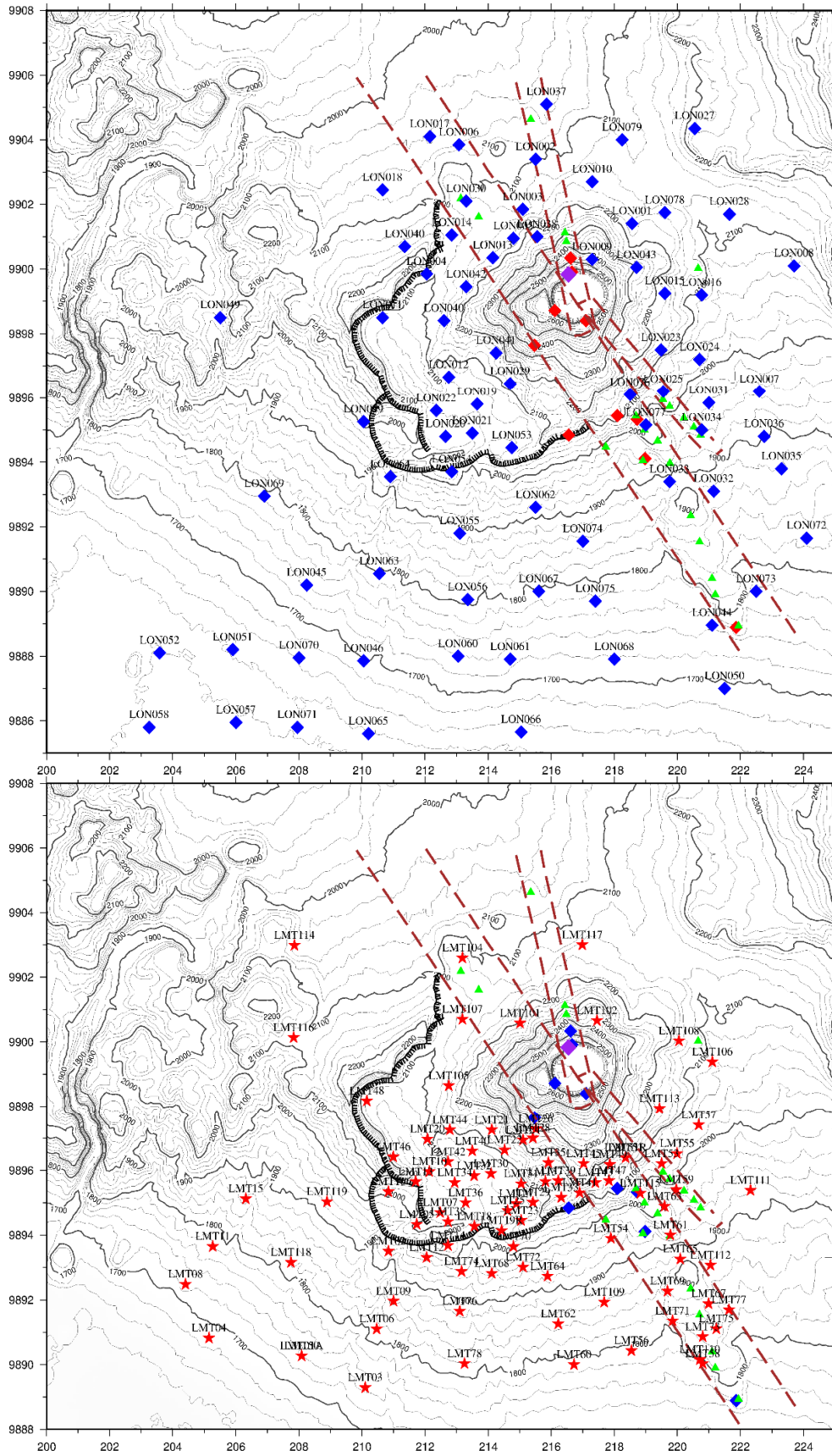


FIGURE 50: TEM location map of the Mt. Longonot field (blue diamond) (upper figure); and MT location map of the same area (red stars) (lower figure)

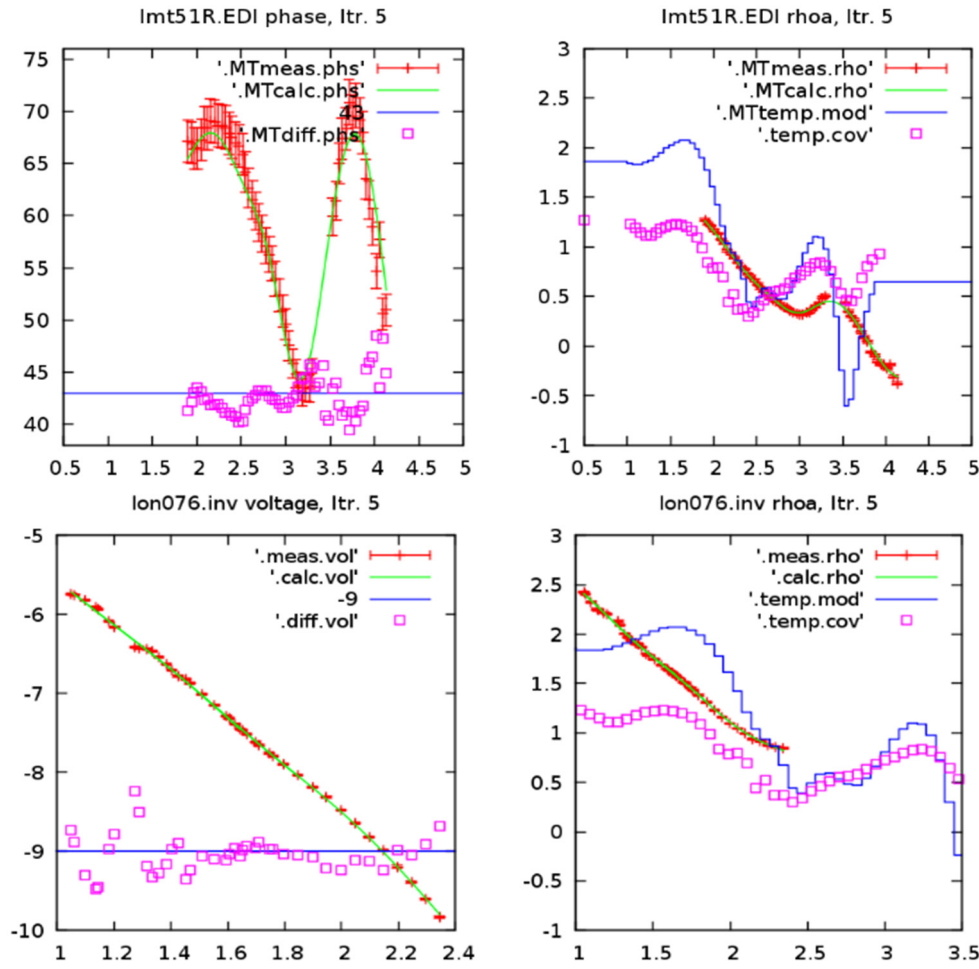


FIGURE 51: Sample MT and TEM data plot after 5 iteration in the Occam's inversion

7.3 1-D joint inversion of TEM and MT soundings

Inversion allows us to derive from geophysical data a model of physical properties in the subsurface. A good model based on inverted data is one that replicates the observed data and is in agreement with other existing information. In MT, we try to find resistivity structures that are consistent with the processed apparent resistivity, phase, and Tipper for a range of frequencies at each station in a survey area. Figure 52 shows the result after 10 iterations of 1-D inversion for the determinant resistivity and phase data. It is independent of the strike direction. More plots for 1-D joint inversion are shown in Appendix C.

7.4 Static shifts correction of MT in Mt Longonot

Near-surface inhomogeneities and topography distort the magnetotelluric (MT) data leading to a shift of apparent resistivity sounding curves by a scaling factor that is almost independent of the frequency as discussed in Chapter 4.5.1 above. The static shift has no effect on the phase data. The shift of the apparent resistivity curves can easily lead to errors in the inverted model. In 1-D layered model, if the scaling factor is S , then the resistivities and depths of the final model will be scaled by S and $S^{\frac{1}{2}}$, respectively. Inversion of shifted apparent resistivity curves results in near-surface heterogeneities in addition to the correct deeper resistivity structure (Grandis, 2010). However, it is clear that correction for the static effect is of prime importance before any interpretation of MT data. Various methods have been developed to compensate for static shift. One of the approaches is based on joint use of active measurements such as DC resistivity (Stephen et al., 2003; Tripaldi et al., 2010) and TEM. TEM measurement at the same site as an MT sounding is commonly used especially for MT studies for

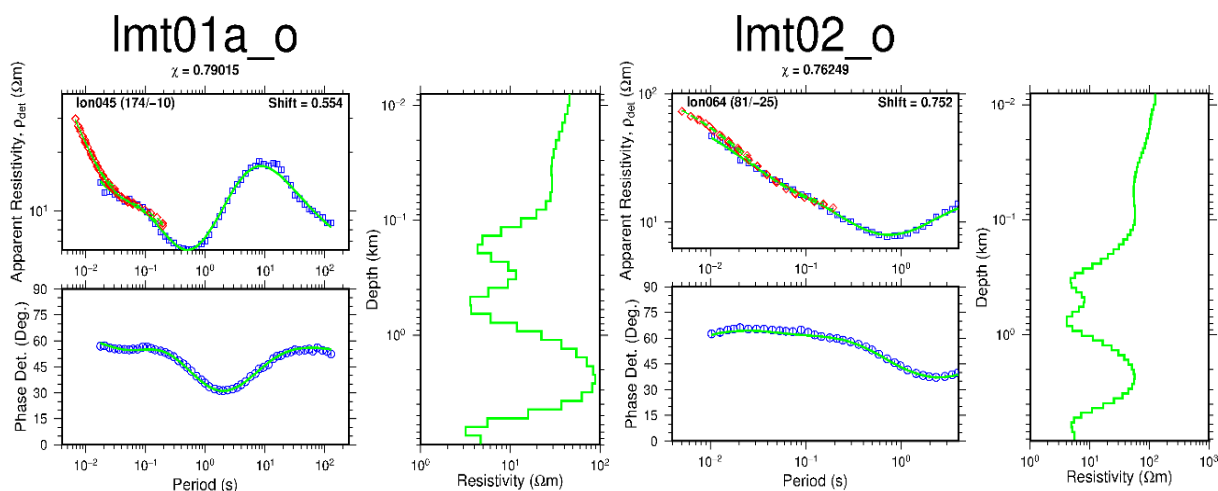


FIGURE 52: Examples of the results of joint 1-D inversion of TEM and MT data. Red diamonds are measured TEM apparent resistivities, blue squares are the measured MT apparent resistivities and blue circles are the MT phase. The green solid lines to the right show the resistivity model vs. depth. The calculated response of the resistivity model is the solid green lines in the two panels on the left. The shift multiplier is shown in the upper right hand corner of the apparent resistivity panel

geothermal exploration. This is because TEM data are less sensitive to near-surface heterogeneities. 1-D inversion model of TEM data is used as the input for 1-D MT forward modeling to infer unbiased MT sounding curve (Sternberg et al., 1988). Another method to solve the shift problem is a statistical approach based on the analysis of the MT data alone (Torres-Verdin and Bostick, 1992).

In Mt. Longonot area, a static shift analysis of the 84 MT sounding data were performed. In 30 of these stations, static shift was corrected by use of nearby TEM data. A TEM station was used if it was less than 400 m away from the MT station. The shift factors were in the range of 0.3 to 1.5 as seen in Figure 53. From the histogram, it can also be seen that the majority of the soundings were shifted down (shift < 1) and only a few shifted upwards (shift > 1). The mean shift for all the soundings is 0.821. Using the static shift factors obtained from the stations with TEM, a spatial distribution map (Figure 53 to the right) was created.

From the contour map of the static shift (Figure 53), an estimation of shift factor was obtained and used for those stations with no nearby TEM data. However, the accuracy might not be good enough but it

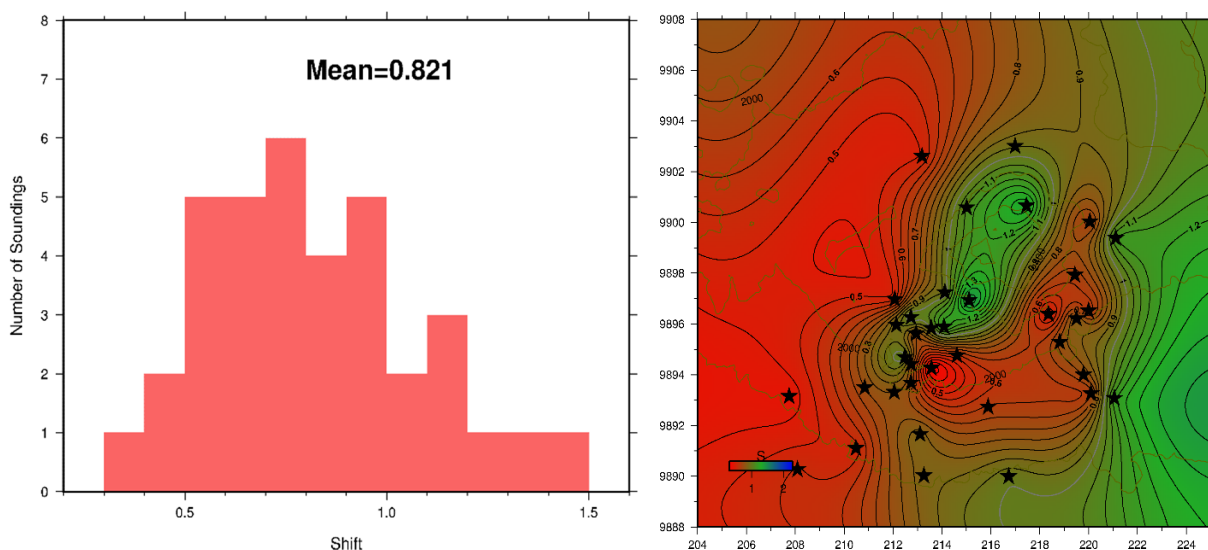


FIGURE 53: Histogram (left) and spatial distribution (right) of static shift parameters for determinant apparent resistivity in the Mt. Longonot area

was fair enough to be performed in this way. Figure 54 is a good example of static shift correction using TEM and the spatial distribution map of static shift values. For interpretation purposes, static shift correction is vital in reducing errors when resolving the resistivity structure and depths in a geothermal field. Correction for static shift by use of a TEM data in a joint inversion with MT data can be actual in providing a more precise picture of the resistivity structure of the Earth. More plots for 1-D inversion using TEM and spatial distribution of static shift estimation are shown in Appendices C and D.

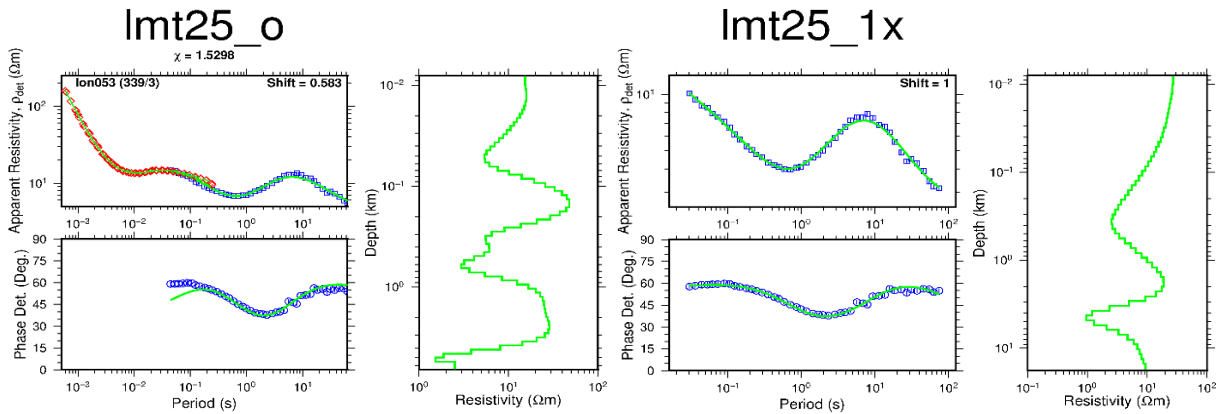


FIGURE 54: A typical example of joint 1-D inversion of TEM and MT data (left) and 1-D inversion of an MT sounding with no shift correction (right)

8. 1-D JOINT INVERSION RESULTS

8.1 1-D Cross-sections

A program called TEMCROSS (Eysteinnsson, 1998); developed at ÍSOR (Iceland GeoSurvey) was used to plot the resistivity cross-section from results that were obtained from the 1-D inversion. The program interpolates the different 1-D models, located underneath each site. The resistivity is contoured so that the colour scale is exponential; the contour lines are resistivity values. Both MT soundings that were static shift corrected using TEM and the ones that were static shift corrected based on the geospatial distribution of static shifts were included in the vertical cross-sections (Figure 55).

The cross-sections display a typical resistivity structure of a high-temperature field. At the top is a high-resistivity layer close to the surface due to un-altered formations; underlain by a low resistivity as a result of alteration minerals like smectites and zeolites; this is underlain by a high-resistivity core below where chlorite and epidote dominate the alteration minerals and give an indication of high temperatures at depth. Below this is usually a conductor. Below we discuss each of the cross-sections. Their locations are shown in Figure 55.

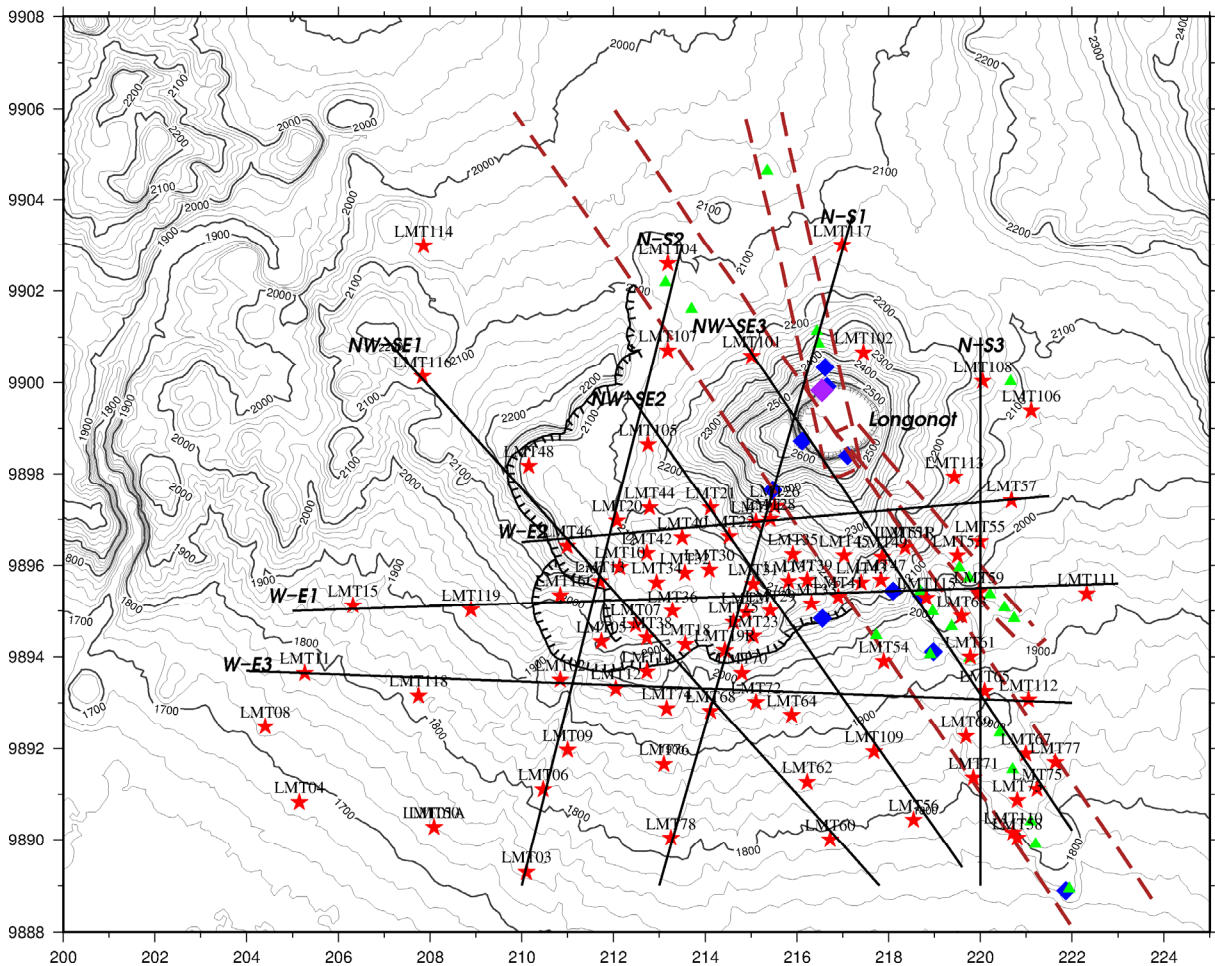


FIGURE 55: Location of the cross-sections. Red stars are MT soundings, blue diamonds are the fumaroles, green triangles are the volcanic centers and the purple diamonds are the hot ground. The coordinates are in UTM coordinates

Cross-section W-E1 as seen in Figure 55

The section runs through the collapsed caldera (Figure 56). The top layer of about 300 m thick shows a high resistivity across the entire profile reflecting un-altered rock formation of recent volcanic rocks or pyroclastics with intermittent resistivity subject to the age of the rocks and vicinity to the fracture

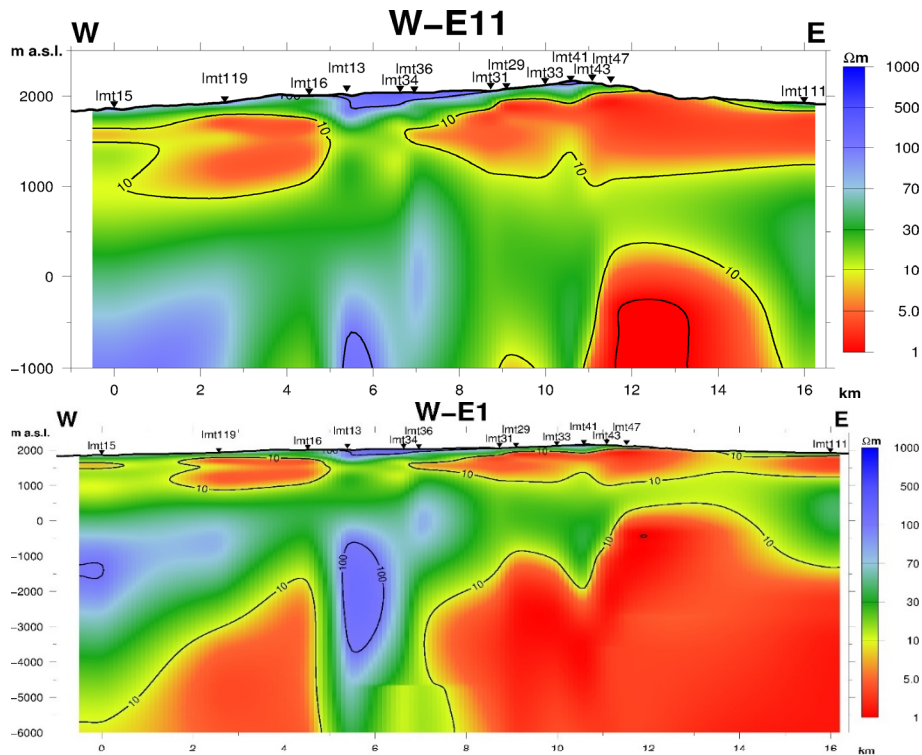


FIGURE 56: Resistivity cross-section obtained from 1-D joint inversion of TEM and MT data and 1-D inversion of MT data as obtained using geospatial distribution of static shift correction

zone. Underlying the high resistivity is a low resistivity layer of less than $10 \Omega\text{m}$, most likely caused by the low temperature alteration minerals like smectite-zeolite. Below the alteration layer, higher resistivity zone is seen which is sharp below sounding lmt13, near the collapsed caldera. This is probably associated with a geothermal reservoir. Below this resistive layer is a low resistivity layer that dominates the eastern side of the profile. This could be attributed to an up-flow zone or probably due to large fractures with fluids present in the vicinity. Fumaroles are manifested on the eastern side as well which could be because of deep circulation of the geothermal fluids enhancing water-rock interaction.

Cross-section W-E2 as seen in Figure 55

The section runs through the collapsed caldera (Figure 57) and lies just south of the crater. The cross-section shows a similar layered resistivity structure as W-E1; a thin high resistivity at the top, followed by a low resistivity layer, which sits on top of a high resistive layer. The bottom layer is a thick low resistivity layer with some topography. Roughly below station lmt46 is a higher resistive layer to greater depths that may be an extension of a structure as seen in station lmt13.

Cross-section W-E3 as seen in Figure 55

The section is just outside the collapsed caldera (Figure 58). The cross-section shows a similar resistivity structure as cross-section W-E1 with a high resistive layer followed by a low resistivity then high resistivity later followed by a low resistivity layer. At around station lmt12, lmt14, lmt74 and lmt68, higher resistivity at greater depths are found that may be an extension of a structure as seen in station lmt13, which is perhaps covered, by pyroclastics and volcanic ash or it might be connected with lithological contacts.

Cross-section N_S1 as seen in Figure 55

The section is just outside the crater (Figure 59) and crosses the TVA structure. There are no data available between lmt02 and lmt26 (4 km distance) due to the terrain at the crater and hence not much to state about this part of the profile. To the south of lmt26, the cross-section shows a similar resistivity structure as other cross-section with a thin high resistivity layer followed by a low resistivity layer then high resistivity later that is still later followed by a conductor. The conductor domes underneath station

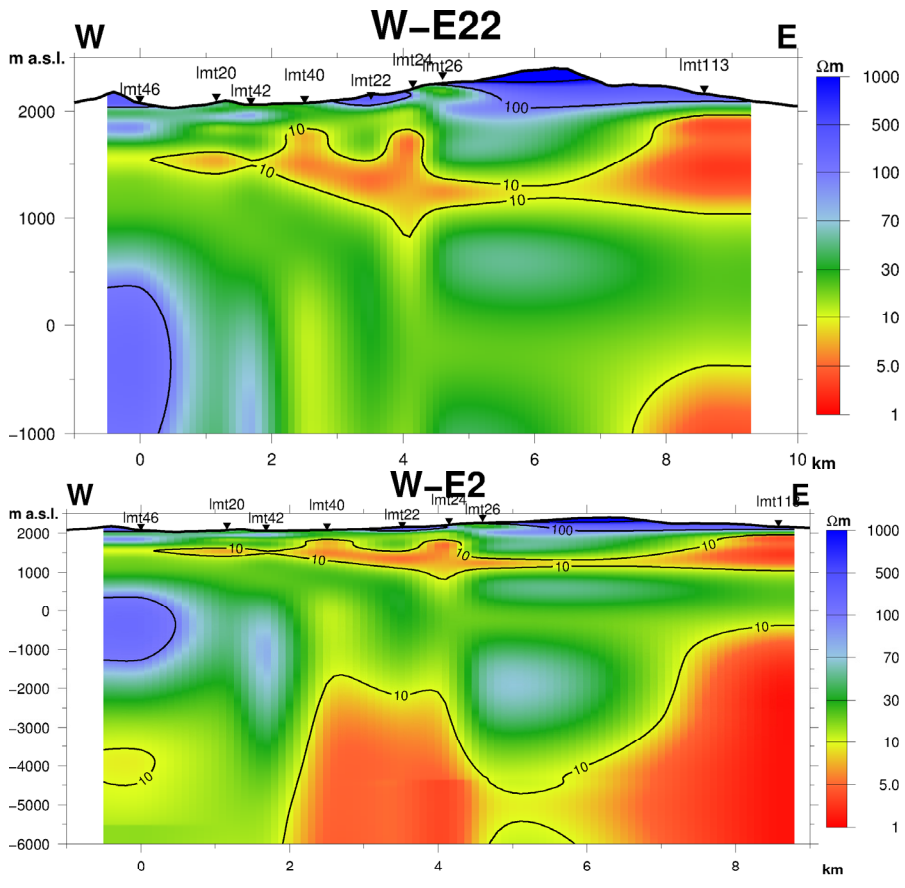


FIGURE 57: Resistivity cross-section obtained from 1-D joint inversion of TEM and MT data and 1-D inversion of MT data as obtained using geospatial distribution of static shift correction

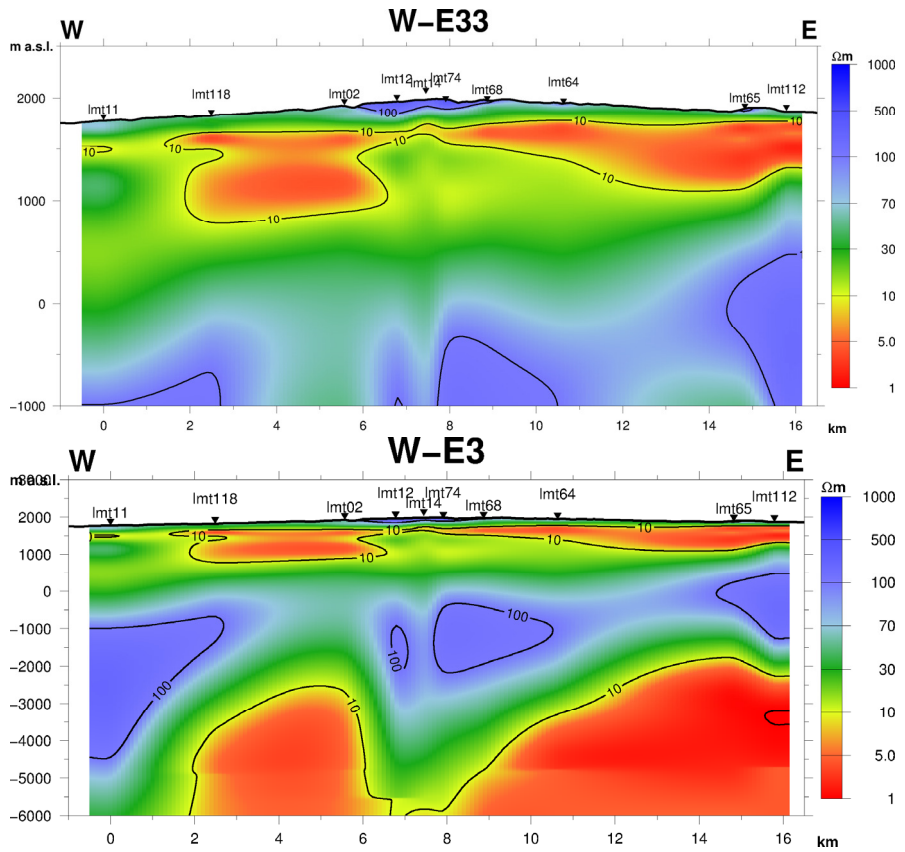


FIGURE 58: Resistivity cross-section obtained from 1-D joint inversion of TEM and MT data and 1-D inversion of MT data as obtained using geospatial distribution of static shift correction

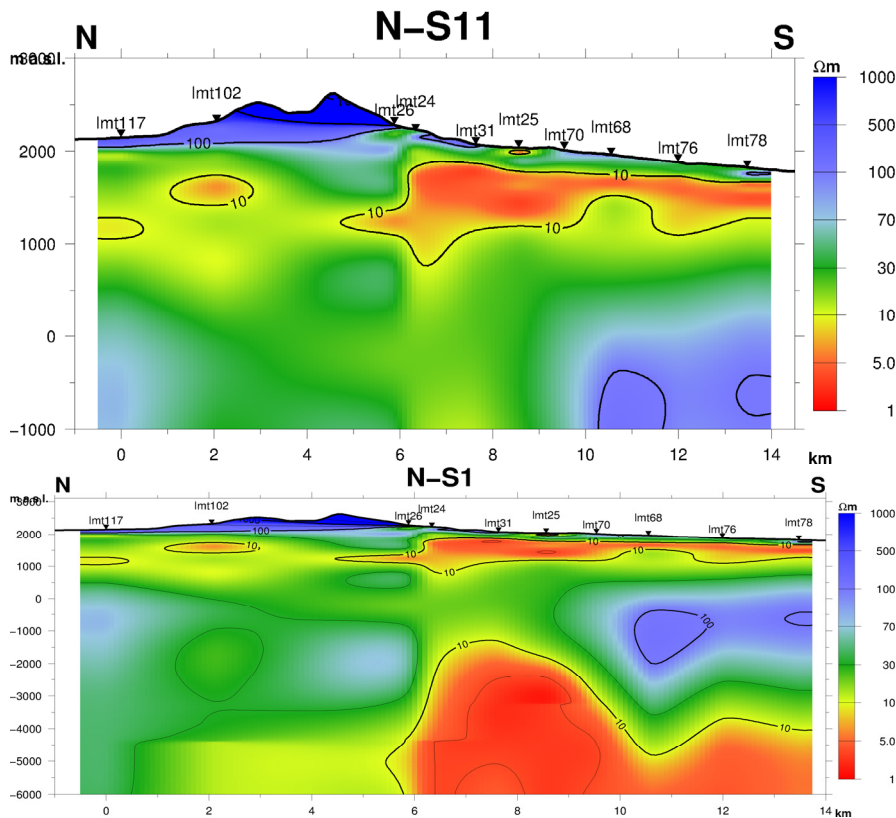


FIGURE 59: Resistivity cross-section obtained from 1-D joint inversion of TEM and MT data and 1-D inversion of MT data as obtained using geospatial distribution of static shift correction

lmt24, lmt25, lmt26 and lmt31. A deeper high resistivity layer is observed in the eastern part of the profile, which can be connected to a structure extending from station 13 as will be shown in the resistivity depth slices (Appendix E).

Cross-section N_S2 as seen in Figure 55

The cross-section is to the east of the crater (Figure 60). The cross-section shows a similar resistivity structure as other cross-section with a thin high resistivity layer followed by low resistivity then high resistivity layer followed by a conductor. The conductor at the bottom around station lmt02 and lmt09 that seems to be an extension of the conductor seen in profile N-S1. A deeper high resistivity layer is observed in both the northern and southern part of the conductor. The southern part of the profile could be associated to the outflow zone of the system.

Cross-section N_S3 as seen in Figure 55

The cross-section is to the east of the crater (Figure 61). The cross-section shows a similar resistivity structure as other cross-section with a high resistivity layer followed by low resistivity then a high resistivity layer followed by a conductor. The conductor at the bottom is extensive and shallower at 1000 m b.s.l.

Cross-section NW_SE1 as seen in Figure 55

The cross-section runs parallel to the dominant structure (TVA) (Figure 62) through a high resistivity structure seen in the depth slices. The eastern side of the profile shows a typical high temperature resistivity structure with all the zones. A high resistivity zone dominates in the western side to greater depths. This could be associated with a thick pyroclastic deposit or volcanic ash deposit in the area.

Cross-section NW_SE2 as seen in Figure 55

The cross-section runs within the dominant structure (TVA) (Figure 63) through a high resistivity structure seen in the depth slices. The profile shows a typical high temperature resistivity structure with all the zones. A low resistivity zone dominates at the centre to greater depths. This could be associated with the heat source.

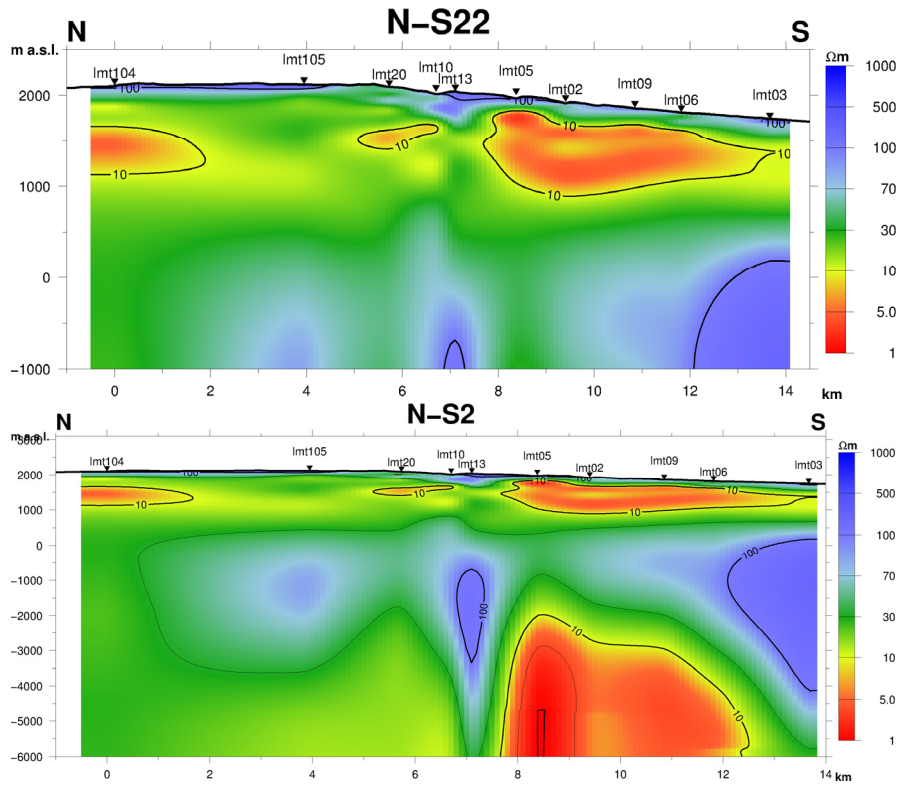


FIGURE 60: Resistivity cross-section obtained from 1-D joint inversion of TEM and MT data and 1-D inversion of MT data as obtained using geospatial distribution of static shift correction

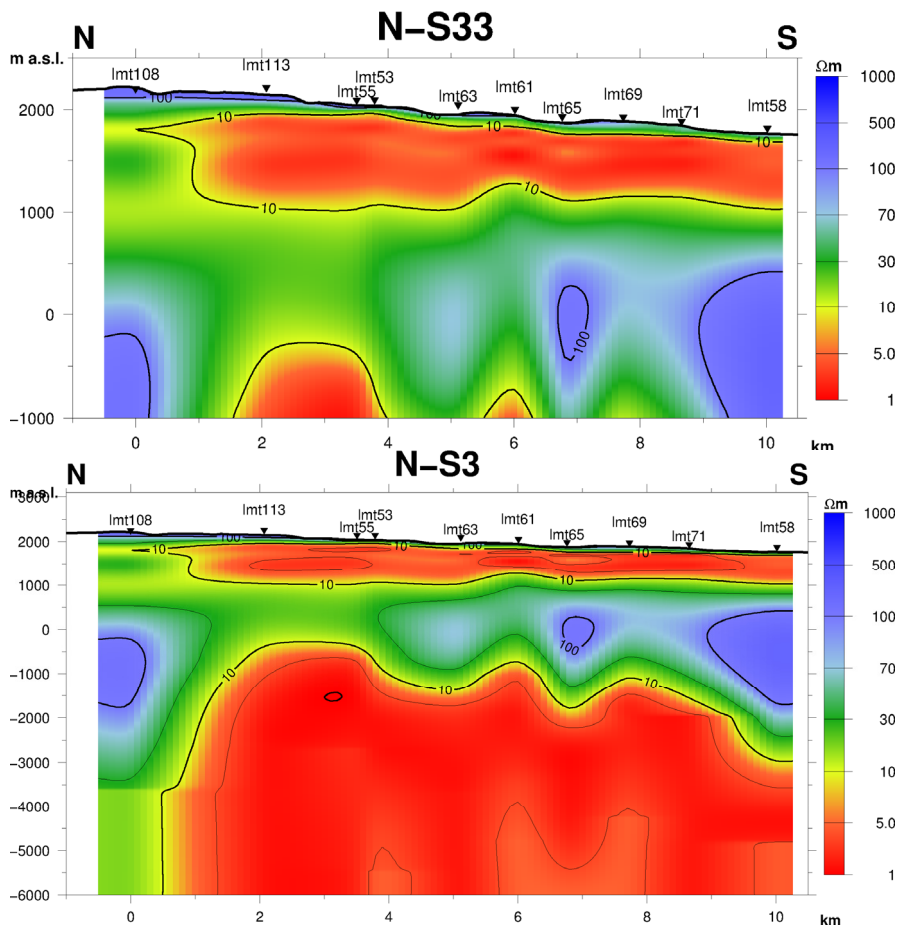


FIGURE 61: Resistivity cross-section obtained from 1-D joint inversion of TEM and MT data and 1-D inversion of MT data as obtained using geospatial distribution of static shift correction

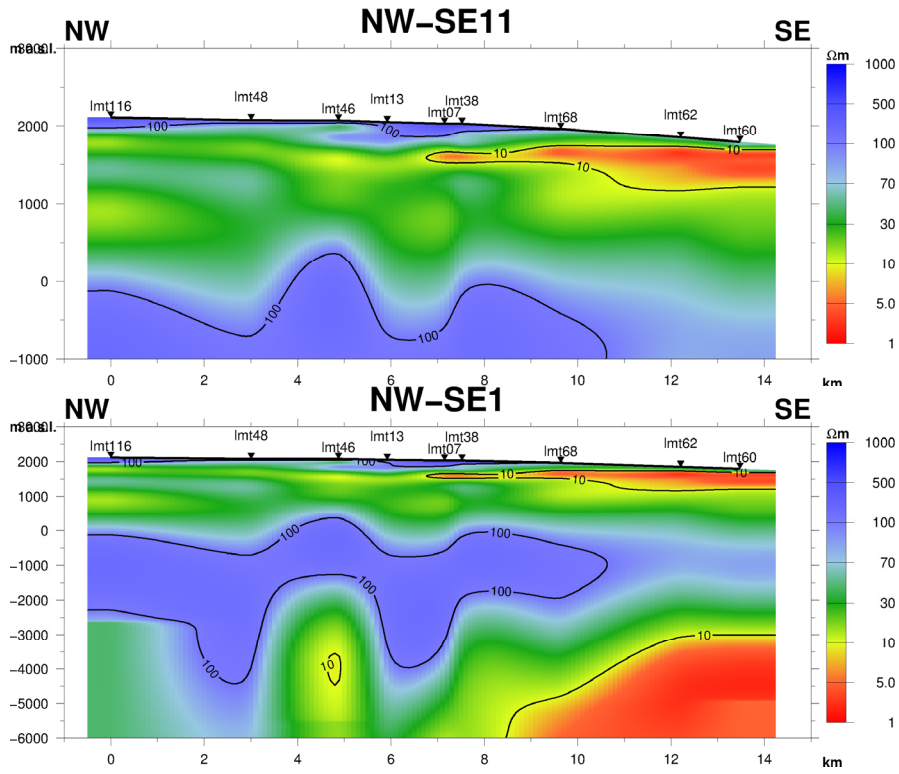


FIGURE 62: Resistivity cross-section obtained from 1-D joint inversion of TEM and MT data and 1-D inversion of MT data as obtained using geospatial distribution of static shift correction

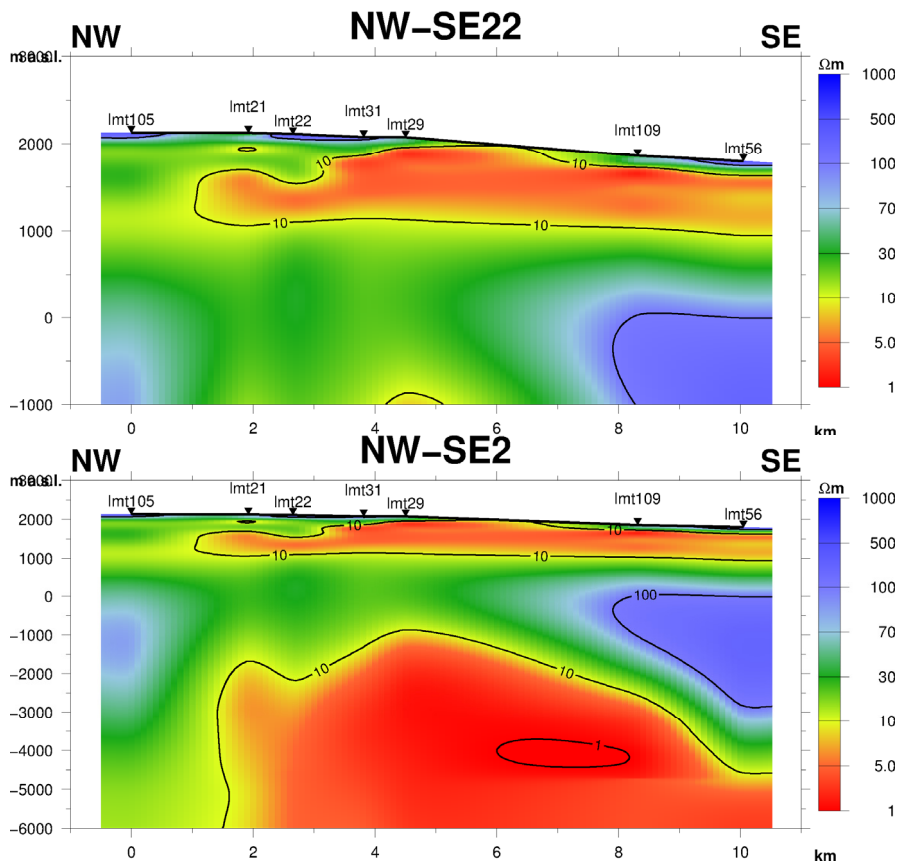


FIGURE 63: Resistivity cross-section obtained from 1-D joint inversion of TEM and MT data and 1-D inversion of MT data as obtained using geospatial distribution of static shift correction

Cross-section NW_SE3 as seen in Figure 55

The cross-section runs parallel and within the dominant structure (TVA) through the crater (Figure 64). There are no data available between 1 to 5 kilometres hence the profile cannot be relied on fully. However, on the eastern side of the profile a conductor is seen at shallow depth < 1000 m b.sl.

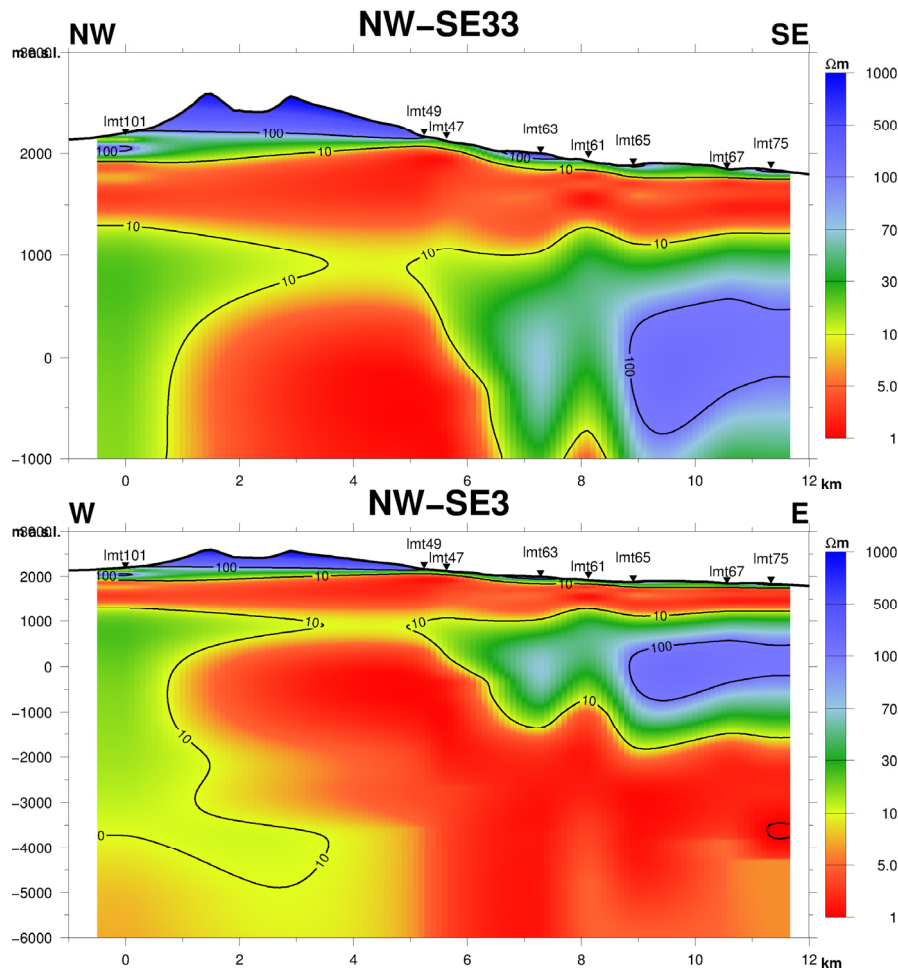


FIGURE 64: Resistivity cross-section obtained from 1-D joint inversion of TEM and MT data and 1-D inversion of MT data as obtained using geospatial distribution of static shift correction

8.2 1-D resistivity depth slices

In this study, TEMRESD program was used to generating the resistivity-depth slices derived from the previously obtained 1-D Occam models (Eysteinnsson, 1998). All stations, both the ones that were static shift corrected using TEM and the ones corrected using geospatial distribution of static shift correction were included in generating the depth slices. From the interpretation of the maps, it will be possible to understand the general trend of resistivity in Mt. Longonot prospect area. The maps display that resistivity varies significantly both laterally and with depth. It is not easy to ascertain the surface appearance of faults in the vicinity of Mt. Longonot because they are filled with dense deposits of pyroclastics. Below are a few selected depth slices for interpretation purposes. More maps can be viewed in Appendix E

1500 m a.sl.

A low-resistivity structure is dominant towards the east and southeast part of the area (Figure 65). A high resistive structure appears to cut across near the outer caldera possibly creating two systems of low resistivity. This structure (as outlined in Figure 65) appears to trend in the same direction as TVA structure. This high resistivity structure might reflect a fault covered by the pyroclastic deposits as

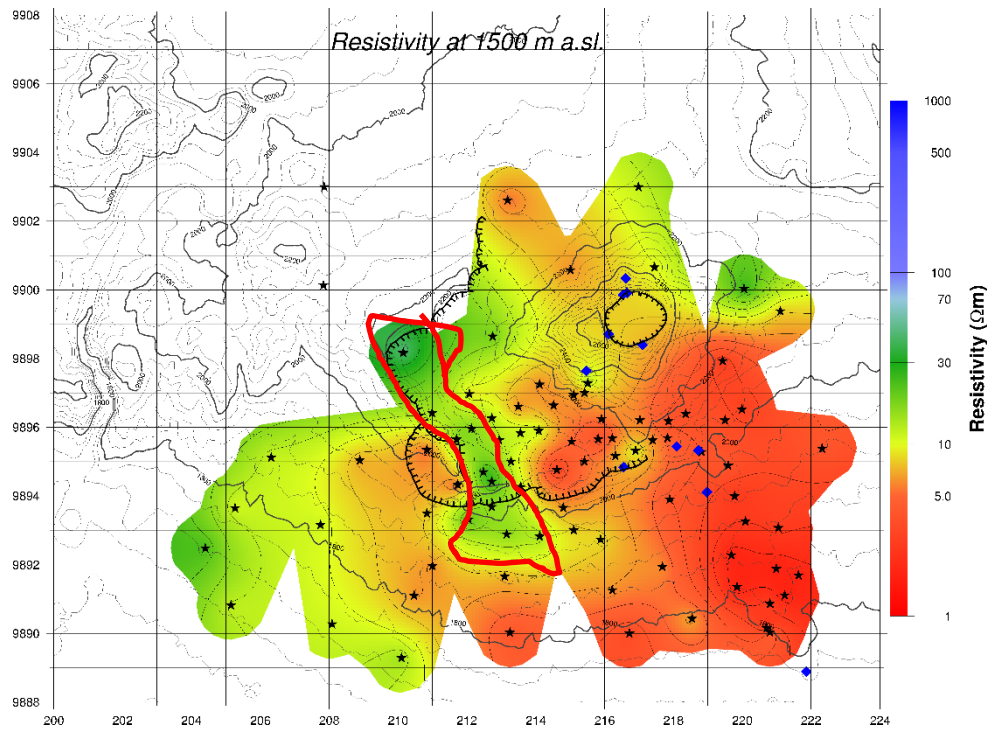


FIGURE 65: Resistivity at 1500 m a.s.l. from 1-D inversion of TEM and MT data. The blue diamond are fumaroles, the black stars are the MT stations and the red thick line outlines a high resistivity structure

discussed in some of the profiles above (W-E1). The low resistivity structure is possibly related to the mineral alteration cap consisting of smectite and zeolites, which lies immediately on top of the high resistivity core.

1000 m b.s.l.

The low resistivity structure to the east and southeast is more pronounced. High resistivity structure that runs across the area (as outlined in red) is also defined separating the bigger low resistivity structure to the east from the perhaps small low resistivity structure to the west. The low resistivity structure at this depth could be associated with the heat source of the system that is right below a high resistivity layer associated with a layer dominated by chlorite and epidote. The low resistivity trends nearly NW-SE, which is in the same direction as TVA structure. It is prominent in the area with several volcanic centers (Figure 66).

4000 m b.s.l.

The low resistivity structure is extensive both towards the southeast, east and to the west of the outlined (red) high resistivity structure that runs across the two systems. The low resistivity structure could be associated to the heat source of the system that is prominent as depth is increased (Figure 67).

A common feature in the interpretation of resistivity from Mt. Longonot is the presence of a highly resistive surface layer of latest volcanic rocks or pyroclastics with variable resistivity values subject to the age of rocks and proximity to fracture zones. The second layer of low resistivity values is related to deduced smectites-zeolite clay layer. The base of the clay cap probably correlates with a geothermal reservoir at a temperature between 200 and 240°C. This is likely to be the case because a shallow well drilled to the SW part of the Longonot caldera struck steam that has geochemical indicators of a hydrothermal reservoir at 240°C.

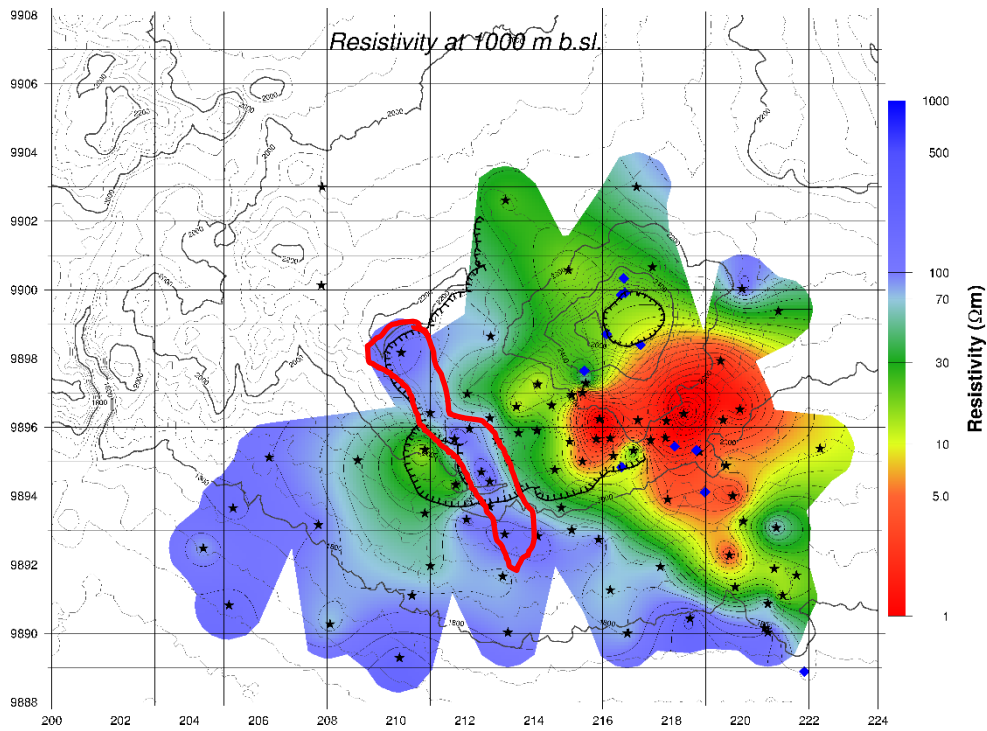


FIGURE 66: Resistivity at 1000 m b.s.l. from 1-D inversion of TEM and MT data. The blue diamond are fumaroles, the black stars are the MT stations and the red thick line outlines a high resistivity structure

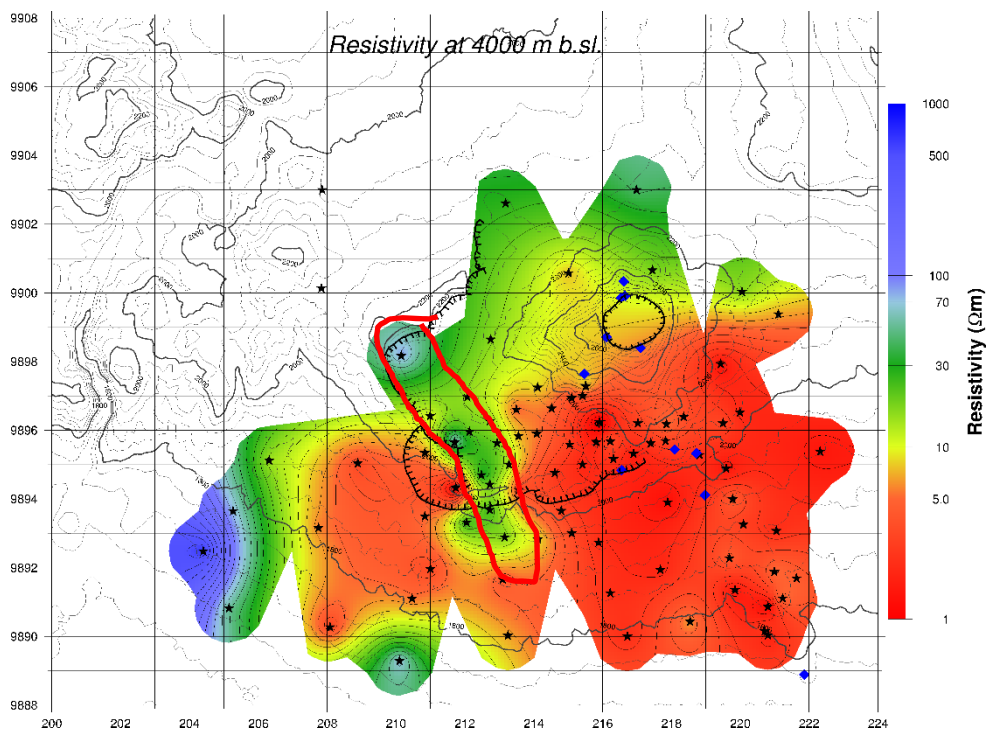


FIGURE 67: Resistivity at 4000 m b.s.l. from 1-D inversion of TEM and MT data. The blue diamond are fumaroles, the black stars are the MT station and the red thick line outlines a high resistivity structure

8.3 Discussion of 1-D inversion results

From inversion of both TEM and rotationally invariant determinant MT data, resistivity structure shows a common trend of a shallow low resistivity layer towards southeast of the crater. The low resistivity layer is at 1500 m a.sl. and underlain by high resistivity layer. The low resistivity layer reflects conductive alteration minerals made at temperatures between 50 and 200°C. This is a zone where hydrothermal alteration products such as smectite and zeolite are dominant. Just below this layer is a resistive core that shows the changes in alteration to resistive high temperature minerals, which could be presenting the geothermal system in Mt. Longonot field. At about 1000 m b.sl. another conductive layer is observed in the southeast and east of the crater. The deep conductive layer could be ascribed to magmatic heat sources. This can be confirmed using other geophysical data to ascertain the nature of the conductive layer.

8.4 Geo-electric strike analysis of MT data

8.4.1 Zstrike

Zstrike (Swift angle) is the horizontal rotation, which maximizes the off-diagonal elements ($|Z_{xy}|^2 + |Z_{yx}|^2$) of the MT tensor and minimizes the diagonal ones ($|Z_{xx}|^2 + |Z_{yy}|^2$) using sum of the squared units of these components. Geoelectrical strike analyses can show the directions of resistivity disparities, which could be used to infer geological features, not essentially seen on the surface. The MT impedance tensor are dependent on the orientation of the x and y-directions of the field layout. For a homogeneous 1-D earth, the impedances $Z_{xy} = -Z_{yx}$ and $Z_{xx} = Z_{yy} = 0$.

The Swift strike has 90° ambiguity where the diagonal elements of the tensor are minimized as if either the x-axis or y-axis is along the geo-electrical strike. There is no way of distinguishing between θ and $\theta + 90^\circ$, from the tensor alone. The strike direction cannot be determined using MT impedance data alone. This ambiguity can be resolved by the information from Tipper vector if vertical magnetic field (Hz) is available. Additional information such as local geology might help to overcome this ambiguity. At short periods, the strike estimates of the Mt Longonot data is not well-defined due to the shallow local structure with resistivity variations at each site (Figure 68) whereas at longer periods, there is a steady strike direction for the dataset that tends to be in the same direction as TVA and tectonics (Figure 69).

Zstrike commonly varies with frequency and may not be in place of the direction of the known geological strike. Strike variations with frequency in Mt. Longonot field may be due to active processes that have continuously changed the Earth's structure. Because of these processes, remnants of past tectonic events are often conserved, giving rise to tectonic environments in which structural lineaments trend in more than one direction. One such environment exists in this sector of the rift where a major generally, NW–SE strike trending is prominent but on impinging the caldera, the direction changes to N-S around Mt. Longonot caldera heading to Mt. Suswa.

8.4.2 Tipper and induction arrow

The magnetic transfer function (T) is a parameter that relates the vertical component of the magnetic field to the two horizontal components (Vozoff, 1991). From Figure 70, Tstrike is approximately aligned along the dominant geological strike (TVA). In Figure 71 the alignment is clearer. However, Tipper appears to align with the orientation of the caldera structure around and within the caldera. From appendix B, the tipper is often almost zero for parts of the spectrum. These low amplitude values in tipper means the structure around is a 1D structure. Tipper can also be seen as a complex vector often represented graphically as induction arrows, the real part and the imaginary part. Normally, the imaginary part is more sensitive to resistivity close to the measurement site and the real part to wider resistivity contrasts (regional structures). Since vertical magnetic fields are produced by lateral conductivity gradients, induction arrows can be used to infer the existence or absence of lateral variations in conductivity. In this case, the size of the induction arrow is dependent on the magnitude

T-strike 0.01 10sec

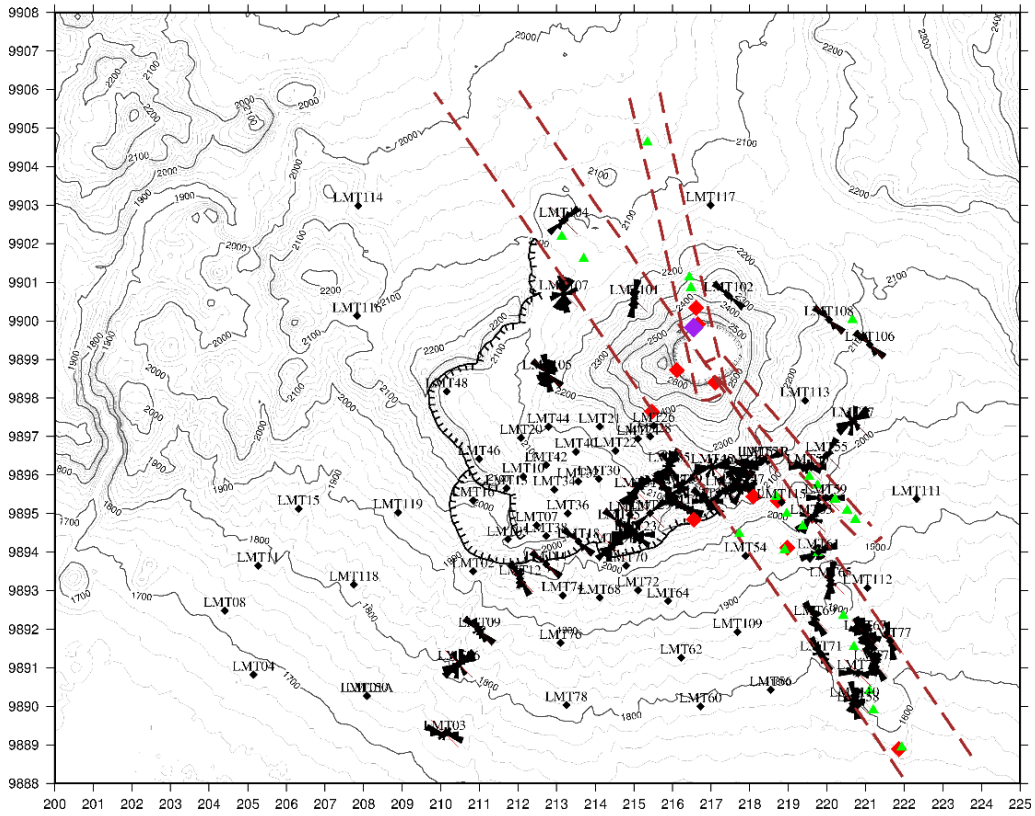


FIGURE 70: Rose diagram of the Tipper strike for the period interval, 0.01-10 s

T-strike 10 1000sec

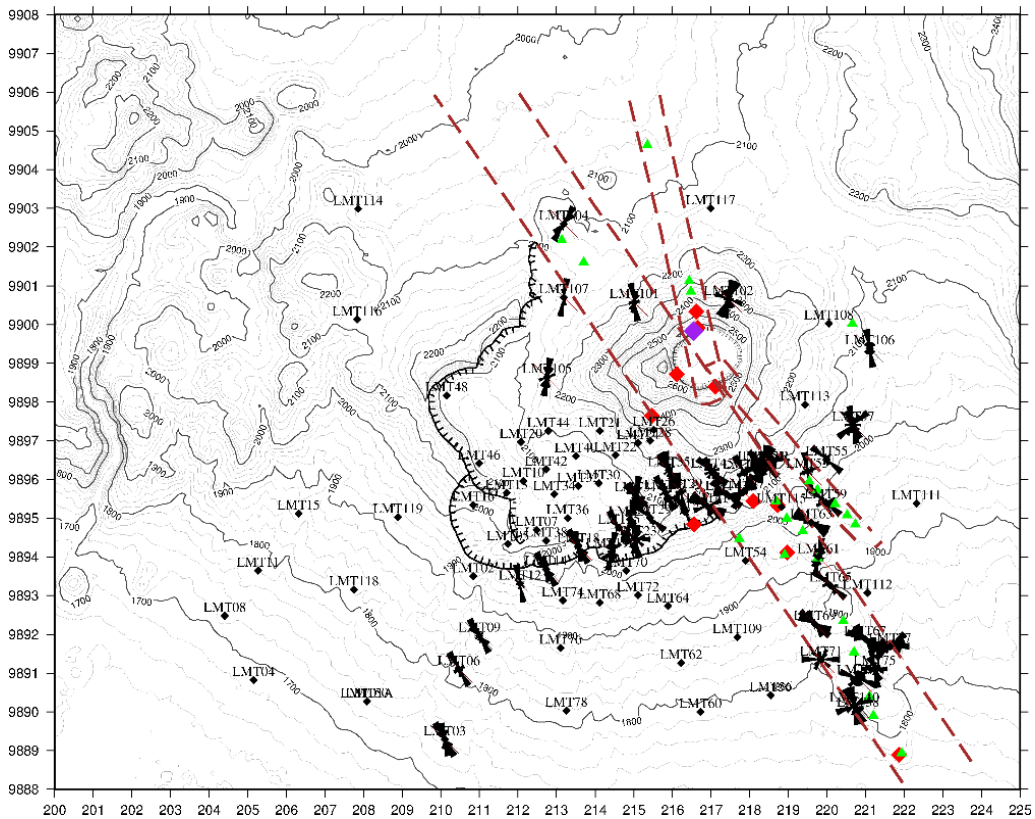


FIGURE 71: Rose diagram of the Tipper strike for the period interval, 10-1000 s

Induction arrow 100sec

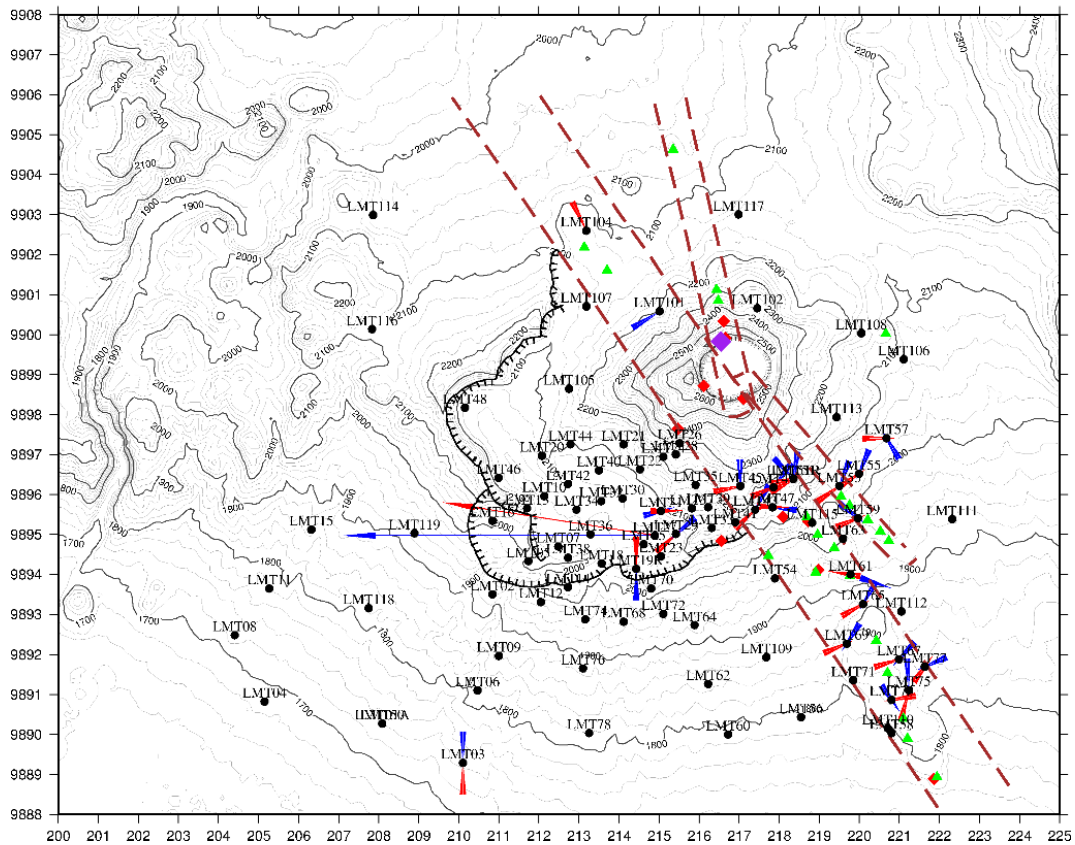


FIGURE 72: Induction arrows for the period 100 s. Blue arrows are the real part and red arrows the imaginary part

of the vertical magnetic field, such that if vertical magnetic field is small then the induction arrow is also small and vice versa. From Figure 72 the real induction arrows point away from a zone of high conductivity and towards a zone of lower conductivity according to Wiese convention (Wiese 1962).

8.5 Geologic and geothermal interpretation

Mt. Longonot geothermal field is within an active hydrothermal system where fluid circulation is present in a tectonically and volcanically active area. Kenyan rift system is still active with several volcanic centers. These hydrothermal systems have heat sources that consist of magma chambers, young dikes, and general heat flow. In Mt. Longonot, fault zones are not seen on the surface but are buried by layers of pyroclastics and volcanic ash. These buried faults is presumably what controls the fluid circulation within the system.

In high temperature geothermal systems, a low resistivity cap normally overlay a resistive core deeper in the reservoir (Árnason et al., 2000). The cap layer is associated with alteration minerals that have different electrical conductivity. These minerals include smectites and zeolites with inferred temperature of between 50 and 200°C. The resistive core comprises the chlorites and epidotes that form at temperature of 240°C with increased resistivity. Another low resistive zone exists just beneath the resistive core. A conductive zone has been interpreted beneath the resistive core, which has been presumed to be the heat source for the geothermal system in this field. Such a sequence of resistivity structure is evident in all other high temperature geothermal systems. In such systems, alteration mineralogy and temperature are connected to its sequence in resistivity structure (Árnason et al., 2000).

9. CONCLUSIONS AND RECOMMENDATIONS

The main purpose of this research was to study the resistivity structure of Mt. Longonot in order to deduce the existence of geothermal system as well as to gain a better understanding of the high-temperature geothermal systems.

The strong geothermal manifestations (fumaroles and hot ground) and the recent eruptions are indicative of a heat source under the caldera, which could be perhaps shallow at the summit crater.

From the results found using 1-D inversion modelling of MT/TEM data, the resistivity structure of Mt. Longonot field has mainly four resistivity sections. A high resistivity zone of unaltered formations at the surface, a low-resistivity anomaly observed at shallow depth. A high resistivity zone associated with the change in alteration minerals to higher temperature mineralogy. A conductive zone that dominates to the southeast of the study area and just below the summit crater that could be associated with a heat source

It can be inferred from the study that Mt. Longonot is a fracture controlled geothermal system. This is because the conductive layer is aligned along the eruption centers that are in line with the TVA structure and the numerous volcanic centers to the southeast of the field.

Additional TEM survey to be done near MT stations. This will enable performing static shift corrections for those MT stations that did not have nearby TEM data. In volcanic situations, electric field and current distortions are quite common. This is due to the presence of the near surface resistivity inhomogeneities e.g. conductive clay minerals. In the presence of water reaching to the surface, very conductive clay alteration minerals surrounded by very resistive lavas are found, producing severe voltage distortion. Conductive clay minerals that may dome up to shallow depth but not quite to the surface, can result in extensive channelling of current.

Electrical strike direction gives valuable information about the subsurface fractures and permeability. They furthermore, confirm the 1-D inversion resistivity model.

Outflow zone of geothermal system is probably to the south and south west of the area

Exploration wells to be drilled in the field will provide more information on the dynamics of geothermal reservoir of Mt. Longonot field

REFERENCES

- Alexander, B.K., and Ussher, G., 2011: Geothermal resource assessment for Mt. Longonot, Central Rift Valley, Kenya. *Geothermal Resources Council, Transactions*, 35.
- Allen, D.J., Darling, W.G., and Burgess, W.G., 1989: *Geothermics and hydrogeology of the southern part of the Kenya Rift Valley with emphasis on the Magadi-Nakuru area*. British Geological Survey Research Rpt SD/89/1, 68 pp.
- Archie, G.E., 1942: The electrical resistivity log as an aid in determining some reservoir characteristics. *Trans. AIME*, 146, 54-67.
- Ármansson, H., 1987: *Studies on the geochemistry of steam in the Suswa and Longonot areas and water in the lake Magadi, Kedong valley and Lake Turkana areas, rift valley, Kenya*. Prepared by the United Nations in cooperation with the government of Kenya for a project of the United Nations Development Programme. Final technical report, KEN/82/002.
- Árnason, K., 1989: *Central-loop transient electromagnetic sounding over a horizontally layered earth*. Orkustofnun, Reykjavík, report OS-89032/JHD-06, 129 pp.
- Árnason, K., 2006a: *TemX short manual*. Iceland GeoSurvey – ÍSOR – Iceland GeoSurvey, Reykjavík, internal report, 17 pp.
- Árnason, K., 2006b: *TEMTD, a program for 1D inversion of central-loop TEM and MT data. Short manual*. ÍSOR – Iceland GeoSurvey, Reykjavík, internal report, 17 pp.
- Árnason, K., 2008: *The Magneto-telluric static shift problem*. ÍSOR - Iceland GeoSurvey, report ISOR-08088, 17 pp.
- Árnason K., Eysteinnsson H., Hersir G. P., 2010: Joint 1-D inversion of TEM and MT data and 3-D inversion of MT data in the Hengill area, SW Iceland. *Geothermics* 39, 13–34.
- Árnason, K., and Flóvenz, Ó. G., 1995: Geothermal exploration by TEM – soundings in the central Assal Rift in Djibouti, East Africa. *Proceedings of the World Geothermal Congress 1995, Florence, Italy*, 933-938.
- Árnason, K., Karlsdóttir, R., Eysteinnsson, H., Flóvenz, Ó.G., and Guðlaugsson, S.Th., 2000: The resistivity structure of high-temperature geothermal systems in Iceland. *Proceedings of the World Geothermal Congress 2000, Kyushu-Tohoku, Japan*, 923-928.
- Arnórsson, S. and Gunnlaugsson, E., 1985: New gas geothermometers for geothermal exploration—calibration and application. *Geochim. Cosmochim. Acta*, 49-6, 1307-1325.
- Berdichevsky, M.N., and Dmitriev, V.I., 1976: Basic principles of interpretation of magnetotelluric sounding curves. In: Adam, A. (ed.), *Geoelectric and geothermal studies*. KAPG Geophys. Mono., Akad. Kiado, 165–221.
- Berdichevsky, M.N., and Dmitriev, V.I., 2002: *Magnetotellurics in the context of the theory of ill-posed problems*. Society of Exploration Geophysicists, USA, 215 pp
- Berdichevsky, M.N., and Zhdanov, M.S., 1984: *Advanced theory of deep geomagnetic sounding*. Methods Geochem. Geophys. 19, Elsevier Science, Ltd. Amsterdam.
- Biggs, J., Anthony, E.Y., and Ebinger, C.J., 2009: Multiple inflation and deflation events at Kenyan volcanoes, East African Rift. *Geology*, 37-11, 979-982.

- Bostick, F.X., and Smith, H.W., 1962: Investigation of large-scale inhomogeneities in the earth by the magnetotelluric method. *Proceedings of the IRE*, 50-11, 2339-2346.
- Cagniard, L., 1953: Basic theory of the magneto-telluric method of geophysical prospecting. *Geophysics*, 18-3, 605-635.
- Cantwell, T., 1960: *Detection and analysis of low frequency magnetotelluric signals*. Massachusetts Institute of Technology, PhD thesis.
- Chorowicz, J., 2005: The East African Rift System. *J. African Earth Sciences*, 43-1, 379-410.
- Christopherson, K.R., 1998: *MT gauges Earth's electric fields*. AAPG explorer, 22-31.
- Clarke, J., Gamble, T.D., Goubau, W.M., Koch, R.H., Miracky, R.F., 1983: Remote reference magnetotellurics: Equipment and procedures. *Geophys. Prosp.*, 31, 149-170.
- Clarke, M.C.G., Woodhall, D.G., Allen, D., and Darling G., 1990: *Geological, volcanological and hydrogeological controls on the occurrence of geothermal activity in the area surrounding Lake Naivasha, Kenya: With coloured 1:100 000 geological maps*. Ministry of Energy, Nairobi, 138 pp.
- Constable, C.S., Parker, R.L., and Constable, C.G., 1987: Occam inversion: A practical algorithm for generating smooth models from electromagnetic sounding data. *Geophysics*, 52, 289-300.
- Dakhnov, V.N., 1962: Geophysical well logging. *Q. Colorado Sch. Mines*, 57-2, 445 pp.
- Eberhart-Phillips, D., Stanley, W.D., Rodriguez, B.D., and Lutter, W.J., 1995: Surface seismic and electrical methods to detect fluids related to faulting. *J. Geophysical Research: Solid Earth*, 100-B7, 12919-12936.
- Egbert, G.D., and Booker, J.R., 1986: Robust estimation of geomagnetic transfer functions. *Geophysical Journal International*, 87-1, 173-194.
- Ellis, D.V., 1987: *Well logging for earth scientists*. Elsevier Science, Ltd., NY, 532 pp
- ESA, 2010: Using ASAR. European Space Agency – ESA, webpage: www.esa.int/spaceinimages/Images/2013/08/Mount_Longonot.
- Eysteinnsson, H., 1998: *TEMMAP and TEMCROSS plotting programs*. ÍSOR – Iceland GeoSurvey, Reykjavík, unpublished programs and manuals.
- Eysteinnsson, H., Árnason, K., Flóvenz, Ó.G., 1994: Resistivity methods in geothermal prospecting in Iceland. *Surv. Geophys.*, 15, 263-275.
- Flóvenz, Ó.G., Hersir, G.P., Sæmundsson, K., Ármannsson, H., and Fridriksson, Th., 2012: *Geothermal energy exploration techniques*. In: Sayigh A, (ed.) *Comprehensive Renewable Energy*, 7, 51-9. Elsevier, Oxford.
- Flóvenz, Ó.G., Spangerberg, E., Kulenkampff, J., Árnason, K., Karlsdóttir, R., Huenges, E., 2005: The role of electrical interface conduction in geothermal exploration. *Proceedings of the World Geothermal Congress 2005, Antalya, Turkey*, 9 pp.
- Gamble, T.D., Goubau, W.M., and Clarke, J., 1979: Magnetotellurics with a remote magnetic reference. *Geophysics*, 44, 53-68.
- Geotermica Italiana, 1989: *Supplement of surface investigations within the calderas of Longonot and Suswa Volcanoes*. Geotermica Italiana, unpublished report to the UNDP, 1, 9 pp.

Goubau, W.M., Gamble, T.D., and Clarke, J., 1979: Magnetotelluric data analysis: removal of bias. *Geophysics*, 43, 1157-1169.

Grandis, H., 2010: *Studi efek statik pada data magnetotellurik (MT) menggunakan pemodelan inversi 2-D*. Prosiding Seminar Nasional Energi, Univ. Padjadjaran.

Gregory, J.W., 1920: The African Rift Valley. *Geog. Jour.*, 56, 13-17.

Henley, R.W., and Ellis, A.J., 1983: Geothermal systems ancient and modern - a geochemical review. *Earth-Science Reviews*, 19-1, 1-50.

Hersir, G.P., 2016: *Resistivity of rocks*. University of Iceland, geophysical exploration, lecture notes.

Hersir, G.P., and Árnason, K., 2010: Resistivity of rocks. Presented at "Short Course V on Exploration for Geothermal Resources", organized by UNU-GTP, KenGen and GDC, Lake Naivasha, Kenya, 8 pp.

Hersir, G.P., Árnason, K., and Vilhjálmsson, A., 2013: 3D inversion of magnetotelluric (MT) resistivity data from Krýsuvík high temperature area in SW Iceland. *Proceedings 38th Workshop on Geothermal Reservoir Engineering, Stanford University, Stanford, CA*, 14 pp.

Hersir, G.P., and Björnsson, A., 1991: *Geophysical exploration for geothermal resources. Principles and applications*. UNU-GTP, Iceland, report 15, 94 pp.

<http://en.openei.org/wiki/Magnetotellurics>

<http://web.ics.purdue.edu/~ecalais/projects/ear/tectonics.jpg>

<http://www.debipattnaik.com/tag/skin-depth/>

http://www.duncaninstr.com/FIG_1.jpg

<http://www.tulane.edu/~sanelson/images/pores.gif>

<http://www.kns.go.ke>

JICA and WestJEC 2010: *Situation analysis study on geothermal development in Africa*. JICA and WestJEC, Annex.

Jiracek, G.R., 1990: Near surface and topographic distortions in electromagnetic induction. *Surveys in Geophysics*, 11-2/3, 163-203.

Jones, A.G., 1983: The problem of current channelling, a critical review. *Surveys in Geophysics*, 6-1, 79-122.

Jones, A.G. and Groom, R.W., 1993: Strike-angle determination from the magnetotelluric impedance tensor in the presence of noise and local distortion: rotate at your peril. *Geophysical Journal International*, 113-2, 524-534.

Keller, G.V., 1989: Electrical properties. In: Carmichael, R.S. (ed.), *Practical handbook of physical properties of rocks and minerals*: CRC Press, Boca Raton, Fla., 359-427.

KenGen, 1998a: *Surface scientific investigation of Longonot geothermal prospect*. Kenya Electricity Generating Company Ltd. (KenGen), unpublished report, September 1998.

- KenGen 1998b: *Surface exploration of Kenya's geothermal resources in the Kenya Rift*. Kenya Electricity Generating Company, Ltd. (KenGen), internal report, 84 pp.
- KWS, 2017: *Kenya Wildlife Service – Mt. Longonot*, website: <http://www.kws.go.ke/sites/default/files/mt%20longonot.jpg>
- Lagat, J., 2003: *Geology and the geothermal systems of the southern segment of the Kenya Rift*. Proceedings of the International Geothermal Conference, IGC2003, Reykjavik, S04, 33-40.
- Lagat, J.K., 2004: *Geology, hydrothermal alteration and fluid inclusion studies of the Olkaria Domes geothermal field, Kenya*. University of Iceland, MSc thesis, UNU-GTP, Iceland, report 2, 79 pp.
- Lasaga, A.C., 1984: Chemical kinetics of water-rock interactions. *J. Geophysical Research: solid earth*, 89-B6, 4009-4025.
- MacGregor, D., 2015: History of the development of the East African Rift System: A series of interpreted maps through time. *J. African Earth Sciences*, 101, 232-252.
- Mariita, N.O., 1986: *Schlumberger vertical soundings: Techniques and interpretations with examples from Krisuvik and Glerárdalur, Iceland and Olkaria, Kenya*. UNU-GTP, Iceland, report 5, 48 pp.
- McNeil, J.A., 2004: The metal detector and Faraday's Law. *The Physics Teacher, Colorado School of Mines*, 42-6, 369-373.
- Mehegan, J.M., Robinson, P.T., and Delaney, J.R., 1982: Secondary mineralization and hydrothermal alteration in the Reydarfjördur drill core, eastern Iceland. *J. Geophysical Research*, 87-NB8, 6511-6524.
- Munyiri, S., 2016: Structural mapping of Olkaria domes geothermal field using geochemical soil gas surveys, remote sensing and GIS. University of Iceland, MSc thesis, UNU-GTP, Iceland, report 5, 100 pp.
- Nabighian M.N., and Macnae, J.C., 1991: Time domain electromagnetic prospecting methods. In: Nabighian M.N. (ed.), *Electromagnetic methods in applied geophysics*, 2. Society of Exploration Geophysicists, Tulsa, OK, 427–520.
- Nelson, P.H., and Anderson, L.A., 1992: Physical properties of ash flow tuff from Yucca Mountain, Nevada. *J. Geophysical Research*, 97-B5, 6,823-6,841.
- Neves, A.S., 1957: *The generalized magneto-telluric method*. Massachusetts Institute of Technology, PhD thesis.
- Omenda, P.A., 1998: The geology and structural controls of the Olkaria geothermal system, Kenya. *Geothermics*, 27-1, 55-74.
- Omiti, A.O., 2013: Resistivity structure of the Eburru geothermal field, Kenya, described through 1D joint inversion of MT and TEM data. Report 26 in: *Geothermal training in Iceland*. UNU-GTP, Iceland, 599-624.
- Palacky, G.J., 1987: Resistivity characteristics of geologic targets. In: Nabighian, M.N. (ed.), *Electromagnetic methods in applied geophysics theory*. Society of Exploration Geophysicists, 1, Tulsa, OK, 53-129.
- Parkinson, W., 1959: Directions of rapid geomagnetic variations. *Geophys. J. R. Astr. Soc.* 2, 1–14.
- Pastor, M.S., 2001: *Geophysical Study of the groundwater system south of Lake Naivasha, Kenya*. International Institute for Aerospace Survey and Earth Sciences Enscheda, The Netherlands, MSc thesis.

- Patra, H.P., and Mallick, K., 1980: *Geosounding principles, 2. Time-varying geoelectric soundings*. Elsevier Scientific Publishing Co., Amsterdam, 419 pp.
- Pellerin, L., and Hohmann, G.W., 1990: Transient electromagnetic inversion: A remedy for magnetotelluric static shifts. *Geophysics*, 55-9, 1242-1250.
- Phoenix Geophysics, 2005: *Data processing user guide*. Phoenix Geophysics Ltd., Canada.
- Phoenix Geophysics, 2009: *V5 system 2000 MT/MTU, a user guide*. Phoenix Geophysics Ltd., Toronto.
- Quist, A.S., and Marshall, W.L., 1968: Electrical conductances of aqueous sodium chloride solutions from 0 to 800°C and at pressures to 4000 bars. *J. Phys. Chem.*, 72, 684-703.
- Radhakrishnamurthy, C. and Likhite, S.D., 1970: Hopkinson effect, blocking temperature and Curie point in basalts. *Earth and Planetary Science Letters*, 7-5, 389-396.
- Reddy, I.K. and Rankin, D., 1975: Magnetotelluric response of laterally inhomogeneous and anisotropic media. *Geophysics*, 40-6, 1035-1045.
- Reddy, I.K., Phillips, R.J. and Rankin, D., 1977: Three-dimensional modelling in magnetotelluric and magnetic variational sounding. *Geophysical Journal*, 51, 313-325.
- Reynolds, J.M., 2011: *An introduction to applied and environmental geophysics* (2nd ed.). John Wiley and Sons, NY, 712 pp.
- Saemundsson, K., 2010: East African Rift System - an overview. *Presented at "Short Course V on Exploration for Geothermal Resources"*, organized by UNU-GTP, GDC and KenGen, at Lake Bogoria and Lake Naivasha, Kenya, 8 pp.
- Scott, S.C., 1980: The geology of Longonot volcano, Central Kenya: A question of volumes. *Philosophical Transactions of the Royal Society of London*, 296-1420, 437-465.
- Simiyu, S.M., 2010: Status of geothermal exploration in Kenya and future plans for its development. *Proceedings of the World Geothermal Congress 2010, Bali, Indonesia*, 11 pp.
- Simpson, F. and Bahr, K., 2005. *Practical magnetotellurics*. Cambridge University Press, Cambridge, UK, 254 pp.
- Siripunvaraporn, W., and Egbert, G., 2000: An efficient data-subspace inversion method for 2-D magnetotelluric data. *Geophysics*, 65, 791-803.
- Siripunvaraporn, W., Egbert, G., Lenbury, Y., and Uyeshima, M., 2005: Three-dimensional magnetotelluric inversion: data-space method. *Phys. Earth Planet. Interiors*, 150, 3-14.
- Smith, J.T., and Booker, J.R., 1991: Rapid inversion of two- and three- dimensional magnetotelluric data. *J. Geophys. Res.*, 96, 3905-3922.
- SOHO, 2010: Solar wind. Solar and Heliospheric Observatory, website: sohowww.nascom.nasa.gov/gallery/images/magfield.html.
- Spies, B., 1989: Depth of investigation in electromagnetic sounding methods. *Geophysics*, 54, 872-888.
- Stamps, D.S., Calais, E., Saria, E., Hartnady, C., Nocquet, J., Ebinger, C.J. and Fernandes, R.M., 2008: A kinematic model for the East African Rift. *Geophysical Research Letters*, 35, 6 pp.

- Stephen, J., Gokarn, S.G., Manoj, C., Singh, S.B., 2003: Effects of galvanic distortions on magnetotelluric data: Interpretation and its correction using deep electrical data, *Proc. Indian Acad. Sci. (Earth Planet. Sci.)*, 112.
- Sternberg, B.K., Washburne, J.C., and Pellerin, L., 1988: Correction for the static shift in magnetotellurics using transient electromagnetic soundings. *Geophysics*, 53-11, 1459-1468.
- Swain, C.J., and Khan, M.A., 1977: Gravity measurements in Kenya. *Geophys. J. Royal Astronomical Society*, 53-2, 427-429.
- Swift, C. M., 1967: *A magnetotelluric investigation of electrical conductivity anomaly in the southern United States*. Massachusetts Institute of Technology, Cambridge, MA. PhD thesis.
- Szarka, L. and Menvielle, M., 1997: Analysis of rotational invariants of the magnetotelluric impedance tensor. *Geophysical Journal International*, 129-1, 133-142.
- Teklemariam, M., 2013: Overview of geothermal resource exploration and development in the East African rift system. Presented at “Short Course VIII on Exploration for Geothermal Resources”, organized by UNU-GTP, GDC and KenGen, Lake Bogoria and Lake Naivasha, Kenya, 11 pp.
- Telford, W.M., Geldart, L.P., and Sheriff, R.E., 1990: *Applied geophysics* (2nd ed.). Cambridge University Press, Cambridge, 792 pp.
- Thomas, E.C., 1976: *Determination of Q_v from membrane potential measurements on shaly sands*. *Transactions American Institute of Mining, Metallurgical, and Petroleum Engineering*, 261, 1087-1096.
- Thompson, A.C., and Dodson, R.G., 1963: *Geology of the Naivasha area: explanation of degree sheet SW 43*. Ministry of Commerce and Industry, Kenya.
- Tikhonov, A.N., 1950: On determining electrical characteristics of the deep layers of the Earth's crust. In: *Doklady*, vol. 73-2, 295-297.
- Torres-Verdín, C., and Bostick, F.X., 1992: Principles of spatial surface electric field filtering in magnetotellurics: Electromagnetic array profiling EMAP, *Geophysics*, 57, 603-622.
- Tripaldi, S., Siniscalchi, A. and Spitzer, K., 2010: A method to determine the magnetotelluric static shift from DC resistivity measurements in practice. *Geophysics*, 75-1, F23-F32.
- Unsworth, M., 2007: Magnetotellurics. In: *Encyclopedia of geomagnetism and paleo-magnetism* (pp. 670-673). Springer Netherlands, 8 pp.
- Vilhjálmsón, A.M., Hersir, G.P. and Flóvenz Ó.G., 2016: *IMAGE Task 3.3 – Physical properties of rock at reservoir conditions. Resistivity vs temperature during heating up of well KJ-18 in Krafla, NE-Iceland*. ÍSOR - Iceland GeoSurvey, Reykjavík, report ÍSOR-2016/045, 22 pp.
- Vozoff, K., 1972: The magnetotelluric method in the exploration of sedimentary basins: *Geophysics*, 37, 98-141.
- Vozoff, K., 1991: The magnetotelluric method. In: Nabighian, M.N. (ed.), *Electromagnetic methods in applied geophysics*, 2B. SEG, Tulsa, OK, 641–711.
- Ward, S.H. and Wannamaker, P.E., 1983: *The MT/AMT electromagnetic method in geothermal exploration*. UNU-GTP, Iceland, report 5, 107 pp.

Weisenberger, T.B., Ingimarsson, H., Hersir, G.P. and Flóvenz, Ó.G., 2016: *IMAGE Task 3.3 - Physical properties of rock at reservoir conditions: Validation of the influence of cation-exchange capacity (CEC) on resistivity logs within hydrothermal systems*. ÍSOR - Iceland GeoSurvey, Reykjavík, report ÍSOR-2016/044, 41 pp.

Wiese, H., 1962: Geomagnetische Tiefentellurik, Teil 2, Die Streichrichtung der Untergrundstrukturen des elektrischen Widerstandes, erschlossen aus geomagnetischen Variationen. *Geofis. Pura. Appl.* 52, 83-103.

Wolf, K.B., 2004: *Geometric optics on phase space*. Springer Science & Business Media, 376 pp.

Wood, J., and Guth, A., 2013: East Africa's Great Rift Valley: a complex rift system. *Geology.com*.

Zhdanov, M.S. and Keller, G.V., 1994: *The geoelectrical methods in geophysical exploration*. (vol. 31). Methods in geochemistry and geophysics, 31, Elsevier Science Ltd., 873 pp.

APPENDIX A: Location and elevation of TEM and MT soundings

TABLE 4: Location and elevation of TEM and MT soundings. Location is in UTM coordinate system. Soundings in italics are the ones used in runs of cross-sections and resistivity depth slices

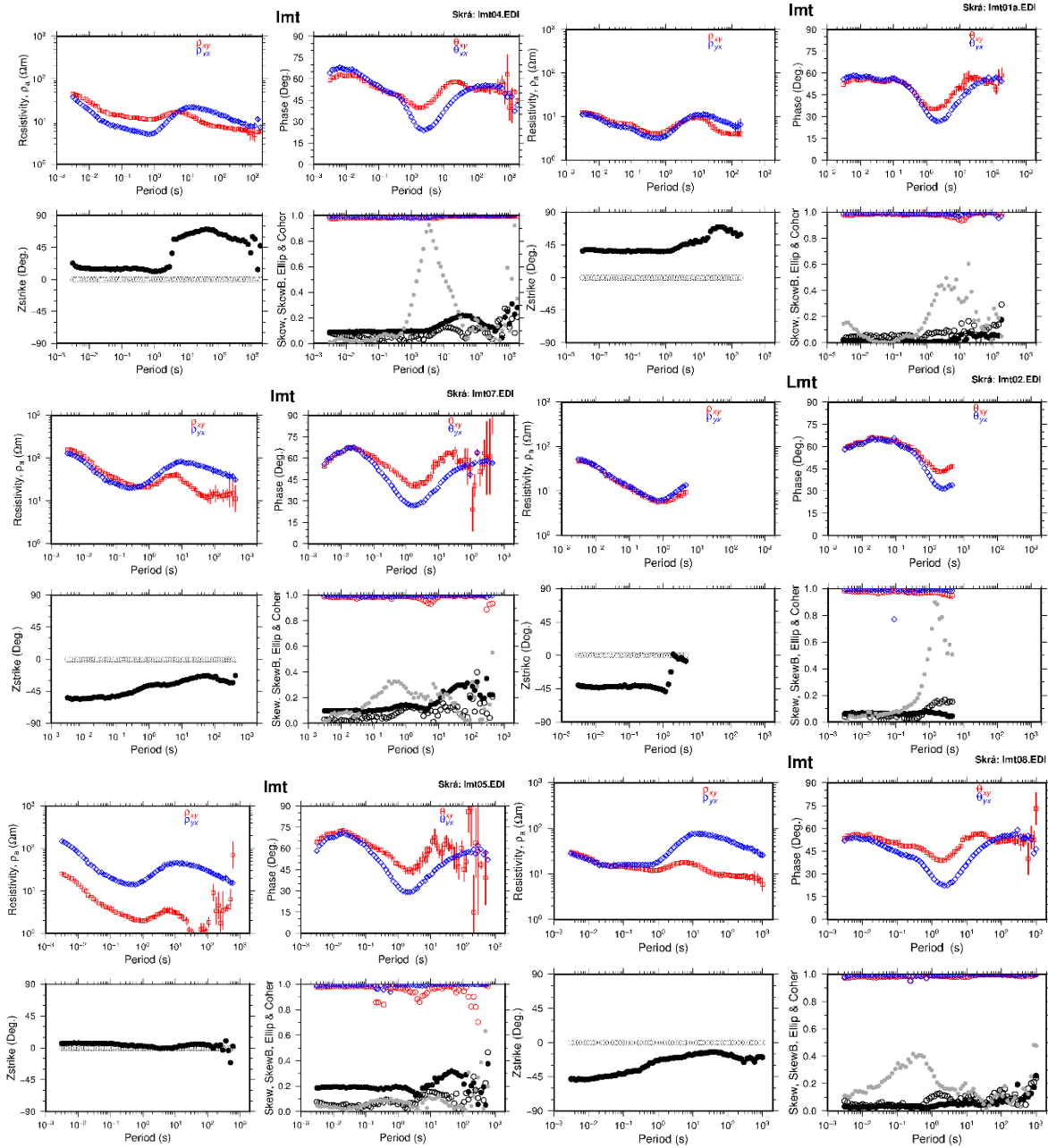
MT				TEM			
Sounding	Easting (m)	Northing (m)	Elevation (m)	Sounding	Easting (m)	Northing (m)	Elevation (m)
<i>lmt01a</i>	208087	9890267	1745	LON01	218560	9901412	2180
<i>lmt02</i>	210838	9893497	1935	LON02	215500	9903400	2095
<i>lmt03</i>	210099	9889285	1743	LON03	215100	9901850	2115
<i>lmt04</i>	205148	9890818	1692	LON04	212050	9899850	2130
<i>lmt05</i>	211735	9894327	2010	LON05	214800	9900950	2170
<i>lmt06</i>	210469	9891099	1822	LON06	213070	9903850	2055
<i>lmt07</i>	212477	9894697	2031	LON07	222600	9896200	2005
<i>lmt08</i>	204404	9892477	1733	LON08	223700	9900100	2080
<i>lmt09</i>	210994	9891096	1870	LON09	217300	9900300	2410
<i>lmt101</i>	215008	9900577	2180	LON10	217300	9902700	2155
<i>lmt102</i>	217452	9900657	2317	LON11	210650	9898500	2070
<i>lmt104</i>	213018	9902604	2116	LON12	212750	9896650	2080
<i>lmt105</i>	212752	9898639	2130	LON13	214150	9900350	2170
<i>lmt106</i>	221104	9899383	2101	LON14	212850	9901050	2130
<i>lmt107</i>	213184	9900699	2118	LON15	219600	9899250	2185
<i>lmt108</i>	220052	9900027	2159	LON16	220770	9899200	2100
<i>lmt109</i>	217677	9891934	1860	LON17	212150	9904100	2045
<i>lmt10</i>	212136	9895956	2047	LON18	210650	9902450	2070
<i>lmt110</i>	220709	9890154	1778	LON19	213650	9895800	2045
<i>lmt111</i>	222314	9895038	1923	LON20	212650	9894800	2025
<i>lmt112</i>	221048	9893074	1877	LON21	213500	9894900	2025
<i>lmt113</i>	219435	9897928	2171	LON22	212350	9895600	2035
<i>lmt114</i>	207861	9902992	2034	LON23	219480	9897500	2140
<i>lmt115</i>	218819	9895285	2037	LON24	220700	9897200	2040
<i>lmt116</i>	207832	9900133	2111	LON25	219550	9896200	2045
<i>lmt117</i>	216988	9902998	2158	LON26	219750	9897000	2085
<i>lmt118</i>	207745	9893156	1827	LON27	220550	9904350	2220
<i>lmt119</i>	208888	9895032	1932	LON28	221650	9901700	2110
<i>lmt11</i>	205269	9893646	1784	LON29	214700	9896450	2065
<i>lmt12</i>	212045	9893313	1975	LON30	213300	9902100	2135
<i>lmt13</i>	211703	9895649	2051	LON31	221000	9895850	1950
<i>lmt14</i>	212725	9893682	2043	LON32	221150	9893100	1870
<i>lmt15</i>	206032	9895122	1875	LON33	219750	9893400	1885
<i>lmt16</i>	210837	9895341	2015	LON34	220700	9895000	1970
<i>lmt18</i>	213056	9894267	2046	LON35	223300	9893800	1860
<i>lmt19R</i>	214427	9894145	2045	LON36	222750	9894800	1890
<i>lmt20</i>	212073	9896097	2098	LON37	215850	9905100	2050
<i>lmt21</i>	214115	9897249	2128	LON38	215550	9901000	2220
<i>lmt22</i>	214518	9896634	2114	LON39	211350	9900700	2145
<i>lmt23</i>	215045	9894452	2052	LON40	212600	9898400	2130
<i>lmt24</i>	215105	9896942	2219	LON41	214250	9897400	2160
<i>lmt25</i>	214612	9894076	2043	LON42	213300	9899450	2160

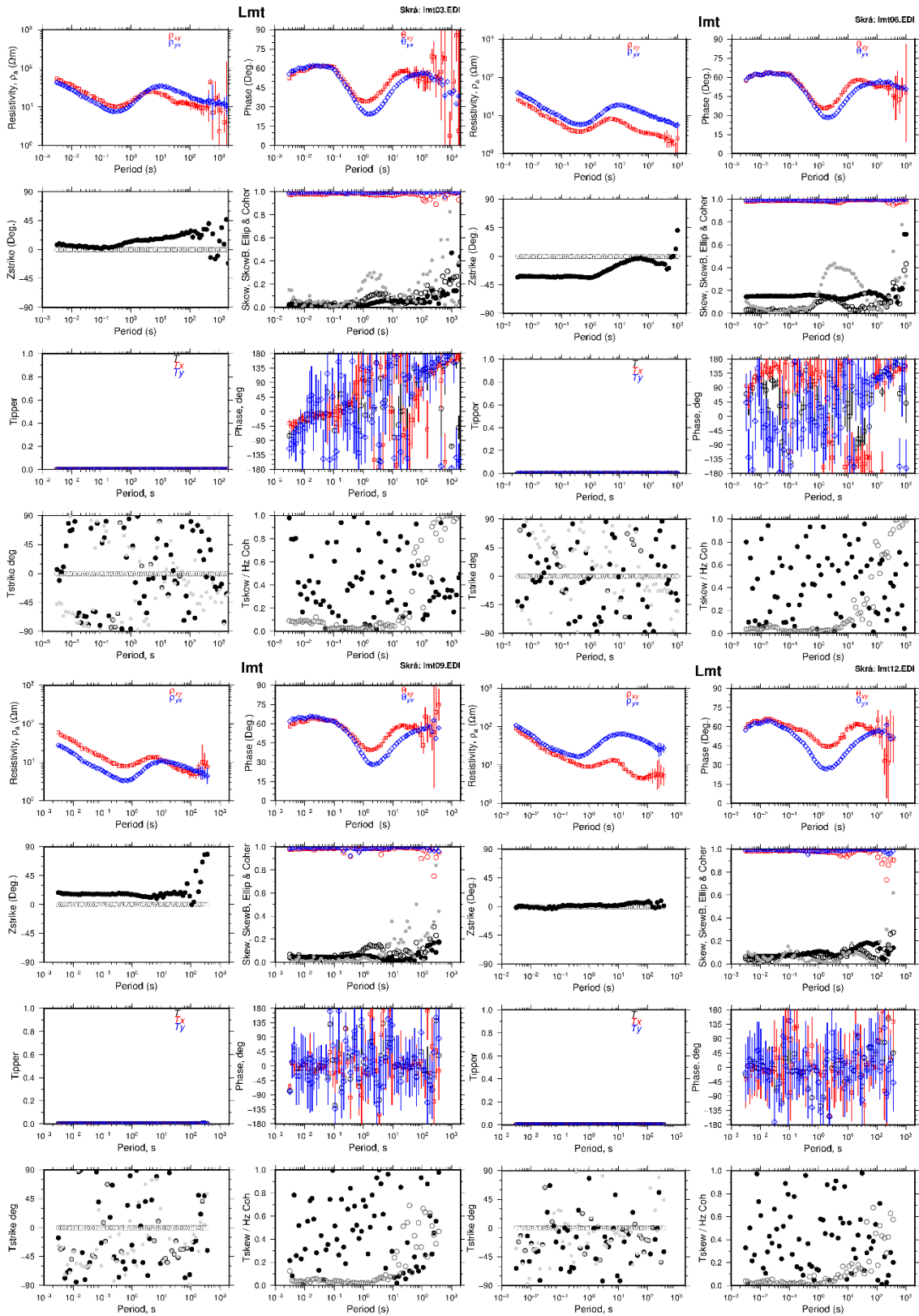
MT				TEM			
Sounding	Easting (m)	Northing (m)	Elevation (m)	Sounding	Easting (m)	Northing (m)	Elevation (m)
<i>lmt26</i>	215507	9897028	2296	LON43	218700	9900050	2290
<i>lmt27</i>	214089	9894975	2051	LON44	221100	9888950	1740
<i>lmt28</i>	215414	9897004	2248	LON45	208250	9890200	1755
<i>lmt29</i>	215416	9895006	2076	LON46	210050	9887850	1690
<i>lmt30</i>	214085	9895896	2056	LON50	221500	9887000	1685
<i>lmt31</i>	215044	9895059	2078	LON51	205900	9888200	1635
<i>lmt32</i>	213559	9895834	2051	LON52	203580	9888100	1610
<i>lmt33</i>	216013	9895016	2129	LON53	214750	9894450	2040
<i>lmt34</i>	212094	9895619	2046	LON54	212850	9893700	2040
<i>lmt35</i>	215091	9896236	2183	LON55	213100	9891800	1890
<i>lmt36</i>	213281	9895004	2037	LON56	213350	9889750	1800
<i>lmt37</i>	215818	9895652	2148	LON57	206000	9885950	1610
<i>lmt38</i>	212725	9894042	2030	LON58	203250	9885800	1610
<i>lmt39</i>	216022	9895683	2160	LON59	210050	9895250	2015
<i>lmt40</i>	213497	9896603	2077	LON60	213050	9888000	1730
<i>lmt41</i>	216901	9895314	2157	LON61	214700	9887900	1720
<i>lmt42</i>	212724	9896264	2057	LON62	215500	9892600	1920
<i>lmt43</i>	217395	9895622	2166	LON63	210550	9890550	1780
<i>lmt44</i>	212785	9897248	2093	LON64	210900	9893550	1960
<i>lmt45</i>	217024	9896206	2247	LON65	210200	9885600	1630
<i>lmt46</i>	210991	9896416	2075	LON66	215050	9885650	1645
<i>lmt47</i>	217828	9895684	2148	LON67	215600	9890000	1780
<i>lmt48</i>	210154	9898168	2077	LON68	218000	9887900	1710
<i>lmt49</i>	217859	9896176	2184	LON69	206900	9892950	1780
<i>lmt50</i>	208087	9890267	1745	LON70	208000	9887950	1655
<i>lmt51</i>	218354	9896391	2180	LON71	207950	9885800	1620
<i>lmt51R</i>	218354	9896391	2181	LON72	224100	9891650	1810
<i>lmt53</i>	219499	9896208	2054	LON73	222500	9890000	1760
<i>lmt54</i>	217892	9893901	1955	LON74	217000	9891550	1840
<i>lmt55</i>	219993	9896515	2049	LON75	217400	9889700	1760
<i>lmt56</i>	218544	9890429	1798	LON76	218500	9896100	2120
<i>lmt58</i>	220802	9890031	1780	LON77	219000	9895150	2020
<i>lmt59</i>	219963	9895409	1968	LON78	219600	9901750	2160
<i>lmt60</i>	216719	9889997	1791	LON79	218250	9904000	2120
<i>lmt61</i>	219779	9893995	1961	LON80	225500	9889000	1790
<i>lmt62</i>	216223	9891257	1849	LON81	225350	9888000	1775
<i>lmt63</i>	219592	9894886	2004	LON82	227450	9890100	1830
<i>lmt64</i>	215882	9892732	1941	LON83	225700	9894100	1880
<i>lmt65</i>	220088	9893258	1889	LON84	225500	9897650	2020
<i>lmt67</i>	220987	9891875	1849				
<i>lmt68</i>	214118	9892823	1965				
<i>lmt69</i>	219687	9892274	1887				
<i>lmt70</i>	214798	9893653	2028				
<i>lmt71</i>	219842	9891352	1845				
<i>lmt72</i>	215108	9893008	1962				
<i>lmt73</i>	220802	9890861	1845				
<i>lmt74</i>	213159	9892884	1963				

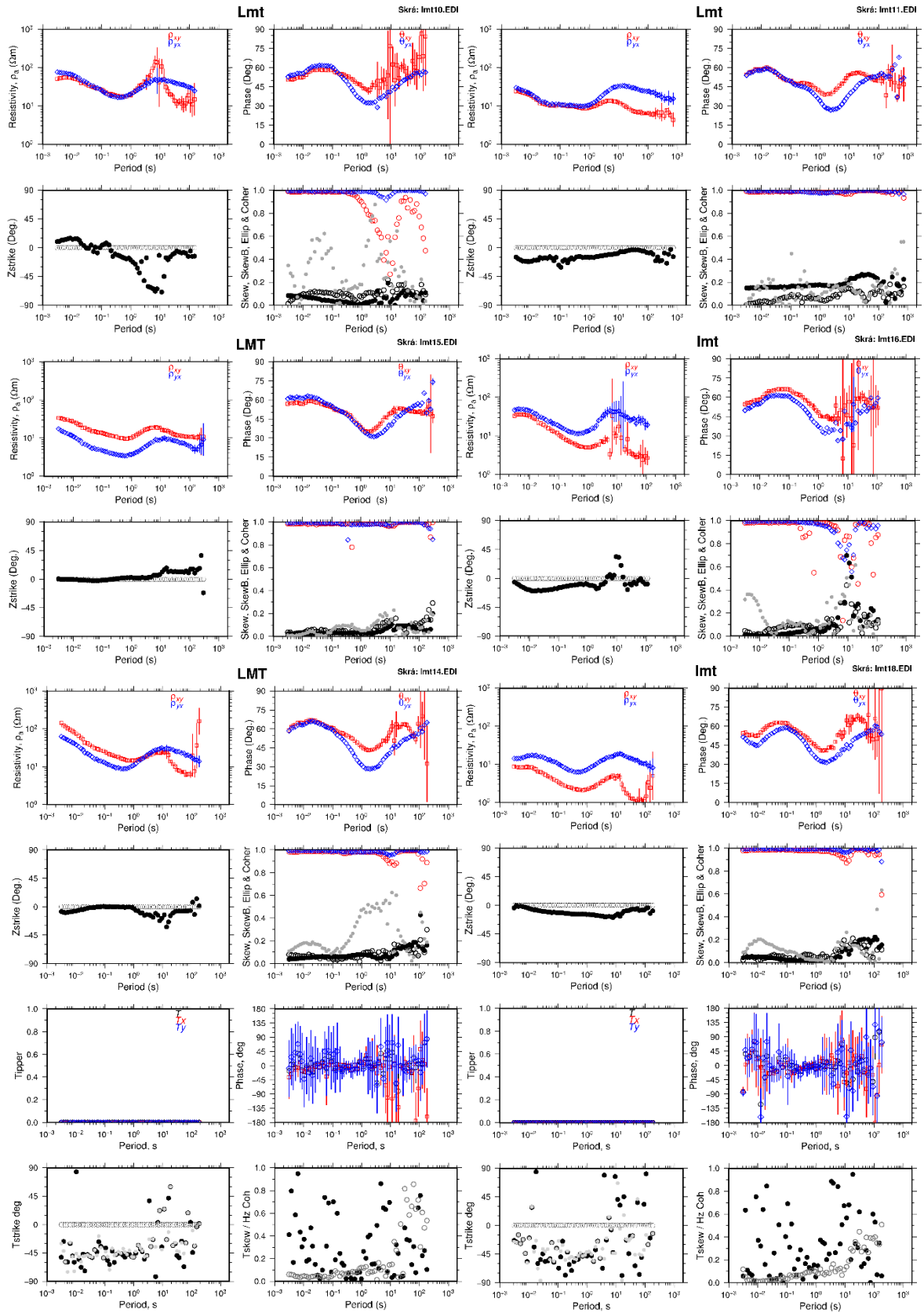
MT				TEM			
Sounding	Easting (m)	Northing (m)	Elevation (m)	Sounding	Easting (m)	Northing (m)	Elevation (m)
<i>lmt75</i>	221235	9891107	1859				
<i>lmt76</i>	213098	9891654	1891				
<i>lmt77</i>	221636	9891691	1836				
<i>lmt78</i>	213254	9890025	1822				

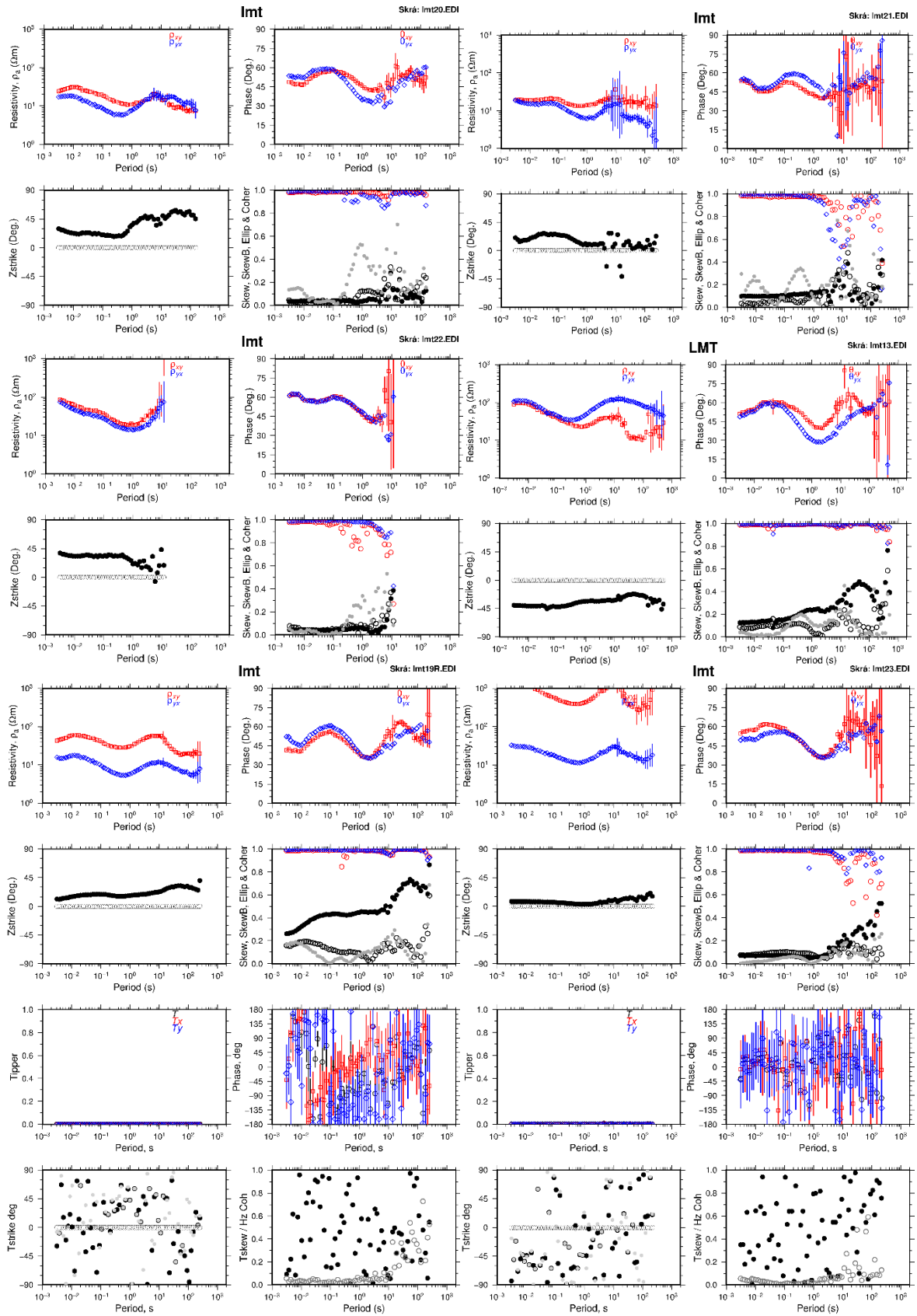
APPENDIX B: Processed MT data

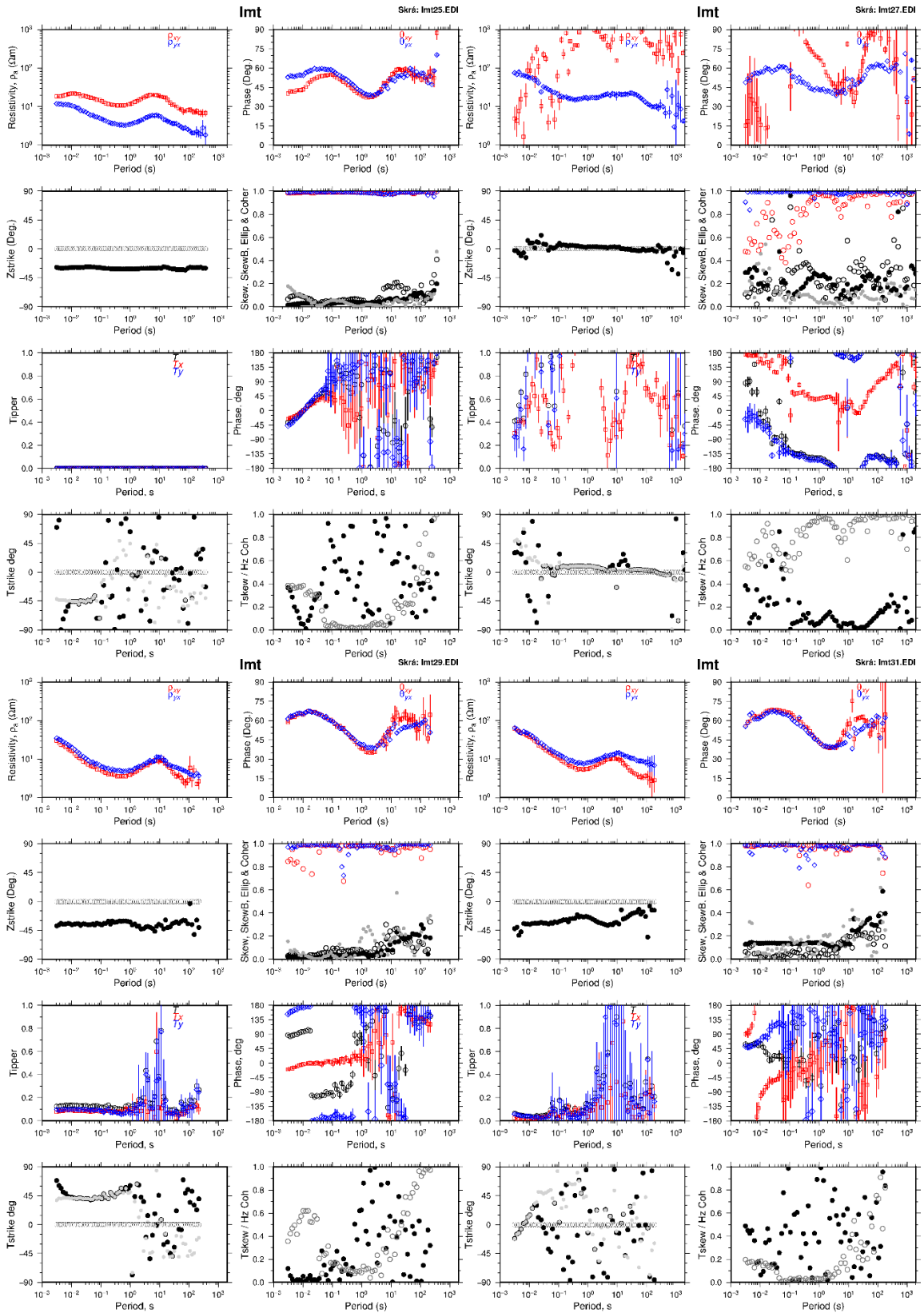
Figures of the processed MT data created with edi2ps. Red diamonds are the resistivity, phase and Tipper in xy direction. Blue diamonds are the resistivity, phase and Tipper in yx direction. Black circles are the Zstrike, Skew, SkewB, Ellip & Coher.

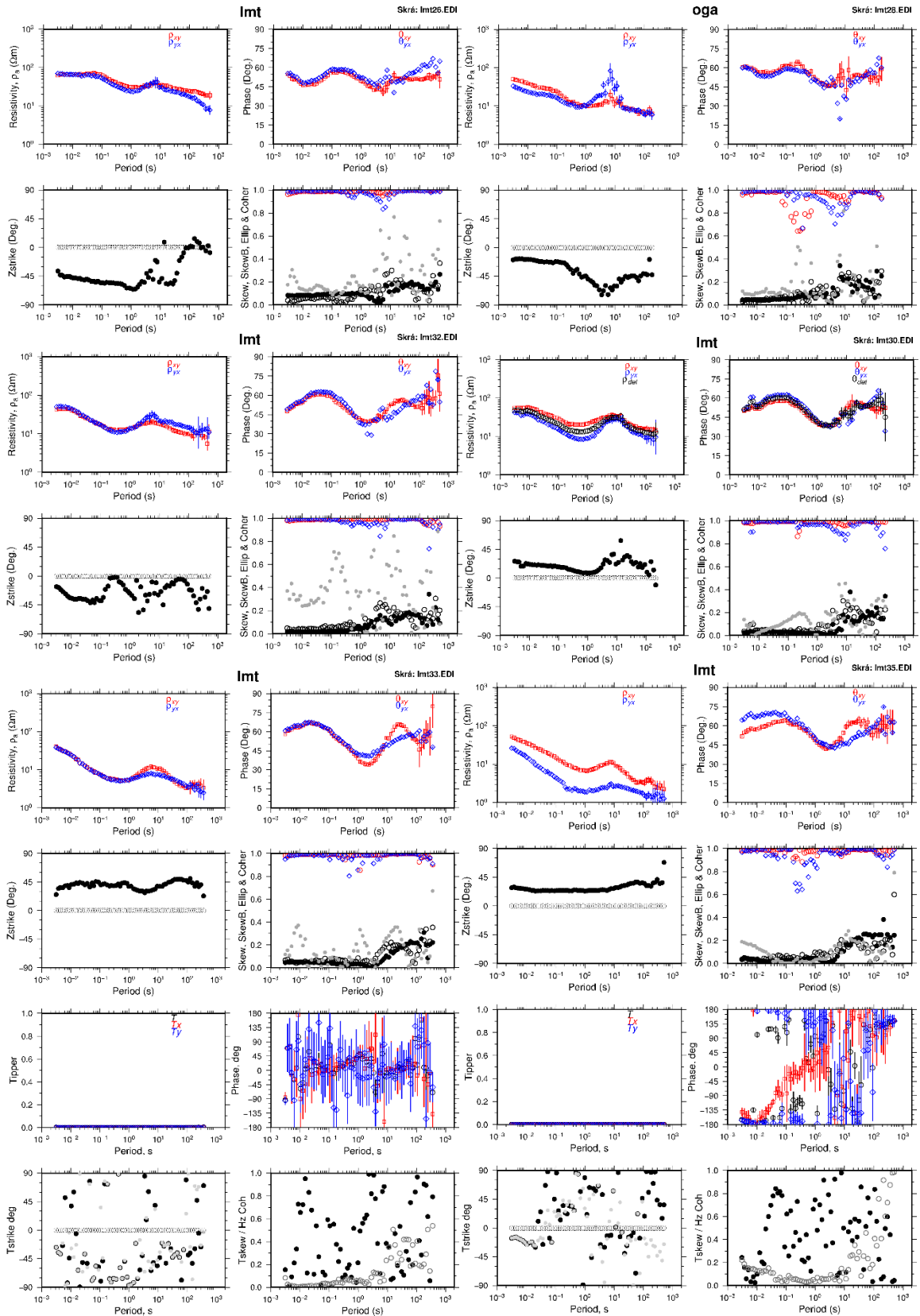


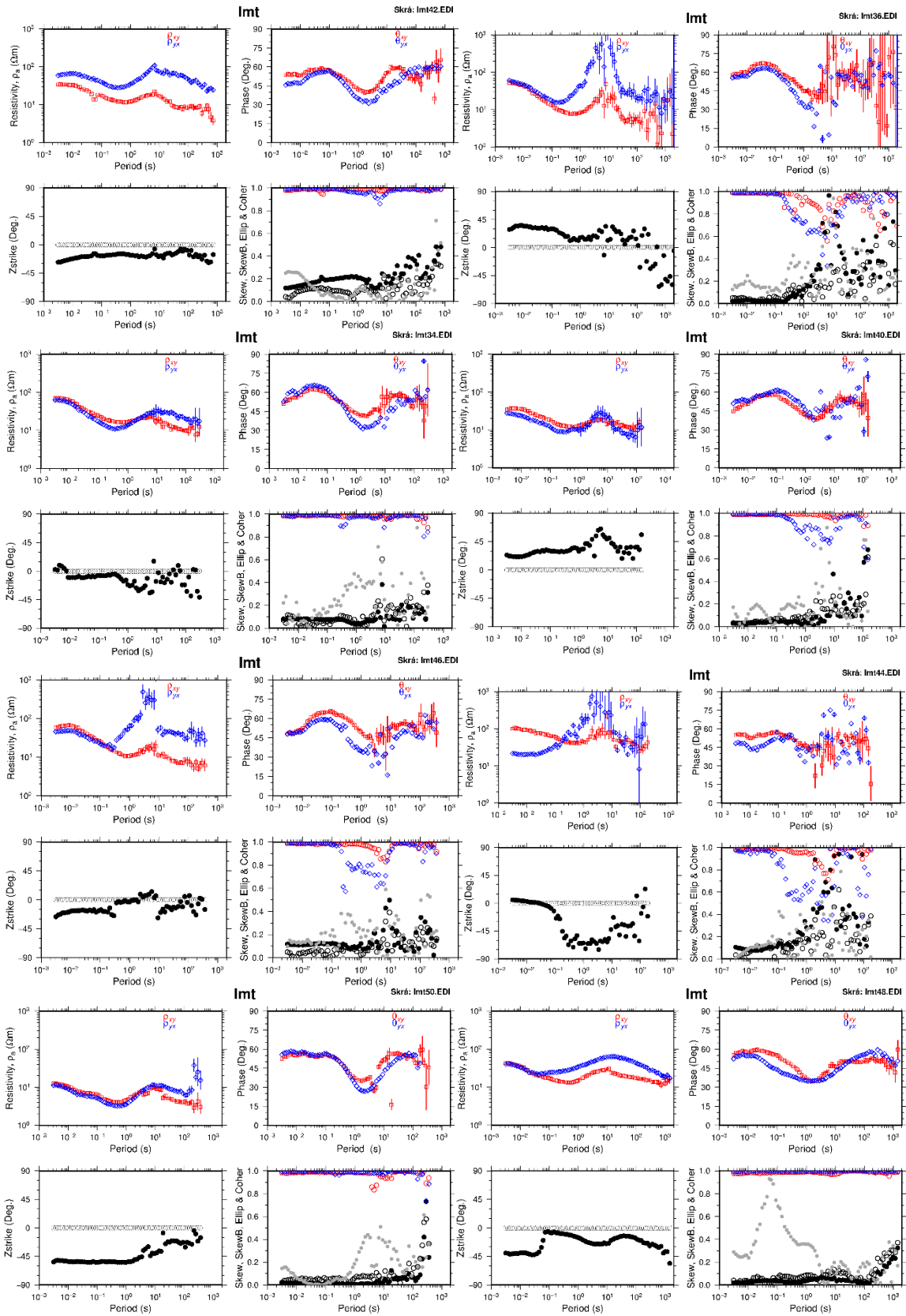


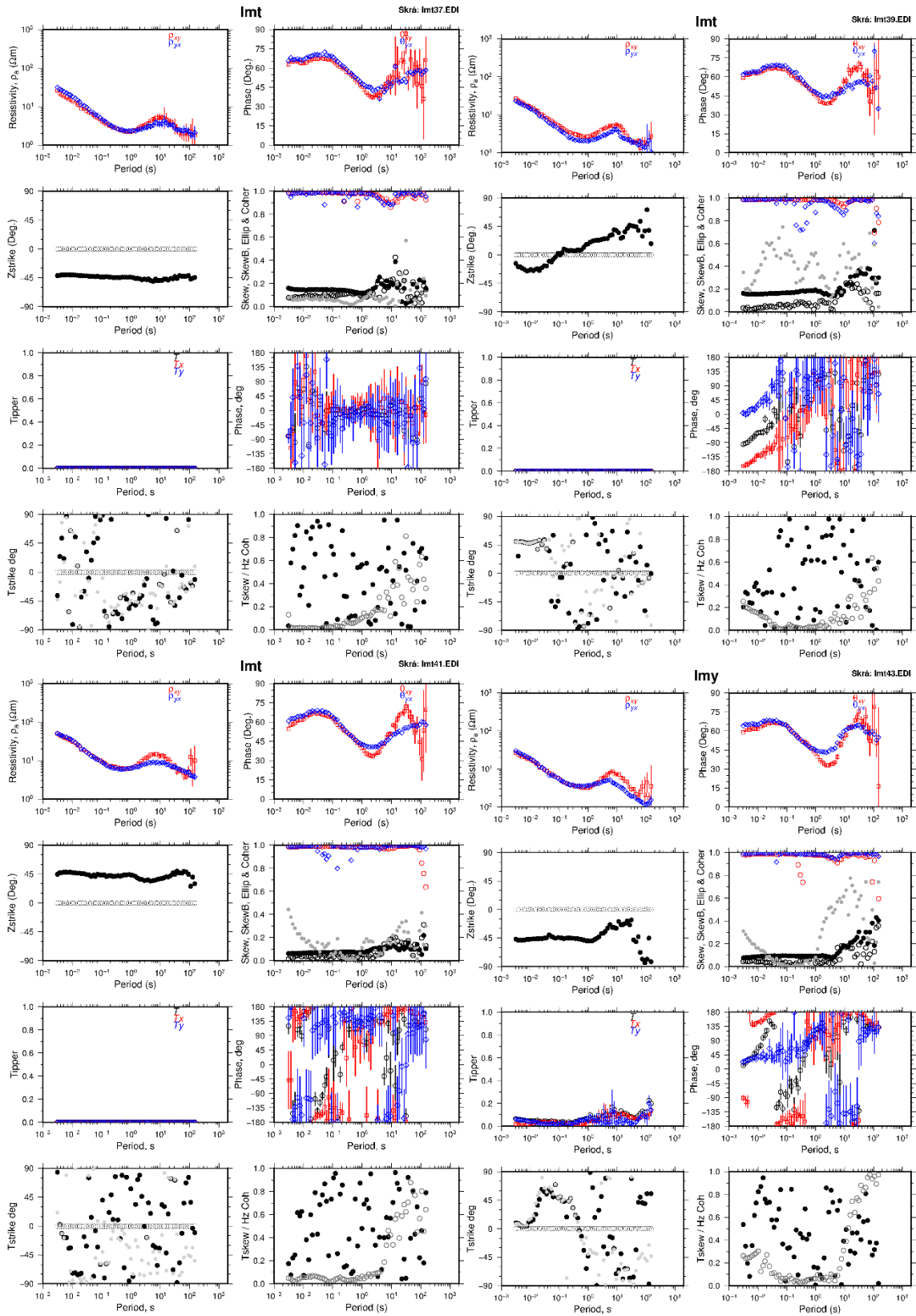


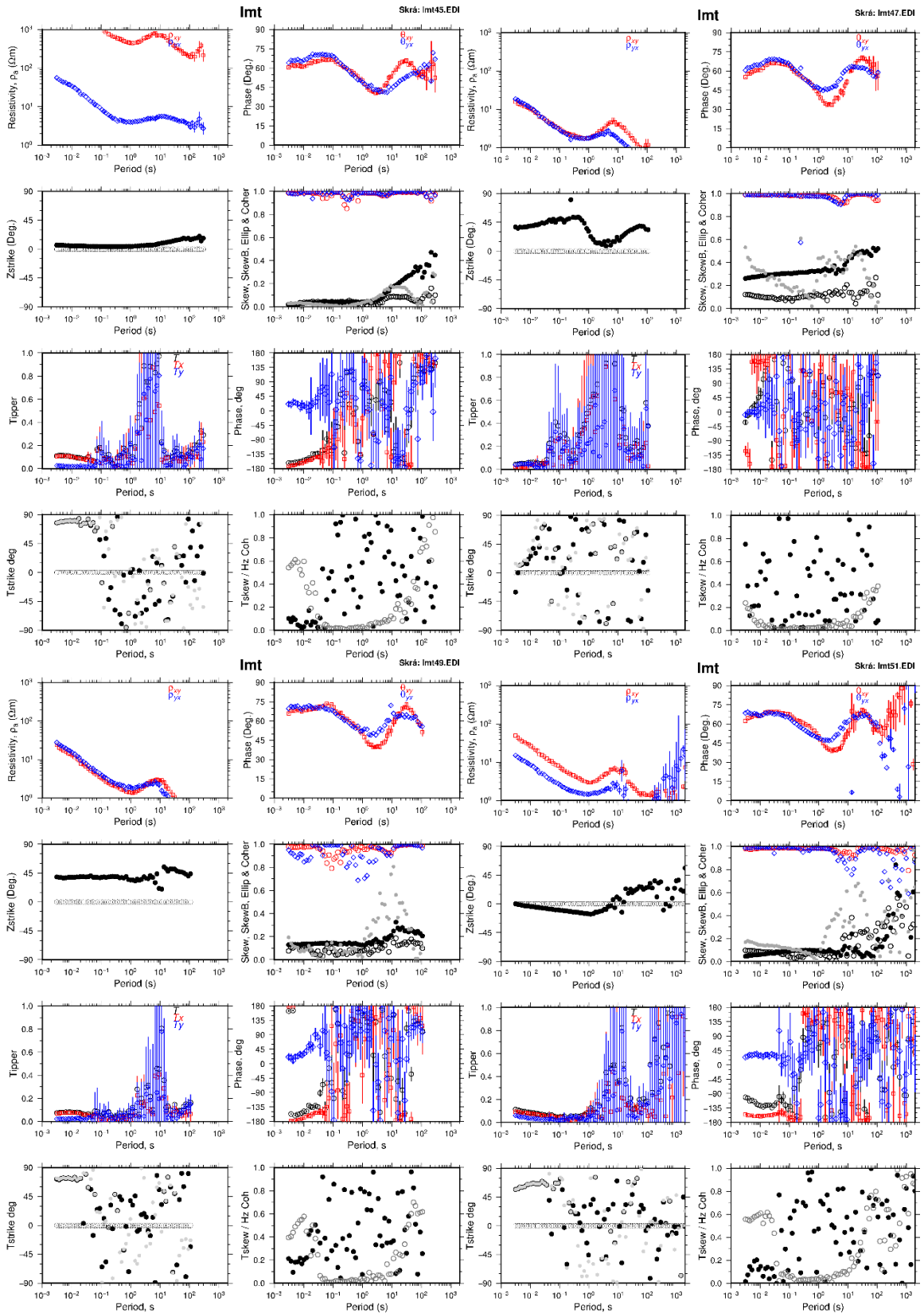


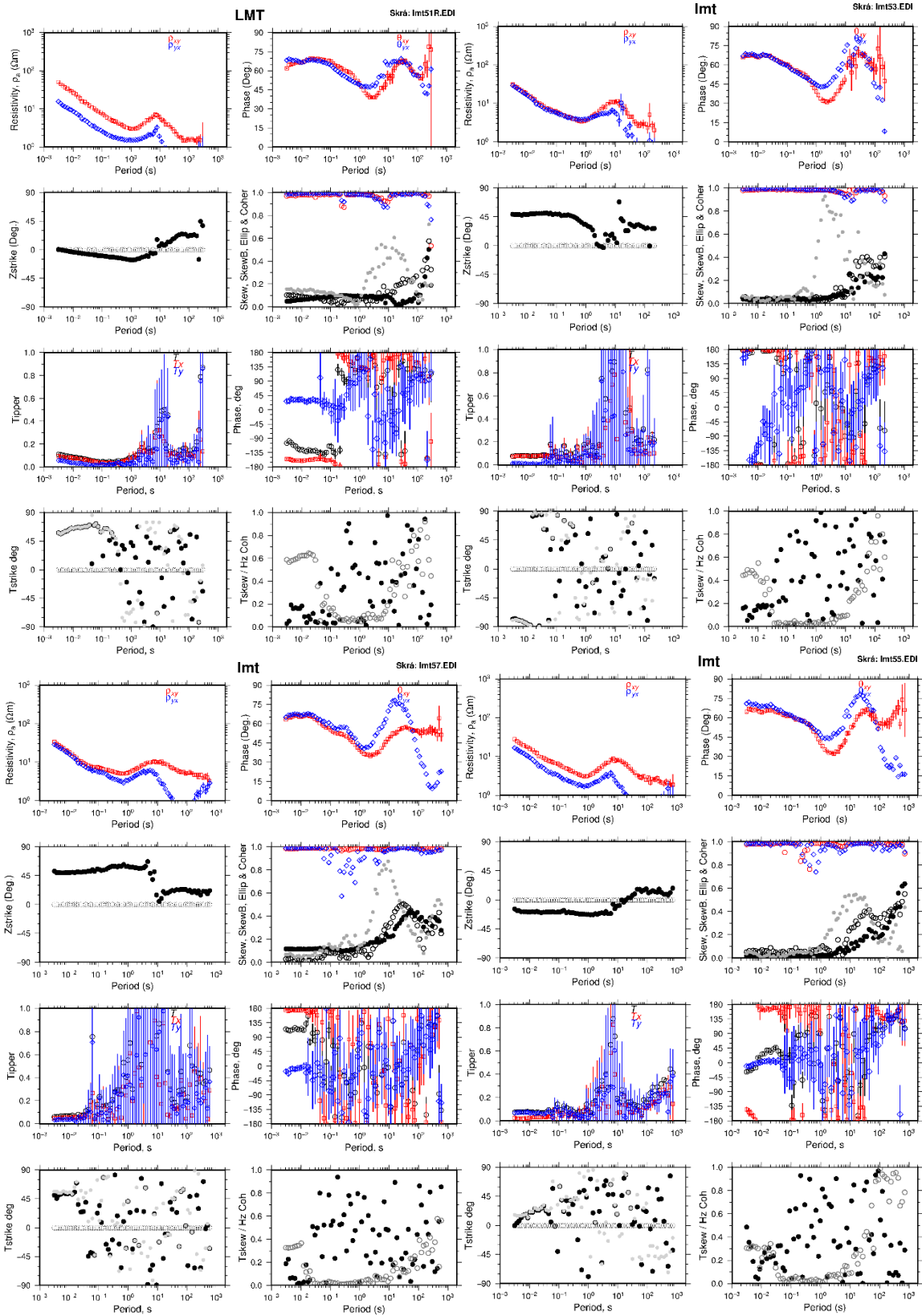


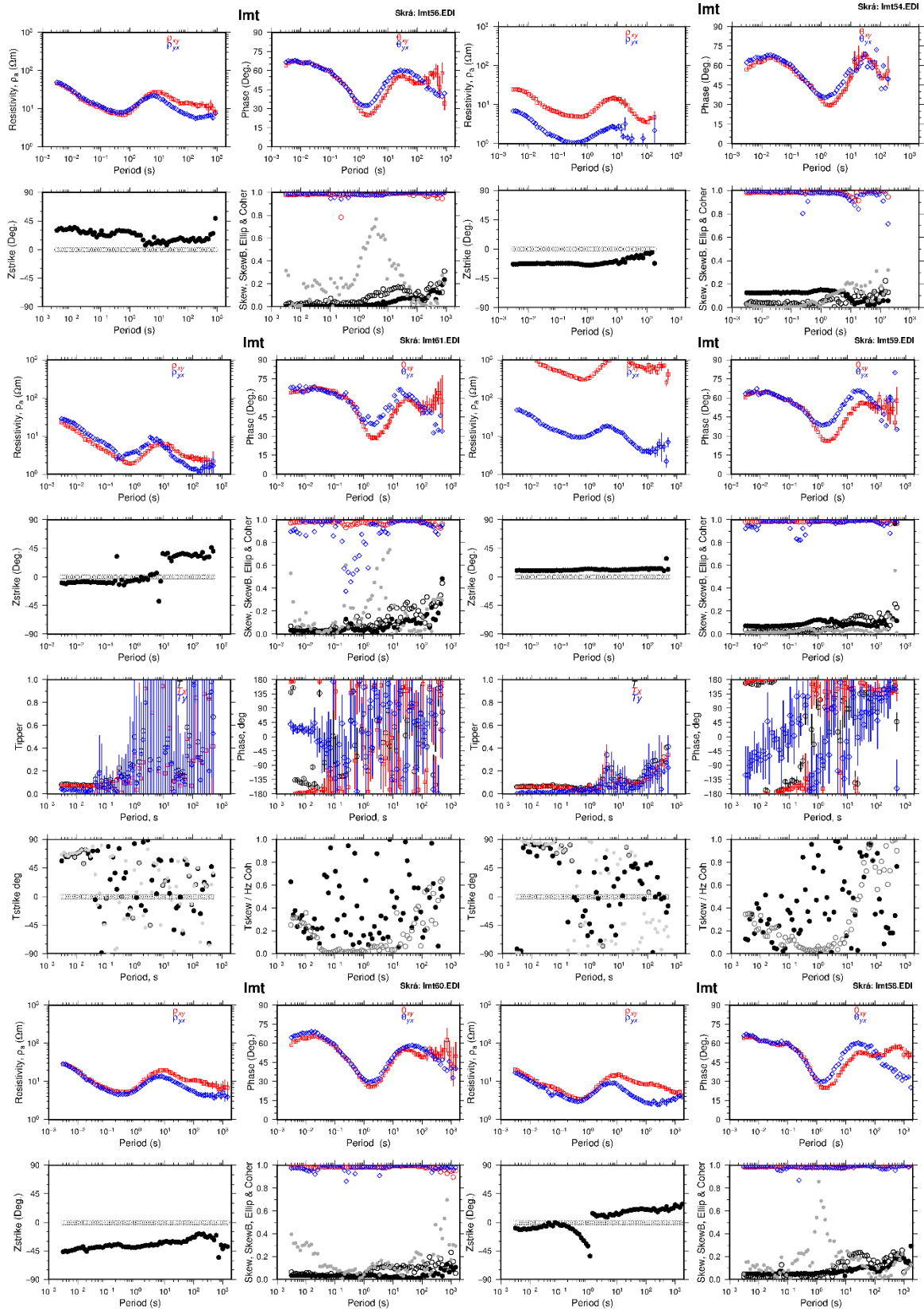


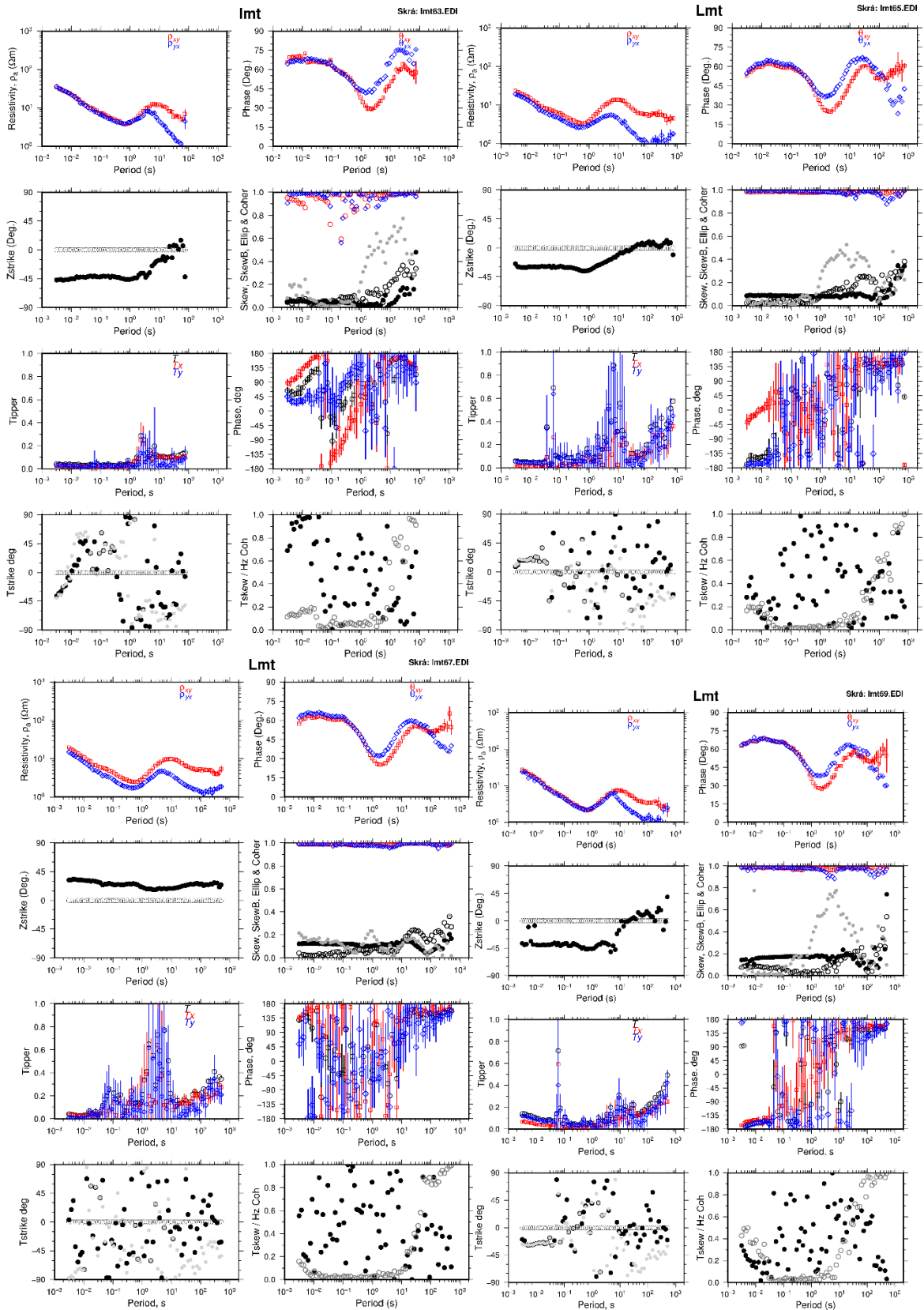


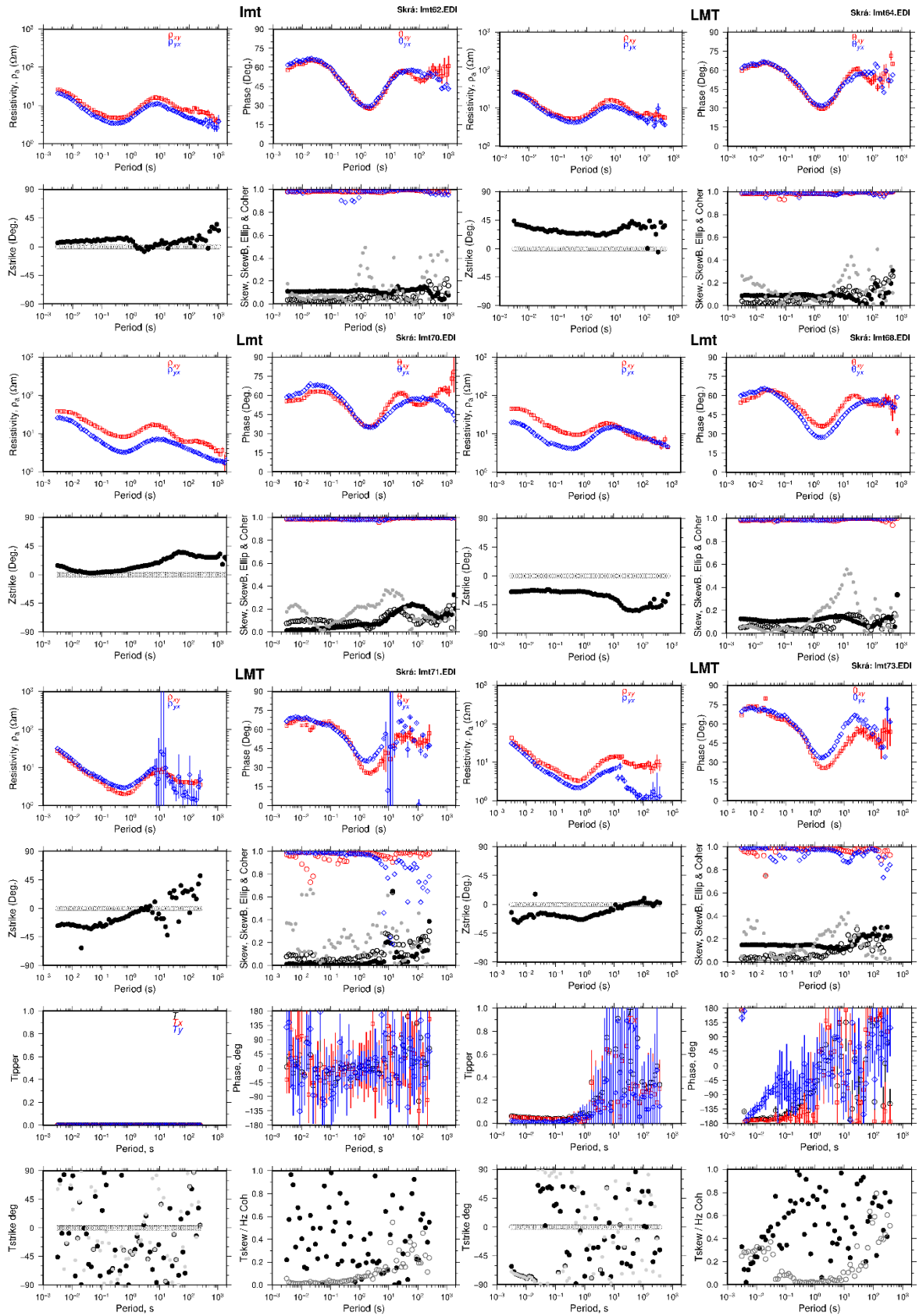


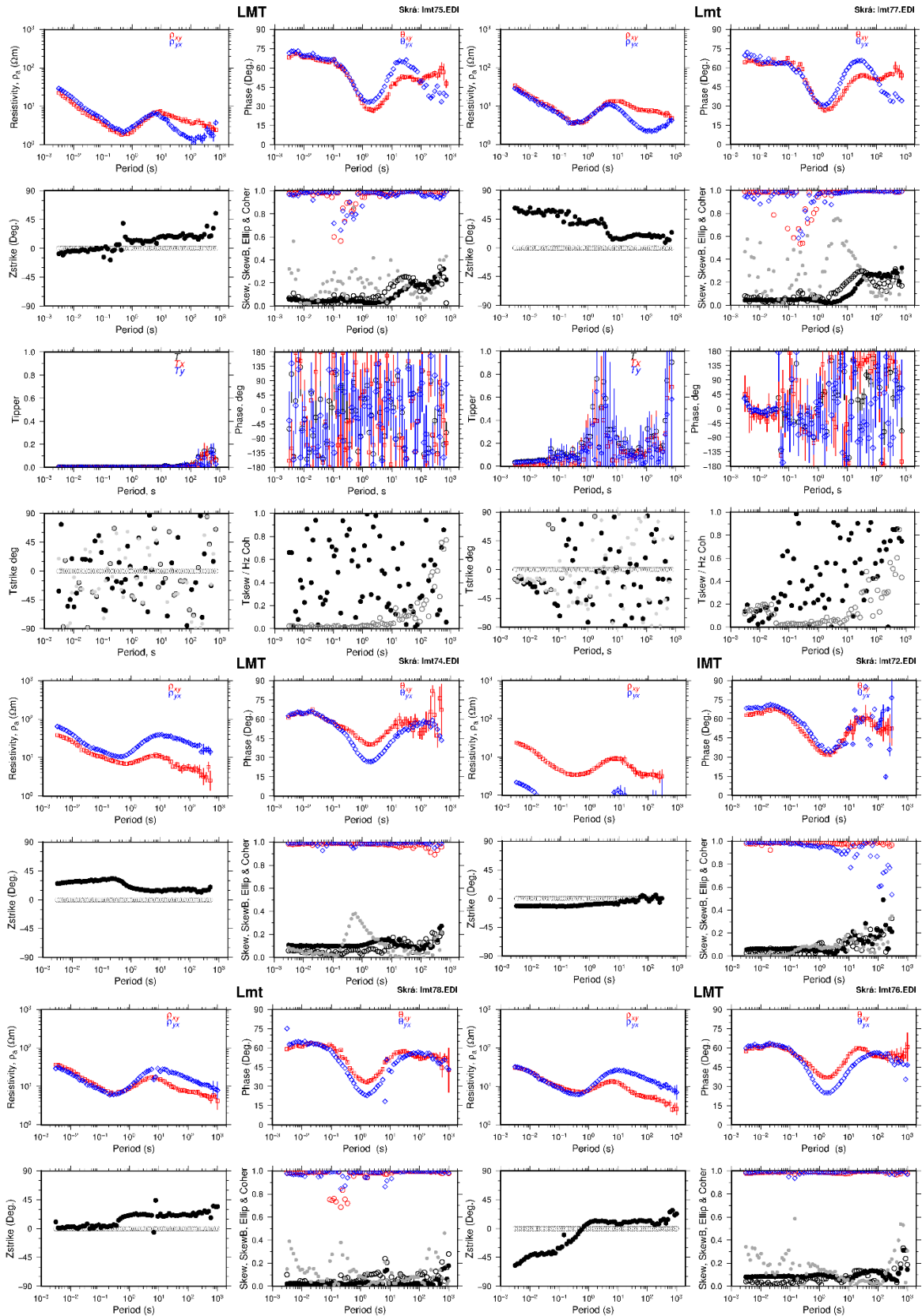


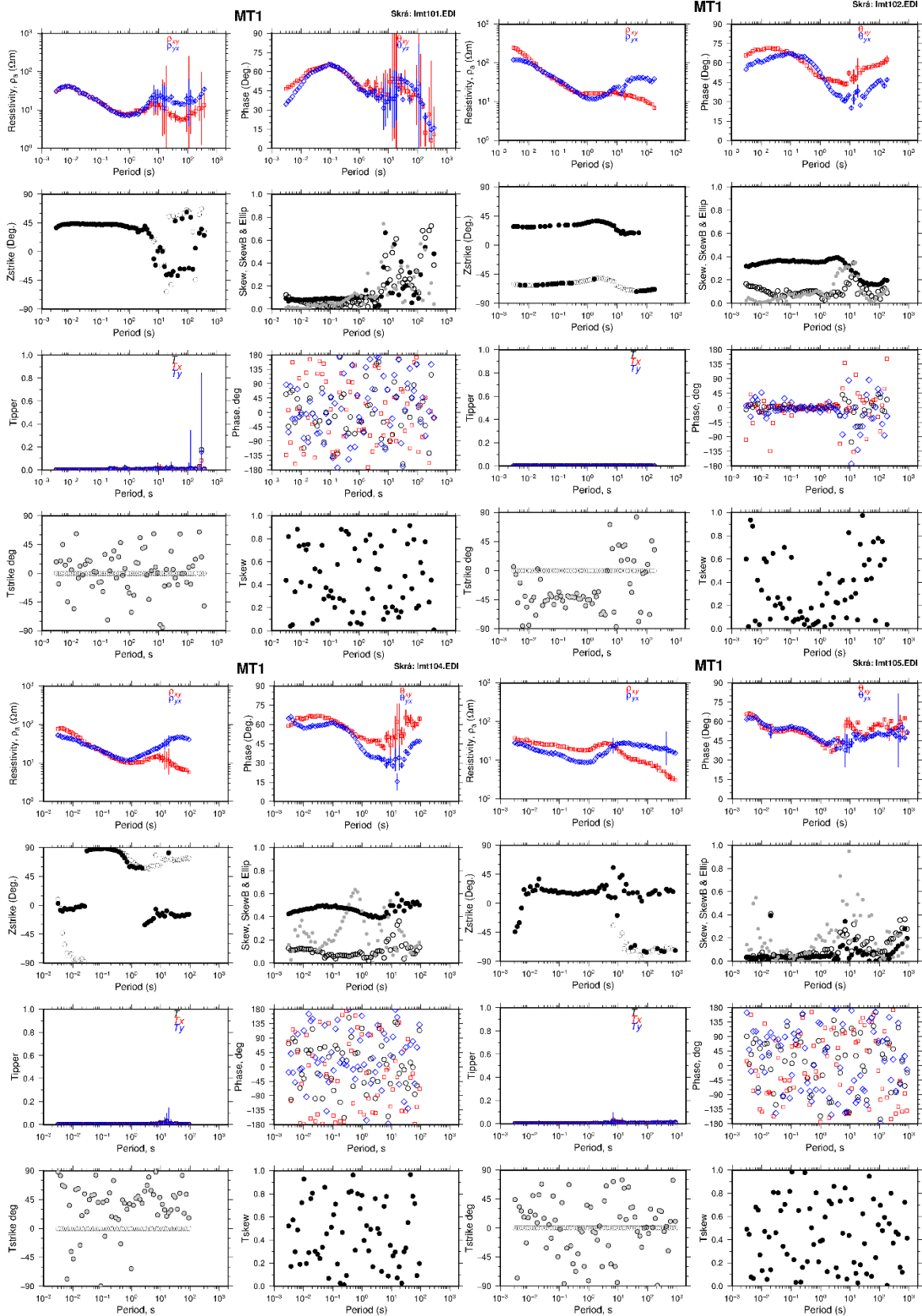


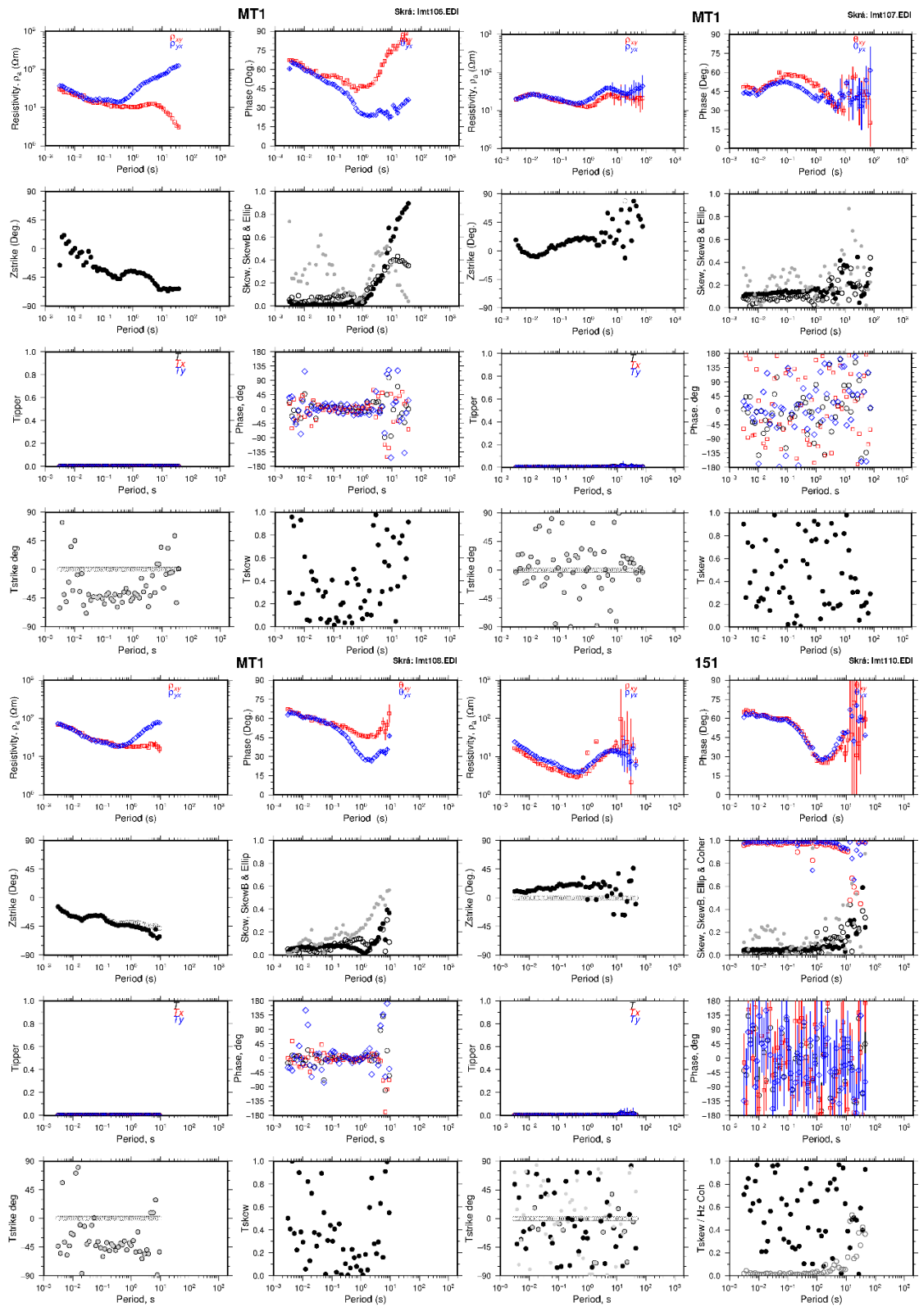


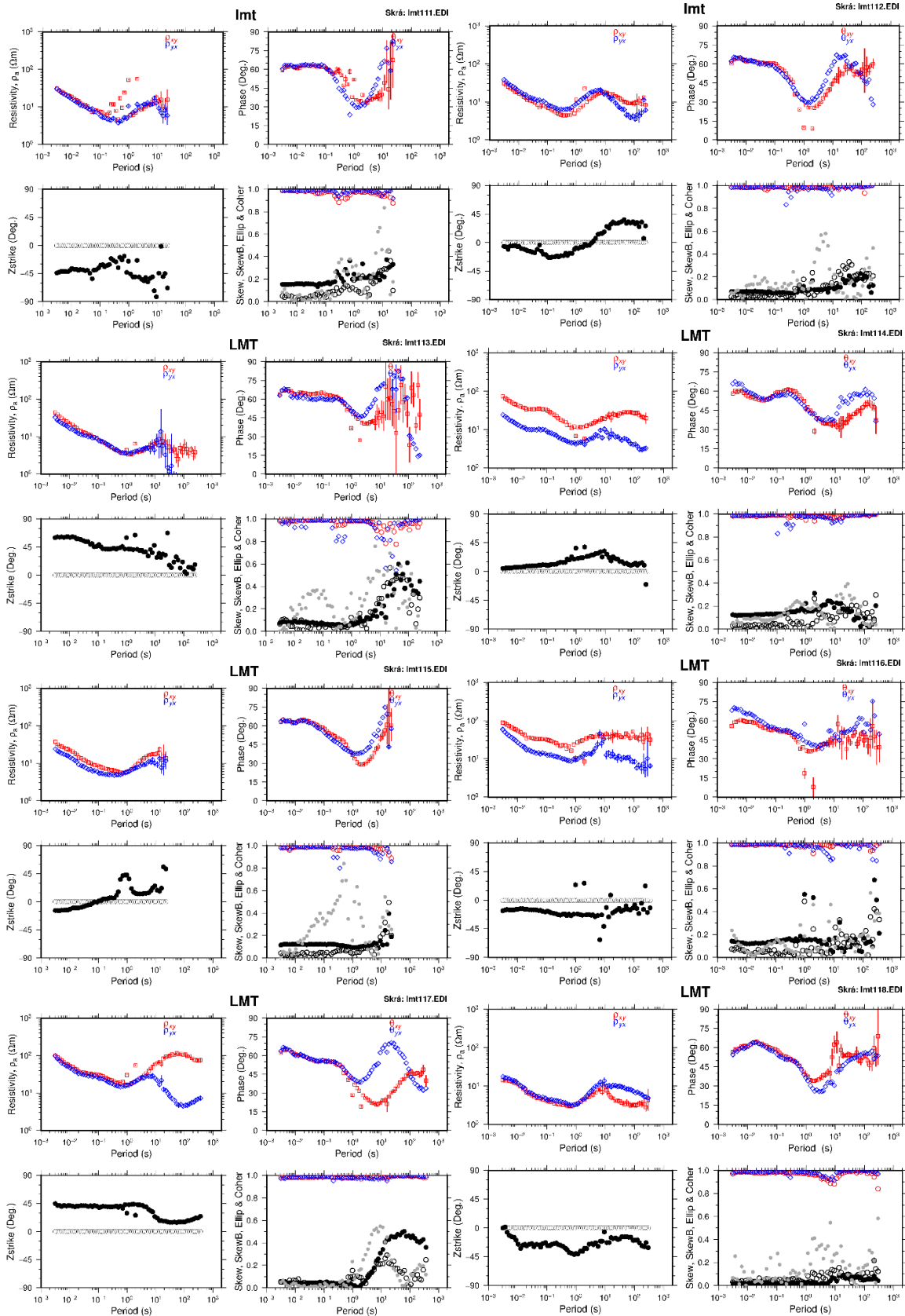


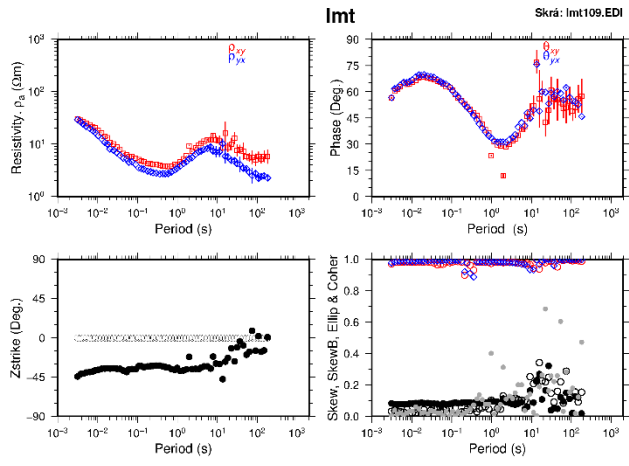






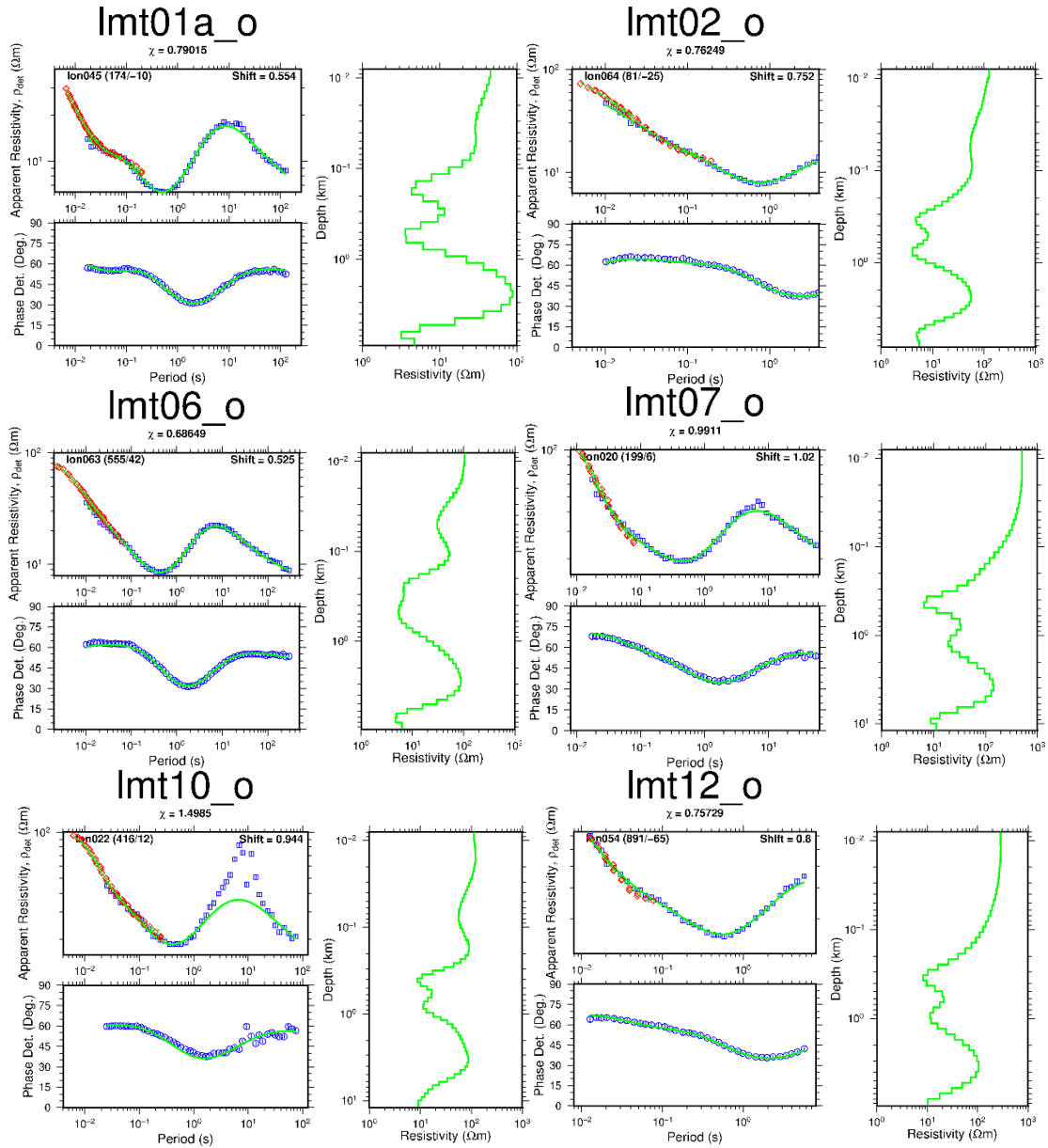


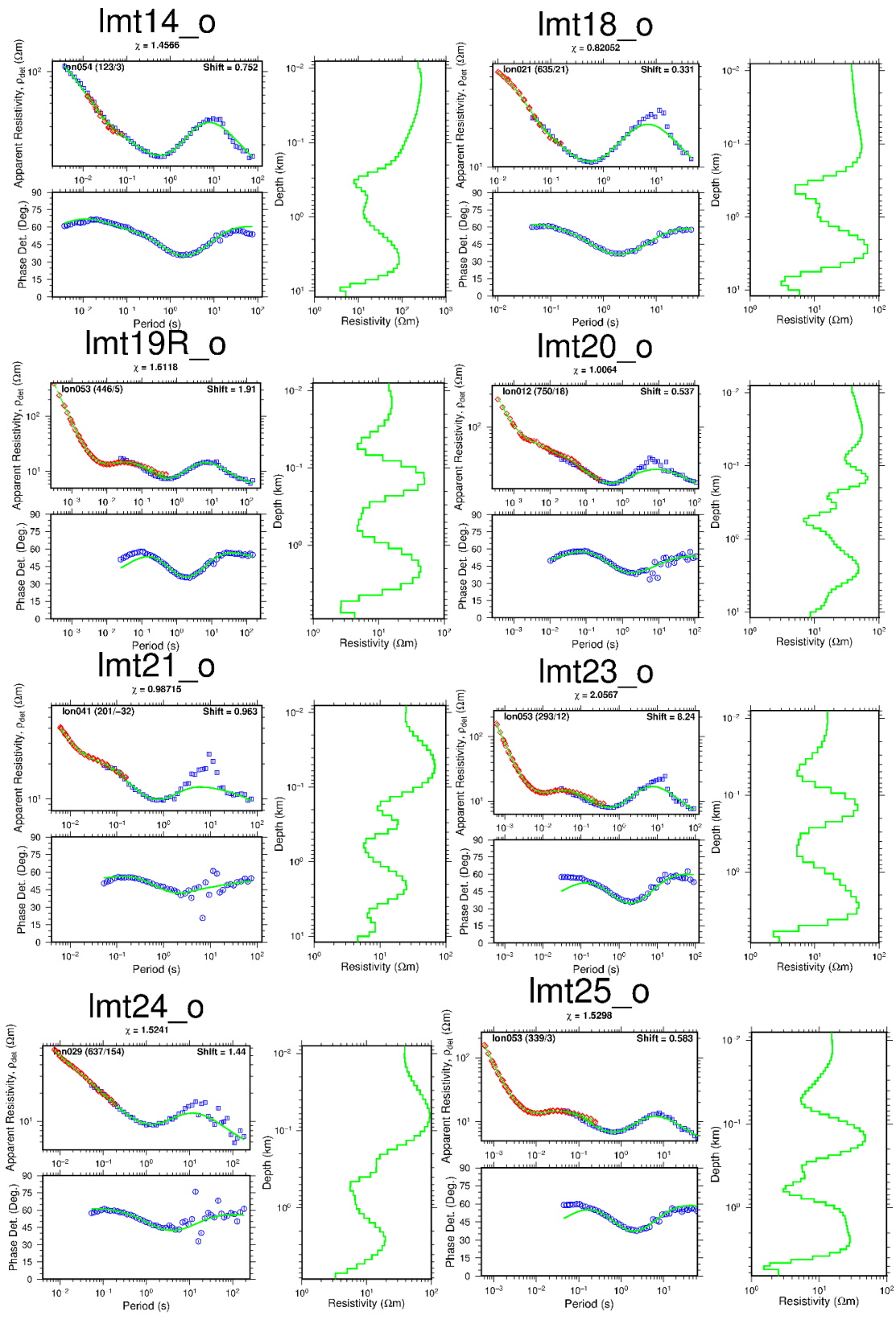


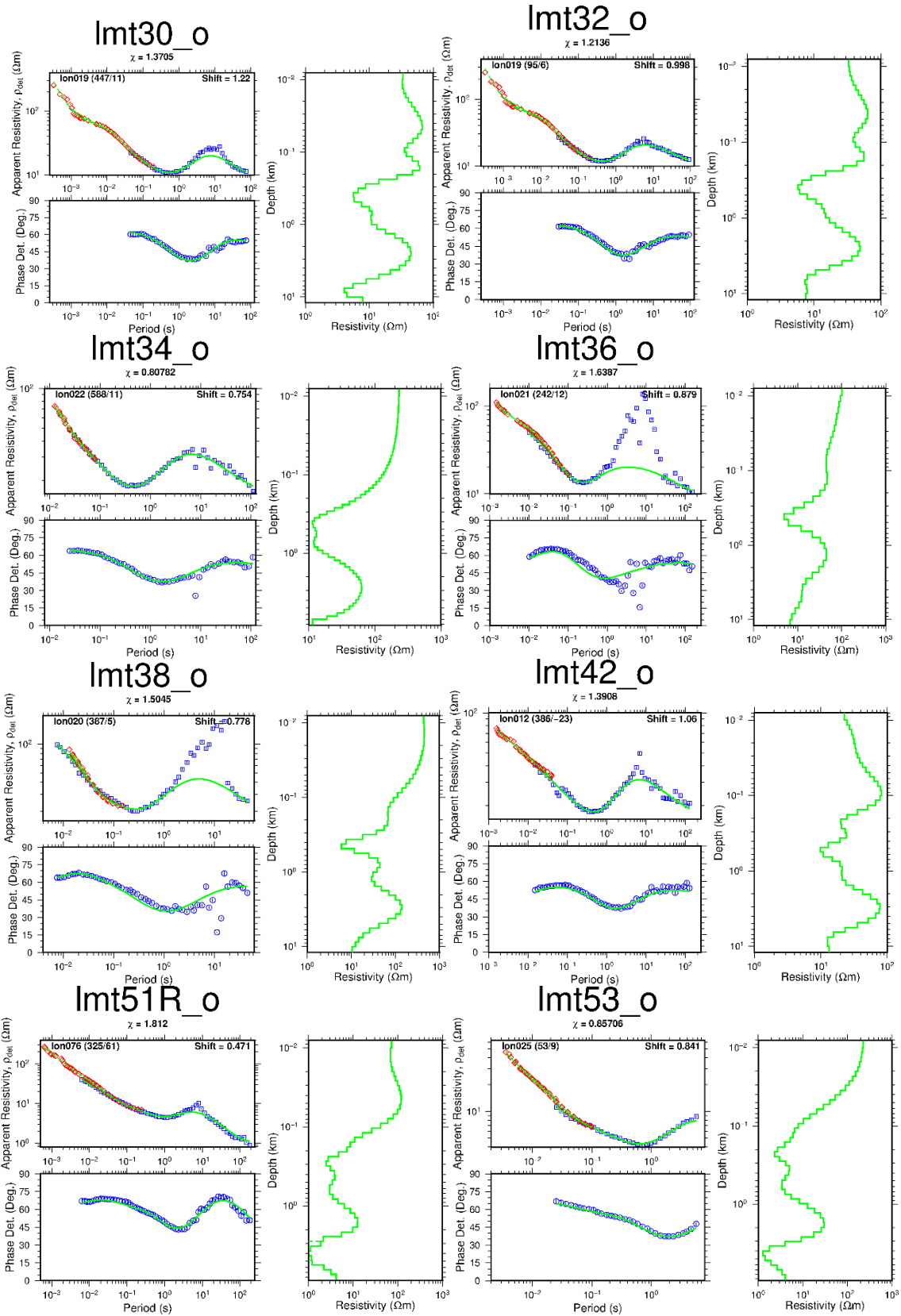


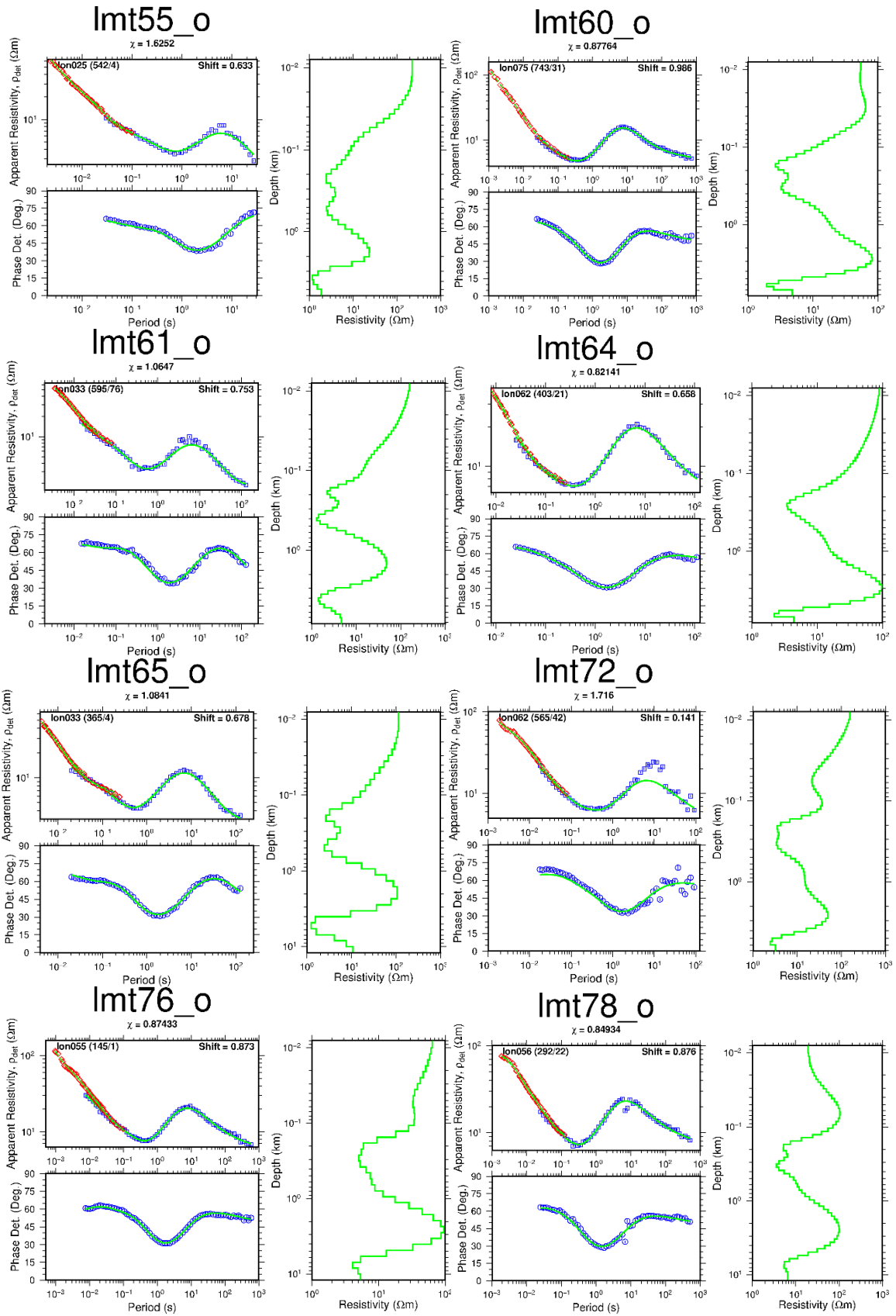
APPENDIX C: 1-D joint inversion of TEM and MT data

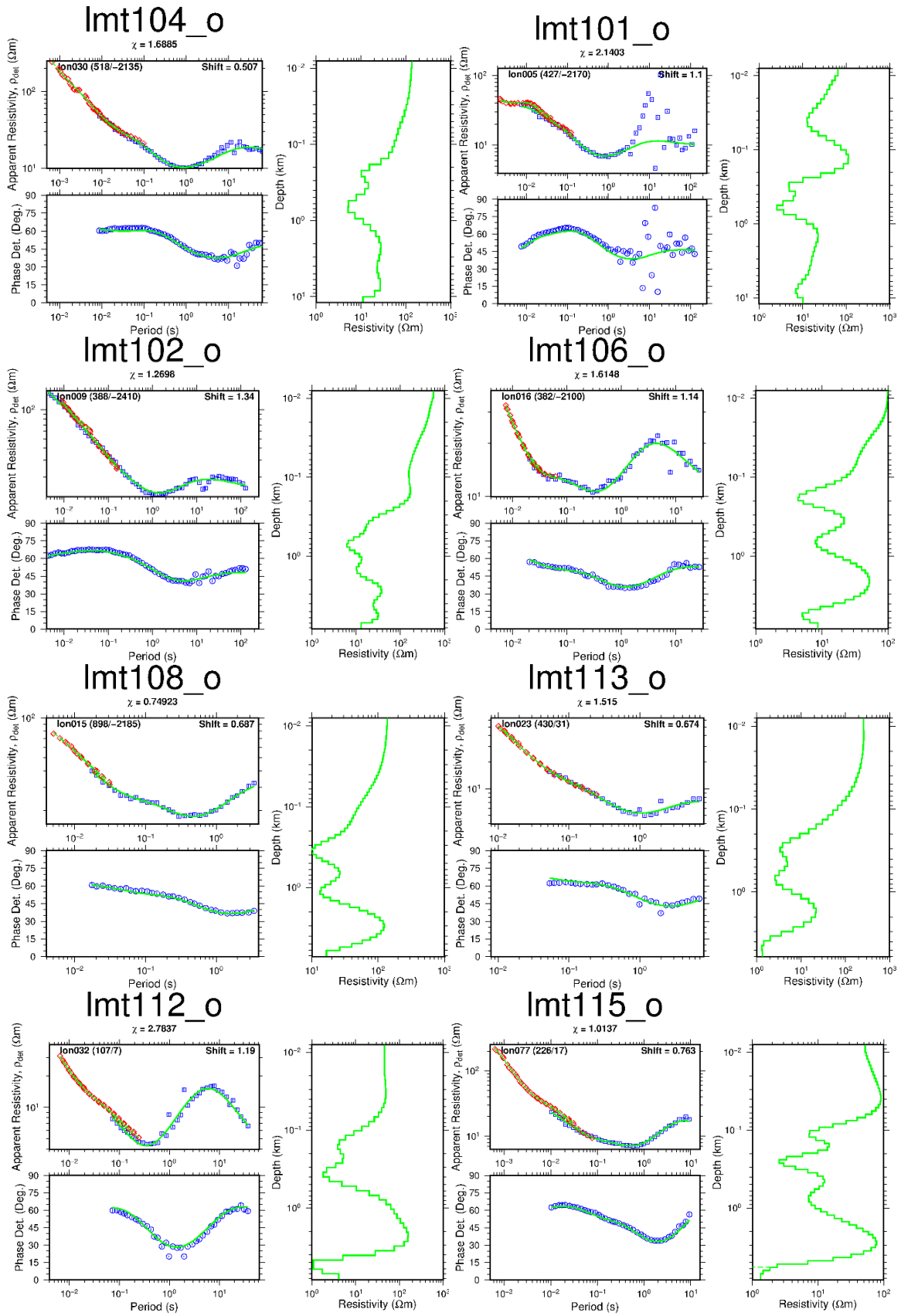
Results of TEM/MT 1-D joint inversion data models. Blue squares are measured MT apparent resistivity. Blue circles are the measured phase. Both the apparent resistivity and phase are gotten from the determinant of the MT impedance tensor. Red squares are the measured TEM data. Green solid lines on the right indicate results of the 1-D resistivity Occam inversion model. The green solid lines in the left panels are calculated responses. The number on top of the figure is the MT station name. Number below the MT station: chi (χ) - a measure of the fit between the measured data and the model data. Number in the upper left panel is the name of the TEM station. The number to the upper right corner is the static shift. The numbers in brackets show the distance between MT and TEM stations and elevation. The scale is in logarithmic.

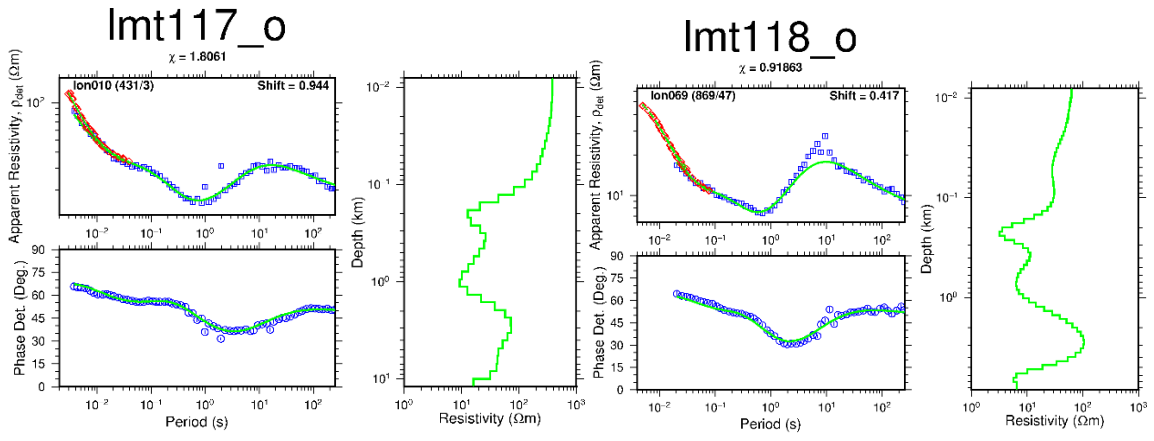






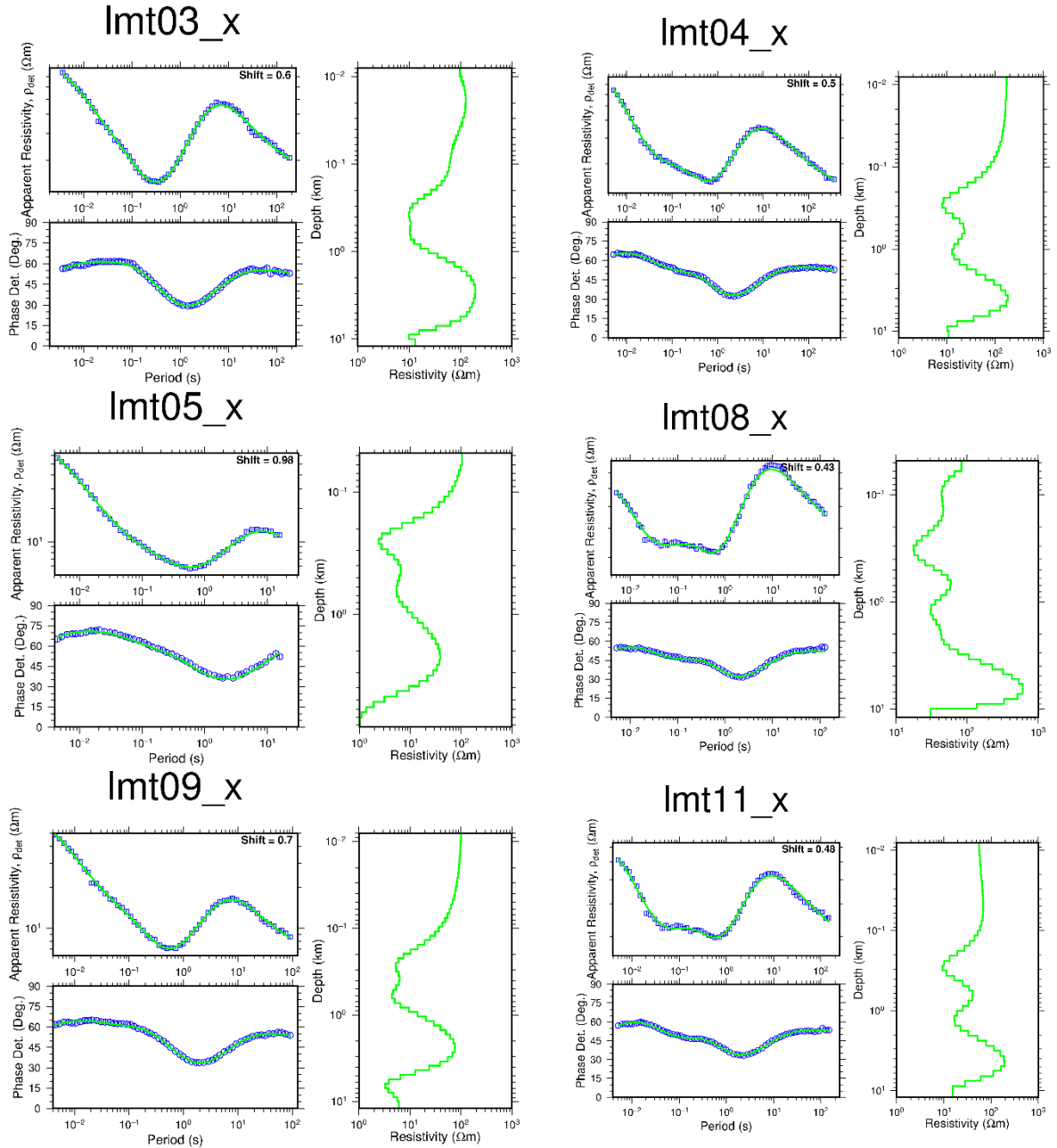


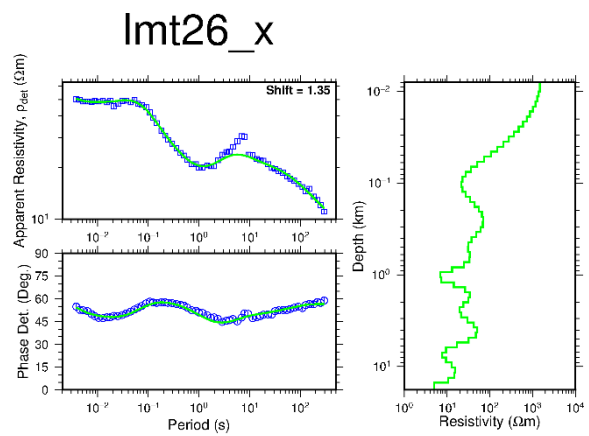
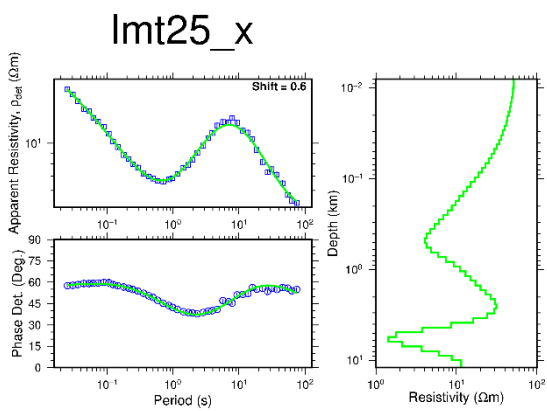
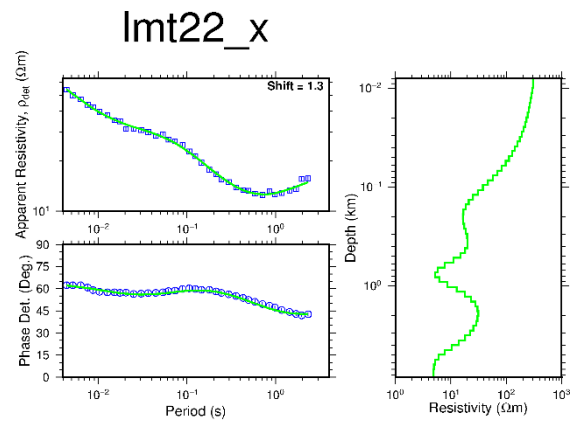
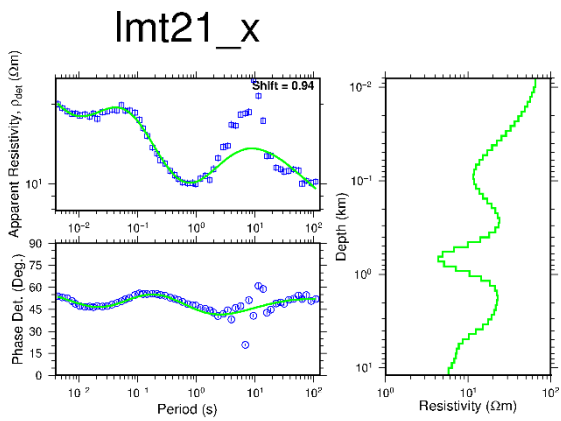
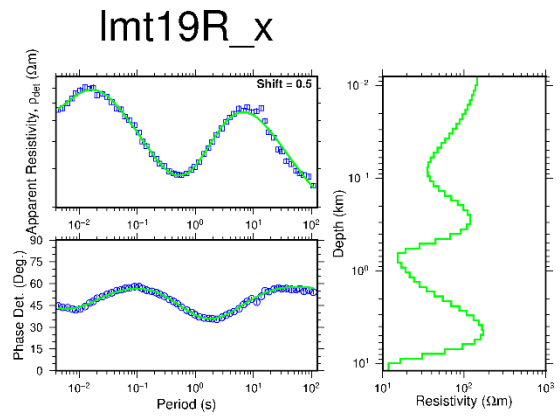
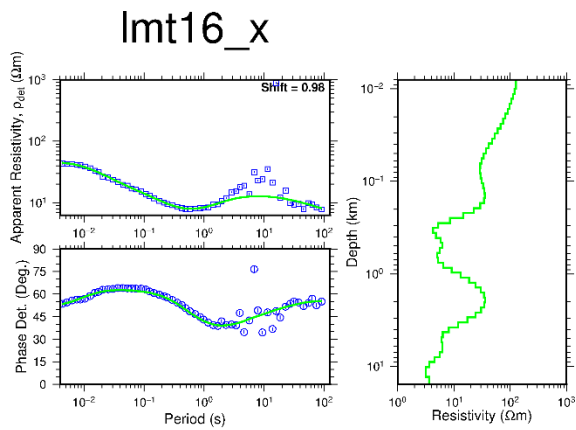
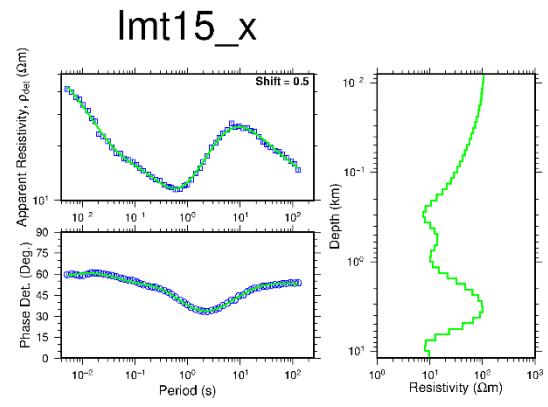
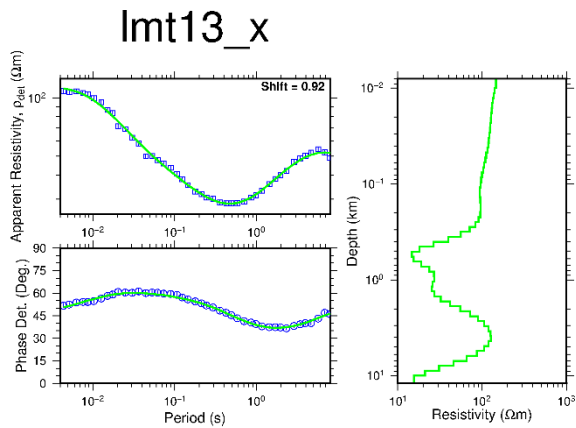


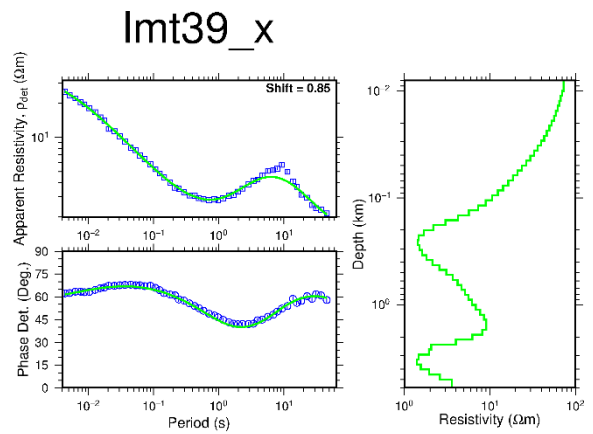
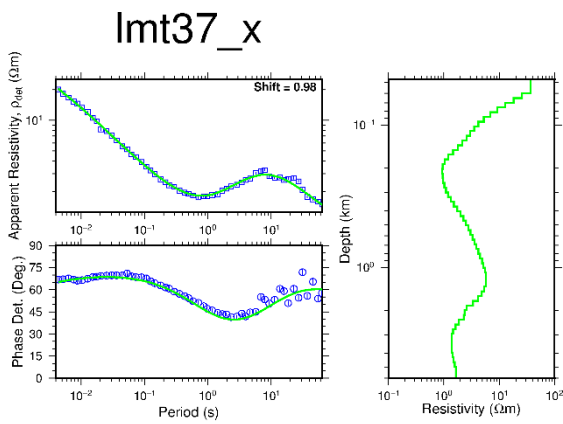
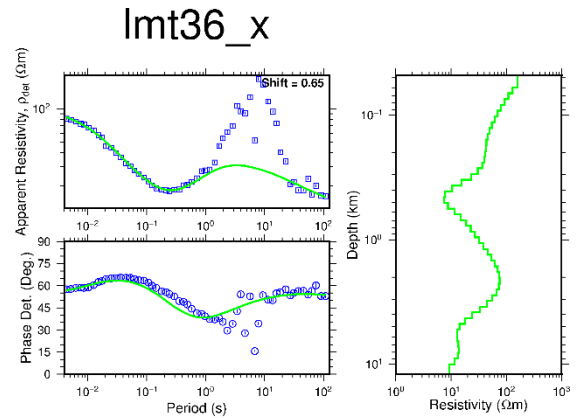
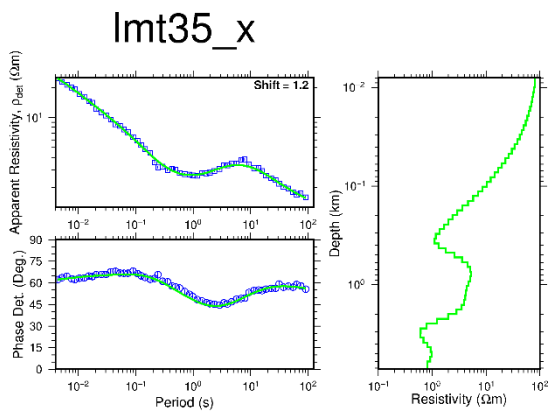
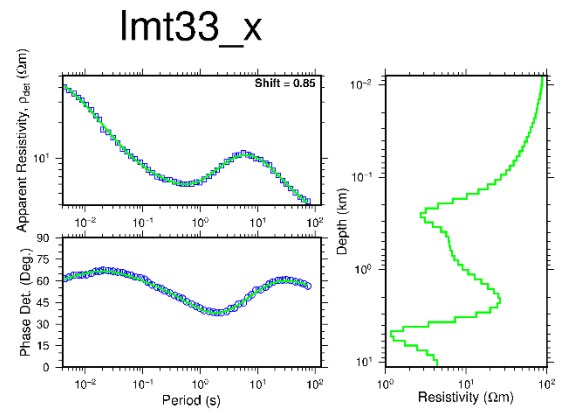
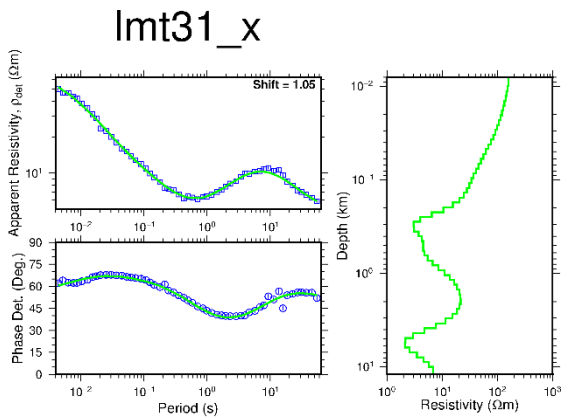
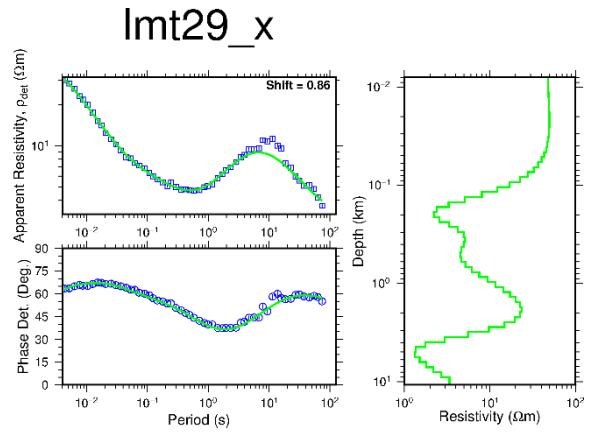
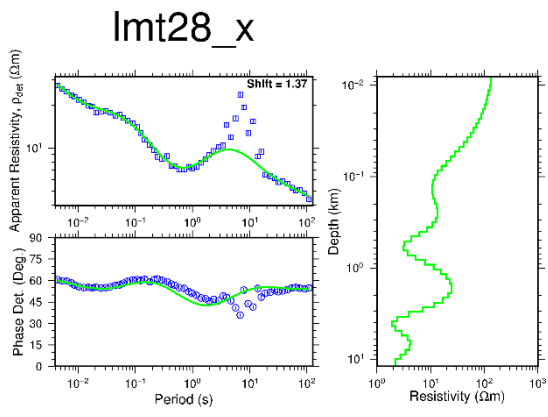


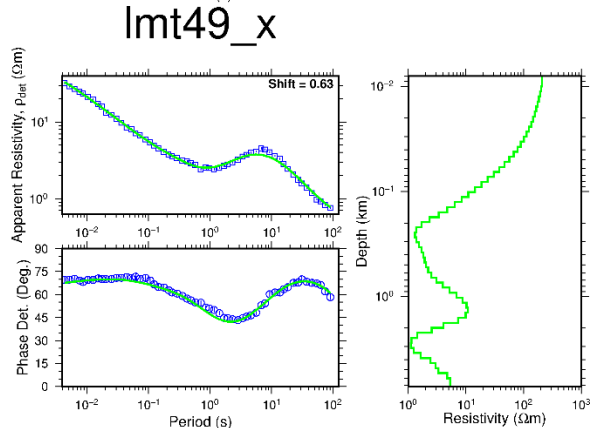
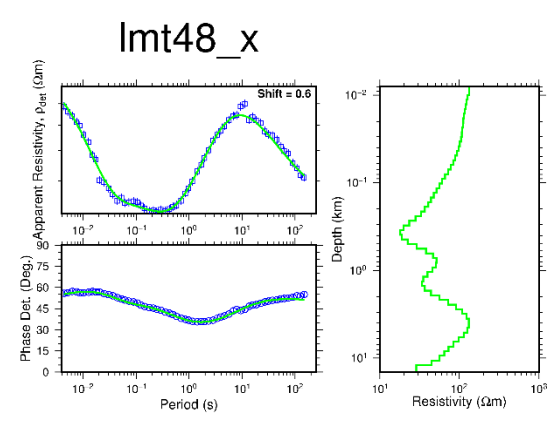
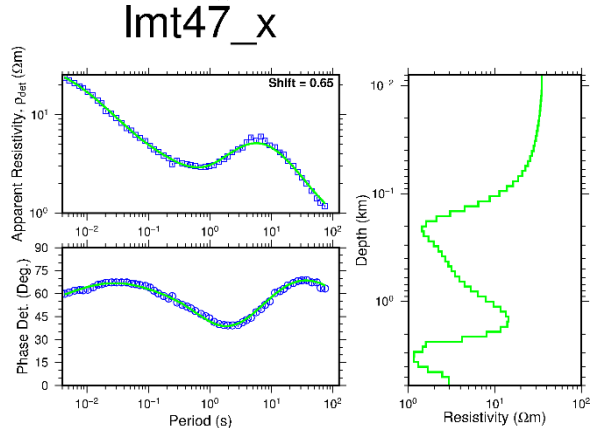
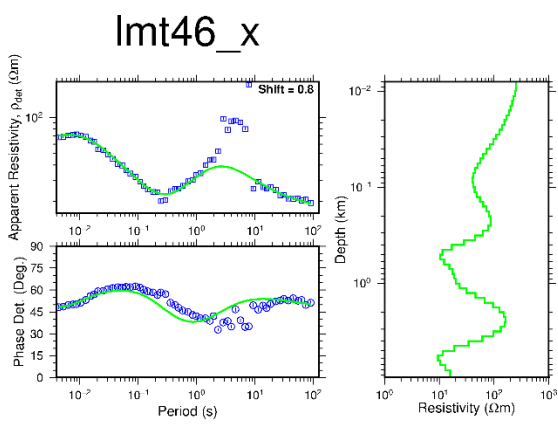
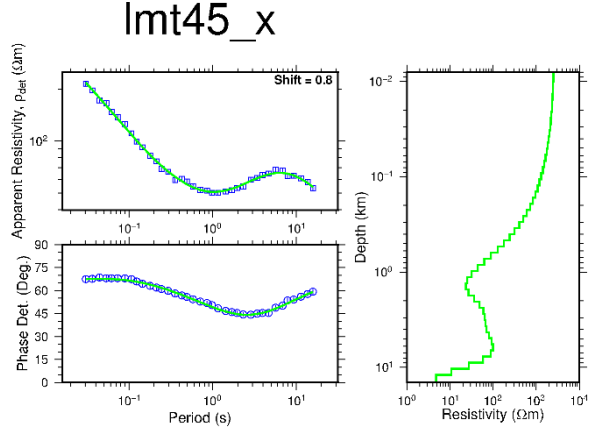
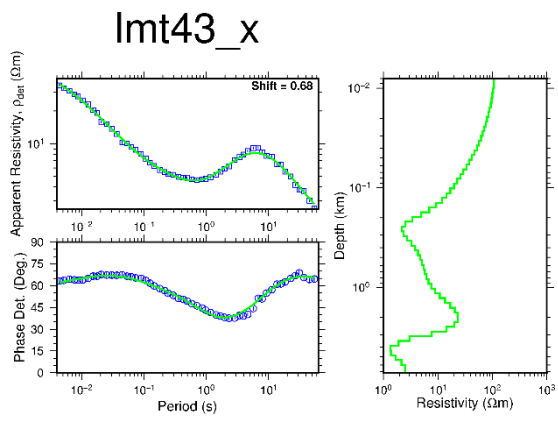
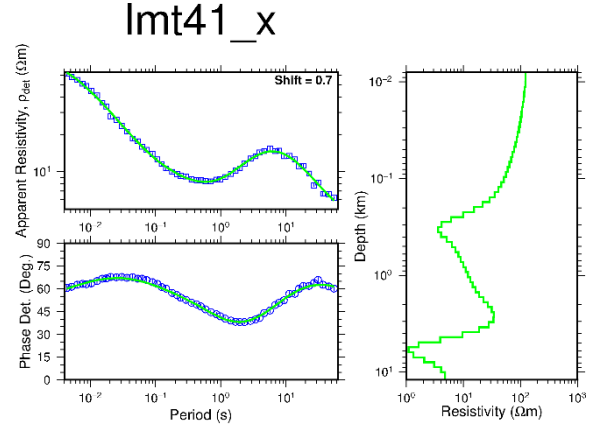
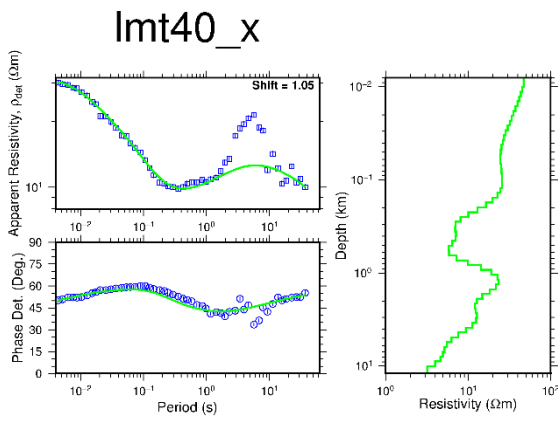
APPENDIX D: 1-D inversion of MT data using geospatial static shift distribution

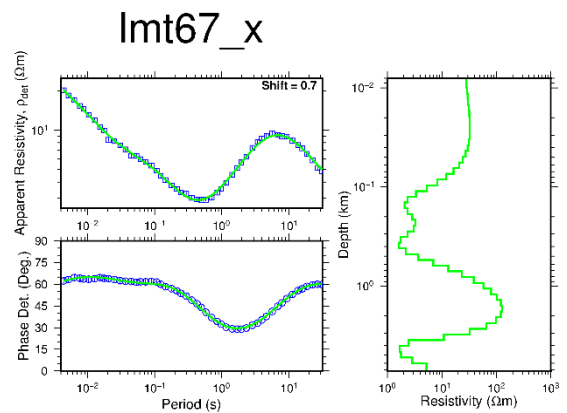
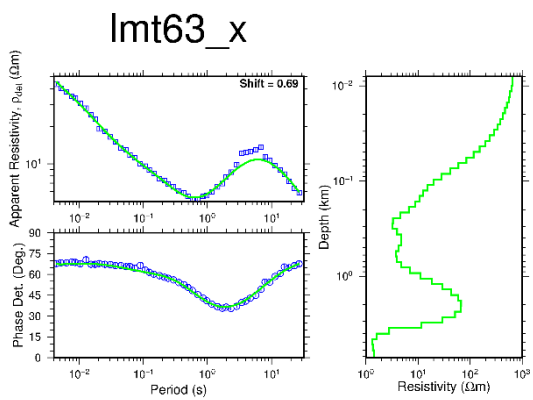
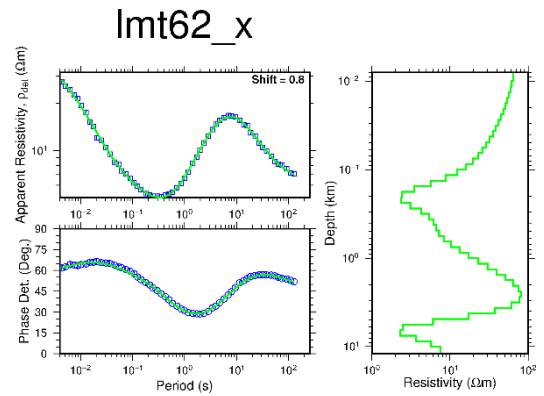
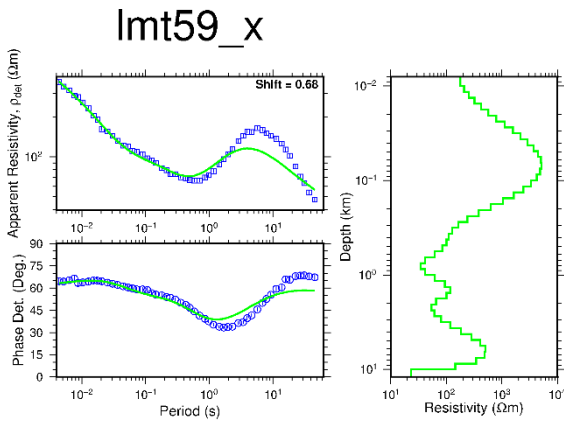
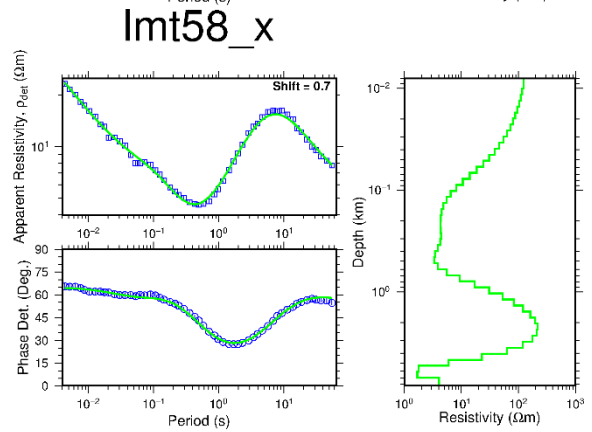
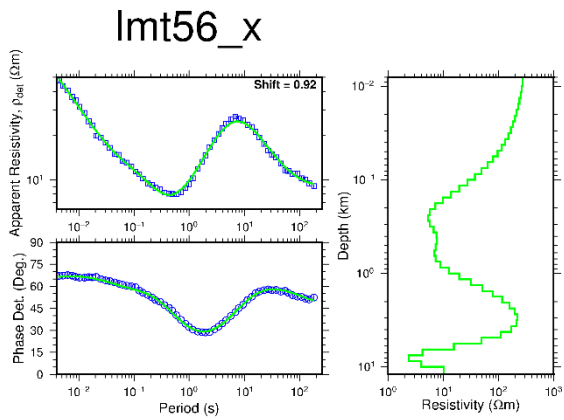
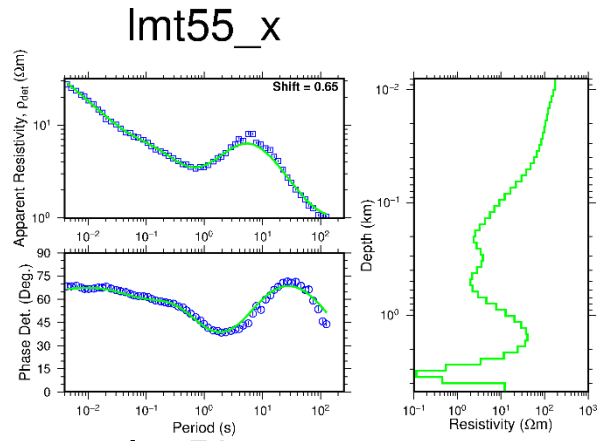
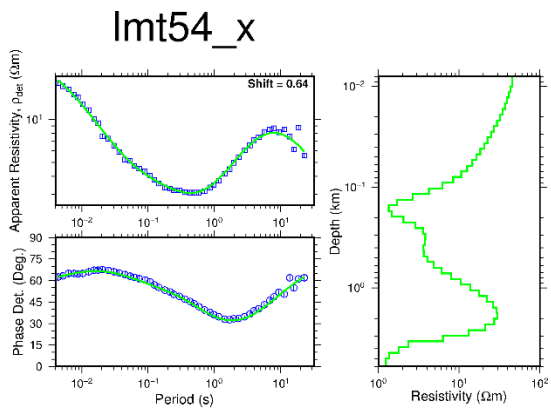
Results of MT 1-D inversion data models. Blue squares are measured MT apparent resistivity. Blue circles are the measured phase. Both the apparent resistivity and phase are gotten from the determinant of the MT impedance tensor. Green solid lines on the right indicate results of the 1-D resistivity Occam inversion model. The green solid lines on the left panels are calculated responses. The number on top of the figure is the MT station name. The number to the upper right corner is the static shift from geospatial distribution map.

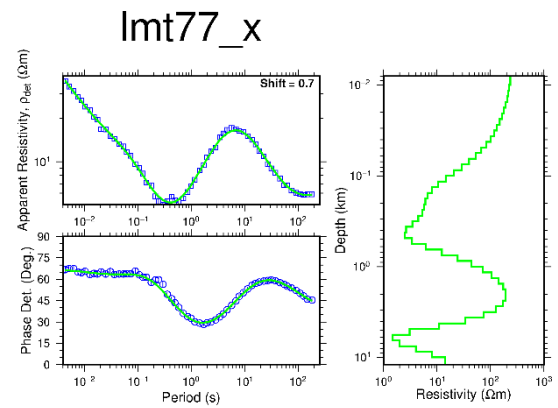
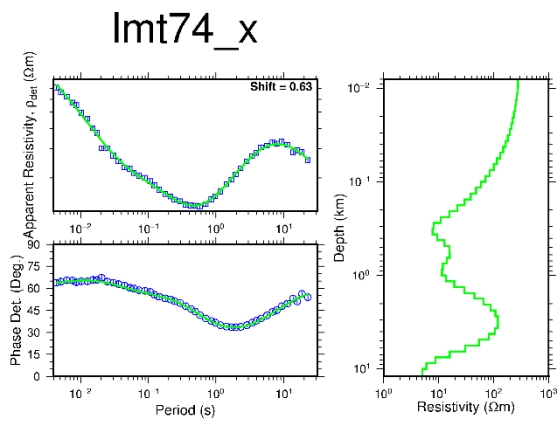
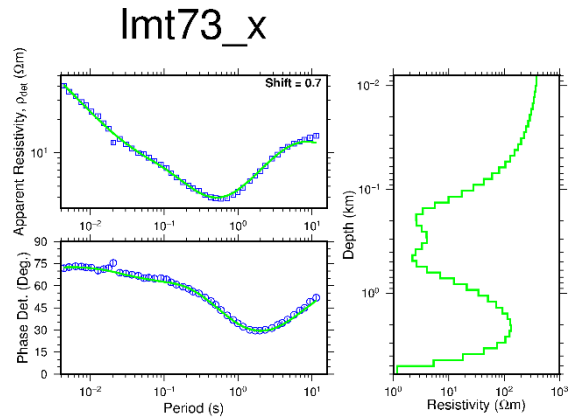
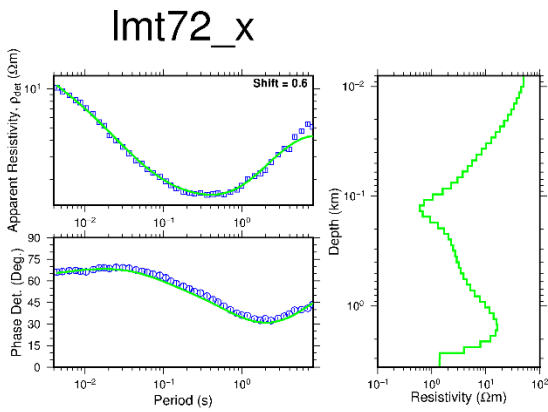
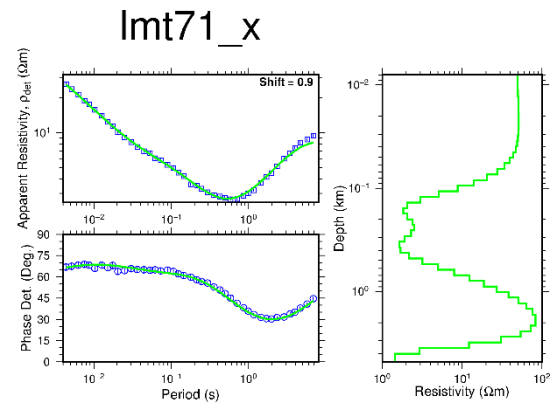
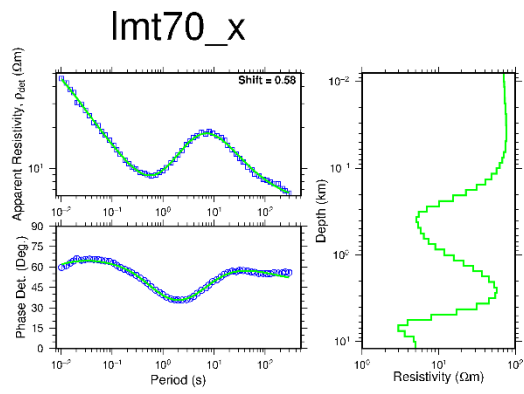
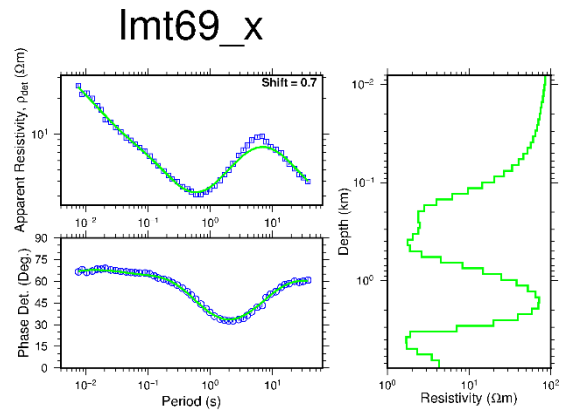
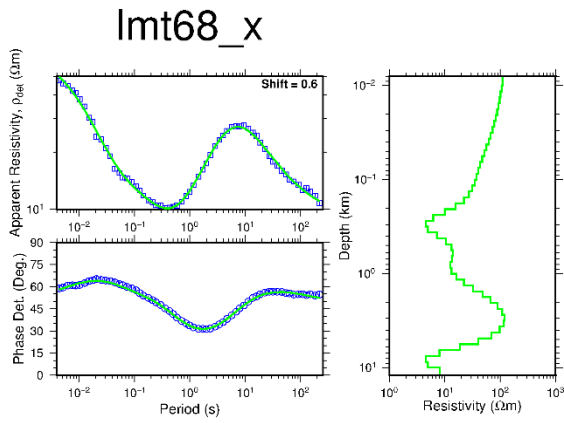


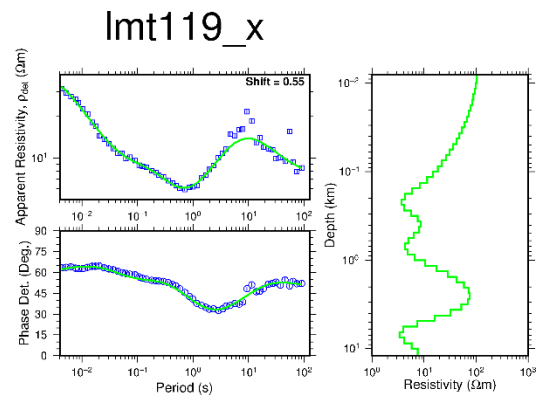
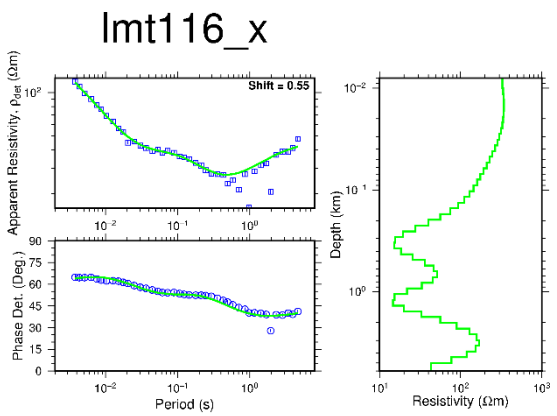
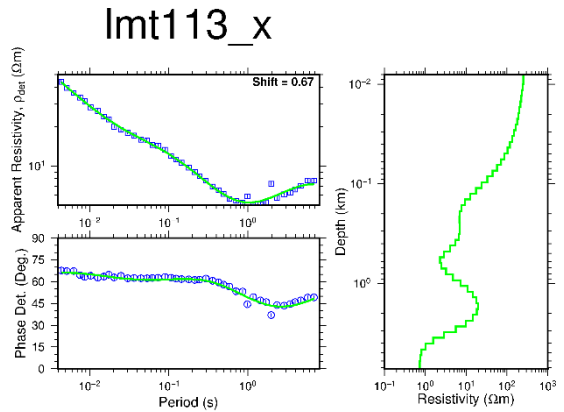
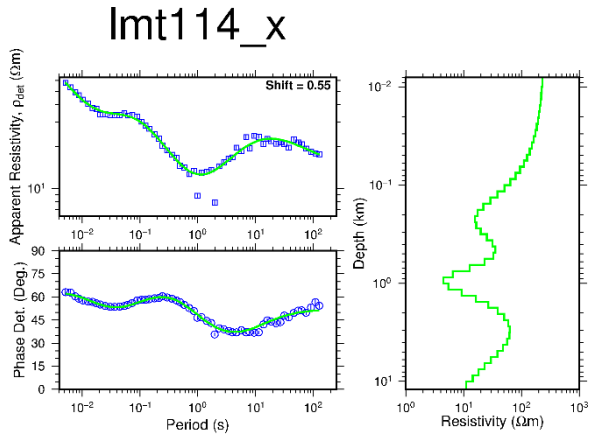
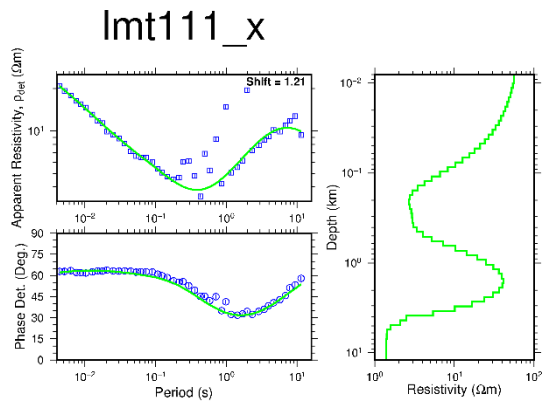
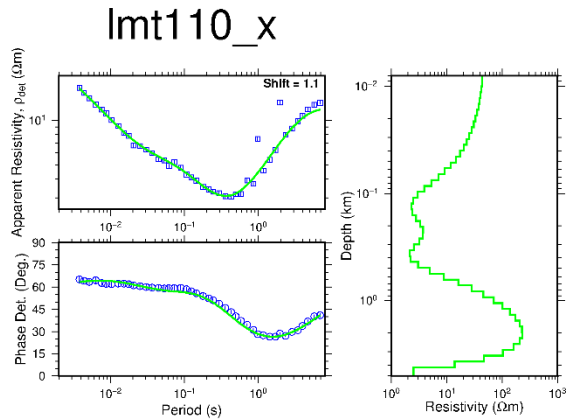
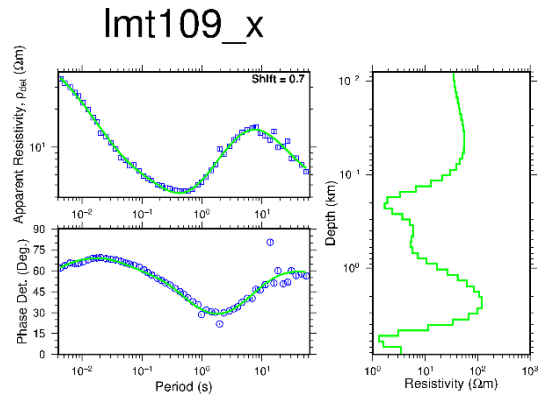
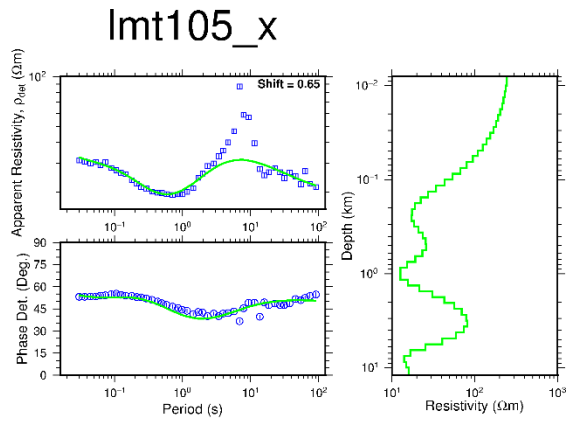












APPENDIX E: Resistivity depth slices

Resistivity depth slices were amassed covering soundings from Mt. Longonot area. The data were used to achieve a general knowledge of the resistivity spreading in area which is a high-temperature geothermal area. The 1-D Occam models were used to generate the resistivity depth slices using the TEMRESD program.

